Strategies to improve the immunogenicity of subunit vaccine candidates

By

Yangjie Wei

Submitted to the graduate degree program in Pharmaceutical Chemistry and the Graduate Faculty of the University of Kansas in partial fulfillment of the requirements for the degree of Doctor of Philosophy.

_____

Chairperson: C. Russell Middaugh, Ph.D.

_____

Wendy L. Picking, Ph.D.

_____

William D. Picking, Ph.D.

_____

Teruna J. Siahaan, Ph.D.

_____

Prajnaparamita Dhar, Ph.D.

Date Defended: October 02, 2018

The Dissertation Committee for Yangjie Wei

certifies that this is the approved version of the following dissertation:

Strategies to improve the immunogenicity of subunit vaccine candidates

Chairperson: C. Russell Middaugh, Ph.D.

Date Approved: October 02, 2018

Abstract

Subunit vaccines contain highly defined macromolecular components of a pathogen that are capable of eliciting protective immunity. They possess several advantages over other vaccine types (e.g. live attenuated and inactivated) such as improved safety profiles, highly defined nature, ease of production, and potential for lower cost of goods. One critical limitation of subunit vaccines, however, is their weak immunogenicity owing to their inability to replicate, monovalent structures, and the absence of other immunostimulatory components. Common approaches to enhance the immunogenicity of subunit vaccines include polyvalent antigen display strategies, the use of adjuvants, etc. The polyvalent antigen display strategy requires the use of a scaffold, which can be protein-based or some other materials. Chapter 2 focuses on the biophysical properties of a potential scaffold for polyvalent antigen display-*Bacillus anthracis* lumazine synthase (LS), an icosahedral homo-oligomeric protein. LS in PBS buffer showed a minor thermal transition around 50 ^{o}C, and a major one at 95 ^{o}C. The minor transition arose from the dissociation of the LS/phosphate complex, which formed in PBS buffer at room temperature. The major transition corresponded to the dissociation of LS oligomers, thermal unfolding, and aggregation. In chapter 3, I describe an attempt to develop ricin vaccine candidates in which LS was used as a scaffold to achieve polyvalent display of a linear neutralizing epitope (designated PB10) from ricin. PB10 was genetically inserted onto the C terminus of LS, and the fusion protein (designated LS_PB10) was expressed in an *E.coli* system. LS_PB10 self-assembled into spherical particles. Fusion of the PB10 peptide did not affect the structure and stability of LS. LS_PB10 showed tight binding to a mAb targeting the PB10 epitope. Immunization of LS_PB10 in mice elicited a moderate level of anti-ricin serum titers, which, however, failed to offer protection during a challenge study using a 10x lethal dose of ricin. Such an unsatisfactory end result may be attributable to 1) limited

efficacies of using the PB10 epitope alone, 2) loss of secondary structure of PB10 on LS; 3) an epitope suppression effect induced by the highly immunogenic nature of the LS scaffold.

Studying antigen/adjuvant compatibility is critical for the development of adjuvanted vaccine formulations. Chapter 4 discusses the utilization of biophysical tools to understand effects of two emulsion-based adjuvants (designated as ME.0 and SE) on the structure and thermal stability of alpha-toxin (AT), a potential vaccine candidate for *Staphylococcus aureus* infection. Both adjuvants are oil-in-water (O/W) emulsions using squalene as the oil phase. DSC analysis showed the ME.0 emulsion thermally destabilized AT, probably because of changes in the buffer composition of AT upon mixing. The SE emulsion caused increased alpha-helix and decreased beta-sheet content in AT, and a blue shift in Trp fluorescence emission spectra of AT. DSC analysis showed SE exerted a dramatic thermal stabilization effect on AT, probably attributable to an interaction between AT and SE. Size exclusion chromatography showed a complete loss in the recovery of AT when mixed with SE, but not ME.0, indicating a high degree of interaction with SE.

The goal of protein formulation development is to identify optimal conditions for long-term storage. Certain commercial conditions (e.g., high protein concentration or turbid adjuvanted samples) impart additional challenges to biophysical characterization. Formulation screening studies for such conditions are usually performed using a simplified format in which the target protein is studied at a low concentration in a clear solution. The failure of study conditions to model the actual formulation environment may cause a loss of ability to identify the optimal conditions for target proteins in their final commercial formulations. In chapter 5, we utilized a steady-state/lifetime fluorescence-based high-throughput platform to develop a general workflow for direct formulation optimization under analytically challenging but commercially relevant

conditions. A high-concentration monoclonal antibody and an Alhydrogel-adjuvanted antigen were investigated. A large discrepancy in screening results was observed for both proteins under these two different conditions (simplified versus commercially relevant). This study demonstrates the feasibility of using a steady-state/lifetime fluorescence plate reader for direct optimization of challenging formulation conditions and highlights the importance of performing formulation optimization under commercially relevant conditions.

Dedicated to:

My parents Xuedong Wei and Wenying Yang,

My brother Yanglu Wei,

and especially my beloved wife Nan Bai

Acknowledgements

First, I would like to express my deepest gratitude to my advisor, Professor Russ Middaugh, for offering me an opportunity to work with him for the last four years. Russ is not only a great mentor with profound wisdom, but also a role model to me. His mentorship has significantly improved my scientific background, critical thinking skills, and writing skills. His passion for science and optimism about life have always been a continuous inspiration to me. I really appreciate his kindness in providing me enough freedom to pursue my scientific interests. My dissertation would not be possible without his guidance, support, and trust.

There are also several other professors, who have provided a tremendous amount of support to the completion of my Ph.D. thesis. I would like to thank Dr. Wendy Picking for allowing me to perform protein expression and purification in her lab to obtain experimental materials. Dr. David Volkin and Dr. Sangeeta Joshi have provided me with support and scientific guidance. I thank Dr. Nicholas Mantis from Wadsworth Center for his help and support on the ricin vaccine project (Chapter 3). In addition, I thank Dr. Bill Picking, Dr. Teruna Siahaan, and Dr. Prajnaparamita Dhar for agreeing to serve on my thesis committee. Their scientific input and knowledge have helped me to complete this dissertation and grow as an independent scientist. I thank all professors (from both the department of Pharmaceutical Chemistry and other departments), who have taught me scientific knowledge in both classes and seminars.

I would like to thank several fellow lab members, who have helped me with my experiments. I would like to first thank Dr. Newton Wahome (a former lab member) for his guidance and training at the very beginning of my Ph.D. career. I would like to thank Nick Larson for his help with the completion of the Chapter 5, to which we both contributed equally. I would

Last but not least, I thank my fellow graduate students in the Pharmaceutical Chemistry Program for their support and friendship. I would like to thank my parents for their support and help. They raised my brother and me in a small town in China. Although they had never attended college, they valued the importance of education and did their best to offer me a good education. Thanks to their support, I had the opportunity to go to a good college in China and later come to the United States to pursue a Ph.D. degree. I sincerely thank my wife, Nan Bai, for her love, support, and sacrifice. Her company has made my Ph.D. life a great journey to me.

Table of Contents

Chapter 1: Introduction

1.0.Overview

Vaccines are considered as one of the most significant medical innovations in modern times and are responsible for eliminating medical conditions cause by toxins, pathogenic bacteria and viruses. Vaccination has effectively controlled the spread of many diseases and some have even been eradicated (e.g. smallpox) with others probably soon to follow. Vaccines are, therefore, considered as one of the most significant medical innovations (1, 2). An effective vaccine needs to elicit protective immune responses targeting a specific type of pathogen without itself causing the disease. Traditional vaccines were primarily based on live attenuated or inactivated pathogens. Even though they are typically highly effective in inducing protective immune responses in the host, there are often safety concerns with these types of vaccines. For example, live attenuated vaccines could possibly regain pathogenicity by reverting to their wild type forms especially in people with immuno-deficiencies (3-8). In addition, such vaccines often require critical storage conditions to maintain their immunological activity (9). Accidental exposure to environmental stresses (e.g. light or temperature) could cause a loss of immunogenicity (10). Inactivated vaccines can also sometimes cause side effects at some frequency in target populations (11-13). Batch-to-batch variability could also be an issue for such vaccines especially when cultures of pathogenic organisms are produced at a large scale (14). Thus, there is a demand for the development of a class of safe, effective and stable vaccines. The early development of toxoid-based vaccines suggests the viability of such an approach. Advances in immunology and pathology have helped to elucidate host-pathogen interactions and identify the components within pathogens that are responsible for protective immunity. Furthermore, the development of recombinant DNA technology provides the ability to produce large quantities of proteins (often referred to as "subunits") that can be used for this purpose. Subunit vaccines are highly defined biological

entities derived from specific components (e.g. a surface protein) of the pathogen. They have improved safety profiles and much less batch-to-batch variation than live attenuated or inactivated vaccines (15). In addition, subunit vaccines can be produced in a less expensive and more efficient manner. However, the immunogenicity of subunit vaccines is usually relatively low due to their monomeric nature and the absence of other immuno-stimulatory components (16).

As shown in Figure 1.1, common strategies to improve the immunogenicity of subunit vaccines include polyvalent antigen display, co-administration of adjuvants, the use of antigen delivery systems, etc. The polyvalent antigen display strategy functions by presentation of multiple copies of subunit vaccines or epitopes in an ordered manner on the surface of a scaffold. The clustering of subunit vaccines creates a polyvalent structure that enables strong "avidity" interactions with B cell receptors. The scaffold can be organic (e.g. proteins) or inorganic systems (e.g. gold nanoparticles). If a protein-based scaffold is used, this strategy is often referred as a virus-like particle (VLP) strategy. Adjuvants activate the immune system by a variety of mechanisms including recruitment of immune cells, enhanced antigen uptake, and engagement of Toll-like receptors. Though fundamental understandings of the mechanism of adjuvant action have been dramatically enhanced in recent decades, a comprehensive mechanistic picture is still lacking. An important analytical aspect related to the use of adjuvants is to investigate antigen/adjuvant comparability to ensure the stability and efficacy of the mixture. Efficient antigen delivery systems use biocompatible and biodegradable polymers to incorporate antigens of interest and slowly release antigens in a controlled manner. Such sustained antigen release profiles mimic repeated immunizations and results in long lasting immune responses. In this chapter, I will introduce these strategies with a specific emphasis on the VLP strategy.
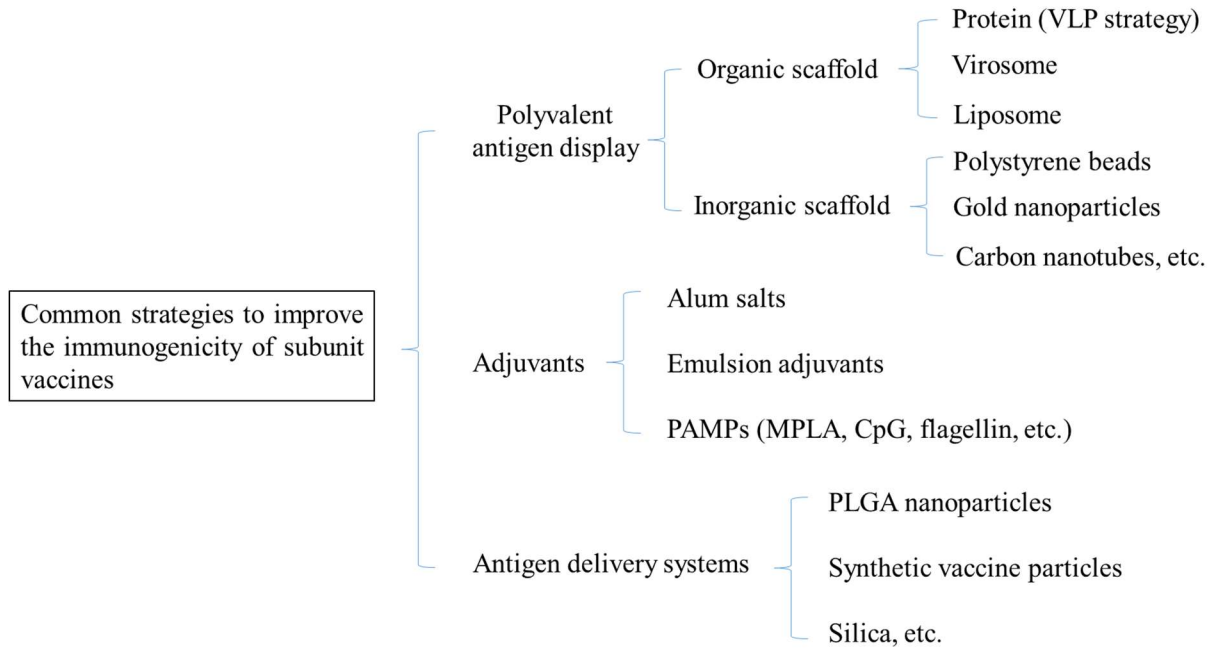
Figure 1.1 Common strategies to improve the immunogenicity of subunit vaccines

1.1. VLP strategy

An effective means to improve the immunogenicity of subunit vaccines is the use of virus-like particles (VLP), which have been developed based on an understanding of high intrinsic immunogenicity of viral pathogens (17). VLPs form an oligomeric protein scaffold capable of presenting immunogenic epitopes and proteins in a highly efficient manner. VLPs are large protein complexes with structures highly analogous to viruses (18). VLPs are considered to be safe since they are non-replicative and devoid of nucleic acids (i.e., DNA, RNA) (19). VLPs are highly immunogenic in nature. Similar to actual viruses, VLPs present multiple copies of antigenic epitopes on their surfaces, resulting in a high local density of structurally ordered epitopes capable of high avidity interactions with B-cell receptors (BCRs) (Figure 1.2), which stimulates strong BCR signaling and strong immunostimulation (e.g. T helper cell-independent B cell activation)

(20-24). Thus, in contrast to monomeric antigens, VLP-based vaccines can elicit immune responses much more efficiently (25). Second, due to their particulate nature and relatively large size (20-200 nm) (26), VLP are efficiently taken up and processed by professional antigen presenting cells (APCs) such as dendritic cells (DCs) and macrophages. DCs present VLP-derived peptides to CD4+ T helper cells, facilitating strong humoral and cellular immune responses (21, 22, 27). VLPs have been successfully employed to develop vaccines for Hepatitis B and human papillomaviruses (HPV, cervical cancer). Many additional VLP-based vaccines are under development (28).
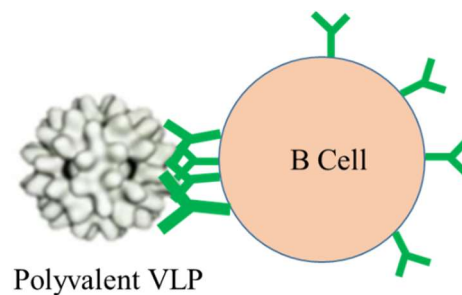
Figure 1.2. The high avidity interaction between a polyvalent VLP and B cell receptors ("Y" shape). The VLP consists of multiple copies of a homo-subunit. Multiple B cell receptors recognize and bind to a VLP simultaneously, resulting in stronger downstream immunological responses.

The VLP strategy can also be applied to enhance the immunogenicity of a monovalent immunogen by employing a self-assembling protein scaffold. A monovalent immunogen of interest can be genetically fused to a subunit of the self-assembling protein scaffold. Correct assembly of the fusion protein complex enables polyvalent presentation of the immunogen on the scaffold surface in an ordered manner to form a pseudo-VLP structure. Currently, various self-

assembling protein systems have been explored as potential VLP scaffolds. Here, we studied the feasibility of an icosahedral bacterial protein-Lumazine synthase-as a protein scaffold for polyvalent antigen display using a model epitope derived from ricin toxin.

1.1.1. Lumazine synthase

Lumazine synthase (LS) is an enzyme involved in the biosynthesis of riboflavin (vitamin B_2), a compound essential for a myriad of biological processes. During cellular metabolism, riboflavin is converted to flavin mononucleotide (FMN) and flavin adenine dinucleotide (FAD), which function as cofactors for a wide range of enzymes involved in cell-based redox reactions. FMN and FAD have also been found to play important roles in several non-redox biological processes such as DNA repair (29).

Humans and other animals cannot synthesize riboflavin by themselves and can only obtain it from nutritional sources. Riboflavin is produced *de novo* in plants, fungi and most microorganisms (29, 30). The synthesis pathway of riboflavin in a variety of species has been described in detail in several research and review papers (31-35). Of these, the bacterial pathway of riboflavin synthesis is the most extensively studied. In bacteria, the synthesis of riboflavin uses guanosine-5'-triphosphate (GTP) as the initial substrate and involves reactions catalyzed by several enzymes. During the terminal steps of riboflavin biosynthesis, LS synthesizes lumazine, which is then converted to riboflavin. LS is composed of homo-oligomers which vary in size and subunit number depending on its species of origin. Because of its oligomeric nature, LS has been widely used for a variety of biomedical applications including antigen presentation, drug delivery and bioengineering among others. Here, we will first briefly discuss the enzymatic mechanism and structural properties of LS, and then focus on applications of LS in the biomedical field with an emphasis on its use for vaccine development (Figure 1.3).
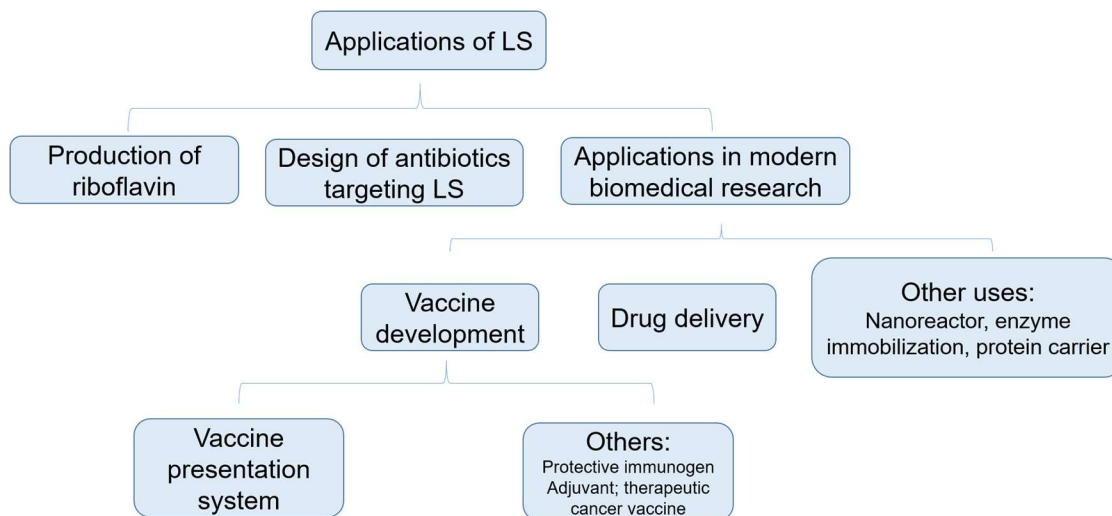
Figure 1.3. Biomedical applications of LS

1.1.2. The discovery of LS

LS was first discovered from *Bacillus subtilis* in the 1970s, when two proteins related to riboflavin synthesis were purified by sucrose density gradient ultracentrifugation (36). The sedimentation velocities of these two proteins were 4.1 S and 26.5 S. They were therefore named "light" and "heavy" riboflavin synthase (RS), respectively. The light RS (4.1 S) was found to be a homo-trimer, which is now known as RS. The heavy RS (26.5 S) showed two bands on sodium dodecyl sulfate polyacrylamide gel electrophoresis. One of these two bands corresponded to the subunit of the light RS (*i.e.*, 4.1S riboflavin synthase). The second protein was hypothesized to consist of sixty copies of a 15 kD monomer that was later named LS, after its biological function was fully elucidated. The heavy RS contains both RS subunits (designated as the α subunits) and LS subunits (designated as β subunits). The crystal structure of the heavy RS was solved in 1983 and its unusual α3β60 stoichiometry was confirmed (37). LS from *Bacillus subtilis* (BsLS) forms an icosahedral quaternary structure (T = 1) consisting of 60 identical subunits with a hollow cavity

in which one trimeric RS molecule is enclosed. These two enzymes form a bi-functional protein complex which catalyzes the last two steps of riboflavin biosynthesis.

1.1.3. Enzymatic mechanisms of LS

The catalytic reaction mediated by RS and LS is illustrated in Figure 1.4. GTP is first converted to 5-amino-6-ribitylamino-2, 4 (1H, 3H)-pyrimidinedione (compound 1) through several catalytic reactions. Compound 1 is then condensed with L-3, 4-dihydroxy-2-butanone 4-phosphate (compound 2) to generate 6, 7-dimethyl-8-ribityllumazine (compound 3) by release of two water molecules and a phosphate ion. The enzyme catalyzing the formation of lumazine (compound 1 + compound 2 → compound 3 + 2 H_2O + PO_4^{3-}) is named *lumazine synthase*. Compound 3 is then converted by RS to form riboflavin (compound 4) and compound 1, which can again be used to synthesize riboflavin. The terminal step of riboflavin biosynthesis is thereby a cyclic reaction. This cyclic pathway is conserved in all flavinogenic organisms, and the structures of LS subunit and enzymatic active sites are almost identical among different organisms.
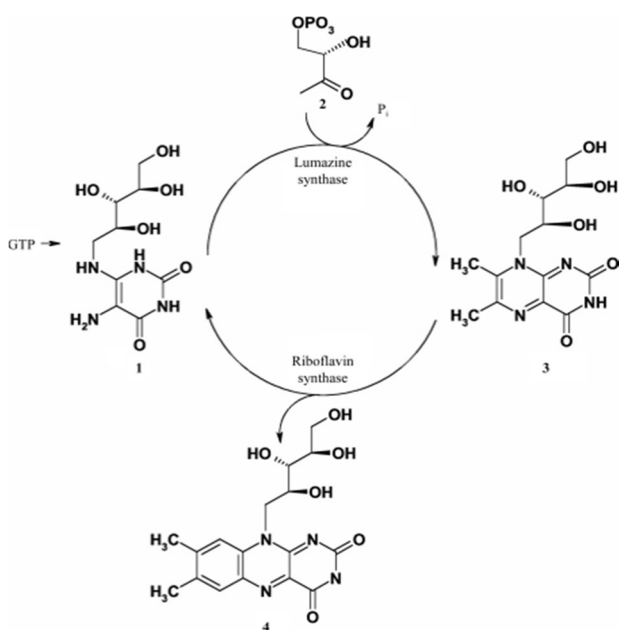
Figure 1.4. The biosynthetic cycle of riboflavin (38). Compound **1**: 5-amino-6-ribitylamino-2, 4 (1H, 3H)-pyrimidinedione; compound **2**: L-3, 4-dihydroxy-2-butanone 4-phosphate; compound **3**: 6, 7-dimethyl-8-ribityllumazine; compound **4**: riboflavin. (This figure is from an open-access article distributed under the terms of the Creative Commons Attribution License, which permits unrestricted use, distribution, and reproduction in any medium.)

1.1.4. Structural properties of LS
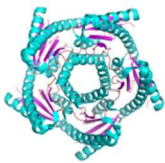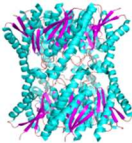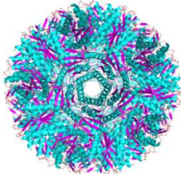
The LS subunit shows a typical α/β/α-sandwich topology (Figure 1.5 A). Four parallel stranded β-sheets (β2- β5) are flanked by two α-helices on one side (α2, α3) and three on the other (α1, α4, α5). An additional β-sheet (β1) may also be present at the N-terminus, but this is not always the case (e.g. LS from *Bacillus anthracis*) (39). If present, each β1 forms an inter-subunit β sheet with an adjacent monomer within an oligomeric block of LS. The fifth β-sheet (β1) offers additional stability to LS oligomers. LS does not exist in monomeric form in nature, but assembles into homo-oligomers with various quaternary structures.

1.1.4.1. Diversity of the quaternary structures of LS

The oligomeric states of LS vary depending on its species of origin (Table 1.1). LS can be a pentamer, decamer, or even icosahedral sixty-mer (Figure 1.5). The structure of the pentameric LS from *Brucella abortus* (PDB ID: 1DI0) is shown in Figure 1.5 B. Each subunit is shown in a different color. Every five α3 helices within this pentamer form a channel along its five-fold symmetry axis. The assembly of the decameric LS derived from *Brucella spp.* RibH2 (PDB ID: 1XN1) is shown in Figure 1.5 C and 5 D. Two pentameric blocks that bind to form the decamer are shown in cyan and magenta. Figure 1.5 C shows the lateral view of this decameric LS. In Figure 1.5 D, the view is along its five-fold symmetry axis. In Figure 1.5 E, the icosahedral

structure of LS from *Aquifex aeolicus* (PDB ID: 5MPP) is illustrated. It consists of twelve

pentamers shown in different colors. Their multiple quaternary orders not only affect the thermal

stability of LS (40) but also offer diverse choices for vaccine use.

Table 1.1. Oligomeric states of LS from different organisms

Oligomeric state of lumazine synthase	Quaternary structure	Organism	PDB ID
Pentamer		*Brucella abortus* (41) *Brucella abortus* RibH1 (42) *Brucella Mesorhizobium loti* RibH2 (42) *Brucella melitensis* RibH1 (42) *Candida albicans* (43) *Magnaporthe grisea* (44) *Mycobacterium tuberculosis* (45-48) *Mycobacterium leprae* (49) *Saccharomyces cerevisiae* (50) *Schizosaccharomyces pombe* (51)	1DI0 2F59 ; 2I0F 2OBX 2O6H 2JFB 1C41 2VI5; 2C9B; 2C92; 2C94; 2C97; 2C9D; 1W19; 1W29 4J07 1EJB 1KYV; 1KYX; 1KYY
Decamer		*Brucella spp.* RibH2 (52, 53) *Candida glabrata* (54) *Mesorhizobium loti* (42)	1T13; 1XN1 4KQ6 2OBX
60-mer		*Aquifex aeolicus* (55-58) *Bacillus anthracis* (38) *Bacillus subtilis* (59) *Escherichia coli* *Spinacia oleracea* (44) *Salmonella typhimurium* (60)	1HQK; 1NQU; 1NQV; 1NQW; 1NQX; 5MPP* 4V7G 1RVV N.A. 1C2Y 3MK3

* indicates that the structure (PDB ID: 5MPP) was solved by cryo-electron microscopy
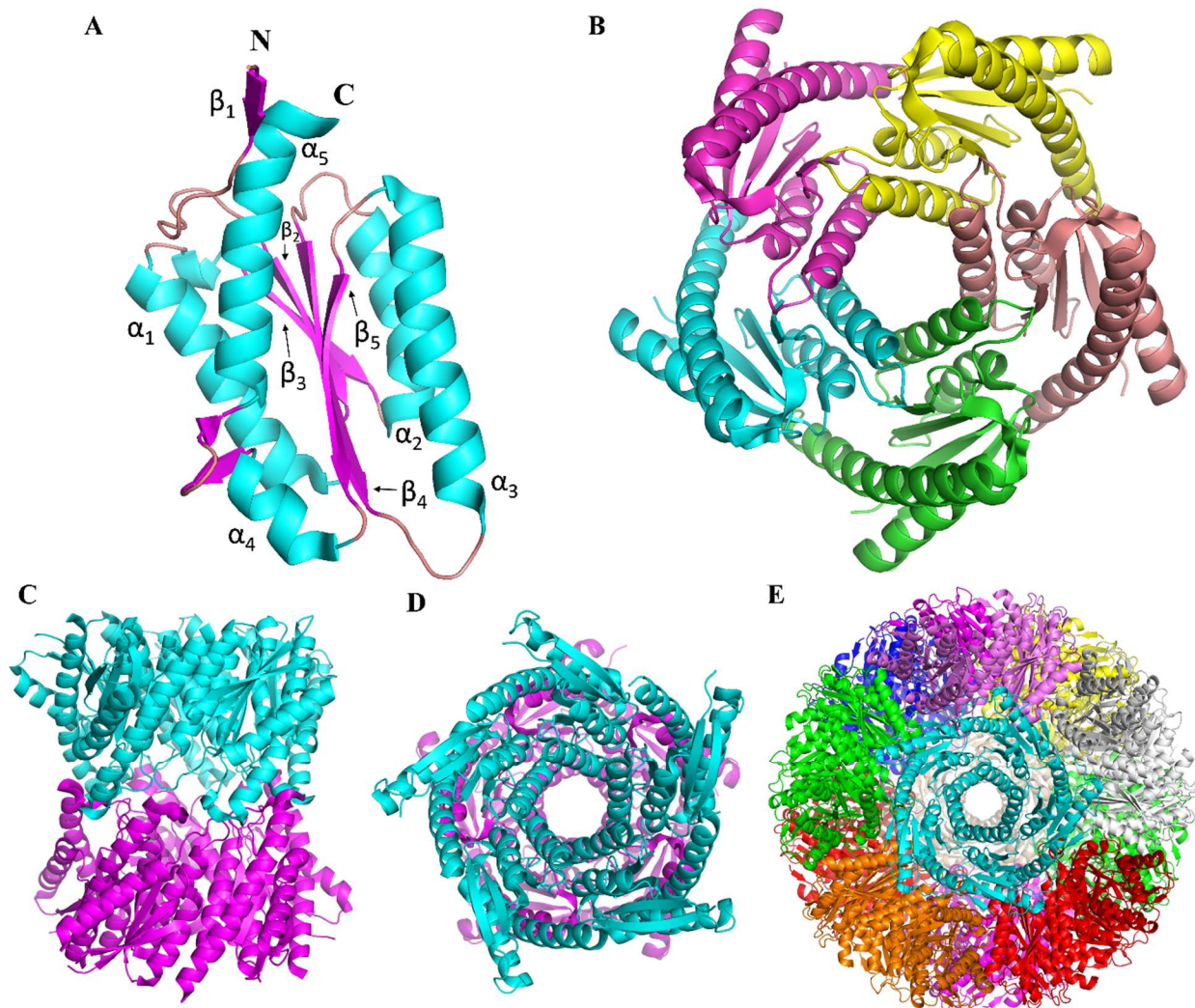
Figure 1.5. Various assembly states of lumazine synthase. (A) Folding pattern of a lumazine synthase monomer from *Aquifex aeolicus*. This LS subunit has a typical α/β/α-sandwich topology. Four parallel stranded β-sheets (β2- β5) are flanked by two α-helices on one side (α2, α3) and three on the other side (α1, α4, α5). N- and C- termini are also marked. (B) The structure of the pentameric lumazine synthase from *Brucella abortus* (PDB ID: 1DI0). Each monomer is shown in a different color. Every five α3 helices within this pentamer form a channel with five-fold symmetry axis. (C and D) The assebmly of the decameric lumazine sythase derived from *Brucella spp.* RibH2 (PDB ID: 1XN1) is shown in lateral and frontal views. Two pentameric blocks

consisting the decamer are shown in cyan and magenta. (E) The icosahedral structurer of lumazine synthase from *Aquifex aeolicus* (PDB ID: 5MPP). It consists of twelve pentamers shown in different colors viewed along its five-fold symmetry.

Fornasari *et al.* have performed a combined analysis to identify the sequence determinants of the diversity of quaternary structures of LS based on protein sequence, structure, and evolutionary information (39). The analysis showed that sequence sites involved in the icosahedral contact interfaces were significantly more conserved than the corresponding sites in non-icosahedral LSs. Eight sequence sites were identified as primarily responsible for the formation of icosahedral LSs. A striking finding of this analysis is that the K131 residue is found to be 100% conserved among all known icosahedral LSs, but nearly absent in non-icosahedral LSs. The K131 side chain projects towards its adjacent pentamer, and this residue shows a larger decrease in entropy in an icosahedral LS than in a non-icosahedral LS. Chen *et al.* has studied the effect of point mutations at pentamer-pentamer contact sites on the assembly state of LS from *Aquifex aeolicus* (AaLS) (61). These sites involve three different types of interactions: ionic (R40), hydrophobic (L121 and I125), and hydrogen bonding (H41). A comprehensive point mutation analysis indicates that mutation of two or three of these types of residues could generate pentameric LS, suggesting their importance in maintaining the icosahedral assembly of AaLS.

LS from *Bacillus subtilis* (BsLS) was the first LS to be identified and is consequently the most extensively studied icosahedral LS. BsLS consists of 60 monomers with a triangulation number of 1 (T = 1). It has a spherical shape formed by twelve identical pentamers. The particle size of BsLS is ~16 nm and the diameter of its hollow cavity around 9 nm (59). The channel formed by five α3 helices within each pentameric block is a possible port for substrate entry and product exit.

The substrates (compound 1 and 2) bind to active sites on LS, which are located at the interface of two neighboring subunits within a pentamer (62). For icosahedral LS, the active sites are enclosed inside the LS cavity. The number of active sites of LS is equal to the number of subunits, with all active sites being topologically equivalent. The catalyzed condensation reaction by LS was found to be strictly regio-specific (63). The interactions between substrates and residues in active sites involve electrostatic, hydrogen bonding, hydrophobic and π-π interactions. Main residues involved include Arg 127, Thr 86 and Phe 22 (numbered based on BsLS) (64). Both Arg 127 and Thr 86 are highly conserved among all known LS. Arg 127 provides a binding site for the phosphate group of the compound 2 via electrostatic interaction. Mutation of Arg 127 to histidine or lysine resulted in the reduction of catalytic rate by 38% and 91%, respectively (55). Compound 2 also hydrogen bonds with Thr 86 and several other surrounding residues. Phe 22 stabilizes the binding of compound 1 to the active site by π-π interaction. Phe 22 is replaced by Trp 22 in some orthologs of LSs.

Another important feature of some icosahedral LSs is the formation of the heavy enzyme complex with the trimeric RS. For instance, the icosahedral BsLS encloses RS inside its interior cavity and the resulting complex is historically designated as "heavy riboflavin synthase". The formation of the BsLS/RS complex is found to improve the rate of riboflavin formation through a substrate-channeling mechanism (65). Inside BsLS/RS complexes, their catalytic sites are in very close proximity, which results in the accumulation of the intermediate in a confined volume inside the BsLS cavity and thereby an increase of the overall reaction rate. The substrate-channeling mechanism is important for the production of riboflavin especially when the substrate concentrations are very low. The compartmentalization of the intermediates inside the BsLS/RS complex may also contribute to protecting them from side reactions and therefore improve the

efficiency of catalysis (62). A variety of *Bacillus* strains have been found to express the LS/RS complex, which, however, does not exist in some other microorganisms (36). For example, LS derived from *E. coli* exists as a hollow icosahedral structure and does not enclose its RS. Currently, it is still unknown whether the LS/RS complex is formed in plant cells.

1.1.4.2. Structural stability of LS

Several types of non-covalent interactions drive the formation of LS capsids. These include hydrophobic interactions, hydrogen bonding and ionic contacts (66). Thermal unfolding studies of LSs performed by differential scanning calorimetry have established their exceptional thermal stability (67). The apparent melting temperatures of icosahedral AaLS and BsLS were 120°C and 93°C, respectively. Even the pentameric LS from *S. cerevisiae* manifested an apparent melting temperature of 74 °C. The higher melting temperature of icosahedral LS (relative to pentameric LS) is apparently a consequence of the icosahedral LS's ability to form more stabilizing contacts as a capsid, and a reduction in accessible apolar surface areas. Being the most thermally stable LS known, AaLS possesses the largest charged surface area consistent with a stabilization effect of surface ionic networks (67).

LS has also shown exceptional stability in response to chemical denaturants such as urea and guanidine HCl. Zylberman *et al.* has studied the chemical unfolding of decameric LS derived from *Brucella sp.* (BspLS) in the presence of urea or guanidine HCl at pH 7.0 and 25 °C (40). It was found that BspLS incubated with 8 M urea did not show a significant change in its secondary, tertiary or quaternary structure, suggesting its extreme conformational stability. In contrast, a two-phase denaturation profile was observed for BspLS in the presence of increasing concentrations of guanidine HCl. The addition of 2 M guanidine HCl was able to dissociate the decamer into pentamers, which further became unfolded monomers at higher guanidine HCl concentration. The

free energies of unfolding of BspLS for each step were found to be 90 ± 20 kJ/mole and 315 ± 15 kJ/mole, respectively. Wei *et al.* has recently investigated the chemical unfolding of an icosahedral LS from *Bacillus anthracis* (BaLS) in PBS at 25 ℃ (68). It was found that the urea induced unfolding kinetics of BaLS was much slower than that produced by guanidine HCl. In addition, BaLS partially unfolded but still retained its icosahedral assembly in response to 8.5 M urea. However, the addition of 3 M guanidine HCl completely unfolded BaLS. The guanidine HCl induced unfolding of BaLS was found to be a multiphasic process involving the appearance of a molten globular state.

The conformational stability of LS is governed by various factors such as pH, ligand concentration, and ionic strength (40, 69, 70). The effects of each factor are discussed briefly here. The capsid of LS from *Bacillus subtilis* (BsLS) was found to be stable within a relative narrow pH range near physiological neutrality. The electrostatic energy for subunit interactions within a pentamer of BsLS was calculated as a function of pH (62). The pentamer was found to be most stable at pH 8. Icosahedral BsLS was found to dissociate and reform a larger capsid with a size of 29 nm in 0.1 M Tris buffer at a pH above 7.0 (70). This finding was compatible with a later finding by Zhang *et al.* on the multiple assembly states of BsLS detected using small angle X-ray scattering and electron microscopy (69). Zylberman *et al.* found that BspLS dissociated at a pH less than 5.0 (40). Wei *et al.* observed that BaLS formed irreversible aggregates at a pH below 4.0. Precipitation was observed when the icosahedral BaLS was dialyzed in citrate-phosphate buffer at pH 3.0 and 4.0 (68). The thermal stability of BaLS was evaluated across a pH range of 5.0 to 8.0 using various biophysical techniques. The multiple biophysical data sets collected were further processed to generate an empirical phase diagram (71) for visualization of the pH dependent

thermal stability of BaLS. The data show that BaLS had its greatest thermal stability at pH 7.0 followed by pH 6.0 and 8.0.

The binding of substrate 1 (i.e. compound 1 in Figure 1.4) analogs or divalent phosphate ions to the active sites of LS could potentially stabilize the enzyme (70). Substrate 1 analogue (5-nitroso-6-ribitylamino-2,4(1H,3H)-pyrimidinedione) was found to suppress the dissociation of icosahedral BsLS in 0.1 M Tris buffer at a pH above 7.0 (70). Wei *et al.* studied the role of phosphate ions in the thermal stability of BaLS (68). A small but distinct transition was observed before the main thermal transition of BaLS in phosphate containing buffers. Further investigation revealed that this small thermal transition was derived from the dissociation of phosphate ions from the active sites of BaLS. The melting temperature of this thermal transition increases with the concentration of phosphate ions. An interfacial energy calculation performed on the subunit pentamer based on the known crystal structure of BaLS showed that each phosphate ion stabilized the interface contact by approximately 6 kcal/mol. Because the interaction between phosphate ions and BaLS is ionic, it can be mitigated by increased ionic strength. Thus, the melting temperature of the first transition of BaLS decreased with increasing NaCl concentration.

1.1.5. Biomedical applications of LS

Research on the biosynthetic process of riboflavin started in the 1950s (72). The driving force to study riboflavin biosynthesis has evolved along with advances in the biotechnology industry (Figure 1.3). Its research goal in the early stage was to use flavinogenic microorganisms for the production of riboflavin (73). Later, it involved the understanding of the highly conserved riboflavin biosynthesis cycle and design of molecular inhibitors of essential enzymes (e.g., LS and RS) for the development of broad-spectrum antibiotics. The fact that LS is present in plants and microorganisms and absent in humans and other animals has made it a potential antibiotic target

(74). Many studies have concerned the development of inhibitors targeting LS by synthesis of analogs of substrates and intermediates (38, 45, 75-88). In one such study, Morgunova *et al.* have shown binding of different substrate-analogue inhibitors to the catalytic site of LS from *Candida albicans* (89). Shankar *et al.* have also designed molecular inhibitors targeting LS derived from pathogenic *Candida glabrata* for the development of antifungal drugs (54). In a recent study, Junaid *et al.* have shown binding between soluble fullerene C60 derivatives and potential drug targets, including LS (90). The C60 derivatives showed strong interactions with the binding sites of LS with the interaction strength higher than their known protein ligands and inhibitors, thereby showing the potential of fullerene C60-like molecules as therapeutics agents targeting LS.

In recent years, the development of nanotechnology and bioengineering has extended the application of LS to modern biomedical applications, including vaccine development (91, 92), targeted drug delivery (93-95), and protein "containers" (96-99). Our primary focus in this review is on its pharmaceutical applications, especially its use as a vaccine carrier.

1.1.5.1 Applications of LS in vaccine development

There is considerable interest in LS as a vaccine platform, especially the decameric and icosahedral forms. As an oligomeric protein complex, LS effectively forms a virus-like particle (VLP) scaffold capable of presenting immunogenic epitopes and proteins in a highly efficient manner.

LS, especially the decameric and icosahedral forms, have the potential to serve as VLPs for the purpose of vaccine development with notable advantages over the HBV and HPV-like VLPs. For example, X-ray crystal structures of most LSs have revealed that both the N and C termini of the monomers are surface exposed [10], permitting insertion of foreign antigenic sequences at two distinct sites. As discussed above, LS also has exceptional thermodynamic

stability. We assume that its highly stable nature would benefit the storage stability of LS-based immunogens. Berguer *et al.* demonstrated that the *Brucella spp.* LS stimulates mouse bone marrow DCs to up-regulate the expression of CD40, CD80 and CD86 and major histocompatibility class II (MHC II) antigens (100). The protein has also been shown to enhance levels of mRNA, chemokines and cytokines of the TLR4 pathway. A typical workflow for the development of LS based vaccines involves the synthesis of chimeric DNA sequences, protein expression and purification, thorough biophysical characterizations, and finally the evaluation of immunogenicity (Figure 1.6). The following section summarizes additional work which has used LS in vaccine development.
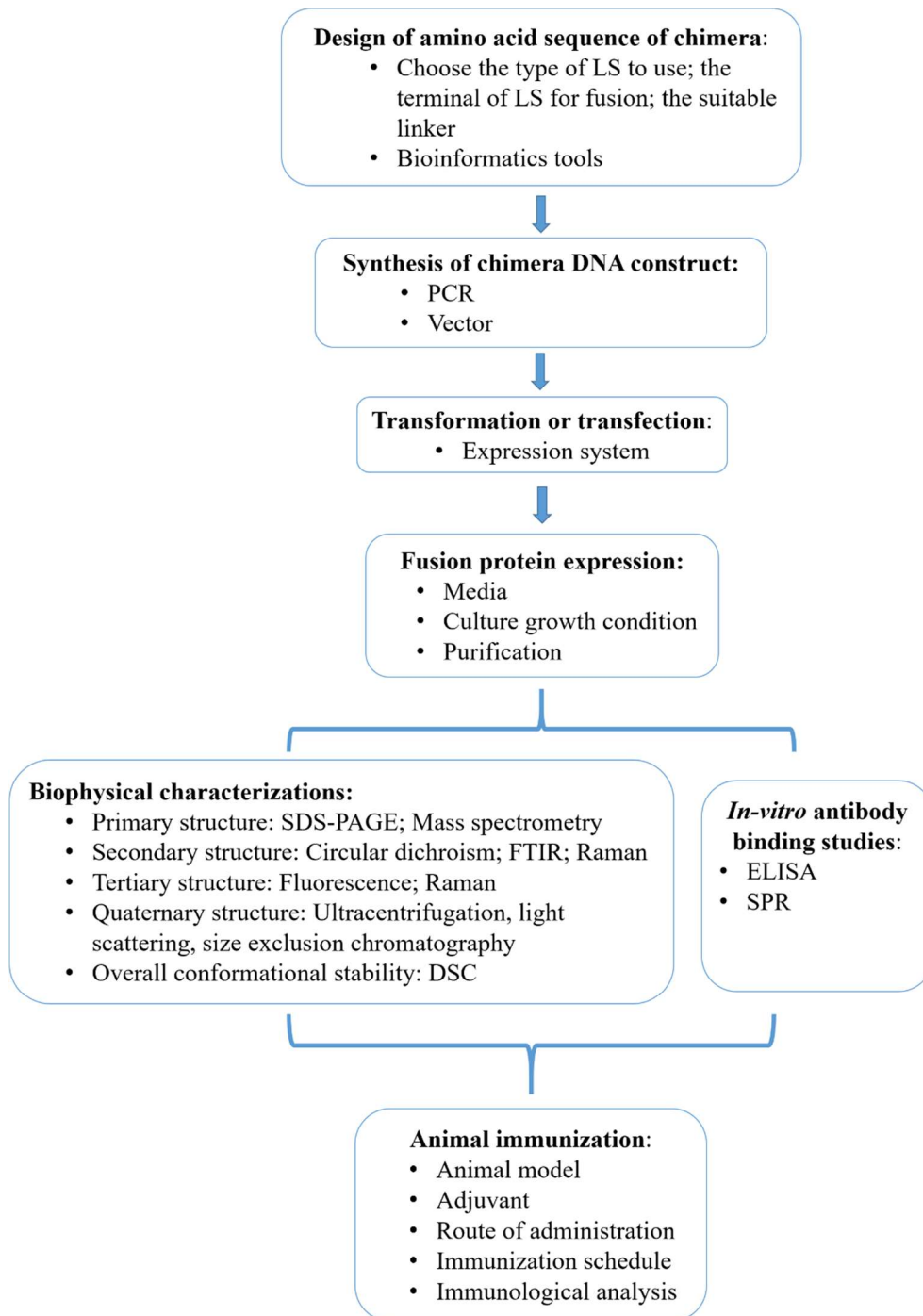
Figure 1.6. A common workflow for developing a lumazine synthase based vaccine presentation system for an antigen.

1.1.5.2. Research on the use of LS in vaccine development

Both decameric and icosahedral lumazine synthases have been extensively exploited as VLP-like presentation systems for a variety of antigens with significant success. In addition, LS itself has shown potential as a protective antigen, mucosal adjuvant, and therapeutic cancer vaccine.

1.1.5.2.1. Decameric LS presentation systems

The decameric LS derived from *Brucella spp.* (BspLS) was the first LS explored as a vaccine presentation system (101). BspLS is a highly stable scaffold comprising of a dimer of pentamers. Laplagne *et al.* studied BspLS as a protein carrier for foreign peptides. It was found that peptides of various lengths (up to 27 amino acids) could be fused to BspLS at its N-terminus. The insertion of these peptides did not cause a detectable change in the folding or stability of the carrier protein. Polyvalent chimeras presenting more than one type of polypeptide could also be generated by dissociation and reassembly of the mixture of monovalent chimeras.

In another study, Mejias *et al.* used BspLS as a stable scaffold to display the B subunit of Shiga toxin type 2 (Stx2B) as a strategy to elicit antibodies against enterohemorrhagic *Escherichia coli* (EHEC) (102). Stx produced by EHEC is responsible for food-borne diseases, systemic complications such as Hemolytic Uremic Syndrome (HUS). In spite of its high incidence, there are no available licensed vaccines or therapies for the treatment or prevention of EHEC infections. A functional immunogen was designed by the insertion of Stx2B at the amino terminus of BspLS. The chimeric immunogen induced strong and sustained anti-Stx2 antibody responses in adult BALB/c mice. The immunized and weaned mice showed complete protection against intravenous administration of Stx2 and EHEC oral challenge. In a similar study, Sacerdoti *et al.* demonstrated that the BspLS-Stx2B chimera induced the generation of high anti-Stx2B specific antibody serum

titers in adult Sprague Dawley female rats and prevented Stx2-induced complications associated with pregnancy loss (103). That same study also showed that pups that were nursed by immunized dams were protected against a lethal dose of Stx2. The BspLS-Stx2B chimera was studied for transferring resistance against Stx to offspring after maternal immunization of BALB/c mice (104). The pups were found to be completely protected against a lethal dose of Stx2 by injection and oral administration of Stx2 producing *E. coli* at weaning. In another study, Martorelli *et al.* vaccinated calves with a chimeric protein consisting BspLS and Stx2B (BspLS-Stx2B) or a trivalent combination vaccine consisting of BspLS-Stx2B, Intimin C280 and EspB (105). The authors found that BspLS-Stx2B appeared to stimulate the humoral responses of the other two antigens (Intimin C280, EspB) in the trivalent vaccine after a booster dose. It was concluded that including BspLS-Stx2B in the trivalent vaccine is necessary to elicit potent humoral responses against Stx producing *Escherichia coli*.

The decameric LS has also been examined for its use in protection against brucellosis. The *Brucella* parasite can infect livestock, potentially destroying their reproductive systems. The infection can also be transferred to humans. In view of the lack of a safe brucellosis vaccine for humans, subunit vaccines are potential candidates for protection against brucellosis. Previous subunit vaccines are lower in efficacy compared to conventional animal vaccines such as live attenuated *B. abortus* S19 (smooth) or strain RB51 (rough). Du *et al.* (106) have engineered a fusion protein immunogen by attaching a recombinant L7/L12 ribosomal protein of *Brucella suis* to *Brucella* LS. The fusion protein in rabbits elicited production of high levels of IgA and upregulation of interferon gamma in rabbit antiserum. Hence, while the *Brucella* L7/L12 protein is an effective immunogen, *Brucella* LS served as a suitable transport vector. In a similar study, *Brucella* outer membrane protein 31 (Omp31) has been presented on LS from *Brucella* as a potent

immunogen for protection against brucellosis in rams (107). The engineered chimera was used for immunizing different groups of rams by intramuscular (i.m.) or subcutaneous injections in adjuvants such as incomplete Freund's adjuvant (IFA). A DNA plasmid encoding the chimeric protein was also administered through i.m., electroporation, or a heterologous prime-boost strategy (multiple electroporations of the DNA plasmid followed by an i.m. injection of the chimeric protein in IFA). Both the chimeric immunogen in IFA (i.m.) and the prime-boost strategy were effective in inducing high IgG titers against *Brucella*. The highest levels of specific IFN-γ and immunity were conferred using the prime-boost and chimera in IFA strategies. Cassataro *et al.* (108) have explored immunization of BALB/c mice with a DNA vaccine encoding chimeric *Brucella* LS and Omp31. This vaccine elicited stronger protection against *Brucella ovis* than both co-delivering plasmids encoding individual proteins and whole *Brucella*. In a similar study, Du *et al.* have demonstrated that, compared to free Omp31, fusion of Omp31 with *Brucella abortus* LS elicited a much higher antibody titer in rabbits (109). These studies suggest the potential use of *Brucella* LS as a delivery vector for such antigens.

The use of *Brucella* LS as a bovine rotavirus antigen delivery system has been demonstrated. The antigen VP8d (the inner core domain from the VP8 spike protein) from C486 bovine rotavirus was expressed as a fusion protein with decameric LS in *E. coli* (110). Mice immunized with the fusion immunogen were reported to have a significantly higher level of protection (97.5-100%) against C486 bovine rotavirus than mice immunized with the mixture of *Brucella* LS and VP8d (44.2-80%) and VP8d alone (36.1-67.4%), confirming the use of the LS scaffold as a potent antigen delivery system for protection against bovine rotavirus. Alfano and coworkers have expressed the BspLS scaffold in plants fused to the VP8d antigen of bovine rotavirus (111). The N-terminally LS fused rotavirus antigen produced very high expression of the

stable and soluble protein in tobacco chloroplasts. The extracted recombinant chimeric protein from tobacco leaves elicited neutralizing IgY antibodies in a laying hen model.

The use of LS from *Brucella* as a prophylactic cancer vaccine has also been studied. The immunogenic peptide $OVA_{257-264}$ (OVA refers to the ovalbumin peptide 257-264, a known T cell epitope) was covalently attached to the N-terminus of BspLS (112). Immunization with this chimera even without adjuvants led to strong activation of cytotoxic T lymphocytes and a TLR4-dependent specific cytotoxic response. In contrast, neither LS nor $OVA257-264$ triggered any cytotoxicity in the absence of adjuvants. This again confirms the highly immunogenic decameric LS to be an effective scaffold/carrier for further vaccine development. In a later study, the same chimera was evaluated for its effect on inducing toll-like receptor 4 (TLR4) mediated anti-tumor immune responses against B16 melanoma in C57BL/6J mice (113). Mice were inoculated with B16-OVA melanoma (a B16-F1 cell line expressing non-secretory OVA) 35 days after the immunization with LS alone or the $LS-OVA_{257-264}$ chimera. Both immunogens induced significant inhibition of tumor growth and longer survival of tumor bearing mice which was not seen in controls employing TLR4 deficient mice. This suggests that LS triggers a tumor suppression effect through TLR4. Surprisingly, the chimera produced a lower level of protection than LS alone, suggesting the conjugation of $OVA_{257-264}$ did not contribute further to the overall protective responses. The exact reason remained unclear.

In view of the global threat of *Taenia solium* (tapeworm) infection in pig and human, a study was conducted by Cruz-Revilla *et al.* (114) that employed the immunogenic peptide KETc1 (a 13 amino acid protective epitope from an anti-cysticercosis vaccine) linked to BspLS for protection against *T. solium* in a golden hamster model. Oral administration of the chimeric immunogen was found to be highly protective and significantly reduced the parasite load.

Subcutaneous administration of S3Pvac (anti-cysticercosis synthetic peptide heterologous antigen) was equally protective but the former is preferred over the synthetic peptide owing to its suitability for mass immunization due to a less invasive and cost effective oral delivery. Following these studies, LS from *Brucella* was again tested to enhance the immunogenicity of KETc1 antigen in mice (115) and found to be effective as an oral vaccine in the form of an LS chimera (up to 98% protection) compared to the protein alone (39%). This construct was also successfully used for the reduction of the parasite load. In yet another study, BspLS was evaluated for its effectiveness as a carrier scaffold for the delivery of KETc1 (116). The results showed KETc1 became highly immunogenic when expressed as a fusion partner with *Brucella* LS. In a similar study, researchers have orally immunized mice using the *Taenia crassiceps* protective peptide GK-1 alone or as an engineered chimera with the protective peptide covalently linked to *Brucella* LS (117). Protection was found to be significantly greater when administering GK-1 with LS as a carrier (96%) compared to GK-1 alone (64.7%). This suggests the potential of LS in vaccine delivery through the oral route.

The use of decameric LS has also been extended to influenza. Despite large antigenic variations in the influenza virus, the protein M2e (from the ectodomain of the protein Matrix 2) is considered to be very similar among various strains of human influenza A virus. This makes it a potential candidate for the development of a broadly protective vaccine against the disease (118). *Brucella abortus* LS (BLS) has been used as a carrier for M2e expressed at its N-terminus in *E. coli* generating decameric oligomers. Chimeras were generated by fusing one or four tandem copies of M2e to decameric BLS. Immunizing mice with the chimera containing a single copy of M2e required adjuvants to elicit responses equivalent to those elicited by the chimera with four tandem copies of M2e alone. The latter also conferred higher levels of protection against influenza

challenge when vaccinated with adjuvants including Iscomatrix (100% protection) and aluminum salts (80%), compared to the chimera alone (60%).

BspLS has been exploited to fuse flagellin for the development of a new vaccine platform. Hiriart *et al.* have recently engineered a fusion protein by attaching *Salmonella* flagellin to the N-terminus of *Brucella* LS (119). Protein folding and thermal stability of the protein remained unaffected after the genetic fusion. The chimeric protein was recognized by anti-flagellin and anti-LS antibodies and found to trigger TLR5 in TLR5 deficient mice. The humoral response evoked by the chimera was more pronounced than that elicited by equimolar amounts of the component proteins administered together.

1.1.5.2.2 Icosahedral LS presentation systems

Icosahedral LS has also been used as a vaccine presentation system. Jardine *et al.* have chosen the icosahedral LS from the hyperthermophile *Aquifex aeolicus* (AaLS) to present sixty copies of a germline-targeting gp120 outer domain immunogen (termed eOD-GT6) for the development of an HIV vaccine (92). Gp120 is a glycoprotein present on the surface of the HIV envelope. This protein recognizes and binds the CD4 receptor, which is located on the surface of subset of T-helper cells. Because of its critical role in HIV infection, gp120 has long been considered to be a promising target for HIV vaccines. Wild-type gp120, however, is a poor immunogen because it does not bind to germline precursors for VRC01-class broadly neutralizing antibodies and thus fails to elicit the necessary neutralizing antibodies. In this study, gp120 was successfully engineered employing computational guidance and *in vitro* screening to generate a germline-targeting gp120 immunogen (i.e. eOD-GT6), which was then fused onto the surface of AaLS for enhanced immunogenicity. A modeling analysis indicated that AaLS could be a suitable scaffold to present eOD-GT6 with the critical epitope exposed. Given its excellent thermal

stability, AaLS was finally chosen as the scaffold. The resulting chimeric particulate immunogen successfully activated the desired germline cells and is a promising candidate for an HIV vaccine priming dose.

AaLS protein cage nanoparticles have also been investigated as efficient vehicles for vaccine delivery to dendritic cell (120). An immunogen was engineered by attaching antigenic ovalbumin peptides OT-1 and OT-2 to the N- and C-terminus of AaLS, respectively. The results showed LS to be an efficient delivery vehicle for antigenic peptides to dendritic cells both *in vitro* and *in vivo,* leading to the proliferation of OT-1 and OT-2-specific T cells. In a recent study, Wei *et al.* have demonstrated the use of the icosahedral *Bacillus anthracis* LS as a scaffold to display a linear neutralizing epitope from ricin toxin recognized by a neutralizing monoclonal antibody called PB10 (121). The chimeric immunogen was created by attaching 60 copies of PB10-peptide to the C-terminus of LS using four different linkers. The different linkers had no effect on protein assembly, stability, or peptide presentation, but did have a minor impact on protein conformation. Chemical crosslinking with formaldehyde further enhanced the complex stability with only a small impact on protein structure. When injected without adjuvant, the chimeras elicited anti-ricin serum IgG titers in mice, but were not protective when challenged with a 10x lethal dose of ricin. This study suggests that the use of the PB10 epitope alone may not be sufficient to provide complete protection against ricin. The authors also postulated that the PB10 epitope, which adopts a helical structure in the ricin molecule, may lose its structure when presented on the surface of LS and thereby elicit antibody titers lacking strong binding to the cognate ricin toxin. Hence, even if LS has been proven to be a potential platform for vaccine development, the chimera has to be designed carefully with the antigen presented being more structurally relevant.

1.1.5.2.3 LS as a protective immunogen, mucosal adjuvant, or therapeutic cancer vaccine

In addition to its use as a vaccine presentation system, LS alone has been used as a protective immunogen. Goldbaum *et al.* reported that BspLS is a useful antigen for serological diagnosis of brucellosis (122, 123). Considering its polymeric nature, the authors proposed that this protein could serve as a promising acellular vaccine candidate. A few years later, Velikovsky *et al.* evaluated the immunogenicity of *Brucella abortus* LS (BLS) using a DNA vaccine (124). The LS gene was cloned into a pcDNA3 plasmid downstream of a cytomegalovirus promoter. Upon injection into BALB/c mice, it evoked both humoral and cellular immunity. The immunized mice showed reduced bacterial burden in comparison to the unvaccinated group. It did not, however, fully protect animals from *Brucella abortus* infection. Mice immunized with recombinant LS produced only a humoral response and no protection was seen upon challenge. Velikovsky *et al.* evaluated the immunogenicity and efficacy of *Brucella abortus* LS (BLS) in mice in a later study (125). BLS was administered in the presence and absence of three different types of adjuvants including aluminum hydroxide, monophosphoryl lipid A, or incomplete Freund's adjuvant. High IgG1 and IgG2 titers were induced by BLS alone. Co-administration of each of the three adjuvants further augmented BLS-specific IgG responses, with incomplete Freund's adjuvant being the most effective. *In vitro* challenge of spleen cells from mice immunized with these adjuvanted BLS formulations resulted in increased levels of interleukin-2, gamma interferon, IL-10, and IL-4, indicating a mixed Th1-Th2 response. Mice inoculated with BLS were found to be protected against *B. abortus* 544 challenge. This study reinforced the potential of BLS as a vaccine candidate against brucellosis.

In addition to its use as an effective vaccine presentation system, *Brucella* LS was also tested by Rosas *et al.* as a mucosal adjuvant for oral immunization of KETc1 (a protective peptide of an anti-cysticercosis vaccine) using murine models (126). It produced a higher level of

protection (79%) than that induced by KETc1 alone (39%). The level of protection induced by the use of LS adjuvant or the cholera toxin adjuvant was similar (79% vs 74%, P = 0.53). LS adjuvanted KETc1 elicited both IgG and IgA antibodies and proliferated B and CD4 activated cells. *Brucella* LS as an oral adjuvant for the *Taenia crassiceps* protective peptide GK-1was studied [101]. Adjuvanted GK-1 (91.8%) triggered a significantly higher protection level in mice compared to GK-1 alone (64.7%), suggesting the potential use of LS as a mucosal adjuvant.

In conjunction with the study of LS-OVA as a cancer prevention vaccine candidate described above (113), BspLS was further evaluated for its therapeutic effects on cancer cells in the same paper. BspLS was injected into mice which had been pre-inoculated with B16 melanoma cells for 2 or 10 days. Treatment with BspLS at day 10 produced delayed tumor progression, but did not improve the overall survival rate. In contrast, the mice which received BspLS treatment at day 2 showed both delayed tumor growth and significantly enhanced survival. This demonstrated therapeutic effects of BspLS on melanoma at an early stage. Further immunological analysis suggested BspLS might elicit its therapeutic effects by its direct impact on TLR4 from B16 melanoma cells. The case studies described above are summarized in Table 1.2.

1.1.5.2.4. Potential issues and solutions

Almost thirty studies have been published in the literature concerning the use of LS as vaccine presentation systems (Table 1.2). LS has shown significant advantages as a scaffold system to improve the immunogenicity of conjugated antigens. As with any such macromolecular system, potential issues with the use of LS-antigen conjugate need to be considered. For most LS-antigen systems, antigens are fused genetically to the LS scaffold. This requires the expression of fusion proteins and correct folding of self-assembled complex. Common issues of expressing fusion protein (127-129) include poor yields, formation of inclusion bodies in bacterial expression

systems, etc. These issues limit the general use of LS scaffold systems. Poor yield of fusion proteins during expression is not unusual for various reasons such as proteolysis and high metabolic burden. Possible solutions include codon optimization, vector optimization, use of enriched media, and increased aeration during culturing among others. Another common issue involving the expression of fusion proteins is the formation of inclusion bodies, which can be primarily caused by poor protein solubility and/or incorrect folding. If protein solubility is an issue, adding a fusion tag to enhance solubility (e.g. maltose-binding protein, MBP) and/or a change of the expression system can be possible solutions. Incorrect folding can result from undesirable interactions between a conjugated antigen and LS. Potential solutions include performing expression at lower temperature, use of lower inducer concentration, co-expression of molecular chaperones, optimization of linkers joining scaffold and antigen using computational modelling (130, 131). In addition, much work has involved the optimization of protocols for dissolution and subsequent refolding to obtain soluble and correctly folded fusion proteins (132).

Many LS based vaccine candidates described above are actually expressed as inclusion bodies and a protracted refolding step is required to obtain immunologically functional proteins. To develop a more generalized platform for *Brucella spp.* LS (BspLS), the Goldbaum lab created a noncovalent conjugation strategy using a pair of small "adaptors" (133). These adaptors are essentially a pair of high affinity coiled coil peptides. These two complementary coiled coil peptides were fused to the target protein and the LS scaffold, respectively. These two fusion proteins were initially purified separately and then mixed *in vitro* to allow conjugation of the target protein onto the LS scaffold driven by strong interactions between the two coiled coil peptides. This strategy is thought to have some general applicability considering that these adaptor peptides are small in size and are therefore well tolerated. This strategy was used to couple the RBD3

antigen to decameric BspLS. The conjugated construct elicited significantly higher antibody titers in mice than the antigen alone.

Another important issue which may often have been underestimated is the intrinsic immunogenicity of LS. As a protein scaffold or carrier, LS itself is highly immunogenic (see above). Carrier-induced epitope suppression (CIES) is an issue for epitope-carrier systems that may result in the reduction of immune responses due to any preexisting immunity to the carrier protein (134-138). CIES can be an issue for LS-antigen systems especially when multiple immunizations are used. Wei *et al.* have observed a much higher immune response to the scaffold than a conjugated epitope (PB10) in mice, which may in part explain the unsatisfactory neutralizing antibody titers to the epitope after three immunizations (139). An ideal scaffold system should have low or negligible immunogenicity. Potential solutions to such problem include point mutations guided by computational design (140) and conjugation of glycans or PEG to immunologically mask the LS scaffold (141). The antigen might need to be large enough in size to significantly cover the LS surface thereby masking the dominant immunogenic effect of the LS platform alone.

1.1.5.3. The use of LS in drug delivery

In addition to the potential success of LS in vaccine development, applications of this protein to drug delivery have also been examined. For example, LS was engineered as a potential drug delivery vehicle to achieve improved RNA delivery employing encapsulation of nucleic acids (142). In a charge tuning approach, four mutations (T86R, D90N, T120R, and E122R.) were made in each subunit of AaLS. This resulted in an increase in the overall positive charge on the inner surface of AaLS, which in turn allowed it to bind RNA and serve as a container. The exploitation

of charge complementarity led to high selectivity and efficient uptake of cellular nucleic acid during synthesis and assembly of the capsid *in vivo*.

Icosahedral LSs have also been developed as a targeted delivery system for treating cancer. Min *et al.* have genetically fused cancer cell targeting peptides (e.g. tumor vasculature targeting peptides) to AaLS and chemically attached anticancer drugs (aldoxorubicin or bortezomib) (93). The targeted delivery system employing AaLS showed specific binding to cancer cells and significantly enhanced the cytotoxic effects of aldoxorubicin and bortezomib. In a later study, Kim *et al.* developed a polyvalent antibody-binding LS system (ABD-AaLS) by genetic insertion of an IgG Fc binding domain into the C-terminus of AaLS (95). The resulting chimeric protein had exposed Fc binding domains, which could serve as a versatile platform to bind IgG molecules for targeted IgG delivery. The study also suggested drugs could be encapsulated in the hollow cavity of the AaLS system or chemically conjugated to free sites on AaLS.

1.1.5.4. Other applications

LS has also been employed in several other applications beyond vaccine development and drug delivery. Engineered AaLS has been used as a nanoreactor encapsulating the enzyme ascorbate peroxidase (APEX2) for polymerization of 3, 3-diaminobenzidine (DAB). This forms a polymer which is strongly attached to the capsids and leads to the formation of polyDAB-capsid nanoparticles with similar dimensions (143). Icosahedral LS with negatively charged inner surfaces have also been used for efficient *in vitro* encapsulation and quantitative packing of cargo proteins genetically fused to positively supercharged green fluorescent proteins for use as nanoreactors (97, 144); (145). In an another application involving enzyme immobilization, researchers have described preparation of a synthetic mimic of Primordial Carboxysome by

attaching ribulose-1,5-bisphosphate carboxylase/oxygenase and carbonic anhydrase in a genetically engineered LS scaffold (146). The study showed enhanced protection of the above biocatalysts from proteolytic damage even if it did not lead to any increase in the overall reaction kinetics. Engineered LS with enhanced negative charges in its luminal surface has also been used as protein carrier for sequestering cytoplasmically produced HIV protease leading to efficient growth of cells even at higher concentrations of the toxic protein inside cells (147). Other applications of LS include its use as a bio-nanoreactor for the synthesis of nanophase iron oxide (148).

1.1.6. Summary of the biomedical applications of LS

LS is an enzyme involved in the biosynthesis of riboflavin. Recent work has elucidated its enzymatic mechanisms and structural properties. It forms oligomeric structures and has excellent conformational stability. These features have led to exploration of its potential biomedical utility. It has shown promising applications in various fields. This review is primarily focused on its use as an antigen presentation system for the improvement of antigen immunogenicity. Both decameric and icosahedral LSs have been successfully used as scaffolds to accommodate a variety of antigens with different sizes. These constructs have significantly increased the immunogenicity of the displayed antigens. LS possesses significant flexibility as a versatile scaffold for antigen presentation as well as many other biomedical applications.

Table 1.2: Applications of lumazine synthase in vaccine development

#	LS source	Fusion terminal	Adjuvant	Injection route	Vaccine	Expression	Results	Reference
1	*Brucella spp.*	N	complete Freund's adjuvant (CFA); incomplete Freund's adjuvant (IFA); Stimune emulsion adjuvant	IM* SC* IP*	Seven different foreign peptides	*E. coli* BL21 (DE3)	The insertion of these peptide did not cause a significant change in the folding and stability of the carrier protein. Polyvalent chimera was successfully produced. Tested chimera elicited strong immune response against the inserted peptide.	Laplagne *et al.* 2004 (101)
2	*Brucella spp.*	N	IP with IFA; SC with aluminum hydroxide (AlOH)	IP	Stx2 (*Shiga* toxin type 2)	*E. coli* BL21 (DE3)	Immunized mice were completely protected against IV* Stx2 challenge	Mejias *et al.* 2013 (102)
3	*Brucella spp.*	N	AlOH	SC	Stx2	*E. coli* BL21 (DE3)	The fusion protein prevented pregnancy loss caused by Stx2 and led to transfer of passive immunity to offspring breastfed by immunized dams.	Sacerdoti *et al.* 2016 (103)
4	*Brucella spp.*	N	AlOH	SC	Stx2B (the B subunit of *Shiga* toxin 2)	*E. coli* BL21 (DE3)	Pups were completely protected against lethal dose of Stx2 injection and oral administration with Stx2	Mejias *et al.* 2014 (104)

							producing *E. coli.* Immunity transferred from immunized BALB/c mice to offspring.	
5	*Brucella spp.*	N	mineral oil-based adjuvant	IM	Stx2B	*E. coli* BL21 (DE3)	BspLS-Stx2B possibly stimulated the humoral responses of the other two antigens in the trivalent combo vaccine after the booster.	Martorelli *et al.* 2017 (105)
6	*Brucella abortus*	--	--	IM	DNA Vaccine	DNA Vaccine expression in BALB/c mice	Immunized mice showed reduced bacterial burden in comparison to the control group, however did not fully protect animals from *B. abortus* infection	Velikovsky *et al.* 2002 (124)
7	*Brucella abortus*	--	AlOH; Monophosph oryl lipid A (MPLA) and IFA	IP	Subunit vaccine against brucellosis	*E. coli* BL21 (DE3)	Immunization of BLS offered protection in mice against challenge with *B. abortus* 544, suggesting the potential of BLS as a vaccine candidate against brucellosis.	Velikovsky *et al.* 2003 (125)
8	*Brucella spp.*	N	CFA	SC	L7/L12 Ribosomal Protein of *Brucella suis*	*E. coli* BL21 (DE3)	*Brucella* L7/L12 attached to BLS served as an ideal immunogen. BLS was a suitable vector for the antigens (L7/L12).	Du *et al.* 2016 (106)
9	*Brucella spp.*	N	IFA; QUIL A adjuvant	IM; SC; IM alone or electropor ation for	Omp31 (*Brucella* outer membrane protein 31)	*E. coli*	Highest levels of specific IFN-γ and immunity against *Brucella* was conferred by using prime-boost	Estein *et al.* 2009 (107)

				the DNA vaccine		and chimera in IFA strategies	
10	*Brucella spp.*	N	--	IM	DNA vaccine encoding BLS-Omp31 (*Brucella* outer membrane protein 31)	*E. coli*	The DNA vaccine evoked strong protection in BALB/c mice against *Brucella ovis.*	Cassataro *et al.* 2007 (108)
11	*Brucella abortus*	N	CFA	SC	Omp31	*E. coli* BL21 (DE3)	LS_Omp31 fusion protein led to a much higher antibody titer than Omp31 in rabbits	Du *et al.* 2015 (109)
12	*Brucella spp.*	N	IFA	IM	VP8d (inner core domain from VP8 spike protein from C486 bovine rotavirus)	Tobacco chloroplasts	Proteins extracted from leaves evoked neutralizing IgY antibodies in laying hen model.	Alfano *et al.* 2015 (111)
13	*Brucella spp.*	N	--	SC	OVA (Ovalbumin)	*E. coli* BL21 (DE3)	Retardation of tumor growth and enhanced survival of tumor-bearing C57BL/6J mice.	Rossi *et al.* 2015 (113)
14	*Brucella spp.*	N	Marcol/Arlacel adjuvant	IP	VP8d	*E. coli* BL21 (DE3)	Strong protection (97.5-100%) against C486 bovine rotavirus.	Bellido *et al.* 2009 (110)
15	*Brucella spp.*	N	--	Oral	KETc1 (a peptide from anti-cysticercosis vaccine)	*E. coli* BL21 (DE3)	Protection against *T. solium* in golden hamster.	Cruz-Revilla *et al.* 2006 (114)
16	*Brucella spp.*	N	--	Oral	*Taenia crassiceps* protective peptide GK-1	*E. coli* BL21 (DE3)	Higher protection in the case of GK-1 with LS as adjuvant (91.8%) and as carrier (96%) as	Fragoso *et al.* 2011 (117)

						compared to GK-1 alone (64.7%).	
17	*Brucella spp.*	N	--	Oral	KETc1	*E. coli* BL21 (DE3)	Protective as chimera (upto 98%) and as adjuvant (79%).	Rosas *et al.* 2006 (115)
18	*Brucella spp.*	N	Saponin	SC	KETc1	*E. coli* BL21 (DE3)	Chimeric protein KETc1 expressed with BspLS shows immunogenicity and protection.	Sciutto *et al.* 2005 (116)
19	*Aquifex aeolicus*	N and C	Poly (I:C)	SC	antigenic ovalbumin peptides OT-1 and OT-2	*E. coli* BL21 (DE3)	LS is an efficient delivery vehicle for the antigenic peptides to dendritic cells leading to induced proliferation of OT-1 and OT-2 specific T cells.	Ra *et al.* 2014 (120)
20	*Brucella spp.*	N	AlOH, CFA or IFA	SC	Immunogenic peptide OVA257–264	*E. coli* BL21 (DE3)	Strong activation of cytotoxic T lymphocyte and a TLR4 dependent cytotoxic response.	Berguer *et al.* 2012 (112)
21	*Brucella abortus*	N	immune stimulating complex MATRIX Q (IMX®); MPLA; -C-galactosylceramide; AlOH	IM SC IN*	M2e (ectodomain of the protein Matrix 2)	*E. coli* BL21 (DE3)	High levels of protection against influenza with adjuvants, Iscomatrix (100% protection) and alum (80%) as compared to chimera alone (60%).	Alvarez *et al.* 2013 (118)
22	*Brucella spp.*	--	--	SC	--	*E. coli* BL21 (DE3)	Evoked systemic and oral immunity in absence of adjuvant through TLR4 dependent pathway.	Berguer *et al.* 2006 (100)

23	*Brucella spp.*	--	AlOH; MPLA; IFA	IP	--	*E. coli* BL21 (DE3)	BspLS elicited high IgG1 and IgG2 titers which were further enhanced by adjuvants.	Velikovsky *et al.* 2003 (125)
24	*Brucella spp.*	N (noncovalent)	--	IP	RBD3 antigen	*E. coli*	The noncovalent conjugation strategy showed an increase in the immunogenicity of RBD3 antigen.	Craig *et al.* 2012 (133)
25	*Bacillus anthracis*	C	--	IP	PB10 (a linear epitope from ricin toxin)	*E. coli* strain BL21 (γDE3)	Elicited anti-ricin serum IgG titers in mice without adjuvant, but couldn't confer protection against a 10x lethal dose of ricin.	Wei *et al.* 2017 (139)
26	*Brucella spp.*	N	--	IP	*Salmonella* flagellin	*E. coli* BL21 (DE3)	The chimeric protein was recognized by anti-flagellin and anti-LS antibodies and triggered TLR5 in TLR5 deficient mice. The humoral response was stronger for the chimera as compared to the proteins administered together.	Hiriart *et al.* 2017 (119)
27	*Aquifex aeolicus*	C	--	--	HIV outer domain immunogen gp120	Mammalian (293) cells	The chimeric immunogen activated germline, can be a candidate of choice for HIV vaccine.	Jardine *et al.* 2013 (92)

*SC: subcutaneous; IM: intramuscular; IN: intranasal; IP: intraperitoneal; IV: intravenous.

1.2. Inorganic scaffolds

Various types of inorganic materials have been explored as potential scaffolds for polyvalent antigen display. These scaffold systems include gold nanoparticles (AuNPs), polystyrene beads, carbon nanotubes, etc.(149-151) Presentation of antigens onto these scaffold systems are achieved by direct adsorption or chemical conjugation. For instance, proteins can adsorb onto the surface of AuNPs via hydrophobic interaction, electrostatic interaction, and formation of sulfur-gold bonds, etc. However, the structural and stability of antigens upon adsorption or conjugation to the scaffold needs to be carefully examined to ensure preservation of essential conformational neutralizing epitopes. One advantage of using inorganic scaffolds is that their shape and size can be easily customized to achieve the optimal immunogenicity of surface displayed antigens. Even though most of these inorganic scaffolds are found to be biocompatible, they are not biodegradable. In addition, there is a lack of long-term *in vivo* safety data. Due to these issues, the development of clinical products using inorganic scaffolds has been quite challenging.

1.3. Adjuvants

Adjuvants are immunological ingredients used in vaccines to create stronger immune responses. There are generally three major classes of adjuvants: aluminum salts, squalene-based emulsions, and pathogen-associated molecular patterns (PAMPs) (e.g. Monophosphoryl lipid A, CpG, etc.). The selection of a suitable adjuvant for a specific antigen depends on the type of response the adjuvant can promote and infection mechanisms of a pathogen (intracellular or extracellular). For example, aluminum salts increase Th2 antibody responses, but do not elicit pronounced Th1 cellular responses. In contrast, emulsion adjuvants are able to induce both Th1 (CD4+) and Th2 antibody responses (152). MPLA has been found to enhance a strong Th1 (both

CD4+ and CD8+) response and therefore is often effective against intracellular pathogens. Different types of adjuvants can be used in combination to achieve more desirable immunological effects. For instance, GlaxoSmithKline's AS04 (Aka. "Adjuvant System 04") consists of aluminum hydroxide (AlOH) and Monophosphoryl lipid A (MPLA). It is used in the human papillomavirus (HPV) vaccine-Cervarix and results in stronger and more sustained immune responses than AlOH alone. Other attempts have also been made to include lipophilic MPLA derivatives in the oil phase of emulsions (153).

1.3.1. Aluminum salts

Aluminum salts are the first class of approved adjuvants for human use and also currently the most widely used adjuvants (154). Common aluminum salts include aluminum hydroxide (Alhydrogel®) and aluminum phosphate (Adju-Phos®). There are two major differences between these two types: their physical forms and points of zero charge (PZC), the pH value at which the surface charge of the adjuvant is neutral. Alhydrogel® exists in a crystalline state, whereas Adju-Phos® is found to be amorphous. In addition, Alhydrogel® and Adju-Phos® have a PZC of 11 and 4-5.5, respectively. At pH 6 to 8 (a common formulation pH range), Alhydrogel® and Adju-Phos® have positive and negative surface charges, respectively. Such a difference affects their electrostatic interaction strength with antigens and possibly the resulting immune responses, since it has been long believed that the adsorption of antigens onto adjuvants is essential for enhanced immune responses, although this idea has occasionally been disputed. Electrostatic interactions are usually considered a dominate force governing interactions between antigens and aluminum adjuvants. Other interactions include ligand exchange, van der Waals interaction, hydrogen bonding, and hydrophobic interactions (155). The interaction strength between antigens and aluminum salts can be affected by a variety of factors: the size of protein antigens, ionic strength,

buffer (especially phosphate) concentration, excipient concentration, the size of adjuvant particle, etc. It is worth noting that adsorption of antigen to aluminum is not always a prerequisite for improved immunogenicity, since several studies have shown that non adsorbed antigens co-administered with aluminum salts can induce equivalent immune responses compared to adsorbed antigens (156).

1.3.2. Emulsions

Emulsion adjuvants are classified into several different types: oil-in-water (O/W), water-in-oil (W/O), water-in-oil-in-water (W/O/W) emulsions, etc. Among these, the O/W emulsions are best tolerated by humans and therefore preferable for human use. The other emulsion types are often used for veterinary vaccines (157). The O/W emulsions usually use squalene, a naturally occurring and fully metabolizable lipid, as the oil phase. A well-established example is MF59 developed by Novartis. It has been widely used in influenza vaccines for more than two decades. MF59 contains emulsion droplets with a size around 160 nm. Many case studies have shown that MF59 induces more potent adjuvant effects (antibody levels and CD4+ responses) than aluminum salts most probably due to MF59's better ability to induce Th1 (CD4+) responses. Antigens can interact with emulsion adjuvants via various types of interactions since emulsions are complex heterogeneous systems. The primary interactions include hydrophobic (with the oil phase) and electrostatic (with ionic surfactants) interactions. Antigen molecules hydrophobically adsorbed on the surface of the oil phase can establish protein-protein interactions, resulting in protein oligomerization and/or flocculation events. Antigen/emulsion interactions can affect the biophysical properties of both antigens and emulsion adjuvants. Studies have shown that adsorption of antigens onto the oil phase of emulsion adjuvants alters protein secondary and tertiary structures and enhanced protein thermal stability (158). Understanding the compatibility

between an antigen and an emulsion adjuvant is critical to optimize the formulation and ensure the safety and stability of the final vaccine product.

1.3.3. Pathogen-associated molecular patterns (PAMPs)

A third important class of adjuvants are also known as PAMPs. PAMPs are molecules broadly present in or on pathogens that can be recognized by the host's innate immune system. Multicellular organisms use pattern recognition receptors (PRRs) to recognize PAMPs. Common PRRs are Toll-like receptors (TLR), C-Type Lectin receptors (CLR), cytoplasmic PRRs, etc. TLRs consist of many subclasses (TLRs 1 to 13) and are responsible for the recognition of a diverse array of PAMPs. TLRs are located at the cell surface or inside cell compartments. One of the most studied PAMPs is lipopolysaccharide (LPS), also known as lipoglycan or endotoxin. LPS is present on the outer cell wall of gram-negative bacteria (e.g. *E. coli*) and consists of both polysaccharide and lipid components. The polysaccharide is composed of an O-specific polysaccharide and core oligosaccharide. The lipid component, often called lipid A, binds to TLR 4 and stimulates proinflammatory cytokine signaling. Although highly immunostimulatory, lipid A adjuvant is endotoxic and can cause septic shock. Monophosporylated lipid A (MPLA) is a safer version for human use and made from lipid A with deletion of a phosphate group and slight alterations in the fatty acid chains. MPLA can elicit both humoral and cellular responses, and is used in combination with aluminum hydroxide in the Cervarix vaccine. Other common PAMPs include flagellin, ssRNA, CpG, etc.

1.3.4. Antigen-adjuvant Interactions from a Formulation Perspective

Understanding the compatibility between antigens and adjuvants is important to rationally develop formulations that ensure long-term vaccine stability. If they are found to be compatible with each other over the period of the shelf life of a vaccine, they can be stored in the same vial to

minimize the storage cost and to simplify injection procedures. Otherwise, they should be stored separately and mixed prior to injection. Biophysical tools are often utilized to study the structure and stability of antigens in the present of adjuvants. Common techniques suitable for characterization of antigen-adjuvant mixtures include differential scanning calorimetry, Fourier-transform infrared spectroscopy, size exclusion chromatography, etc. Adjuvants (e.g. aluminum salts, emulsions) are turbid in nature and thereby pose analytical challenges to many other spectroscopic techniques such as UV/Visible absorption spectroscopy, light scattering, conventional fluorescence, etc. Thanks to the advancement of modern instrumentation, several marketed instruments allow us to directly analyze proteins in highly turbid samples. For example, the concentration of protein in turbid sample can be directly quantified by using an integrating cavity absorbance spectrometer (159). High quality fluorescence spectra can be collected by integrating a high quality laser as the excitation source, several essential optical components to eliminate Rayleigh scattering, and a microplate with a suitable detection angle (160). The microplate format also enables screening vaccine formulations in a high-throughput manner.

1.4. Summary and dissertation outline

In this dissertation, we will first discuss the biophysical properties of LS, a potential protein scaffold for polyvalent antigen display. The conformational stability of LS in response to various stress conditions (e.g. chemical denaturants, temperature, and pH) will be presented. The effects of phosphate ions on the tertiary structure and thermal stability of LS will be discussed as well. In chapter 3, we will describe an attempt to use LS as the scaffold to develop highly immunogenic vaccine candidates against ricin toxin. The content will include the design, expression, purification, biophysical characterization, and *in vivo* immunization of the vaccine candidates. Although the end goal of developing highly effective ricin vaccines is not achieved, this work

provides valuable lessons and suggestions for future researchers, who are interested in using LS as a vaccine scaffold and/or in developing ricin vaccines. Chapter 4 will include a study utilizing biophysical tools to understand antigen-adjuvant interactions. The potential interactions between the alpha toxin from *S. aureus* and two emulsion-based adjuvants will be described, and how these interactions affect the protein's structure and stability will be presented. Chapter 5 will introduce an improved fluorescence method for direct screening of challenging formulations (e.g. turbid adjuvanted vaccines, and high concentration antibodies). Chapter 6 provides a discussion, conclusion and future direction of the work described in the previous chapters.

1.5. References

1.   Andre, F.E., et al., *Vaccination greatly reduces disease, disability, death and inequity worldwide.* Bulletin of the World Health Organization, 2008. **86**(2): p. 140-146.

2.   Greenwood, B., *The contribution of vaccination to global health: past, present and future.* Phil. Trans. R. Soc. B, 2014. **369**(1645): p. 20130433.

3.   Agol, V.I., *Vaccine-derived polioviruses.* Biologicals, 2006. **34**(2): p. 103-108.

4.   Esteves, K., *Safety of oral poliomyelitis vaccine: results of a WHO enquiry.* Bulletin of the World Health Organization, 1988. **66**(6): p. 739.

5.   Fachinger, V., et al., *The effect of vaccination against porcine circovirus type 2 in pigs suffering from porcine respiratory disease complex.* Vaccine, 2008. **26**(11): p. 1488-1499.

6.   Horaud, F., *Ethical and safety considerations for the use in clinical trials of new attenuated poliovirus strains.* Developments in biological standardization, 1993. **78**: p. 149.

7.   Sanders, B.P., et al., *Brunenders: A partially attenuated historic poliovirus Type I vaccine strain.* Journal of General Virology, 2015. **96**(9): p. 2614-2622.

8.   Wang, H.-B., et al., *An Outbreak of Type Π Vaccine-Derived Poliovirus in Sichuan Province, China: Emergence and Circulation in an Under-Immunized Population.* PloS one, 2014. **9**(12): p. e113880.

9.   Thomas, J.C., *Toward the Development of an Improved Ricin Vaccine*. 2013, University of Kansas.

10.   Atkinson, W., S. Wolfe, and J. Hamborsky, *Epidemiology and prevention of vaccine-preventable diseases*. 2011: Public Health Foundation.

11.   Plotkin, S.A., *Vaccines: past, present and future.* Nature medicine, 2005. **10**(4s): p. S5.

12. Tauber, E., et al., *Safety and immunogenicity of a Vero-cell-derived, inactivated Japanese encephalitis vaccine: a non-inferiority, phase III, randomised controlled trial.* The Lancet, 2007. **370**(9602): p. 1847-1853.

13. Holzer, B.R., et al., *Immunogenicity and adverse effects of inactivated virosome versus alum-adsorbed hepatitis A vaccine: a randomized controlled trial.* Vaccine, 1996. **14**(10): p. 982-986.

14. Jones, L.H., *Recent advances in the molecular design of synthetic vaccines.* Nature chemistry, 2015. **7**(12): p. 952.

15. Moyle, P. and I. Toth, *Modern subunit vaccines: development, components, and research opportunities. Chem-MedChem 2013; 8: 360-76; PMID: 23316023*.

16. Purcell, A.W., J. McCluskey, and J. Rossjohn, *More than one reason to rethink the use of peptides in vaccine design.* Nature reviews. Drug discovery, 2007. **6**(5): p. 404.

17. Jennings, G.T. and M.F. Bachmann, *Designing recombinant vaccines with viral properties: a rational approach to more effective vaccines.* Current molecular medicine, 2007. **7**(2): p. 143-155.

18. Zeltins, A., *Construction and characterization of virus-like particles: a review.* Molecular biotechnology, 2013. **53**(1): p. 92-107.

19. Kushnir, N., S.J. Streatfield, and V. Yusibov, *Virus-like particles as a highly efficient vaccine platform: diversity of targets and production systems and advances in clinical development.* Vaccine, 2012. **31**(1): p. 58-83.

20. Liu, W., et al., *It's all about change: the antigen-driven initiation of B-cell receptor signaling.* Cold Spring Harbor perspectives in biology, 2010. **2**(7): p. a002295.

21.   Grgacic, E.V. and D.A. Anderson, *Virus-like particles: passport to immune recognition.* Methods, 2006. **40**(1): p. 60-65.

22.   Chackerian, B., *Virus-like particles: flexible platforms for vaccine development.* Expert review of vaccines, 2007. **6**(3): p. 381-390.

23.   Bachmann, M.F., H. Hengartner, and R.M. Zinkernagel, *T helper cell-independent neutralizing B cell response against vesicular stomatitis virus: Role of antigen patterns in B cell induction?* European journal of immunology, 1995. **25**(12): p. 3445-3451.

24.   Thyagarajan, R., N. Arunkumar, and W. Song, *Polyvalent antigens stabilize B cell antigen receptor surface signaling microdomains.* The Journal of Immunology, 2003. **170**(12): p. 6099-6106.

25.   Baschong, W., et al., *Repetitive versus monomeric antigen presentation: direct visualization of antibody affinity and specificity.* Journal of structural biology, 2003. **143**(3): p. 258-262.

26.   Bachmann, M.F. and G.T. Jennings, *Vaccine delivery: a matter of size, geometry, kinetics and molecular patterns.* Nature Reviews Immunology, 2010. **10**(11): p. 787.

27.   Deml, L., et al., *Recombinant HIV-1 Pr55 gag virus-like particles: potent stimulators of innate and acquired immune responses.* Molecular immunology, 2005. **42**(2): p. 259-277.

28.   Jain, N.K., et al., *Formulation and stabilization of recombinant protein based virus-like particle vaccines.* Advanced drug delivery reviews, 2015. **93**: p. 42-55.

29.   Bornemann, S., *Flavoenzymes that catalyse reactions with no net redox change.* Natural product reports, 2002. **19**(6): p. 761-772.

30.   Vitreschak, A.G., et al., *Regulation of riboflavin biosynthesis and transport genes in bacteria by transcriptional and translational attenuation.* Nucleic acids research, 2002. **30**(14): p. 3141-3151.

31.   Fischer, M. and A. Bacher, *Biosynthesis of flavocoenzymes.* Natural product reports, 2005. **22**(3): p. 324-350.

32.   Fischer, M. and A. Bacher, *Biosynthesis of vitamin B2 in plants.* Physiologia Plantarum, 2006. **126**(3): p. 304-318.

33.   Ladenstein, R., et al., *Metamorphosis of an enzyme.* Conformational Proteomics of Macromolecular Architecture: Approaching the Structure of Large Molecular Assemblies and Their Mechanisms of Action, 2004: p. 198-221.

34.   KATAGIBI, H., I. TAKEDA, and K. IMAI, *Synthesis of riboflavin by microorganisms. 4. The studies of 4-C-donor involved in the enzymatic riboflavin synthesis from 8-N-ribityl-6, 7-dimethyllumazine.* Journal of Vitaminology, 1958. **4**: p. 278-284.

35.   Maley, G.F. and G. Plaut, *THE CONVERSION OF 6, 7-DIMETHYL-8-RIBITYLLUMAZINE (6, 7-DIMETHYL-8-RIBITYL-2, 4 [1H, 3H]-PTERIDINEDIONE) TO RIBOFLAVIN BY EXTRACTS OF ASHBYA GOSSYPII.* Journal of the American Chemical Society, 1959. **81**(8): p. 2025-2025.

36.   Bacher, A., et al., *Riboflavin synthases of Bacillus subtilis. Purification and properties.* Journal of Biological Chemistry, 1980. **255**(2): p. 632-637.

37.   Ladenstein, R., H.C. Ludwig, and A. Bacher, *Crystallization and preliminary X-ray diffraction study of heavy riboflavin synthase from Bacillus subtilis.* Journal of Biological Chemistry, 1983. **258**(19): p. 11981-11983.

38. Morgunova, E., et al., *Structural study and thermodynamic characterization of inhibitor binding to lumazine synthase from Bacillus anthracis.* Acta Crystallographica Section D: Biological Crystallography, 2010. **66**(9): p. 1001-1011.

39. Fornasari, M.S., et al., *Sequence determinants of quaternary structure in lumazine synthase.* Molecular biology and evolution, 2004. **21**(1): p. 97-107.

40. Zylberman, V., et al., *High order quaternary arrangement confers increased structural stability to Brucella sp. lumazine synthase.* Journal of Biological Chemistry, 2004. **279**(9): p. 8093-8101.

41. Braden, B.C., et al., *Divergence in macromolecular assembly: X-ray crystallographic structure analysis of lumazine synthase from Brucella abortus.* Journal of molecular biology, 2000. **297**(5): p. 1031-1036.

42. Klinke, S., et al., *Structural and kinetic properties of lumazine synthase isoenzymes in the order Rhizobiales.* J Mol Biol, 2007. **373**(3): p. 664-80.

43. Morgunova, E., et al., *Lumazine synthase from Candida albicans as an anti-fungal target enzyme structural and biochemical basis for drug design.* Journal of Biological Chemistry, 2007. **282**(23): p. 17231-17241.

44. Persson, K., et al., *Crystal structure analysis of a pentameric fungal and an icosahedral plant lumazine synthase reveals the structural basis for differences in assembly.* Protein Science, 1999. **8**(11): p. 2355-2365.

45. Zhang, Y., et al., *A new series of N-[2, 4-dioxo-6-d-ribitylamino-1, 2, 3, 4-tetrahydropyrimidin-5-yl] oxalamic acid derivatives as inhibitors of lumazine synthase and riboflavin synthase: design, synthesis, biochemical evaluation, crystallography, and mechanistic implications.* The Journal of organic chemistry, 2008. **73**(7): p. 2715-2724.

46. Morgunova, E., et al., *Structural and thermodynamic insights into the binding mode of five novel inhibitors of lumazine synthase from Mycobacterium tuberculosis.* Febs j, 2006. **273**(20): p. 4790-804.

47. Zhang, Y., et al., *A new series of N-[2,4-dioxo-6-d-ribitylamino-1,2,3,4-tetrahydropyrimidin-5-yl]oxalamic acid derivatives as inhibitors of lumazine synthase and riboflavin synthase: design, synthesis, biochemical evaluation, crystallography, and mechanistic implications.* J Org Chem, 2008. **73**(7): p. 2715-24.

48. Morgunova, E., et al., *Crystal structure of lumazine synthase from Mycobacterium tuberculosis as a target for rational drug design: binding mode of a new class of purinetrione inhibitors.* Biochemistry, 2005. **44**(8): p. 2746-58.

49. *Crystal structure of a Probable Riboflavin Synthase, Beta chain RIBH (6,7-dimethyl-8-ribityllumazine synthase, DMRL synthase, Lumazine synthase) from Mycobacterium leprae*. http://www.rcsb.org/pdb/explore/explore.do?structureId=4J07.

50. Meining, W., et al., *The atomic structure of pentameric lumazine synthase from Saccharomyces cerevisiae at 1.85 Å resolution reveals the binding mode of a phosphonate intermediate analogue.* Journal of molecular biology, 2000. **299**(1): p. 181-197.

51. Gerhardt, S., et al., *The structural basis of riboflavin binding to Schizosaccharomyces pombe 6, 7-dimethyl-8-ribityllumazine synthase.* Journal of molecular biology, 2002. **318**(5): p. 1317-1329.

52. Klinke, S., et al., *Crystallographic studies on decameric Brucella spp. Lumazine synthase: a novel quaternary arrangement evolved for a new function?* Journal of molecular biology, 2005. **353**(1): p. 124-137.

53.   Klinke, S., et al., *Crystallographic studies on decameric Brucella spp. Lumazine synthase: a novel quaternary arrangement evolved for a new function?* J Mol Biol, 2005. **353**(1): p. 124-37.

54.   Shankar, M., et al., *Catalysis product captured in lumazine synthase from the fungal pathogen Candida glabrata.* Acta Crystallogr D Biol Crystallogr, 2013. **69**(Pt 8): p. 1580-6.

55.   Zhang, X., et al., *A structure-based model of the reaction catalyzed by lumazine synthase from Aquifex aeolicus.* Journal of molecular biology, 2003. **328**(1): p. 167-182.

56.   Sasaki, E., et al., *Structure and assembly of scalable porous protein cages.* Nat Commun, 2017. **8**: p. 14663.

57.   Zhang, X., et al., *X-ray structure analysis and crystallographic refinement of lumazine synthase from the hyperthermophile Aquifex aeolicus at 1.6 A resolution: determinants of thermostability revealed from structural comparisons.* J Mol Biol, 2001. **306**(5): p. 1099-114.

58.   Zhang, X., et al., *A structure-based model of the reaction catalyzed by lumazine synthase from Aquifex aeolicus.* J Mol Biol, 2003. **328**(1): p. 167-82.

59.   Ritsert, K., et al., *Studies on the Lumazine Synthase/Riboflavin Synthase Complex ofBacillus subtilis: Crystal Structure Analysis of Reconstituted, Icosahedral β-subunit Capsids with Bound Substrate Analogue Inhibitor at 2.4 Å Resolution.* Journal of molecular biology, 1995. **253**(1): p. 151-167.

60.   *Crystal structure of Lumazine synthase from Salmonella typhimurium LT2*. http://www.rcsb.org/pdb/explore/explore.do?structureId=3NQ4.

61.   Chen, H.-N. and K.J. Woycechowsky, *Conversion of a dodecahedral protein capsid into pentamers via minimal point mutations.* Biochemistry, 2012. **51**(23): p. 4704-4712.

62.   Ladenstein, R., M. Fischer, and A. Bacher, *The lumazine synthase/riboflavin synthase complex: shapes and functions of a highly variable enzyme system.* FEBS Journal, 2013. **280**(11): p. 2537-2563.

63.   Volk, R. and A. Bacher, *Biosynthesis of riboflavin. Studies on the mechanism of L-3, 4-dihydroxy-2-butanone 4-phosphate synthase.* Journal of Biological Chemistry, 1991. **266**(31): p. 20610-20618.

64.   Fischer, M., et al., *Enzyme catalysis via control of activation entropy: site-directed mutagenesis of 6, 7-dimethyl-8-ribityllumazine synthase.* Journal of molecular biology, 2003. **326**(3): p. 783-793.

65.   Kis, K. and A. Bacher, *Substrate channeling in the lumazine synthase/riboflavin synthase complex of Bacillus subtilis.* Journal of Biological Chemistry, 1995. **270**(28): p. 16788-16795.

66.   Hickman, S.J., J.F. Ross, and E. Paci, *Prediction of stability changes upon mutation in an icosahedral capsid.* Proteins: Structure, Function, and Bioinformatics, 2015. **83**(9): p. 1733-1741.

67.   Zhang, X., *Structural studies of lumazine synthases: Thermostability, catalytic mechanism and molecular assembly*. 2005: Biovetenskaper och näringslära/Biosciences and Nutrition.

68.   Wei, Y., et al., *Effect of Phosphate Ion on the Structure of Lumazine Synthase, an Antigen Presentation System From Bacillus anthracis.* Journal of pharmaceutical sciences, 2017.

69.   Zhang, X., et al., *Multiple assembly states of lumazine synthase: a model relating catalytic function and molecular assembly.* Journal of molecular biology, 2006. **362**(4): p. 753-770.

70.   Bacher, A., et al., *Heavy riboflavin synthase from Bacillus subtilis: quaternary structure and reaggregation.* Journal of molecular biology, 1986. **187**(1): p. 75-86.

71.   Alsenaidy, M.A., et al., *An empirical phase diagram approach to investigate conformational stability of "second-generation" functional mutants of acidic fibroblast growth factor-1.* Protein Science, 2012. **21**(3): p. 418-432.

72.   MacLaren, J.A., *The effects of certain purines and pyrimidines upon the production of riboflavin by Eremothecium ashbyii.* Journal of bacteriology, 1952. **63**(2): p. 233.

73.   Demain, A., et al., *Tryptophan Entry into the Brain: Modifications in Response to Food Ingestion and Albumin Binding.* Rev. Microbiol, 1972. **26**: p. 369-388.

74.   Zhang, Y., et al., *A novel lumazine synthase inhibitor derived from oxidation of 1, 3, 6, 8-tetrahydroxy-2, 7-naphthyridine to a tetraazaperylenehexaone derivative.* The Journal of organic chemistry, 2007. **72**(8): p. 2769.

75.   Cushman, M., et al., *Synthesis of epimeric 6, 7-bis (trifluoromethyl)-8-ribityllumazine hydrates. Stereoselective interaction with the ligh riboflavin synthase of Bacillus subtilis.* Journal of organic chemistry, 1991. **56**(15): p. 4603-4608.

76.   Cushman, M., et al., *19F NMR studies on the mechanism of riboflavin synthase. Synthesis of 6-(trifluoromethyl)-7-oxo-8-(D-ribityl) lumazine and 6-(trifluoromethyl)-7-methyl-8-(D-ribityl) lumazine.* Journal of organic chemistry, 1992. **57**(21): p. 5630-5643.

77.   Talukdar, A., et al., *Synthesis and enzyme inhibitory activity of the s-nucleoside analogue of the ribitylaminopyrimidine substrate of lumazine synthase and product of riboflavin synthase.* The Journal of organic chemistry, 2007. **72**(19): p. 7167-7175.

78.   Zhang, Y., et al., *A new series of 3-alkyl phosphate derivatives of 4, 5, 6, 7-tetrahydro-1-D-ribityl-1 H-pyrazolo [3, 4-d] pyrimidinedione as inhibitors of lumazine synthase: design, synthesis, and evaluation.* The Journal of organic chemistry, 2007. **72**(19): p. 7176-7184.

79.   Cushman, M., et al., *Design, synthesis, and biochemical evaluation of 1, 5, 6, 7-tetrahydro-6, 7-dioxo-9-D-ribitylaminolumazines bearing alkyl phosphate substituents as inhibitors of lumazine synthase and riboflavin synthase.* The Journal of organic chemistry, 2005. **70**(20): p. 8162.

80.   Chen, J., et al., *Design, synthesis, and evaluation of acyclic C-nucleoside and N-methylated derivatives of the ribitylaminopyrimidine substrate of lumazine synthase as potential enzyme inhibitors and mechanistic probes.* The Journal of organic chemistry, 2004. **69**(21): p. 6996-7003.

81.   Cushman, M., et al., *Design, synthesis, and evaluation of 9-D-ribitylamino-1, 3, 7, 9-tetrahydro-2, 6, 8-purinetriones bearing alkyl phosphate and α, α-difluorophosphonate substituents as inhibitors of riboflavin synthase and lumazine synthase.* The Journal of organic chemistry, 2004. **69**(3): p. 601-612.

82.   Cushman, M., et al., *Design, synthesis, and evaluation of 6-carboxyalkyl and 6-phosphonoxyalkyl derivatives of 7-oxo-8-ribitylaminolumazines as inhibitors of riboflavin synthase and lumazine synthase.* The Journal of organic chemistry, 2002. **67**(16): p. 5807-5816.

83.   Cushman, M., et al., *Incorporation of an amide into 5-phosphonoalkyl-6-D-ribitylaminopyrimidinedione lumazine synthase inhibitors results in an unexpected reversal of selectivity for riboflavin synthase vs lumazine synthase.* The Journal of organic chemistry, 2002. **67**(20): p. 6871-6877.

84.   Cushman, M., et al., *Design, synthesis, and evaluation of 9-D-ribityl-1, 3, 7-trihydro-2, 6, 8-purinetrione, a potent inhibitor of riboflavin synthase and lumazine synthase.* The Journal of organic chemistry, 2001. **66**(25): p. 8320-8327.

85.   Cushman, M., et al., *Synthesis and biochemical evaluation of bis (6, 7-dimethyl-8-D-ribityllumazines) as potential bisubstrate analogue inhibitors of riboflavin synthase.* The Journal of organic chemistry, 1999. **64**(13): p. 4635-4642.

86.   Cushman, M., et al., *Design, synthesis, and biological evaluation of homologous phosphonic acids and sulfonic acids as inhibitors of lumazine synthase.* The Journal of Organic Chemistry, 1999. **64**(11): p. 3838-3845.

87.   Cushman, M., et al., *Design and synthesis of 6-(6-D-ribitylamino-2, 4-dihydroxypyrimidin-5-yl)-1-hexylphosphonic acid, a potent inhibitor of lumazine synthase.* Bioorganic & medicinal chemistry letters, 1999. **9**(1): p. 39-42.

88.   Cushman, M., et al., *Synthesis of 2, 6-dioxo-(1H, 3H)-9-N-ribitylpurine and 2, 6-dioxo-(1H, 3H)-8-aza-9-N-ribitylpurine as inhibitors of lumazine synthase and riboflavin synthase.* Bioorganic & medicinal chemistry, 1998. **6**(4): p. 409-415.

89.   Morgunova, E., et al., *Lumazine synthase from Candida albicans as an anti-fungal target enzyme: structural and biochemical basis for drug design.* J Biol Chem, 2007. **282**(23): p. 17231-41.

90.   Junaid, M., et al., *Analyses of the Binding between Water Soluble C60 Derivatives and Potential Drug Targets through a Molecular Docking Approach.* PloS one, 2016. **11**(2): p. e0147761.

91. Ra, J.-S., et al., *Lumazine synthase protein cage nanoparticles as antigen delivery nanoplatforms for dendritic cell-based vaccine development.* Clinical and experimental vaccine research, 2014. **3**(2): p. 227-234.

92. Jardine, J., et al., *Rational HIV immunogen design to target specific germline B cell receptors.* Science, 2013. **340**(6133): p. 711-716.

93. Min, J., et al., *Lumazine synthase protein cage nanoparticles as modular delivery platforms for targeted drug delivery.* RSC Advances, 2014. **4**(89): p. 48596-48600.

94. Moon, H., et al., *Developing genetically engineered encapsulin protein cage nanoparticles as a targeted delivery nanoplatform.* Biomacromolecules, 2014. **15**(10): p. 3794-3801.

95. Kim, H., et al., *Development of an antibody-binding modular nanoplatform for antibody-guided targeted cell imaging and delivery.* RSC Advances, 2016. **6**(23): p. 19208-19213.

96. Wörsdörfer, B., K.J. Woycechowsky, and D. Hilvert, *Directed evolution of a protein container.* Science, 2011. **331**(6017): p. 589-592.

97. Seebeck, F.P., et al., *A simple tagging system for protein encapsulation.* Journal of the American Chemical Society, 2006. **128**(14): p. 4516-4517.

98. Wörsdörfer, B., Z. Pianowski, and D. Hilvert, *Efficient in vitro encapsulation of protein cargo by an engineered protein container.* Journal of the American Chemical Society, 2012. **134**(2): p. 909-911.

99. Sasaki, E. and D. Hilvert, *Self-Assembly of Proteinaceous Multishell Structures Mediated by a Supercharged Protein.* The Journal of Physical Chemistry B, 2016. **120**(26): p. 6089-6095.

100. Berguer, P.M., et al., *A polymeric bacterial protein activates dendritic cells via TLR4.* J Immunol, 2006. **176**(4): p. 2366-72.

101. Laplagne, D., et al., *Engineering of a polymeric bacterial protein as a scaffold for the multiple display of peptides.* Proteins: Structure, Function, and Bioinformatics, 2004. **57**(4): p. 820-828.

102. Mejias, M.P., et al., *Immunization with a chimera consisting of the B subunit of Shiga toxin type 2 and brucella lumazine synthase confers total protection against Shiga toxins in mice.* J Immunol, 2013. **191**(5): p. 2403-11.

103. Sacerdoti, F., et al., *Immunization with BLS-Stx2B chimera totally protects dams from early pregnancy loss induced by Shiga toxin type 2 (Stx2) and confers anti-Stx2 immunity to the offspring.* Vaccine, 2016. **34**(39): p. 4732-7.

104. Mejias, M.P., et al., *Protection of mice against Shiga toxin 2 (Stx2)-associated damage by maternal immunization with a Brucella lumazine synthase-Stx2 B subunit chimera.* Infect Immun, 2014. **82**(4): p. 1491-9.

105. Martorelli, L., et al., *Immune Response in Calves Vaccinated with Type Three Secretion System Antigens and Shiga Toxin 2B Subunit of Escherichia coli O157: H7.* PloS one, 2017. **12**(1): p. e0169422.

106. Du, Z.Q., X. Li, and J.Y. Wang, *Immunogenicity Analysis of a Novel Subunit Vaccine Candidate Molecule-Recombinant L7/L12 Ribosomal Protein of Brucella suis.* Appl Biochem Biotechnol, 2016. **179**(8): p. 1445-55.

107. Estein, S.M., et al., *The polymeric antigen BLSOmp31 confers protection against Brucella ovis infection in rams.* Vaccine, 2009. **27**(48): p. 6704-11.

108. Cassataro, J., et al., *A DNA vaccine coding for the chimera BLSOmp31 induced a better degree of protection against B. ovis and a similar degree of protection against B. melitensis than Rev.1 vaccination.* Vaccine, 2007. **25**(32): p. 5958-67.

109. Du, Z. and J. Wang, *A novel lumazine synthase molecule from Brucella significantly promotes the immune-stimulation effects of antigenic protein.* Genetics and Molecular Research, 2015. **4**: p. 13084-13095.

110. Bellido, D., et al., *Brucella spp. lumazine synthase as a bovine rotavirus antigen delivery system.* Vaccine, 2009. **27**(1): p. 136-45.

111. Alfano, E.F., et al., *Expression of the Multimeric and Highly Immunogenic Brucella spp. Lumazine Synthase Fused to Bovine Rotavirus VP8d as a Scaffold for Antigen Production in Tobacco Chloroplasts.* Front Plant Sci, 2015. **6**: p. 1170.

112. Berguer, P.M., et al., *A polymeric protein induces specific cytotoxicity in a TLR4 dependent manner in the absence of adjuvants.* PLoS One, 2012. **7**(9): p. e45705.

113. Rossi, A.H., et al., *Brucella spp. Lumazine Synthase Induces a TLR4-Mediated Protective Response against B16 Melanoma in Mice.* PLoS One, 2015. **10**(5): p. e0126827.

114. Cruz-Revilla, C., et al., *Effective protection against experimental Taenia solium tapeworm infection in hamsters by primo-infection and by vaccination with recombinant or synthetic heterologous antigens.* J Parasitol, 2006. **92**(4): p. 864-7.

115. Rosas, G., et al., *Brucella spp. lumazine synthase: a novel adjuvant and antigen delivery system to effectively induce oral immunity.* Microbes Infect, 2006. **8**(5): p. 1277-86.

116. Sciutto, E., et al., *Brucella spp. lumazine synthase: a novel antigen delivery system.* Vaccine, 2005. **23**(21): p. 2784-90.

117. Fragoso, G., et al., *Heterologous prime-boost oral immunization with GK-1 peptide from Taenia crassiceps cysticerci induces protective immunity.* Clin Vaccine Immunol, 2011. **18**(7): p. 1067-76.

118.   Alvarez, P., et al., *Tandem repeats of the extracellular domain of Matrix 2 influenza protein exposed in Brucella lumazine synthase decameric carrier molecule induce protection in mice.* Vaccine, 2013. **31**(5): p. 806-12.

119.   Hiriart, Y., et al., *Characterization of structural and immunological properties of a fusion protein between flagellin from Salmonella and lumazine synthase from Brucella.* Protein Sci, 2017. **26**(5): p. 1049-1059.

120.   Ra, J.S., et al., *Lumazine synthase protein cage nanoparticles as antigen delivery nanoplatforms for dendritic cell-based vaccine development.* Clin Exp Vaccine Res, 2014. **3**(2): p. 227-34.

121.   Wei, Y., et al., *Evaluation of lumazine synthase from Bacillus anthracis as a presentation platform for polyvalent antigen display.* Protein Science, 2017. **26**(10): p. 2059-2072.

122.   Goldbaum, F.A., et al., *The 18-kDa cytoplasmic protein of Brucella species–an antigen useful for diagnosis–is a lumazine synthase.* Journal of medical microbiology, 1999. **48**(9): p. 833-839.

123.   Baldi, P., et al., *Structural, functional and immunological studies on a polymeric bacterial protein.* Brazilian Journal of Medical and Biological Research, 2000. **33**(7): p. 741-747.

124.   Velikovsky, C.A., et al., *A DNA vaccine encoding lumazine synthase from Brucella abortus induces protective immunity in BALB/c mice.* Infect Immun, 2002. **70**(5): p. 2507-11.

125.   Velikovsky, C.A., et al., *Brucella lumazine synthase elicits a mixed Th1-Th2 immune response and reduces infection in mice challenged with Brucella abortus 544 independently of the adjuvant formulation used.* Infection and immunity, 2003. **71**(10): p. 5750-5755.

126.   Rosas, G., et al., *Brucella spp. lumazine synthase: a novel adjuvant and antigen delivery system to effectively induce oral immunity.* Microbes and infection, 2006. **8**(5): p. 1277-1286.

127.   Rosano, G.L. and E.A. Ceccarelli, *Recombinant protein expression in Escherichia coli: advances and challenges.* Frontiers in microbiology, 2014. **5**.

128.   Baneyx, F., *Recombinant protein expression in Escherichia coli.* Current opinion in biotechnology, 1999. **10**(5): p. 411-421.

129.   Papaneophytou, C.P. and G. Kontopidis, *Statistical approaches to maximize recombinant protein expression in Escherichia coli: a general review.* Protein expression and purification, 2014. **94**: p. 22-32.

130.   Huang, P.-S., et al., *RosettaRemodel: a generalized framework for flexible backbone protein design.* PloS one, 2011. **6**(8): p. e24109.

131.   Hsia, Y., et al., *Design of a hyperstable 60-subunit protein icosahedron.* Nature, 2016. **535**(7610): p. 136.

132.   Tsumoto, K., et al., *Practical considerations in refolding proteins from inclusion bodies.* Protein expression and purification, 2003. **28**(1): p. 1-8.

133.   Craig, P.O., V. Alzogaray, and F.A. Goldbaum, *Polymeric display of proteins through high affinity leucine zipper peptide adaptors.* Biomacromolecules, 2012. **13**(4): p. 1112-1121.

134.   Schutze, M.-P., et al., *Carrier-induced epitopic suppression, a major issue for future synthetic vaccines.* The Journal of immunology, 1985. **135**(4): p. 2319-2322.

135.   Pöllabauer, E.M., R. Petermann, and H.J. Ehrlich, *The influence of carrier protein on the immunogenicity of simultaneously administered conjugate vaccines in infants.* Vaccine, 2009. **27**(11): p. 1674-1679.

136. Herzenberg, L.A., T. Tokuhisa, and L.A. Herzenberg, *Carrier-priming leads to hapten-specific suppression.* Nature, 1980. **285**(5767): p. 664-667.

137. Schutze, M.-P., et al., *Carrier-induced epitopic suppression is initiated through clonal dominance.* The Journal of Immunology, 1989. **142**(8): p. 2635-2640.

138. Renjifo, X., et al., *Carrier-induced, hapten-specific suppression: a problem of antigen presentation?* The Journal of immunology, 1998. **161**(2): p. 702-706.

139. Wei, Y., et al., *Evaluation of lumazine synthase from Bacillus anthracis as a presentation platform for polyvalent antigen display.* Protein Sci, 2017.

140. Lu, Y., et al., *Assessing sequence plasticity of a virus-like nanoparticle by evolution toward a versatile scaffold for vaccines and drug delivery.* Proceedings of the National Academy of Sciences, 2015. **112**(40): p. 12360-12365.

141. Bianchi, E., et al., *Vaccination with peptide mimetics of the gp41 prehairpin fusion intermediate yields neutralizing antisera against HIV-1 isolates.* Proceedings of the National Academy of Sciences, 2010. **107**(23): p. 10655-10660.

142. Lilavivat, S., et al., *In vivo encapsulation of nucleic acids using an engineered nonviral protein capsid.* J Am Chem Soc, 2012. **134**(32): p. 13152-5.

143. Frey, R., T. Hayashi, and D. Hilvert, *Enzyme-mediated polymerization inside engineered protein cages.* Chem Commun (Camb), 2016. **52**(68): p. 10423-6.

144. Azuma, Y., et al., *Quantitative Packaging of Active Enzymes into a Protein Cage.* Angew Chem Int Ed Engl, 2016. **55**(4): p. 1531-4.

145. Worsdorfer, B., Z. Pianowski, and D. Hilvert, *Efficient in vitro encapsulation of protein cargo by an engineered protein container.* J Am Chem Soc, 2012. **134**(2): p. 909-11.

146.   Frey, R., et al., *Bottom-up Construction of a Primordial Carboxysome Mimic.* J Am Chem Soc, 2016. **138**(32): p. 10072-5.

147.   Worsdorfer, B., K.J. Woycechowsky, and D. Hilvert, *Directed evolution of a protein container.* Science, 2011. **331**(6017): p. 589-92.

148.   Shenton, W., et al., *Synthesis of Nanophase Iron Oxide in Lumazine Synthase Capsids This work was supported by the BBSRC (W.S.). We thank A. M. Seddon for help with transmission electron microscopy and analytical ultracentrifufation studies and G. D. Ruggiero for the generation of computer images.* Angew Chem Int Ed Engl, 2001. **40**(2): p. 442-445.

149.   Pokharkar, V., et al., *Gold nanoparticles as a potential carrier for transmucosal vaccine delivery.* Journal of biomedical nanotechnology, 2011. **7**(1): p. 57-59.

150.   Scheerlinck, J.-P.Y., et al., *Systemic immune responses in sheep, induced by a novel nano-bead adjuvant.* Vaccine, 2006. **24**(8): p. 1124-1131.

151.   Pham, N.B., et al., *Nanodiamond enhances immune responses in mice against recombinant HA/H7N9 protein.* Journal of nanobiotechnology, 2017. **15**(1): p. 69.

152.   O'Hagan, D.T., *MF59 is a safe and potent vaccine adjuvant that enhances protection against influenza virus infection.* Expert review of vaccines, 2007. **6**(5): p. 699-710.

153.   Cauwelaert, N.D., et al., *The TLR4 agonist vaccine adjuvant, GLA-SE, requires canonical and atypical mechanisms of action for TH1 induction.* PloS one, 2016. **11**(1): p. e0146372.

154.   Vogel, F.R. and M.F. Powell, *A compendium of vaccine adjuvants and excipients*, in *Vaccine Design*. 1995, Springer. p. 141-228.

155.   Huang, M. and W. Wang, *Factors affecting alum–protein interactions.* International journal of pharmaceutics, 2014. **466**(1-2): p. 139-146.

156.   Méndez, I.Z.R., et al., *Potentiation of the immune response to non-adsorbed antigens by aluminum-containing adjuvants.* Vaccine, 2007. **25**(5): p. 825-833.

157.   Aucouturier, J., L. Dupuis, and V. Ganne, *Adjuvants designed for veterinary and human vaccines.* Vaccine, 2001. **19**(17-19): p. 2666-2672.

158.   Wei, Y., et al., *Effect of Two Emulsion-Based Adjuvants on the Structure and Thermal Stability of S. aureus Alpha-toxin.* Journal of pharmaceutical sciences, 2018.

159.   Wei, Y., et al., *Improved Fluorescence Methods for High-Throughput Protein Formulation Screening.* SLAS TECHNOLOGY: Translating Life Sciences Innovation, 2018: p. 2472630318780620.

Chapter 2: Effect of Phosphate Ion on the Structure of Lumazine Synthase, an Antigen

Presentation System from *Bacillus anthracis*

2.1. Introduction

Lumazine synthase (LS) is a metabolic enzyme present in plants, fungi and most microorganisms which is involved in the biosynthesis of riboflavin (vitamin B_2), a compound involved in many biological processes (62). The catalytic reaction mechanism of lumazine synthase involves a condensation reaction between two compounds (5-amino-6-ribitylamino-2, 4(1H,3H)-pyrimidinedione and L-3,4-dihydroxy-2-butanone 4-phosphate) to form 6,7-dimethyl-8-ribityllumazine, which is then converted by riboflavin synthase to riboflavin. LS forms a homo-oligomeric protein with a highly conserved monomeric structure among different organisms. Depending on the organisms, LS can form a pentamer, decamer or icosahedral 60-mer (69). The icosahedral LS consists of 60 monomers with a Caspar-Klug derived triangulation number of 1 (T=1). It has a spherical shape formed by twelve identical pentamers and is often described as a dodecamer of pentamers (161).

Because of its pivotal functional role in microorganism growth and interesting structural properties, LS has been a target of interest in recent years. The structure-function relationship of LS has been explored extensively to elucidate its enzymatic mechanism during the biosynthesis of riboflavin (55). Such knowledge has helped scientists to design antibiotics or anti-fungal drugs which target lumazine synthase and block the supply of riboflavin in pathogenic microorganisms (38, 74, 84, 162-164). LS has also been used as a carrier protein for a variety of applications in biomedical science. These applications include its use as a protein container (96), targeted drug delivery (93), bioimaging (165), construction of nanobuilding block (166), enzyme-based bionanoreactor (167), and vaccine development as a multi-epitope carrier (91, 168, 169).

B. anthracis is a gram-positive bacterium and causes the life-threating disease anthrax (170). LS derived from *Bacillus anthracis* (BaLS) has been crystallized in phosphate buffer and its

structure was solved using X-ray crystallography (38). Several competitive inhibitors targeting BaLS have been synthesized to develop antibiotics against *B. anthracis*. BaLS has also been recently used as a scaffold system to display a linear neutralizing epitope from the ricin toxin and the resulting fusion protein successfully elicited a serum anti-ricin antibody response in mice. (171) The stability and dynamic conformation of BaLS, however, has yet not been extensively investigated. This work describes biophysical characterizations on BaLS to obtain further knowledge of its conformational properties. In the present study, a series of biophysical methods was employed to study: 1) the chemical and thermal unfolding of BaLS; 2) the thermal stability of BaLS as a function of pH; 3) the origins of thermal transitions and 4) the effect of phosphate binding on its structure. Our data show that the native BaLS has two conformational states mediated through the binding/dissociation of phosphate ions. These finding provide important information for the design of efficient formulation of this protein as an antigen presentation system.

2.2. Experimental methods

2.2.1. Cloning, protein expression and purification

The plasmid producing BaLS (pTBSG) was transformed into *E. coli* strain BL21 (λDE3) pLysS competent cells (Promega, Madison, WI) for protein expression. pTBSG plasmid and BL21(λDE3) were described previously (172, 173). The cells were grown in Terrific Broth (P212121, MI) at 37 °C under shaking conditions and induced using 1mM IPTG (ThermoFisher Scientific, Waltham, MA) at OD_{600} between 0.8 to 1.0, followed by growing overnight at 20 °C. Cells were pelleted, resuspended in anion exchange binding buffer (5 mM Tris, 5 mM EDTA, pH 8.0) and lysed by sonication. The supernatant of the lysate were loaded onto three HiTrap Q HP columns (5 ml; GE healthcare, Germany) connected in series. Protein was eluted by a linear

gradient elution method using the anion exchange elution buffer (1M NaCl, 5 mM Tris, 5 mM EDTA, pH 8.0). The elution fractions containing BaLS were pooled, concentrated and loaded onto a Superose 6 10/300 GL column (GE healthcare, IL, USA) using PBS buffer (10 mM Na_2HPO_4, 1.8 mM KH_2PO_4, 2.7 mM KCl, 137 mM NaCl, pH 7.4) as the mobile phase. The purity of BaLS samples was analyzed by SDS-PAGE (12%, w/v). The SDS-PAGE data has been reported previously.(174) Purified BaLS (at 2 mg/ml) was stored at -80 °C in PBS buffer for future use. BaLS samples were thawed at room temperature and filtered through syringe filters (0.1 μm, Millex, Billerica, MA) before biophysical analysis. The molecular weight (MW) of the LS oligomer was determined using multiangle light scattering and was reported previously.(174) The determined MW matched with the theoretical MW based on a 60-mer.

2.2.2. Far-UV Circular Dichroism (CD)

Far-UV CD spectra were measured using an Applied Photophysics Chirascan-plus CD spectrometer equipped with a 6-position, Peltier-controlled cell holder (Applied Photophysics, UK). Protein samples (at 0.2 mg/ml) were loaded into a 1-mm quartz cuvette and the spectra were obtained from 200 nm to 260 nm in 1-nm increment with an integration time of 1 sec per data point. For thermal melting experiments, the temperature ramp was performed from 10 to 95 °C and the CD spectra were recorded every 2.5 °C with an equilibration time of 2 min at each temperature point.

2.2.3. Intrinsic tryptophan fluorescence and static light scattering

Intrinsic tryptophan (Trp) fluorescence was measured using a steady-state fluorometer (Photon Technology International, NJ). Protein samples (at 0.2 mg/ml) loaded in a 1X1 cm quartz

cuvette were excited at 295 nm (> 95% Trp emission) and the emission spectra were collected from 310 to 400 nm at one nanometer intervals with an integration time of 1 sec per data point. Both excitation and emission slit widths were set to 4 nm. The mean center of spectral mass peak position (MSM peak position) and ratio of fluorescence intensity at 330 to 350 (F330/F350) values were calculated from the buffer-subtracted spectra using an in-house software (Middaugh suite) (175). The MSM peak values are approximately 8 to 10 nm higher than the actual peak position but results in a better signal to noise ratio. The static light scattering of BaLS was collected simultaneously with the measurement of intrinsic tryptophan fluorescence using a second PMT detector placed at 180^0 to the fluorescence detector. The signal was collected at 295 nm with an integration time of 1 sec. Thermal melt studies were performed from 10 to 99 ^{o}C with an increment of 2.5 ^{o}C and an equilibration time of 2 min.

2.2.4. Dynamic light scattering

Dynamic light scattering (DLS) was performed using a DynaPro (Wyatt Technology, Santa Barbara, CA) DLS plate reader. Protein samples were added into a 384-well plate flat clear bottom black plate (Corning Incorporated, Corning, NY). Each sample was measured 5 times with an acquisition time of 30 sec each time. A cummulant analysis was performed and intensity-averaged hydrodynamic diameters were reported. For thermal unfolding studies, silicone oil was added to cover sample surfaces to avoid sample evaporation at high temperature. Temperature was set from 25 to 80 ^{o}C and measurements were taken every 2.5 ^{o}C with an equilibration time of 2 min at each temperature.

2.2.5. Extrinsic fluorescence

Extrinsic fluorescence study was performed using an Mx3005P qPCR system (Agilent Technologies, Santa Clara, CA). A Sypro orange stock (5000 x) (Invitrogen, Inc. Carlsbad, California) was added to BaLS samples (at 0.2 mg/ml) at a dilution factor of 1000 and incubated for 30 min prior to analysis. The samples were excited at 492 nm and emission was collected at 610 nm. For thermal studies, the temperature was ramped from 25 to 99 ^{o}C using 1 ^{o}C as step size with an equilibration time of 2 min at each temperature.

2.2.6. Differential scanning calorimetry

Differential scanning calorimetry was performed with MicroCal VP-Capillary DSC (Malvern, UK) to study the overall conformational stability of BaLS. Four hundred microliters of BaLS samples were loaded into a 96-well plate and stored at 5 ^{o}C. Samples were scanned from 10 to 110 ^{o}C at a rate of 1 ^{o}C/min using a filtering period of 16 sec. The data were processed using Origin 7.0 (OriginLab; Northampton, MA).

2.2.7. Chemical unfolding of BaLS

Chemical unfolding of the BaLS in PBS buffer containing 1mM DTT (PanReac AppliChem, Maryland Heights, MO) was performed by addition of increasing amounts of the chaotrope. BaLS samples (at 0.2 mg/ml) containing either urea (up to 8.5 M with an increment of 0.5 M) or guandidine HCl (up to 6 M with an increment of 0.25 M) were equilibrated for 24 hr or 4 hr, respectively, to reach equilibrium. The samples were then analyzed using CD, intrinsic Trp fluorescence, extrinsic fluorescence, static light scattering, and dynamic light scattering. All measurement was performed at 25 ^{o}C.

2.2.8. Thermal stability of BaLS

The thermal unfolding profiles of the BaLS (at 0.2 mg/ml) in PBS buffer were collected using CD, intrinsic Trp fluorescence, static light scattering and dynamic light scattering. The thermal stability of BaLS as a function of pH (5.0, 6.0, 7.0 and 8.0) was further studied. BaLS samples were dialyzed against 20 mM citrate-phosphate buffers (I = 150 mM adjusted by NaCl) overnight at 4 $^{\circ}$C and the protein concentration was adjusted to 0.2 mg/ml. For pH dependent thermal stability studies, DSC and extrinsic fluorescence were added as additional methods. Thermal unfolding curves were plotted and the melting temperature (T_m) was calculated by a first derivative method using Origin 8.0 (OriginLab; Northampton, MA).

Radar charts were constructed using multiple biophysical data sets collected over a range of pH and temperature (CD, DSC, light scattering, extrinsic fluorescence and intrinsic fluorescence) to visualize the thermal stability of BaLS using in-house software (MiddaughSuite). (175) The construction of the radar chart was previously described. (175) All radar charts were then integrated to generate an empirical phase diagram (EPD) (71) showing protein structural changes as a function of pH and temperature. A k-means clustering algorithm was applied to define boundaries for different regions.(176) Within each cluster, data were averaged to create a radar chart with five radial axes corresponding to separate biophysical data sets. For each radial axis, the minimal value of that specific data within that cluster was mapped to the center of the radar chart and the maximum value to the outer circumference. A polygon generated by connecting values in each axis represents the structural state within that cluster.(175-177) A polygon corresponding to the native state of proteins has a relatively small area and a larger polygon area indicates more structurally altered states.

2.2.9. The origin of two thermal transitions by DSC

To better understand the origin of the thermal transitions detected with BaLS, protein samples in PBS buffer of increasing concentration (0.2 to 1.0 mg/ml) were analyzed by DSC. The T_m values were plotted as a function of protein concentration. BaLS sample was then dialyzed against 10 mM citrate buffer (pH 6.0) at 4°C overnight. Final protein concentration was adjusted to 0.2 mg/ml for DSC analysis.

Aldehydes have been found to readily react with the guanidino group of arginine (178, 179) and therefore can be used to deactivate phosphate binding sites (in this case Arg126) of BaLS. To prepare enzymatically inactivated BaLS, samples were dialyzed against 20 mM citrate-phosphate buffer pH 8.0 and the protein concentration was adjusted to 1.0 mg/ml. Molar ratio excess amounts of formaldehyde (100 µL, 37% w/w, ThermoFisher Scientific, Waltham, MA) were mixed with 0.5 mL BaLS samples (at 1.0 mg/ml). The reaction mixture was kept at room temperature for 30 min and was then quenched by addition of 250 µL of 1M Tris solution (pH 7.8) (Sigma, St. Louis, MO). The formaldehyde-treated BaLS was dialyzed against 20 mM citrate-phosphate buffer pH 6.0 and analyzed using DSC.

2.2.10. Phosphate binding on BaLS conformation

BaLS samples (at 0.2 mg/ml) were prepared in 20 mM citrate buffer pH 6.0 with an increasing concentration of sodium phosphate (0 to 500 mM), potassium phosphate (0 to 500 mM) or sodium pyrophosphate (0 to 15 mM) or in a base buffer (10 mM citrate, 50 mM phosphate buffer, pH 6.0) containing an increasing concentration of sodium chloride (0 to 500 mM). These protein samples were subjected to extrinsic fluorescence and intrinsic Trp fluorescence analysis. For the extrinsic fluorescence study, the fluorescence intensities at 25 °C or T_m1 values were plotted against phosphate or NaCl concentration. BaLS samples containing sodium phosphate (0

to 500 mM) were also analyzed by DSC to validate the T_m values obtained from extrinsic fluoresce analysis. The intrinsic fluorescence study was performed at 25 °C and the MSM peak position and F330/F350 value were plotted against phosphate or NaCl concentration.

2.3. Results

2.3.1. Chemically induced unfolding

Conformational alternations of BaLS at 25 °C in response to increasing concentration of urea or guanidine HCl were monitored by various techniques (Figure 2.1). The CD signal was collected at 222 nm where both urea and guanidine are CD transparent. The increase in CD signal (becoming less negative) is an indication of loss of secondary structure. As shown in Figure 2.1A, guanidine is able to unfold the BaLS at a much lower concentration than urea suggesting that guanidine is more effective in altering the secondary structure of BaLS, as is usually seen with most proteins. Guanidine (at 6 M) was able to unfold to BaLS to a larger extent than urea (at 8.5 M). Tertiary structure changes of BaLS during chemical unfolding was monitored by Sypro orange fluorescence. Sypro orange binds to exposed hydrophobic regions and such binding results in an increase in the fluorescence signal. Dramatic differences in the unfolding profiles of BaLS induced by urea and guanidine (Figure 2.1B) were observed. Urea unfolding of BaLS shows a simple profile with a sigmoidal shape. In contrast, guanidine caused a sudden increase in the Sypro orange fluorescence signal followed by a quick drop. Guanidine at low concentration (< 2 M) is able to induce much greater exposure of apolar regions in BaLS than urea. The decrease in the Sypro orange fluorescence signal at high guanidine concentration (> 2 M) is probably because of the dissociation of the dye from the protein induced by aggregation of the unfolded protein.(180) The urea induced unfolding of BaLS monitored by intrinsic Trp fluorescence analysis (MSM peak

position and F330/F350) shows one transition, while guanidine induces a biphasic denaturation profile (Figure 2.1C and 2.1D). Compared to urea, guanidine, at a lower concentration, is able to alter BaLS and expose buried indole side-chains to a more polar environment. The aggregation behavior monitored by static light scattering is plotted in Figure 2.1E. Urea (at 8.5 M) induced a slight decrease in the static light scattering signal and possibly resulted in the altered BaLS with a less dense structure with a decreased dn/dc value. Guanidine ($\leq$ 1 M), however, caused a dramatic increase in the signal indicating the formation of large aggregates. At relatively higher guanidine concentrations (> 1 M), the static light scattering signal of BaLS considerably dropped and quickly reached a level even lower than that of BaLS in 8.5 M urea (Figure 2.1E inset). Such observations may reflect that 6 M guanidine rather than 8.5 M urea is able to induce a more complete dissociation and unfolding of the icosahedral structure of BaLS.

The hydrodynamic diameter (d_h) of BaLS in the presence of urea or guanidine were then studied using dynamic light scattering (Figure 2.1F). Urea (at 8.5 M) only caused a minor increase (approximately 0.4 nm) in the d_h of BaLS. This indicates that the assembly state of BaLS probably remained unchanged in the presence of 8.5M urea. The slight increase in d_h was presumably because of the "swelling" of the particle which correlates well with a possible reduced dn/dc value of BaLS observed by static light scattering. In contrast, guanidine resulted in formation of aggregates of BaLS at a concentration above 0.5 M (data not shown). The d_h of BaLS in the presence of guanidine (at 1 to 2 M) could not be reproducibly measured because of the presence of large aggregates and the heterogeneity of the sample. At higher denaturant concentrations (> 2.0 M), guanidine decreased the d_h of BaLS which eventually dropped below 2 nm. Guanidine at low concentration, therefore, causes aggregation of BaLS, but completely dissociates and unfolds BaLS at a relatively high concentration.

Based on the data collected, chemically induced unfolding pathways induced by urea (up to 8.5 M) and guanidine (up to 6 M) of BaLS can be proposed. A mono-phasic unfolding profile of BaLS by urea (up to 8.5 M) in PBS was observed using all biophysical techniques indicating a two-state denaturation process. Urea at 8.5 M is able to convert BaLS into a partially unfolded state with a possibly loosen structure but an unchanged assembly state. In contrast, guanidine denatures BaLS through multiple phases. A putative intermediate state of BaLS exists in the presence of low guanidine concentration (at 1 M). Such state has exposed hydrophobic regions and is prone to aggregation which is a phenomenon commonly observed for guanidine denaturation of protein (181). The secondary structure of this intermediate remained unchanged when guanidine concentration is less than 1.5 M (Figure 2.1A) indicating that the intermediate is essentially a molten globular state.

2.3.2. Thermal unfolding of BaLS

The secondary structure of BaLS in PBS buffer in response to thermal stress were studied using CD (Figure 2.2A). The CD signal at 222 nm plotted as a function of temperature suggests thermal unfolding initiating above 80 °C, indicating strong thermal stability of BaLS in PBS buffer. The temperature was ramped up to 95 °C at which BaLS was not yet fully unfolded. The tertiary structure of BaLS was analyzed using intrinsic Trp fluorescence (Figure 2.2B). BaLS contains two Trp residues (Trp 51 and Trp 151) in each monomer. A mean spectral center of mass (MSM) method was used to calculate the peak position of the emission spectra at each temperature. The ratio of the emission intensity at 330 and 350 (F330/350) was also plotted as a function of temperature to monitor alterations in the protein's tertiary structure. Both MSM peak position and F330/F350 plots show two distinct thermal transitions (Figure 2.2B) and correlate well with each other. The aggregation behavior of BaLS in PBS buffer was monitored by plotting the static light

scattering intensity as a function of temperature (Figure 2.2C). Only one thermal transition (starting from 80 ºC) was observed. The hydrodynamic diameter of BaLS did not show any significant change from 25 to 80 ºC as analyzed by dynamic light scattering (Figure 2.2D). The thermal transitions were in good agreement with those of BaLS previously determined using DSC and Sypro orange extrinsic fluorescence (171). In addition, the first thermal transition was found to be reversible (Figure 2.S2).

The biophysical properties of BaLS as a function of pH and temperature were further investigated. Protein samples dialyzed at pH 5.0 overnight at 4 ºC precipitated and therefore was not subjected to biophysical studies. The thermal stability of BaLS samples (at 0.2 mg/ml) dialyzed at pH 6.0, 7.0 and 8.0 were characterized using various methods (Figure 2.3). As shown in Figure 2.3H, radar charts constructed from multiple sets of biophysical data showed five structurally distinct regions over the pH (5.0 to 8.0) and temperature range (25 to 99 ºC) studied here. Region I corresponds to the native state of BaLS. Region II indicates the early thermal transition of BaLS that indicates only a slight conformational alternation. Region III represents the structural state post the first thermal transition. Region IV indicates the main thermal transition of BaLS. Region V indicates protein precipitation. Overall two pH-dependent thermal transitions were observed. Under these pH conditions, BaLS has the highest T_m values for both transitions at pH 7.0. Interestingly, the early thermal transition was not observed using CD, static light scattering or dynamic light scattering (Figure 2.3A, 2.3C and 2.3D), but clearly appeared in melting curves monitored using the other techniques. This suggests that the early transition is associated with an alteration in the protein's tertiary structure rather than its secondary structure or assembly state.

2.3.3. The origin of the two thermal transitions of BaLS seen by DSC

DSC was performed to better tease out the origin of thermal transitions of BaLS. The dissociation behavior of an oligomeric protein under thermal stress can be studied using DSC by examining protein samples of increasing concentrations. If protein dissociation is coupled with thermal unfolding, protein samples at a higher concentration are expected to manifest higher apparent T_m values.(182) A previous study has confirmed that LS in solution exists as an icosahedral oligomer consisting of 60 identical monomers using multiangle light scattering.(171) The concentration dependency of the thermal transitions of LS in 20 mM citrate-phosphate buffer pH 6.0 studied using DSC are shown in Figure 2.4A. For protein concentrations ranging from 0.2 mg/ml to 1.0 mg/ml, T_m1 is independent of the protein concentration, while T_m2 increases with increasing protein concentration. This suggests that the dissociation of oligomeric BaLS is involved in the second thermal transition. This result correlates with the observation that protein hydrodynamic diameters did not change from 25 to 80 °C using DLS. Unfortunately, the DLS instrument cannot be used at temperatures exceeding 80 °C where the oligomeric structure could be altered. Furthermore, aggregation also prevents any direct observation of dissociation events. It can therefore be concluded that the late thermal transition results from the dissociation and unfolding of the oligomeric BaLS.

A phosphate ion has been found to bind to the enzymatic site of BaLS, a pocket located at the interface between two neighboring BaLS subunits.(38) Phosphate ions interact with Arg126 on one monomer, Thr85' and Ala84' on a joining subunit (Figure 2.5). Interface energy calculations were performed on the subunit pentamer, obtained from lumazine synthase from *Bacillus anthracis* (PDB ID: 1VSW), either bound or unbound with phosphate ions (Table 2.1). The starting conformations were minimized in Yasara Structure (183) for 5 nanoseconds. The two pentamers (bound & unbound), were then analyzed for interfacial residue stabilization energy with

the PISA module (Proteins, Interfaces, Surface, and Assemblies service at the European Bioinformatics Insitute) (184). The calculations showed that each phosphate ion increased the stability of the interface assembly by approximately 6 kcal/mol (with both intra and inter-chain contacts, Table 2.1).

The effect of phosphate binding on the conformational stability of BaLS was studied by DSC. Figure 2.4B shows that the early thermal transition of BaLS completely disappeared in a non-phosphate containing buffer (10 mM citrate buffer, pH 6.0) or in a phosphate containing buffer (20 mM citrate-phosphate buffer, I = 150 mM adjusted by NaCl, pH 6.0) after the deactivation of active sites by formaldehyde treatment. The disappearance of T_m1 of BaLS in a non-phosphate containing buffer or after formaldehyde treatment confirms the direct correlation of BaLS/phosphate binding events with the occurrence of the early thermal transition (T_m1). Thus, the first thermal transition can presumably be attributed to the thermal dissociation of phosphate ions from active sites on BaLS.

2.3.4. Phosphate binding on the conformation of BaLS

The level of exposure of hydrophobic regions on BaLS and the T_m1 values of BaLS in the presence of varying concentrations of three different phosphate salts were monitored using Sypro orange extrinsic fluorescence. In the absence of phosphate ions, BaLS did not show the early transition (Figure 2.S1) and this result was in good agreement with the DSC data (Figure 2.5B). As shown in Figure 2.6A, T_m1 increased as sodium phosphate concentration increases and these T_m1 values are in good agreement with T_m values obtained from the DSC analysis. Sodium phosphate at 500 mM is able to increase the T_m1 by more than 30 °C. Such a large shift is attributed to the stabilization of the protein by phosphate binding. It was also noted that the Sypro orange

fluorescence intensity of BaLS decreased when sodium phosphate concentration increased at 25 °C (Figure 2.6A). This suggests that sodium phosphate decreased the exposure level of apolar regions of LS. Both potassium phosphate and sodium pyrophosphate resulted in a similar trend on the T_m1 value and the exposure level of hydrophobic regions as sodium phosphate (Figure 2.6B and 2.6C). Compared to phosphate salts, sodium pyrophosphate, a diphosphate ion, was able to more efficiently decrease the Sypro orange fluorescence intensity of BaLS to the same level as at a much lower concentration, possibly because it has a higher association constant with BaLS.

In the base buffer (10mM citrate, 50mM phosphate buffer, pH 6.0), titration of NaCl, however, resulted in a decrease in protein T_m1 values but an increase in the Sypro orange fluorescence intensity of BaLS (Figure 2.6D). Because ionic interactions of Arg126 are involved in formation of the BaLS/phosphate complex, addition of NaCl increases the ionic strength and weakens interactions between phosphate and BaLS. Such an effect thereby drops T_m1 values and increases the exposure of hydrophobic regions. This result in turn confirms that titration of phosphate salts into BaLS samples alters protein conformation (Figure 2.6A, 2.6B and 2.6C) through specific BaLS/phosphate interactions rather than just increases in ionic strength.

The effect of phosphate ion on the tertiary structure of BaLS at 25 °C was studied using intrinsic Trp fluorescence. The MSM peak position and F330/F350 value of a protein are associated with the overall polarity of the neighboring environment of tryptophan in the protein. These two parameters were recorded to monitor alterations in protein tertiary structures in response to increasing concentration of phosphate ions or sodium chloride. All three phosphate salts resulted in changes with the same trend (Figure 2.7A, 2.7B and 2.7C). LS in the presence of higher phosphate concentrations underwent a blue shift of λ_{em} with an increased F330/F350 value indicating reduced solvent accessibility of Trp residues. Addition of NaCl into BaLS stored in a

base buffer (10 mM citrate, 50 mM phosphate, pH 6.0) resulted in a red shift of λ_{em} and a decrease in the F330/F350 ratio (Figure 2.7D). This presumably reflects a reduction in BaLS/phosphate interactions in response to the increasing ionic strength. The data correlate well with the Sypro orange extrinsic fluorescence analysis. It can therefore be concluded that BaLS/phosphate interactions are able to reduce the solvent accessibility of Trp residues in BaLS.

2.3.5. Pathway

A hypothetical pathway of the thermal unfolding of BaLS is proposed in Figure 2.8. In phosphate-free buffers, BaLS adopts a conformation (N^2) with icosahedral symmetry. In the presence of phosphate ions, they bind to BaLS rendering a subtle conformational change and resulting in protein conformation (N^1) that is a relatively more "compact", with lower exposure of hydrophobic regions and Trp residues. Upon heating, the complex starts to pay an entropy penalty until eventually phosphate ions dissociate from BaLS at a high temperature (e.g. 50 $^\circ$C in PBS buffer) and BaLS turns into N^2 conformation again. Further thermal stress on LS (N^2) causes the dissociation and unfolding of BaLS.

2.4. Discussion

A comprehensive biophysical analysis of the conformation of BaLS was performed in the present study. This analysis required a total of 45 mg of protein. The chemically induced unfolding of BaLS using urea or guanidine HCl showed two distinct unfolding profiles. In contrast to guanidine, urea was much less effective in altering the conformation of BaLS both kinetically (urea unfolding takes approximately one day to reach equilibrium) and thermodynamically. Even in the presence of 8.5 M urea, BaLS is only partially unfolded and apparently still maintains its icosahedral assembly. Goldbaum *et al* has reported that a decameric BaLS derived from *Brucella*

sp. showed no changes in protein secondary or tertiary structures in the presence of 8 M urea.(40) This indicates an exceptional stability of the quaternary structure of BaLS to high urea concentration. In contrast, BaLS was completely denatured by guanidine HCl at 3M. Because BaLS/phosphate binding involves ionic interactions with R126, an ionic shielding effect by electrolytes such as guanidine HCl can weaken and perhaps even dissociate the BaLS/phosphate complex with induction of a conformational change. Thus, the dissociation of the BaLS/phosphate complex was apparently involved in the guanidine denaturation of BaLS and may in part contribute to its multi-phasic unfolding profile.

The thermal unfolding study showed that BaLS in PBS has considerable thermal stability with a primary thermal transition above 80 $^{\circ}$C. The transition with a T_m around 50 $^{\circ}$C is only observed by techniques which are expected to detect protein tertiary structure and overall conformation changes (intrinsic fluorescence, extrinsic fluorescence and DSC). Further investigation using these techniques showed that the first thermal transition of BaLS originates from the dissociation of phosphate ions and the second from the dissociation and unfolding of the icosahedral structure. The presence of the two conformational states was further confirmed using Sypro orange extrinsic fluorescence and intrinsic fluorescence. The binding of phosphate to BaLS (N^2) induces a slight conformational change rending a protein state (N^1) with less exposed hydrophobic regions and Trp residues. Conformation N^1 seems to be more compact which could be attributed to phosphate ions having polar interactions with residues from two neighboring subunits along the twofold icosahedral axis. The difference between the two states (N^1 and N^2) was relatively minor and was not detected using dynamic or static light scattering.

This work may offer insights into the molecular mechanism of the enzymatic function of BaLS. Phosphate binding to the enzymatic pocket is highly conserved for LS from various

organisms. Therefore, the observed conformational change of BaLS upon phosphate binding may also occur for other orthologous LS as well. Because phosphate ions and the phosphate moiety of the substrate (L-3,4-dihydroxy-2-butanone 4-phosphate) bind to the same pocket on LS, binding of this substrate may also induce a similar or even more pronounced (because of more extensive interactions) structural changes to LS to render a relatively closed conformation. Upon the formation and subsequent release of the product, LS changes back to the open conformation (N^2). These structural dynamics of LS during catalysis may also explain the unsolved question of how the product is released from the inside of the complex.

The enzymatic activity of BaLS occurs in the interior of the oligomer to produce lumazine which is further used to synthesize riboflavin by riboflavin synthase which is encapsulated inside the BaLS cavity.(62) X-ray crystal structures of BaLS show that the size of the largest port (i.e. the channel along the fivefold symmetry axes) in BaLS is still not wide enough to permit these two bulky compounds to diffuse out of the enzyme's interior. This indicates that an alternative conformation with a wider opening must exist for BaLS during catalysis. The X-ray crystal structures of icosahedral BaLS from various organisms (*B. anthracis, B. subtilis, S. pombe,* and *A. aeolicus*) have all been obtained in phosphate-containing buffers in which LS may adopt a relatively closed conformation (N^1) with a narrow port not sufficient for product exit. Our data shows that BaLS without phosphate bound has an "open" conformation (N^2) with possibly broader channels that may serve as an intermediate conformation permitting the exit of product. The binding of the substrate and release of the product may sequentially alter the size of the channel and control the release of the product. This work also supports the "breathing" motions of the enzyme during catalytic cycles proposed by Ladenstein *et al.*(62) These results may also explain why LS has never been successfully crystallized in a phosphate-free buffer system.(43) This may

be attributed to an increased hydrophobicity of LS in the absence of phosphate ions. Lastly, these results provide guideline in the use of phosphate buffers in the formulation of LS-based vaccines.

2.5. References

1.   Ladenstein, R., M. Fischer, and A. Bacher, *The lumazine synthase/riboflavin synthase complex: shapes and functions of a highly variable enzyme system.* FEBS Journal, 2013. **280**(11): p. 2537-2563.

2.   Zhang, X., et al., *Multiple assembly states of lumazine synthase: a model relating catalytic function and molecular assembly.* Journal of molecular biology, 2006. **362**(4): p. 753-770.

3.   Karshikov, A. and R. Ladenstein, *Electrostatic effects in a large enzyme complex: Subunit interactions and electrostatic potential field of the icosahedral β60 capsid of heavy riboflavin synthase.* Proteins: Structure, Function, and Bioinformatics, 1989. **5**(3): p. 248-257.

4.   Zhang, X., et al., *A structure-based model of the reaction catalyzed by lumazine synthase from Aquifex aeolicus.* Journal of molecular biology, 2003. **328**(1): p. 167-182.

5.   Cushman, M., et al., *Design, synthesis, and evaluation of 9-D-ribitylamino-1, 3, 7, 9-tetrahydro-2, 6, 8-purinetriones bearing alkyl phosphate and R, R-difluorophosphonate substituents as inhibitors of tiboflavin synthase and lumazine synthase.* J. Org. Chem, 2004. **69**(3): p. 601-612.

6.   Zhang, Y., et al., *A novel lumazine synthase inhibitor derived from oxidation of 1, 3, 6, 8-tetrahydroxy-2, 7-naphthyridine to a tetraazaperylenehexaone derivative.* The Journal of organic chemistry, 2007. **72**(8): p. 2769.

7.   Cushman, M., et al., *Design, synthesis, and evaluation of 9-D-ribityl-1, 3, 7-trihydro-2, 6, 8-purinetrione, a potent inhibitor of riboflavin synthase and lumazine synthase.* The Journal of organic chemistry, 2001. **66**(25): p. 8320-8327.

8.   Chen, J., et al., *A high-throughput screen utilizing the fluorescence of riboflavin for identification of lumazine synthase inhibitors.* Analytical biochemistry, 2005. **338**(1): p. 124-130.

9.   Talukdar, A., et al., *Discovery and development of a small molecule library with lumazine synthase inhibitory activity.* The Journal of organic chemistry, 2009. **74**(15): p. 5123.

10. Morgunova, E., et al., *Structural study and thermodynamic characterization of inhibitor binding to lumazine synthase from Bacillus anthracis.* Acta Crystallographica Section D: Biological Crystallography, 2010. **66**(9): p. 1001-1011.

11. Wörsdörfer, B., K.J. Woycechowsky, and D. Hilvert, *Directed evolution of a protein container.* Science, 2011. **331**(6017): p. 589-592.

12. Min, J., et al., *Lumazine synthase protein cage nanoparticles as modular delivery platforms for targeted drug delivery.* RSC Advances, 2014. **4**(89): p. 48596-48600.

13. Song, Y., et al., *Lumazine Synthase Protein Nanoparticle-Gd (III)-DOTA Conjugate as a T1 contrast agent for high-field MRI.* Scientific reports, 2014. **5**: p. 15656-15656.

14. Moon, H., et al., *Fabrication of uniform layer-by-layer assemblies with complementary protein cage nanobuilding blocks via simple His-tag/metal recognition.* Journal of Materials Chemistry B, 2013. **1**(35): p. 4504-4510.

15. Shenton, W., et al., *Synthesis of nanophase iron oxide in lumazine synthase capsids.* Angewandte Chemie International Edition, 2001. **40**(2): p. 442-445.

16. Velikovsky, C.A., et al., *A DNA vaccine encoding lumazine synthase from Brucella abortus induces protective immunity in BALB/c mice.* Infection and immunity, 2002. **70**(5): p. 2507-2511.

17.   Mejias, M.P., et al., *Immunization with a chimera consisting of the B subunit of Shiga toxin type 2 and brucella lumazine synthase confers total protection against Shiga toxins in mice.* The Journal of Immunology, 2013. **191**(5): p. 2403-2411.

18.   Ra, J.-S., et al., *Lumazine synthase protein cage nanoparticles as antigen delivery nanoplatforms for dendritic cell-based vaccine development.* Clinical and experimental vaccine research, 2014. **3**(2): p. 227-234.

19.   Sever, J.L., et al., *Safety of anthrax vaccine: a review by the Anthrax Vaccine Expert Committee (AVEC) of adverse events reported to the Vaccine Adverse Event Reporting System (VAERS).* Pharmacoepidemiology and drug safety, 2002. **11**(3): p. 189-202.

20.   Wei, Y., et al., *Evaluation of Lumazine Synthase from Bacillus anthracis as a Presentation Platform for Polyvalent Antigen Display.* Protein Science: p. n/a-n/a.

21.   Studier, F.W. and B.A. Moffatt, *Use of bacteriophage T7 RNA polymerase to direct selective high-level expression of cloned genes.* Journal of molecular biology, 1986. **189**(1): p. 113-130.

22.   Wahome, N., et al., *Production of Well-Characterized Virus-like Particles in an Escherichia coli-Based Expression Platform for Preclinical Vaccine Assessments.* Vaccine Design: Methods and Protocols, Volume 2: Vaccines for Veterinary Diseases, 2016: p. 437-457.

23.   Wei, Y., et al., *Evaluation of Lumazine Synthase from Bacillus anthracis as a Presentation Platform for Polyvalent Antigen Display.* Protein Science, 2017.

24.   Kim, J.H., et al., *Improved data visualization techniques for analyzing macromolecule structural changes.* Protein Science, 2012. **21**(10): p. 1540-1553.

25.   Alsenaidy, M.A., et al., *An empirical phase diagram approach to investigate conformational stability of "second-generation" functional mutants of acidic fibroblast growth factor-1.* Protein Science, 2012. **21**(3): p. 418-432.

26.   Alsenaidy, M.A., et al., *Physical Stability Comparisons of IgG1-Fc Variants: Effects of N-Glycosylation Site Occupancy and Asp/Gln Residues at Site Asn 297.* Journal of pharmaceutical sciences, 2014. **103**(6): p. 1613-1627.

27.   Maddux, N.R., et al., *Multidimensional methods for the formulation of biopharmaceuticals and vaccines.* Journal of pharmaceutical sciences, 2011. **100**(10): p. 4171-4197.

28.   Trézl, L., et al., *Antagonistic reactions of arginine and lysine against formaldehyde and their relation to cell proliferation, apoptosis, folate cycle and photosynthesis.* Molecular and cellular biochemistry, 2003. **244**(1): p. 167-176.

29.   TRÉZL, L., et al., *ESSENTIAL DIFFERENCES IN SPONTANEOUS REACTION OF L-LYSINE AND L-ARGININE WITH FORMALDEHYDE AND ITS QUANTUM CHEMICAL INTERPRETATION.* Periodica Polytechnica. Chemical Engineering, 1988. **32**(4): p. 251.

30.   Vollrath, F., et al., *Differential Scanning Fluorimetry provides high throughput data on silk protein transitions.* Scientific reports, 2014. **4**: p. 5625.

31.   Povarova, O.I., I.M. Kuznetsova, and K.K. Turoverov, *Differences in the pathways of proteins unfolding induced by urea and guanidine hydrochloride: molten globule state and aggregates.* PLoS One, 2010. **5**(11): p. e15035.

32.   Grasso, D., et al., *The effects of scan rate and protein concentration on DSC thermograms of bovine superoxide dismutase.* Thermochimica acta, 1995. **265**: p. 163-175.

33.   Krieger, E. and G. Vriend, *New ways to boost molecular dynamics simulations.* Journal of computational chemistry, 2015. **36**(13): p. 996-1007.

34.   Krissinel, E. and K. Henrick, *Inference of macromolecular assemblies from crystalline state.* Journal of molecular biology, 2007. **372**(3): p. 774-797.

35.   Zylberman, V., et al., *High order quaternary arrangement confers increased structural stability to Brucella sp. lumazine synthase.* Journal of Biological Chemistry, 2004. **279**(9): p. 8093-8101.

36.   Morgunova, E., et al., *Lumazine synthase from Candida albicans as an anti-fungal target enzyme structural and biochemical basis for drug design.* Journal of Biological Chemistry, 2007. **282**(23): p. 17231-17241.

2.6. Figures and Tables

2.6.1. Tables

	Interface Area	$\Delta G_{interface}$	$\Delta G_{interface}$	N	N
	(Å^2)	(kcal/mol)	(P-value)	(Hydrogen Bonds)	(Salt Bridges)
Pentamer	1298.8	-13.5	0.3	9	6
Pentamer_PO₄	1273.2	-12.9	0.3	10	6
PO₄_intrachain	80.8	-5.1	0.7	2	0
PO₄_interchain	41.7	-1.1	0.9	2	0

Table 2.1. Average interface energy of Lumazine Synthase pentamer in the absence and presence of phosphate ions. The intra and inter-chain contribution of phosphate binding is also shown. The energy calculations (184) were performed on pentamer constructs that were minimized for 5 ns in Yasara Structure (183), with and without bound phosphate ions (Pentamer derived from PDBid: 1VSW). Interface area (Å^2) represents the difference in surface area that is accessible between monomeric and pentameric assembly states. ΔG of the interface is a thermodynamic term describing the change in solvation free energy when transitioning from a monomer to an assembled pentamer. The P-value of the interface indicates the probability of interfacial hydrophobicity, with less than 0.5 implying increased hydrophobicity and more than 0.5 showing a decrease in expected hydrophobicity (184).

2.6.2. Figures
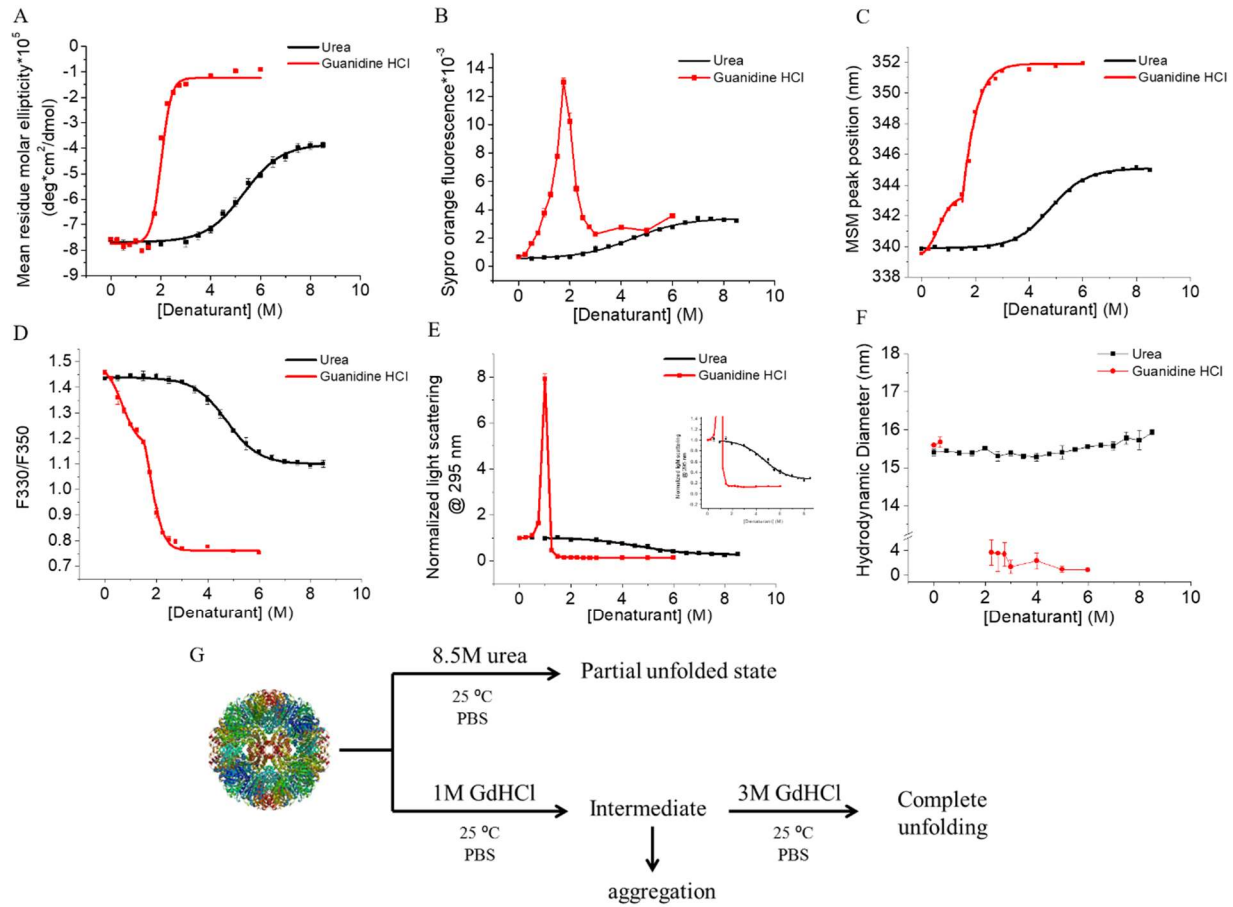
Figure 2.1. Chemically induced unfolding of BaLS in PBS buffer using urea and guanidine chloride at 25 °C monitored by (A) CD signal at 222 nm; (B) Sypro orange fluorescence; (C) Mean spectral center mass peak position calculated from intrinsic Trp fluorescence measurement; (D) The ratio of fluorescence intensity at 330 nm by 350 nm calculated from intrinsic Trp fluorescence measurement; (E) static light scattering; (F) dynamic light scattering; (G) Proposed chemical unfolding pathways of BaLS induced by urea and guanidine chloride. Error bars are standard deviations (N=3).
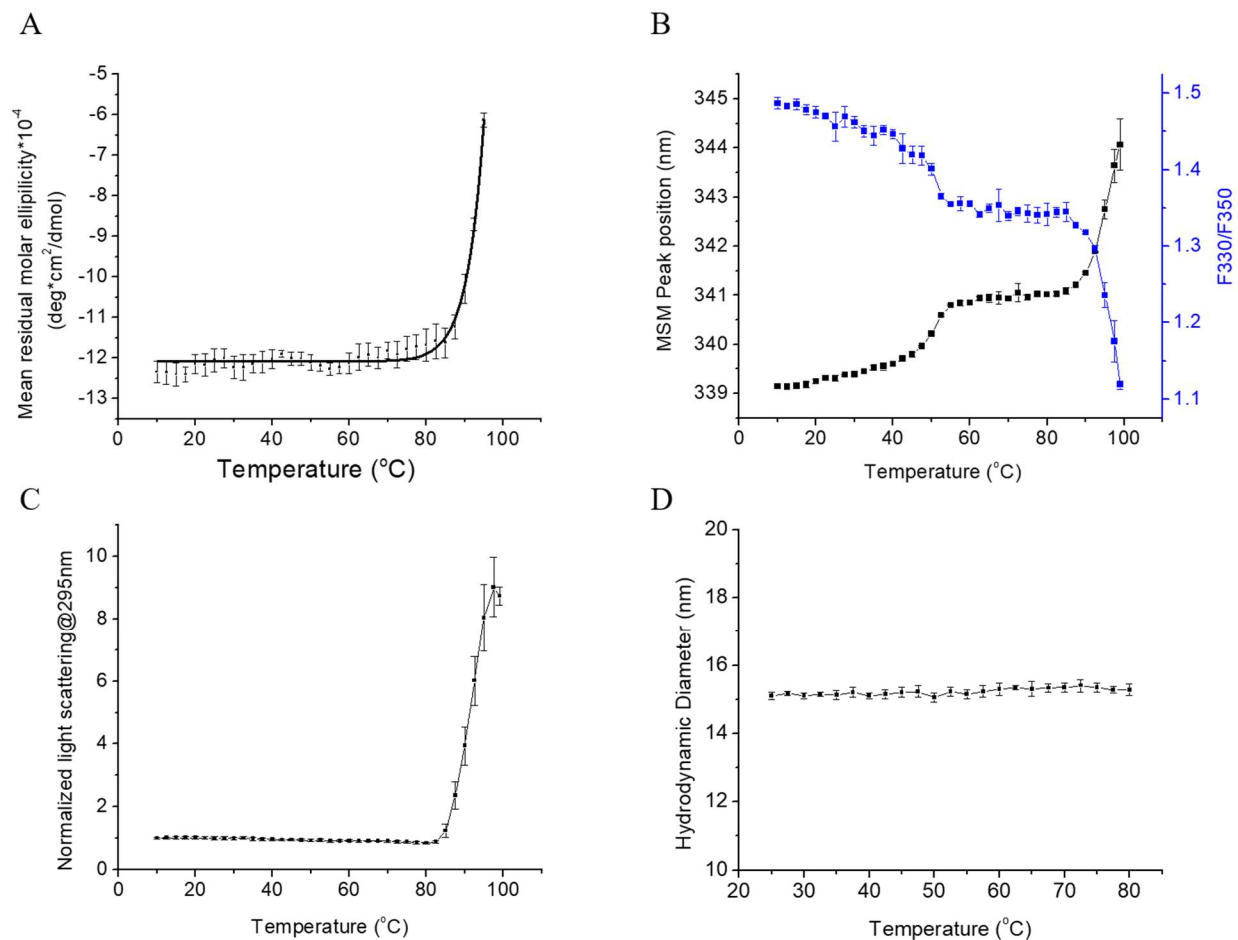
Figure 2.2. Thermal unfolding of BaLS (at 0.2 mg/ml) in PBS buffer monitored by (A) the CD signal at 222 nm; (B) intrinsic Trp fluorescence; (C) static light scattering at 295 nm; (D) dynamic light scattering. Error bars are standard deviations (N=3).
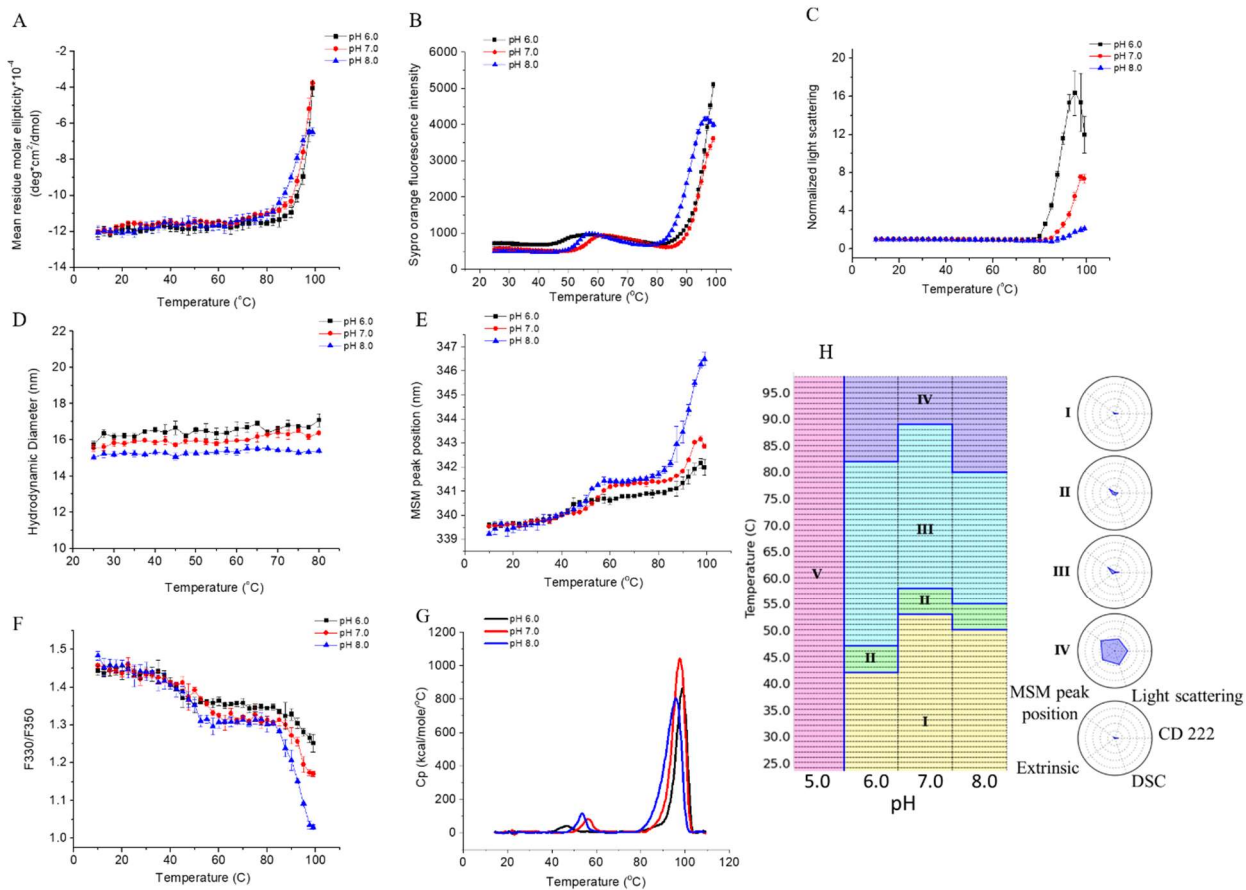
Figure 2.3. The thermal stability of BaLS as a function of temperature and pH monitored by (A) the CD signal at 222 nm; (B) Sypro orange fluorescence; (C) static light scattering; (D) dynamic light scattering; (E) MSM peak position; (F) The ratio of fluorescence intensity at 330 nm by 350 nm; (G) differential light scattering; (H) Empirical phase diagram and radar charts of BaLS constructed using data from CD, light scattering, MSM peak position, Sypro orange extrinsic fluorescence, and differential light scanning. Error bars are standard deviations (N=3).
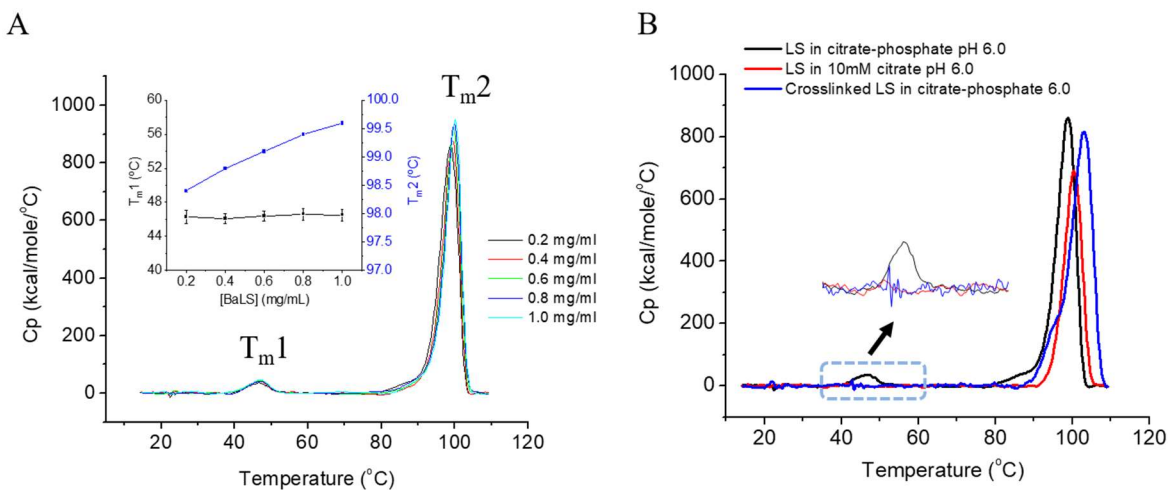
Figure 2.4. DSC thermograms of (A) BaLS (at 0.2 to 1.0 mg/ml) in citrate-phosphate buffer pH 6.0. The inset graph shows Tm values as a function of the concentration of BaLS; (B) BaLS (at 0.2 mg/ml) in citrate-phosphate buffer pH 6.0, BaLS in 20 mM citric buffer pH 6.0, formaldehyde crosslinked BaLS in citrate-phosphate buffer pH 6.0. Error bars are standard deviations (N=3).
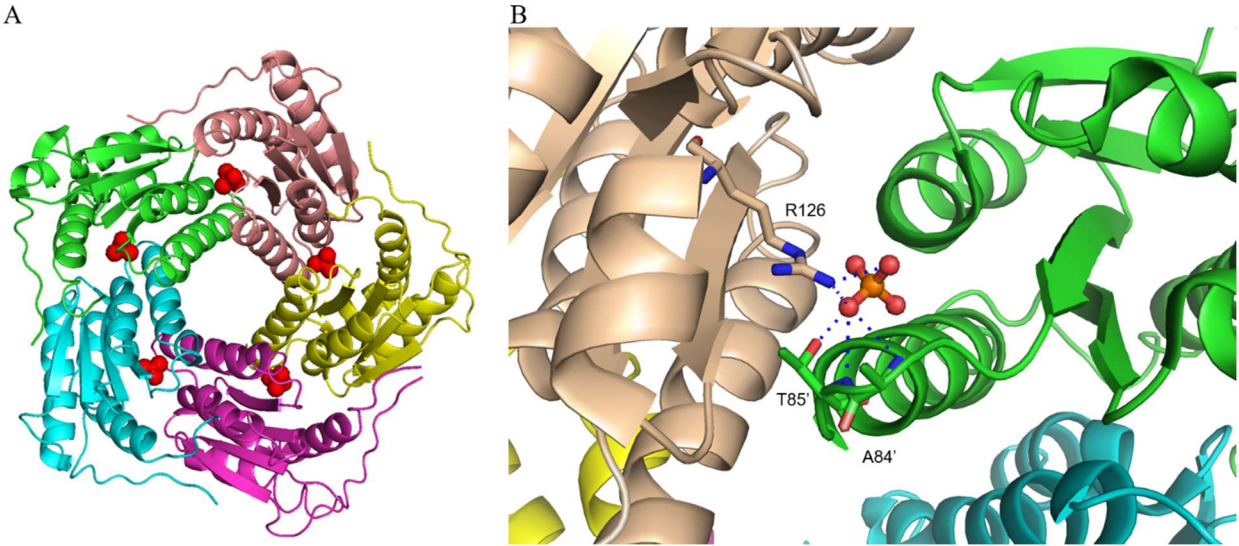
Figure 2.5. Structural representations of the BaLS/phosphate complex. (A) A pentameric block of BaLS viewed along the fivefold symmetry axis. Each monomer is shown in a different color and phosphate ions shown as red spheres at the active sites. (B) An expanded view of the active site of BaLS with bound phosphate ion. Each phosphate ion make polar interactions with Arg126, Thr85' and Ala84' indicated using blue dashed lines. Figures were made based on the crystal structure of lumazine synthase from Bacillus anthracis (PDB ID: 1VSW) using the program PyMOL V 1.7 (https://www.pymol.org/).
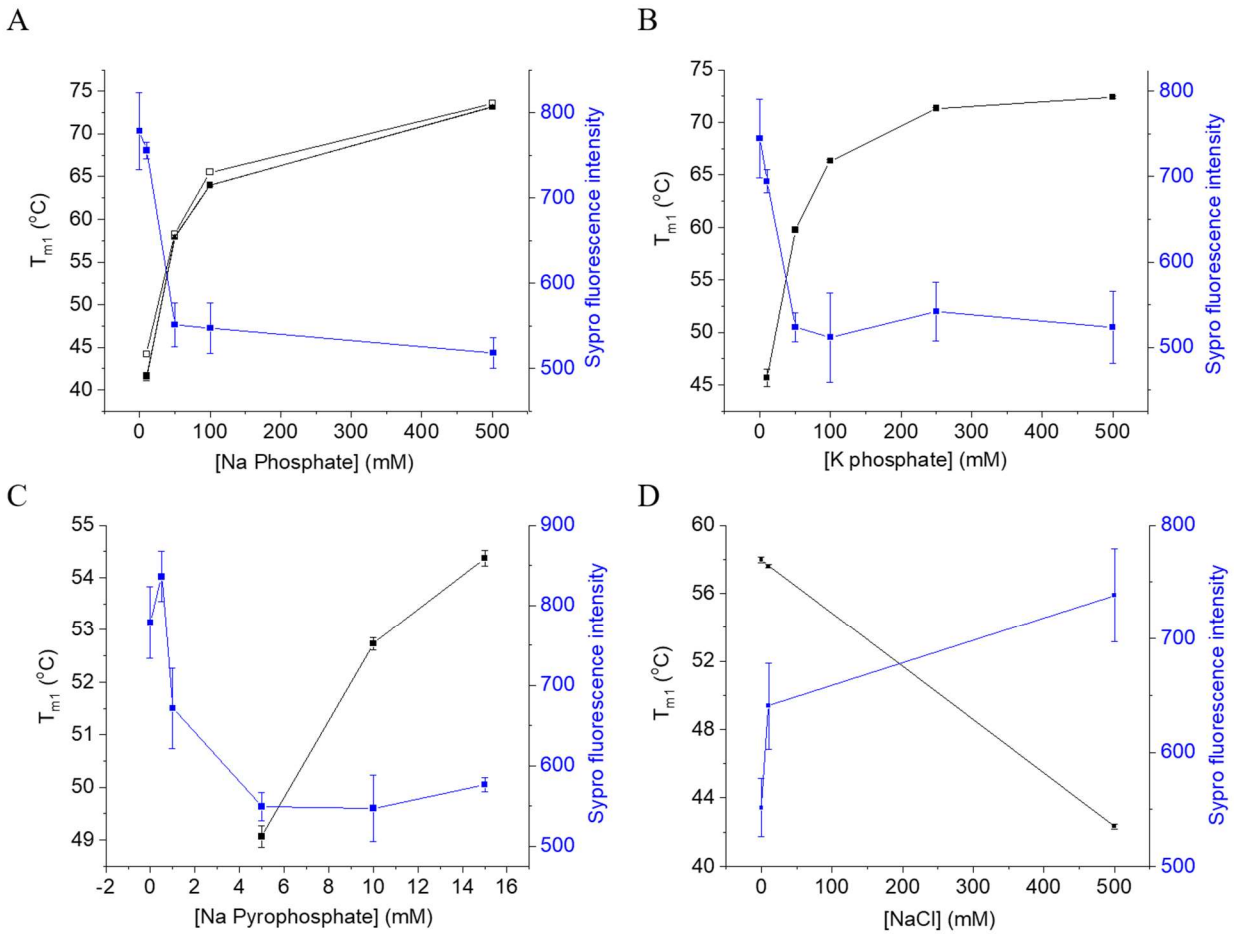
Figure 2.6. Effects of the phosphate concentration on Tm1 values and the Sypro orange fluorescence intensity of BaLS (in 10 mM citrate pH 6.0) at 25 °C by titration of (A) sodium phosphate. The open square represents the DSC Tm values; (B) potassium phosphate; (C) sodium pyrophosphate; (D) sodium chloride in presence of 50 mM sodium phosphate. Error bars are standard deviations (N=3).
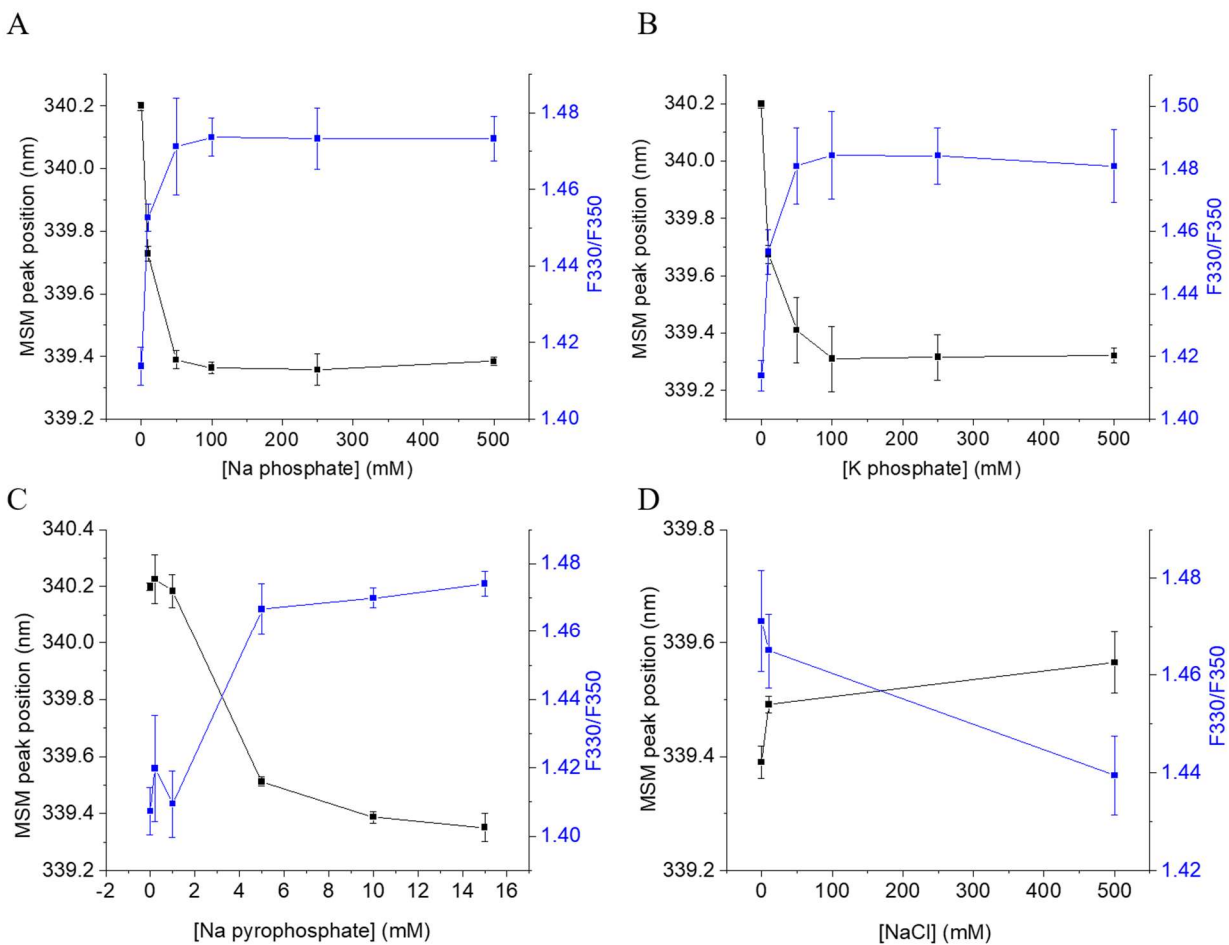
Figure 2.7. Effects of phosphate concentration on the MSM peak position and F330/F350 value of BaLS (in 10 mM citrate pH 6.0) by titration of (A) sodium phosphate; (B) potassium phosphate; (C) sodium pyrophosphate; (D) sodium chloride in presence of 50 mM sodium phosphate. Error bars are standard deviations (N=3).
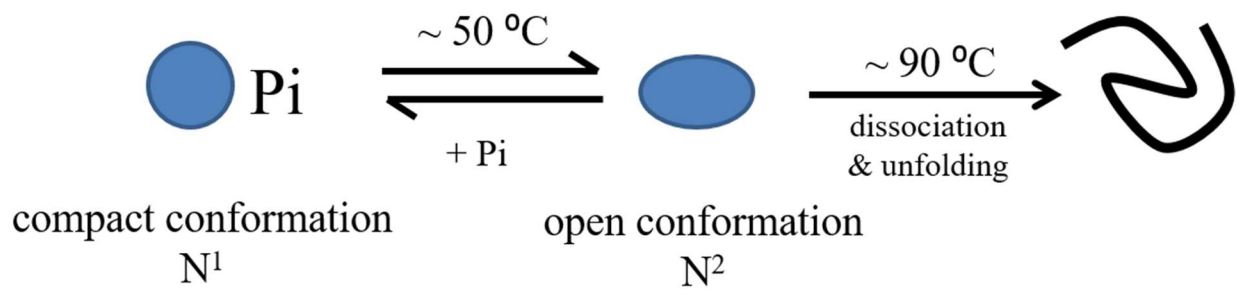
Figure 2.8. Proposed thermal unfolding pathway of BaLS in PBS buffer.
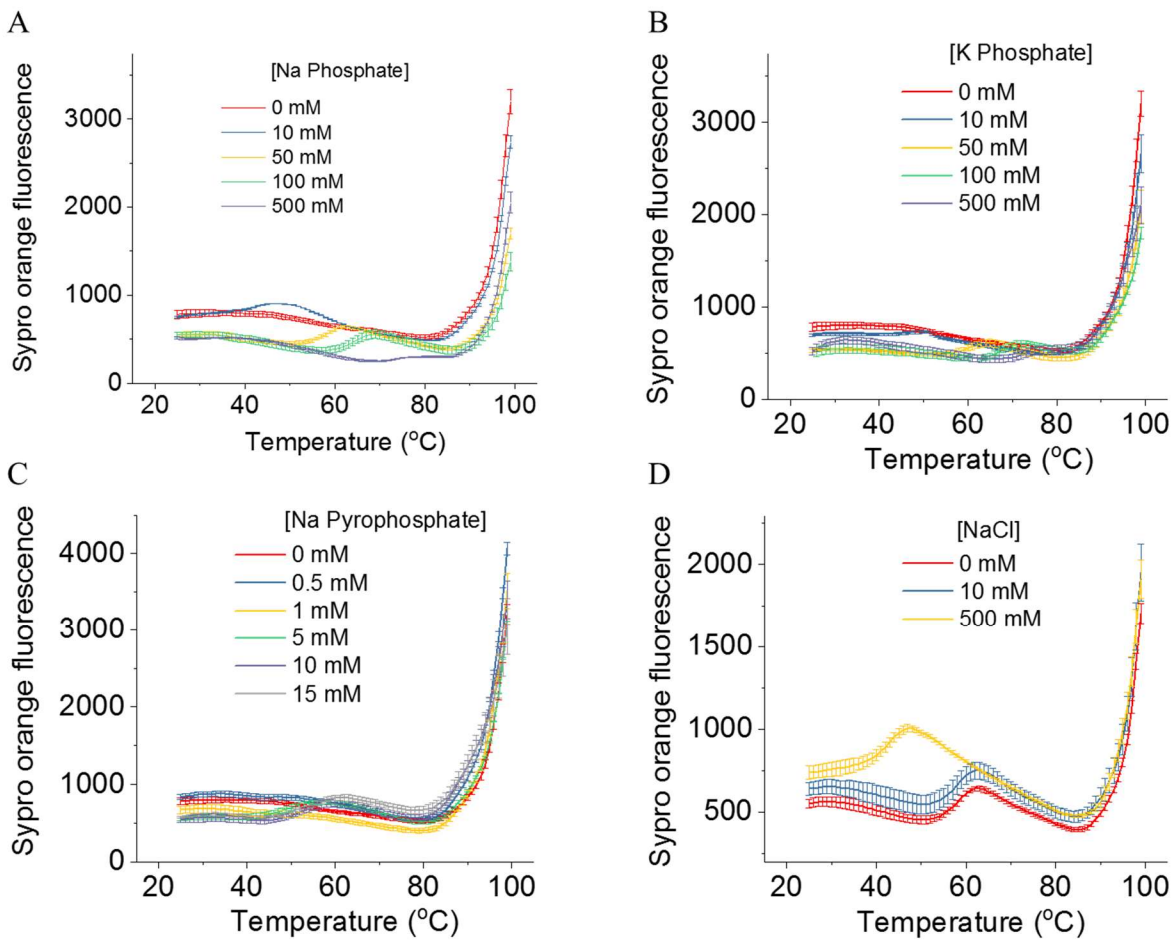
Figure 2.S1. Melting curve of BaLS in PBS buffer measured using Sypro orange extrinsic fluorescence. Error bars are standard deviations (N=3).
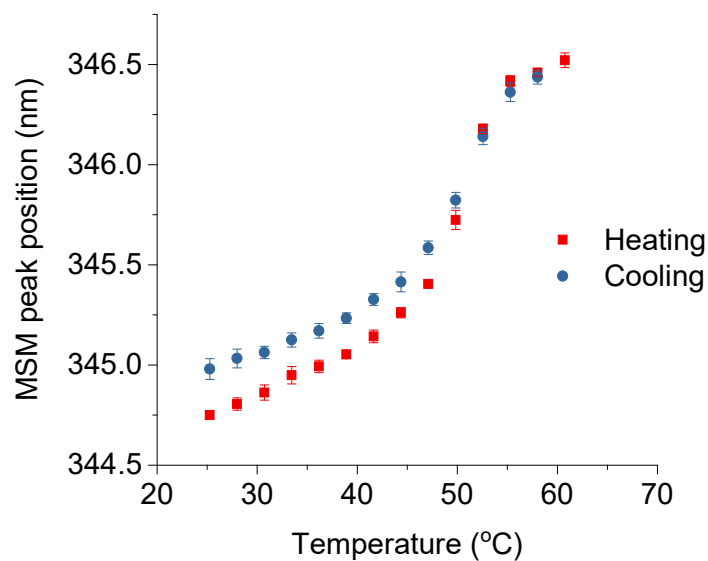
Figure 2.S2. Thermal unfolding and refolding of BaLS (at 0.2 mg/mL) in PBS buffer measured using intrinsic tryptophan fluorescence. BaLS samples were excited at 295 nm and emission spectra were collected from 300 to 400 nm. To investigate the reversibility of the first transition of BaLS (at ~50 °C), a temperature ramp was run from 25 to 60 and finally returned to 25 °C. The fluorescence was recorded every 2.5 °C with an equilibration time of 2 min at each temperature. MSM peak position was calculated employing Matlab (Natick, MA). This transition was found to be thermally reversible. Error bars are standard deviations (N=4).

Chapter 3: Evaluation of Lumazine Synthase from *Bacillus anthracis* as a Presentation Platform for Polyvalent Antigen Display

3.1. Introduction

Polyvalent antigen display has become a powerful strategy to enhance the immunogenicity of subunit vaccine antigens (185). This strategy generates vaccine candidates which present multiple copies of an antigen on the surface of a scaffold and thereby mimic the surface of microbial pathogens. B cells, in particular, react strongly to exogenous antigens that have repetitive structures. At the molecular level, a high local density of structurally ordered antigens triggers activation of the B cell receptor (BCR), which promotes B cell activation and proliferation (20). In contrast to monomeric antigens, polyvalent antigen display can generate IgG secretion and long-lived memory B cells in a more efficient manner. For example, Baschong *et al.* found that the presentation of antigenic systems in a repetitive array on viral surfaces elicited higher antibody level than those elicited by non-oligomeric proteins (25). This general strategy has been successfully employed with natural self-assembling antigens to develop vaccines for prevention of hepatitis B virus and human papillomavirus and others under development (28).

Many classes of scaffold nanoparticle systems have been examined for use in polyvalent antigen display including synthetic polymers, self-assembled proteins, inorganic particles, and various others (186). Self-assembling proteins are one of the more attractive scaffold systems because they offer precise size control, ease of production using recombinant DNA technology, and biocompatibility (173). The aim of this work is to evaluate the potential of a self-assembling protein, lumazine synthase (LS), as a scaffold system for polyvalent antigen display. LS is an enzyme involved in the biosynthesis of riboflavin in bacteria, fungi and plants. LS synthesizes 6,7-dimethyl-8-ribityllumazine, which is then catalyzed by riboflavin synthase to form riboflavin (62). LS exists as a homo-oligomer and its oligomeric state (e.g., pentamer, decamer, or 60mer) varies depending on the species.

The structure of LS, especially the 60-mer capsid, has inspired immunologists to explore its use as a scaffold for vaccine development (92, 93). LS consists of 60 identical monomers forming an icosahedral quaternary structure (T = 1 state) capsid with a diameter of about 16 nm. The least-common multiple assembly unit for LS is a pentameric block, of which twelve pentamers coalesce into a quasi-sphere, forming along the five-fold symmetry axes of an icosahedron. The N- and C-termini of all LS monomers are surface exposed and face outwards (38). Antigens of interest can be fused to either or both of the two termini without inhibiting scaffold formation. Moreover, the icosahedral LS system shows significant conformational stability (187). These features make icosahedral LS an attractive scaffold to display antigens. For example, the icosahedral LS from *Aquifex aeolicus* has been used for the presentation of the HIV-1 envelope glycoproteins gp120 (92). LS derived from *B. anthracis* is an icosahedral oligomer (38) and has not been studied as a vaccine delivery system, even though it is a potentially attractive platform for subunit vaccines. Therefore, a *B. anthracis* variant of LS was studied here as a vaccine display platform by presenting a known linear neutralizing epitope from ricin.

Ricin is a ribosome-inactivating protein (RIP) produced by the castor bean plant, *Ricinus communis*, which is grown worldwide for the production of castor oil. Ricin is toxic to humans through several routes of exposure, including injection and inhalation (188). Due to its ease of preparation and high toxicity, ricin is classified as a biothreat agent (189). There are, however, no available FDA-approved vaccines or antidotes against ricin (190). Therefore, there is an urgent need to develop an effective ricin vaccine to protect both first responders and the public from the threat of ricin.

Several linear B-cell epitopes have been identified on ricin, as defined by a collection of toxin-neutralizing monoclonal antibodies (MAbs) (191). The MAb PB10, for example, binds an

immunodominant linear epitope on ricin's enzymatic subunit (RTA). PB10 has an estimated equilibrium dissociation constant (K_D) of less than 10 pM and has been shown to passively protect mice against lethal dose ricin challenge via injection or inhalation. Kumar *et al.* successfully displayed on the surface of tomato bushy stunt virus a 16-amino acid peptide that encompasses 12-residues of PB10 epitope (192). The resulting construct elicited serum antibodies in mice that recognized RTA by Western blot analysis. However, no *in vivo* challenge studies were attempted to test the efficacy of the candidate vaccine. Nonetheless, the study successfully demonstrated that the PB10 epitope when conjugated onto a virus-like particle is immunogenic in mice. For that reason we chose to display PB10 peptide as model epitope to be fused to the C terminus of LS to develop novel ricin vaccine candidates (designated here as LS_PB10).

Since the immunogenicity of epitopes displayed on a scaffold system is influenced by several factors including the length and rigidity of the linker (193, 194) as well as the plasticity of the scaffold (140), LS_PB10 constructs containing four linkers with varying length and rigidity were produced and the effects of linkers on protein stability and immunogenicity were examined. The rigidity of the LS_PB10 scaffold was also enhanced by intra-molecular crosslinking using formaldehyde which is a commonly used chemical crosslinker and has been previously used to stabilize HIV virions and induce high-titer neutralizing antibodies against HIV in mice and rabbits (195, 196). In the present study, the feasibility of LS as a potential presentation platform for polyvalent antigen display was systematically investigated.

3.2. Experimental Procedures

3.2.1. Plasmids and Bacterial Strains

The plasmid producing LS (pTBSG) was transformed into *E. coli* strain BL21 (λDE3) competent cells for protein expression. pTBSG plasmid and BL21(λDE3) were described previously (172, 173). The PB10 epitope was fused to the C terminus of LS with a linker. The chimeric gene fragment (LS_PB10_78) was cloned into a pET9a vector by Genscript[®] (Piscataway, NJ). The restriction sites used were BamHI and HindIII. The upstream T7 tag was later removed by PCR with the primers Forward 5'-GGAGATATACATATGGTTTTTGAAGGTCATCTGGTGGGCACG-3' and Reverse 5'-CATATGTA TATCTCCTTCTTAAAGTTAAACAAAATT-3'. The resulting T7 tag free sequence was verified by DNA sequencing. The original LS_PB10 construct (LS_PB10_78) has a 14-aa flexible linker-"GGSGGSGGSGGSGG". Three more LS_PB10 constructs with different linker sequences were also generated employing LS_PB10_78 as template by an In-fusion HD Plus cloning kit (Takara Bio, CA). The primer sequences for the linker modification are summarized in Supplemental Table 3.S1. The LS_PB10 plasmids were transformed into *E. coli* strain Tuner[TM] (DE3) pLysS (Novagen, WI) competent cells for protein expression.

3.2.2. Protein expression and purification

Recombinant proteins were expressed and purified using the protocol described below. Ten milliliters of starter culture was grown in LB media (P212121, MI) at 37 $^\circ$C overnight. The next morning, the 10 ml starter culture was transferred into a 1 L Terrific Broth media (P212121, MI) at 37 $^\circ$C. Protein expression was induced by addition of 1 mM IPTG after the OD$_{600}$ of the culture reached approximately 0.8-1.0 and the media was incubated at 20 $^\circ$C overnight. After harvesting, the cell pellet was then resuspended in the hydrophobic interaction binding buffer (0.75 M ammonium sulfate, 20 mM phosphate, 5 mM EDTA, pH 7.0). The cells were lysed by sonication and the supernatant was collected after centrifugation at 15,000 g for 30 min. The supernatant was

passed through a HiTrap Butyl HP column (5 ml; GE healthcare, Germany) which had been pre-equilibrated with the hydrophobic interaction binding buffer. The column was then washed with the elution buffer (20mM phosphate, 5 mM EDTA, pH 7.0) with a linear gradient elution method in a total volume of 200 ml. The elution fractions were analyzed by SDS-PAGE and those containing the protein of interest were then dialyzed against anion exchange binding buffer (5 mM Tris, 5 mM EDTA, pH 8.0) overnight. The dialyzed sample was loaded onto three HiTrap Q HP columns (5 ml; GE healthcare, Germany) in tandem. The bound protein was eluted using the anion exchange elution buffer (1M NaCl, 5 mM Tris, 5 mM EDTA, pH 8.0).

Each of the four purified LS_PB10 constructs was further stabilized by formaldehyde treatment. LS_PB10 samples were buffer exchanged into citrate-phosphate buffer (pH 8.0) using spin filters (10K MW cutoff, EMD Millipore, Germany). Protein concentration was then adjusted to 1 mg/ml by dilution. Molar ratio excess amounts of formaldehyde (100 µL, 37% w/w, Fisher Scientific) were added to 0.5 mL protein samples (1 mg/mL) and thoroughly mixed. After 30 min, the reaction was quenched by adding 250 µL of 1 M Tris solution (pH 7.8). Protein samples were dialyzed against storage buffer (20 mM sodium phosphate, 0.1 M NaCl, 5mM EDTA, pH 7.0) and filtered through 0.1 µm syringe filters (Millex®, Germany). Protein samples (non-crosslinked and crosslinked) were analyzed by SDS-PAGE under reducing condition (16.7 mM DTT). The gel was stained by Coomassie blue R-250 dye (Teknova, CA) and imaged using an Alpha Imager HP system (ProteinSimple, San Jose, CA). LS_PB10 samples were purified from one batch of protein expression and were used for the following analysis.

3.2.3. Size exclusion chromatography and multi-angle light scattering

LS and LS_PB10 samples were injected onto a Superose 6 10/300 GL column connected to an ÄKTA explorer (GE healthcare, IL, USA) equipped with UV absorbance and conductivity detectors. Protein samples were analyzed by SEC with PBS buffer (10 mM Na_2HPO_4, 1.8 mM KH_2PO_4, 2.7 mM KCl, 137 mM NaCl, pH 7.4) running at a flow rate of 0.5 ml/min. SEC purified protein samples were then analyzed for the measurement of absolute molecular weights by multi-angle light scattering (MALS). The concentration of each protein was first measured by an Agilent 8453 UV-visible spectrophotometer (Agilent Technologies, Santa Clara, CA) and the value was used for MW calculation. An automated Calypso sample delivery unit (Wyatt Technology, Santa Barbara, CA) was used to pump protein samples into the MALS detector (Wyatt Technology, Santa Barbara, CA) equipped with a 661 nm laser at a flow rate of 0.5 ml/min. The detector was equilibrated with PBS buffer until a stable baseline was obtained (< 0.0001 AU). Otherwise, Contrad 70 (Decon Labs, PA) was used to thoroughly clean the tubing and detector. One hundred microliter of the sample was sequentially injected into the detector 5 times, and 500 microliter two times followed by a prime using PBS buffer. A narrow segment from the highest plateau of the intensity-time plot was selected and used for data analysis. Sample eluted from the MALS detector was fractionated and the concentration of the fraction corresponding to the selected segment for data analysis was measured to calculate the concentration factor. The absolute molecule weight was calculated by Zimm's equation (197). Three replicates were performed for each sample.

3.2.4. Dynamic light scattering

The hydrodynamic diameters of the LS and LS_PB10 samples at 25 $^\circ$C were measured by a Brookhaven ZetaPALS Analyzer (Brookhaven Instruments Corporation, Holtsville, NY). The instrument was equipped with a laser (653 nm) and the detector was placed at 90 degree. Two hundred microliter of protein sample at a concentration of 0.2 mg/ml was added to a 1X0.2 cm

quartz cuvette. For each run, three acquisitions were taken with an acquisition time of 30 sec. Three runs were measured for each sample. The viscosity value used for calculation was 1.019 cP. The data was analyzed using a polynomial distribution model and number-averaged diameters were determined.

3.2.5. Transmission electron microscopy

Protein samples were applied to a carbon grid (Ted Pella, Redding, CA) and left to air dry. Glutaraldehyde solution (1%, v/v, Sigma-Aldrich) was then added to fix the sample. The grid was washed twice with ultrapure water. The sample was then negatively stained by adding 2% uranyl acetate (Sigma-Aldrich) for 2 min. The morphology of the LS and LS_PB10_78 was studied using a FEI Tecnai F20 XT Transmission Electron Microscope equipped with a CCD camera (FEI Tecnai^{TM}, Oregon). The particle size was calculated by averaging the diameters of 50 particles using ImageJ (https://imagej.nih.gov/ij/).

3.2.6. Sample preparation for analysis of protein conformations

Protein samples were dialyzed overnight at 4 ^oC into PBS buffer. Samples for spectroscopic analysis (circular dichroism, intrinsic and extrinsic fluorescence) were prepared at a concentration of 0.2 mg/ml and 0.5 mg/ml for DSC analysis. Three replicates were performed for each technique.

3.2.7. Circular dichroism

The secondary structure of LS and LS_PB10 constructs was studied by recording circular dichroism (CD) spectra from 200 to 260 nm in 1-nm increments with a Chirascan-plus CD spectrometer equipped with a 4-position, Peltier-controlled cell holder (Applied Photophysics,

UK). Measurements were made in a 1-mm pathlength cuvette at 25 °C. The content of secondary structure for each protein sample were calculated employing the online server BeStSel (198).

3.2.8. Intrinsic fluorescence

The tertiary structure of LS and LS_PB10 constructs was studied by measuring tryptophan fluorescence emission spectrum at 25 °C. The samples were excited at 295 nm and emission spectra were recorded from 310 nm to 400 nm by a steady-state fluorometer (Photon Technology International, NJ). Data was collected at one nanometer interval with an integration time of 1 sec per data point. The excitation and emission slit widths were set to 4 nm. Spectra were buffer subtracted and normalized for comparison using in-house software (Middaugh Suite) (199).

3.2.9. Extrinsic fluorescence

An Mx3005P qPCR system (Agilent Technologies, Santa Clara, CA) was used to perform extrinsic fluorescence melting studies of the LS and LS_PB10 constructs. Sypro orange dye (5000x, Invitrogen) was added as a sensitive probe to monitor protein structural change during thermal unfolding. Sypro orange was added into protein samples at a dilution factor of 1000. The excitation and emission wavelength were set at 492 nm and 610 nm, respectively. The temperature ramp was set from 25 to 99 °C with an increment of 1 °C per step and an equilibration time of 2 min at each temperature. T_m values for LS and LS_PB10 constructs were calculated by a first derivative method employing Origin 8.0.

3.2.10. Differential scanning calorimetry

Differential scanning calorimetry was performed with a MicroCal VP-Capillary DSC (Malvern, UK) to investigate the conformational stability of LS and LS_PB10. The temperature was ramped

from 10 to 110 ⁰C at a scan rate of 1 ⁰C/min. The sample cell was equilibrated for 15 min at 10 ⁰C at the beginning of each run. The filtering period was set to be 16 sec. Four hundred microliter of sample was loaded into a 96-well plate for each run. The plate was sealed and kept inside a sample container maintained at 5 ⁰C through all of the runs. Apparent transition temperatures were calculated using a non-two-state equilibrium model in Origin 7.0 (OriginLab; Northampton, MA).

3.2.11. Stability study in storage buffer

Purified LS_PB10 samples were stored in storage buffer (20mM phosphate, 5 mM EDTA, 0.1 M NaCl, pH 7.0). A long-term stability study of LS_PB10 constructs in storage buffer was performed at 4 and 37 ⁰C for a period of 1 month. Samples were analyzed on days 15 and 30. The colloidal stability and chemical stability of LS_PB10 constructs were evaluated by DLS and reducing SDS-PAGE, respectively.

3.2.12. In-vitro antibody binding

The binding kinetics of LS_PB10 constructs with a murine monoclonal IgG targeting the PB10 epitope was characterized with an Octet Red 96 system employing anti-mouse IgG Fc capture biosensors (Pall ForteBio, Fremont, CA). The PB10 murine IgG was as described (191). The biosensors were hydrated for 20 min before use. Buffers, antibody samples, and LS_PB10 samples were loaded into a black bottom 96 well plate with a volume of 200 μL in each well. A stable baseline was obtained on the sensorgram for 300 sec. PB10 IgG (at 30 nM) prepared in kinetic buffer (PBS, 0.02% Tween 20, 0.2% BSA, pH 7.4) was then loaded onto the biosensors for a period of 300 sec. The biosensors with bound PB10 IgG were dipped into kinetic buffer for 300 sec to remove any non-bound PB10 IgG. The biosensors were then dipped into 4.17 nM LS_PB10 samples prepared in kinetic buffer for 300 sec to induce the association between PB10 IgG and

LS_PB10 constructs. The biosensors were then dipped into kinetic buffer for 0.5 hr for dissociation. Ten regeneration cycles were performed to fully regenerate biosensors by incubating biosensors in 10 mM glycine (pH 1.7) for 10 sec followed by a 10-sec incubation in kinetic buffer. The data were processed using Data Analysis 8.2 (ForteBIO, Fremont, CA).

3.2.13. Mouse immunization

The mouse immunization study was conducted at the Wadsworth Center. Animals were housed according to conventional specific-pathogen-free conditions and animal experiments were performed in strict accordance with the Center's Institutional Animal Care and Use Committee guidelines. Female Swiss Webster mice, 5-6 weeks of age, were purchased from Taconic Labs (Hudson, NY). LS and LS_PB10 constructs were diluted in a 20 mM sodium phosphate, 100 mM sodium chloride, 5 mM EDTA buffer (pH 7.0) and cohorts of Swiss Webster mice were I.P. immunized on days 0 and 24 with either 100 μg of a single LS_PB10 construct or LS as a non-protective control; on day 60 mice were I.P. immunized with an increased dose of 250 μg LS_PB10 construct or LS to compensate for weight gain. Serum was collected by retro-orbital bleed from each mouse to determine anti-ricin antibody titers by ELISA. Mice were administered ricin by I.P. injection equal to 10-times the LD_{50} based on average weight (4 μg/mouse) on Day 95. Mice were monitored and weighed daily for signs of intoxication and were euthanized if they became moribund.

3.2.14. ELISA

Ricin-specific serum IgG titers were determined by ELISA, as previously described (191). Briefly, Nunc Maxisorb F96 microtiter plates (ThermoFisher Scientific) were coated and incubated with 1 μg/ml ricin toxin or 1 μg/ml lumazine synthase and then treated with dilutions of mouse serum.

Horseradish peroxidase (HRP)-labeled goat anti-mouse IgG (SouthernBiotech) was used as the secondary reagent and the plates were developed using 3,3',5,5' tetramethylbenzidine (Kirkegaard & Perry Labs, Gaithersburg, MD). The plates were analyzed with a SpectroMax 250 spectrophotometer with Softmax Pro 5.4.5 software (Molecular Devices, Sunnyvale, CA).

3.3. Results

3.3.1. Purity and integrity of LS_PB10 samples

LS_PB10 constructs containing one of the four linkers with varying length and rigidity were designed, produced, purified and treated with formaldehyde (Figure 3.1). The purity of each LS_PB10 construct was analyzed by reducing SDS-PAGE (Figure 3.2). Since the interactions between LS subunits are non-covalent, LS and non-crosslinked LS_PB10 samples were dissociated into monomers in the presence of DTT and SDS at room temperature (Figure 3.2, samples 12, 34, 56 and 78). All four non-crosslinked LS_PB10 showed acceptable purity on SDS-PAGE and had a higher monomer molecular weight than LS itself (sample LS).

Formaldehyde is a reactive electrophile and primarily reacts with the amine groups of lysine residues or the N-terminus (200, 201). Formaldehyde can covalently link two neighboring amine groups within a protein molecule to generate covalent oligomers, potentially enhancing the rigidity and stability of the protein. LS as a scaffold has several exposed neighboring lysine residues (e.g. three K28 residues along the three-fold symmetry axis). In contrast, the PB10 epitope does not contain free amine groups and should not be chemically modified upon formaldehyde treatment. Hence, formaldehyde crosslinking was performed in this study to study its effect on the stability and immunogenicity of LS_PB10 constructs. The formaldehyde crosslinking reaction was performed under relatively mild conditions (pH 8.0, 30 min) to generate intra-molecular covalent

linkages rather than inter-scaffold crosslinking. As shown in Figure 3.2 (samples 12CL, 34CL, 56CL and 78CL), formaldehyde crosslinking induced a partial formation of oligomers (primarily dimer and slightly higher order oligomers). The disappearance of oligomeric bands observed in Figure 3.2 (samples 12CL_B, 34CL_B, 56CL_B and 78CL_B) show a conversion of covalent oligomers back to monomers after 30 min of boiling, indicating that formaldehyde crosslinking is reversible at elevated temperature. This observation is consistent with the finding that formaldehyde crosslinked bonds are relatively stable at room temperature, but tend to break at high temperature (202).

3.3.2. Protein assembly state: DLS, SEC, MALS and TEM

The assembly states of LS_PB10 capsid were investigated by DLS, SEC, MALS and TEM. Table 3.1 summarizes the hydrodynamic diameter, elution volume and molecular weights (experimental and theoretical MWs) of each of the LS and LS_PB10 samples. DLS measures the hydrodynamic size of a protein sample and uses polydispersity as a measure of the size distribution of a sample. All samples showed low polydispersity (< 0.1) indicating a relatively homogenous size distribution (Table 3.1). The diameters of icosahedral lumazine synthases from various microorganisms have been found to be around 16 nm (38). DLS analysis shows that LS had a hydrodynamic diameter of 15.5 ± 0.19 nm in storage buffer at 25 $^{\circ}$C, consistent with the size of LS oligomers with icosahedral geometry. All four non-crosslinked LS_PB10 constructs were larger in size than LS by 2 to 3 nm. This can be attributed to the addition of the peptide linker and PB10 epitope on LS. LS_PB10 constructs with longer linkers (samples 56 and 78) had slightly larger hydrodynamic diameters than those with short linkers (samples 12 and 34). All of the crosslinked LS_PB10 constructs had similar or slightly larger diameters compared to their corresponding non-crosslinked counterparts.

To minimize the variation caused by varying injection volumes among samples, SEC chromatographs for LS_PB10 samples were normalized for comparison. SEC analysis shows that all LS_PB10 assemblies eluted earlier than LS indicating LS_PB10 had a larger hydrodynamic size than LS (Table 3.1 and Supplemental Figure 3.S1). LS_PB10 56 and 78 had an earlier elution volume than LS_PB10 12 and 34. These data are in good agreement with the DLS results. In contrast, all of the crosslinked LS_PB10 constructs had longer elution volumes than non-crosslinked LS_PB10. This counterintuitive phenomenon is probably attributable to the reduction of surface positive charges (primarily amine groups) induced by formaldehyde, increasing the surface hydrophobicity of LS_PB10 thereby potentially enhancing weak protein-column interactions.

MALS analysis shows that LS_PB10 constructs had larger absolute molecular weights (MWs) than LS (Table 3.1). The experimental MWs of LS and non-crosslinked constructs match their theoretical MW values calculated based on a 60-mer. All crosslinked LS_PB10 had higher MWs than the parent non-crosslinked constructs presumably due to the covalent changes induced by formaldehyde.

As an example of the microscopic morphology of the capsid constructs, TEM images (Figure 3.3) of LS_PB10_78 and LS show that they share a highly similar spherical shape and hollow interior, suggesting that LS_PB10_78 successfully assembled driven by interactions between LS subunits. The size analysis shows LS and LS_PB10_78 having a size of 14.5 ± 1.0 nm and 18.5 ± 0.9 nm, respectively, which are in good agreement with DLS data. Since all of the LS_PB10 constructs shared similar hydrodynamic diameters, SEC elution times and absolute molecular weight, it seems reasonable to assume all of the other LS_PB10 constructs would show

a similar morphology to LS_PB10_78, even though TEM images were not performed for the other samples.

3.3.3. Protein conformation: CD, intrinsic fluorescence, extrinsic fluorescence, DSC

To characterize the structural integrity of the various LS_PB10 assemblies, the secondary, tertiary, and overall conformational stability of the protein molecules within the capsid were studied by several biophysical techniques. As shown in Figure 3.4 and Supplemental Figure 3.S2, at 25 ºC LS and LS_PB10 constructs share similar CD spectra. In contrast to LS, however, all LS_PB10 showed slightly less negative signals at 222 nm suggesting a small loss of secondary structures (Figure 3.4B). The content of secondary structures for each construct was deconvoluted by BeStSel for comparison (198). The secondary structure content of LS based on its crystal structure (PDB: 1VSX) was also plotted and shows good agreement with the experimental data (Supplemental Figure 3.S2). All LS_PB10 constructs showed decreased helical contents compared to LS. This reduction was relatively minor for non-crosslinked LS_PB10 constructs, but more pronounced for crosslinked constructs indicating that formaldehyde treatment slightly reduced the helical content in the LS_PB10 constructs.

The tertiary structure of LS_PB10 was studied using intrinsic tryptophan (Trp) fluorescence spectroscopy. The LS_PB10 particles contain two Trp residues (Trp 51 and Trp 151) in each subunit. Neither PB10 peptide nor peptide linkers contain any Trp residue. The mean spectral center of mass (MSM) peak position was used instead of λ_{max} to study protein tertiary structure because MSM peak position shows better sensitivity for detecting subtle conformational changes. To minimize inter-day variations, the emission spectra for LS_PB10 samples were normalized for comparison (Figure 3.5A and Supplemental Figure 3.S3). As shown in Figure 3.5A,

LS and all LS_PB10 constructs showed emission λ_{max} around 330 nm indicating that the proteins are in a folded state. Compared to LS, non-crosslinked LS_PB10 showed a minor red shift in MSM peak position (by 0.2 to 0.4 nm). This suggests that fusion of the linker and PB10 epitope produced only minor alterations of the overall tertiary structure of LS. Formaldehyde crosslinking, however, red shifted the MSM peak position by 1.1 to 1.4 nm suggesting greater alteration of the tertiary structure of the modified LS_PB10 constructs. Additionally, ratios of fluorescence intensity at 350 nm to 330 nm (F350/F330) were calculated to compare protein tertiary structures. The 330 and 350 nm values are taken to correspond to the emission maxima of Trp in buried and exposed environments, respectively. F350/F330 thus reflects the relative population of exposed Trp versus buried Trp and the overall exposure level of Trp residues in proteins. Proteins with more exposed Trp have higher F350/F330 values. The F350/F330 value for each sample manifested the same trend as the MSM peak position (Figure 3.5B). It should be noted that there are only two Trp residue in each LS monomer which contains 153 amino acid. Trp fluorescence may not however be able to sufficiently probe the overall protein's tertiary structure. Extrinsic fluorescence was therefore further performed to study protein tertiary structure and showed good agreement with Trp fluorescence data (see below).

The stability of the tertiary structure of LS_PB10 was investigated using extrinsic Sypro orange fluorescence. Sypro orange is a fluorescent dye commonly used to probe changes in protein tertiary structure. At 25 $^\circ$C, all of the crosslinked constructs showed higher initial Sypro orange fluorescent intensity than their parent non-crosslinked particles. This suggests that formaldehyde crosslinking treatment increases the exposure of hydrophobic regions of LS_PB10 constructs. Upon heating of the samples, LS showed two major thermal transitions (52.0 and 93.6 $^\circ$C) in PBS buffer (Figure 3.6A). The first thermal transition (52.0 $^\circ$C) results from a conformational change

induced by the thermal dissociation of phosphate ions from LS/phosphate complex (Y. Wei and CR Middaugh, manuscript in preparation). The second transition presumably corresponds to the dissociation and unfolding of LS oligomers. All four non-crosslinked LS_PB10 constructs had T_m values similar to LS, suggesting that the display of PB10 on the LS surface by four different linkers had no significant effect on the thermal stability of LS. Interestingly, the first transition (52.0 ℃) disappeared in all four formaldehyde crosslinked constructs. The disappearance of this transition could potentially be attributed to the change in the conformation of the scaffold induced by formaldehyde crosslinking. The T_{m2} value of all crosslinked constructs are above 100 ℃ and are thus dramatically higher than those of non-crosslinked ones. The exact values of T_{m2} were not obtained due to the limitation of the thermal control (max 99 ℃) of the instrument. The significant increase in the T_{m2} value for crosslinked particles indicated a considerable thermal stabilization by formaldehyde on LS_PB10 constructs.

The overall conformational stability of the LS_PB10 variants was studied by DSC from 10 to 110 ℃. Two major thermal transitions were observed for LS and non-crosslinked LS_PB10 constructs while only one major transition was observed for crosslinked LS_PB10 varients (Figure 3.6B). Compared to LS, there is no significant shift in the first transition for the four non-crosslinked LS_PB10 constructs, indicating that fusion of the linkers and the PB10 epitope had no significant effect on the first transition. This transition, however, was not detected in crosslinked LS_PB10 constructs and this is consistent with results observed by the extrinsic fluorescence thermal melt study described above. All four crosslinked constructs showed a T_m around 105 ℃, which is about 9 ℃ higher than the T_{m2} of the non-crosslinked particles. Therefore, formaldehyde crosslinking significantly stabilized the LS_PB10 constructs.

3.3.4. Storage stability: Chemical and Colloidal Stability

Reducing SDS-PAGE was performed to analyze the chemical stability of the LS_PB10 constructs, including the stability of formaldehyde crosslinked bonds, proteolysis and covalent oligomerization, in storage buffer. As shown in Figure 3.7B and 3.7C, all samples stored at 4 $^{\circ}$C did not produce significant degradation bands or any changes in the pattern of bands on days 15 and 30. This shows that all particles tended to be chemically stable at 4 $^{\circ}$C for at least 1 month. At 37 $^{\circ}$C, all of the non-crosslinked constructs did not manifest significant changes on the gel. However, each of crosslinked constructs stored at 37 $^{\circ}$C showed a significant decrease in the intensity of the dimer band on days 15 and 30. The probable explanation is that formaldehyde crosslinked bonds were unstable and tended to break at elevated temperature (202, 203).

The hydrodynamic diameter of each LS_PB10 construct was measured by DLS to monitor their colloidal stability at 4 and 37 $^{\circ}$C over 30 days (Supplemental Figure 3.S6). The sizes of all constructs remain unchanged except for LS_PB10_78 and LS_PB10_78CL stored at 37 $^{\circ}$C which showed a small but statistically significant increase ($p < 0.05$) in the hydrodynamic diameter on day 30.

3.3.5. In-vitro antibody binding

The murine MAb PB10 was used to test the accessibility of the PB10 epitope on LS_PB10 constructs using Bio-layer interferometry (BLI). BLI is a label-free technique for measuring biomolecular interactions between the ligand captured by the biosensor and the analyte in solution. This technique monitors the real-time changes of the interference pattern of white light reflected from two surfaces (i.e. an internal surface layer and the ligand/analyte interaction interface) upon the analyte binding to the ligand. The readout is recorded in the form of wavelength shift (in nm) and is a direct measure of the level of binding. In the context of this study, the ligand and analyte

are PB10 MAb and LS or LS_PB10 constructs, respectively. As shown in Figure 3.8A and Supplemental Figure 3.S7, all eight constructs (at 4.2 nM) were readily recognized by PB10 MAb. LS, at the same concentration, was not bound by PB10. These results indicate that the PB10 epitope is successfully presented on the surface of LS and readily accessible on all of the constructs. It is interesting to note that the four linkers of different length and rigidity did not influence the exposure of the epitope, because there was no significant differences in their association constant with PB10 MAb (Figure 3.8B). This may be due to the inherent flexibility of the C-terminus of LS, which could diminish the effect of the linker length or rigidity. The PB10 epitope was also impervious to formaldehyde treatment, since formaldehyde crosslinking did not significantly affect the association rate of LS_PB10 constructs. Because no discernible dissociation was observed for any of the LS_PB10 constructs even though the dissociation was monitored for 30 min (only the first 7 min is shown in Figure 3.8A and Supplemental Figure 3.S7), dissociation rate constant values could not be obtained (i.e. they are lower than the detection limit: 1.0^{-7} 1/s), which is consistent with MAb PB10 having picomolar binding affinity for ricin (Y. Rong and N. Mantis, manuscript in preparation). The multivalency of the PB10 epitope displayed on the surface of LS_PB10 particles might also contribute to the tight binding to the antibody.

3.3.6. Immunogenicity of LS_PB10 constructs

The LS_PB10 constructs were administered to groups of Swiss Webster mice three times by the intraperitoneal route. All eight LS_PB10 candidates elicited measurable levels of anti-LS as well as anti-ricin antibodies in mice (Table 3.2), as determined by ELISA. The LS_PB10 constructs stimulated detectable levels of anti-ricin antibodies after the second immunization, with a discernible further increase in endpoint titers after a third immunization for LS_PB10_12CL, 34CL, 56 and 78. It should be noted that the levels of anti-ricin antibodies in mouse sera following

the second and third LS_PB10 construct immunizations were variable. Moreover, there was no discernible effect of linker length or formaldehyde crosslinking on the immunogenicity of LS_PB10 constructs. The LS-PB10 mice were challenged with ricin (10 x LD$_{50}$) approximately three months following the first immunization. Ultimately, all groups of ricin-challenged mice succumbed to ricin intoxication 36-48 hours post challenge (data not shown), indicating that the LS_PB10 constructs did not confer any benefit against ricin exposure, possibly because the serum antibody titers were not sufficiently high.

3.4. Discussion

In this study, an immunodominant linear B cell epitope derived from ricin toxin's enzymatic subunit was chosen as a model epitope to evaluate the feasibility of *B. anthracis* LS as a platform for polyvalent antigen display. The PB10 epitope is a 12-amino acid peptide that adopts a helical conformation within the context of ricin (204). The PB10 epitope was fused to the C terminus of the LS monomer through different peptide linkers. Four linkers of varying length and amino acid composition were chosen to study their effect on the stability and immunogenicity of LS_PB10. In addition, LS_PB10 constructs were further stabilized by formaldehyde crosslinking. The addition of PB10 epitopes with linkers onto the LS scaffold retained correct macromolecular assembly and had only a minor effect on the conformation of LS_PB10 constructs. This demonstrates the versatility of LS in presenting peptides with different sequences and lengths. LS_PB10 constructs with four different linkers showed rapid binding to a PB10 MAb, but the extremely slow off-rates prevented accurate determination of K$_D$ values. Indeed, it is estimated that PB10's binding affinity for ricin is less than 10 pM (Y. Rong and N. Mantis, manuscript in preparation). Formaldehyde crosslinking only slightly altered the protein's overall secondary and tertiary structure, but dramatically stabilized the protein's conformation by an increase of 9 °C in

the T_m values determined by DSC and extrinsic fluorescence. Such crosslinking did not affect the presentation of the PB10 epitope which showed no significant difference between their association rate constants with a murine PB10 antibody. After three immunizations, all LS_PB10 constructs successfully elicited detectable levels of anti-ricin antibodies in mouse sera, as measured by ELISA. This illustrates the potential of LS as a presentation system for the generation of an immunogenic response to a short monomeric non-immunogenic peptide via polyvalent antigen display which permits B-cell receptor crosslinking.

The LS_PB10 constructs, however, failed to elicit a protective antibody response in mice. This suggests that protective immunity may not be achievable by a single immunogen containing just the PB10 epitope. Thus, a vaccine candidate containing multiple epitopes may be required to offer improved protection. Alternatively, the LS_PB10 constructs could be used with other ricin vaccine antigens in a prime-boost regimen to "focus" the immune response against the PB10 epitope. Our data also suggest that antibody titers were not sufficiently robust. This issue could be overcome with the addition of an adjuvant. In fact, we are currently in the process of testing the immunogenicity of LS_PB10 constructs in the presence of Alhydrogel® and other adjuvants in mice. Several possible reasons are proposed as follows to explain the suboptimal level and specificity of antibodies elicited by these LS_PB10 constructs.

At physiological pH, the PB10 peptide fused to the C terminus of LS contains four negative charges (NQ**EDAE**AITHL**F**) and negligible positive charge which could potentially make it a poor immunogen. The presentation of sixty copies of the PB10 epitope on the LS scaffold gives the surface of LS_PB10 a high density of negative charge. It has been shown that extensive negative charge on the surface of an immunogen could significantly inhibit and even completely shut down its immunogenicity (205).

The X-ray crystal structure of ricin shows that the helical PB10 epitope interacts with several surrounding positively charged residues (e.g., R48, R56, and R114) (204). These interactions reduce the negative charge density on the PB10 epitope and may have a stabilizing effect on its helical structure. When this peptide was displayed on LS, the absence of stabilizing interactions may alter the conformation of the PB10 peptide. High charge density has been shown to destabilize helicity because of increased side chain repulsion and disruption of intramolecular hydrogen bonding (206). In fact, deconvolution of the far-UV circular dichroism spectrum of the PB10 peptide (synthesized by Genscript®, Piscataway, NJ) in PBS buffer at 25 °C (at 0.2 mg/ml) shows that it has completely lost helical structure and exists primarily as disordered structure (Supplemental Figure 3.S8). Thus, the PB10 peptide displayed on the surface of LS may also possess little structure because of the lack of stabilizing interactions. This assumption is further supported by the following two experimental observations. First, there is a general decreasing trend in the helix content in the non-crosslinked LS_PB10 constructs (Supplemental Figure 3.S2E). The second observation is that all four non-crosslinked LS_PB10 constructs showed almost the same thermal transitions as LS alone (Figure 3.6B and 3.S5). If the fused PB10 peptide had adopted helical structure on the surface of LS, it might have produced an alteration in the thermal melting curve. It is, therefore, possible that the unstructured PB10 peptide presented on the capsid of the LS elicited an antibody response which lacked the strong binding affinity to the cognate ricin molecule.

Finally, it is worth mentioning that a large immunogenic response to the LS itself in all mice immunized was detected presumably due to the strong immunogenicity of the scaffold. The possibly immunodominant role of the LS may somehow suppress the immunogenicity of the PB10 epitope which resulted in only moderate levels of anti-ricin antibodies. A scaffold system with low

or no immunogenicity is preferred for polyvalent antigen display (140). Therefore, efforts, such as mutation and guided computational design, could be undertaken to improve the immune response of the epitope displayed by minimizing or re-directing the intrinsic immunogenicity of the LS scaffold.

Even though the end goal of designing neutralizing and protective ricin vaccine candidates based on LS was not shown within this work, we established the potential of LS from *B. anthracis* as a platform for antigen display. The next step is to incorporate a combination of more diverse linear epitopes, plus antigens that maintain the structural environment of the displayed epitopes.

3.5. References

1. Karch CP, Burkhard P. 2016. Vaccine technologies: From whole organisms to rationally designed protein assemblies. Biochemical pharmacology. 120:1-14.

2. Liu W, Sohn HW, Tolar P, Pierce SK. 2010. It's all about change: The antigen-driven initiation of b-cell receptor signaling. Cold Spring Harbor perspectives in biology. 2(7):a002295.

3. Baschong W, Hasler L, Häner M, Kistler J, Aebi U. 2003. Repetitive versus monomeric antigen presentation: Direct visualization of antibody affinity and specificity. Journal of structural biology. 143(3):258-262.

4. Jain NK, Sahni N, Kumru OS, Joshi SB, Volkin DB, Middaugh CR. 2015. Formulation and stabilization of recombinant protein based virus-like particle vaccines. Advanced drug delivery reviews. 93:42-55.

5. Zhao L, Seth A, Wibowo N, Zhao C-X, Mitter N, Yu C, Middelberg AP. 2014. Nanoparticle vaccines. Vaccine. 32(3):327-337.

6. Wahome N, Cooper A, Thapa P, Choudhari S, Gao FP, Volkin DB, Middaugh CR. 2016. Production of well-characterized virus-like particles in an escherichia coli-based expression platform for preclinical vaccine assessments. Vaccine Design: Methods and Protocols, Volume 2: Vaccines for Veterinary Diseases.437-457.

7. Ladenstein R, Fischer M, Bacher A. 2013. The lumazine synthase/riboflavin synthase complex: Shapes and functions of a highly variable enzyme system. FEBS Journal. 280(11):2537-2563.

8. Min J, Kim S, Lee J, Kang S. 2014. Lumazine synthase protein cage nanoparticles as modular delivery platforms for targeted drug delivery. RSC Advances. 4(89):48596-48600.

9. Jardine J, Julien J-P, Menis S, Ota T, Kalyuzhniy O, McGuire A, Sok D, Huang P-S, MacPherson S, Jones M. 2013. Rational hiv immunogen design to target specific germline b cell receptors. Science. 340(6133):711-716.

10. Morgunova E, Illarionov B, Saller S, Popov A, Sambaiah T, Bacher A, Cushman M, Fischer M, Ladenstein R. 2010. Structural study and thermodynamic characterization of inhibitor binding to lumazine synthase from bacillus anthracis. Acta Crystallographica Section D: Biological Crystallography. 66(9):1001-1011.

11. Zhang X, Meining W, Fischer M, Bacher A, Ladenstein R. 2001. X-ray structure analysis and crystallographic refinement of lumazine synthase from the hyperthermophile aquifex aeolicus at 1.6 å resolution: Determinants of thermostability revealed from structural comparisons. Journal of molecular biology. 306(5):1099-1114.

12. Audi J, Belson M, Patel M, Schier J, Osterloh J. 2005. Ricin poisoning: A comprehensive review. Jama. 294(18):2342-2351.

13. Wolfe DN, Florence W, Bryant P. 2013. Current biodefense vaccine programs and challenges. Human vaccines & immunotherapeutics. 9(7):1591-1597.

14. Roxas-Duncan VI, Smith LA. 2014. Progress in the development of vaccines against ricin intoxication.

15. O'Hara JM, Neal LM, McCarthy EA, Kasten-Jolly JA, Brey RN, Mantis NJ. 2010. Folding domains within the ricin toxin a subunit as targets of protective antibodies. Vaccine. 28(43):7035-7046.

16. Kumar S, Ochoa W, Singh P, Hsu C, Schneemann A, Manchester M, Olson M, Reddy V. 2009. Tomato bushy stunt virus (tbsv), a versatile platform for polyvalent display of antigenic epitopes and vaccine design. Virology. 388(1):185-190.

17. Klein JS, Jiang S, Galimidi RP, Keeffe JR, Bjorkman PJ. 2014. Design and characterization of structured protein linkers with differing flexibilities. Protein Engineering Design and Selection. 27(10):325-330.

18. Tissot AC, Renhofa R, Schmitz N, Cielens I, Meijerink E, Ose V, Jennings GT, Saudan P, Pumpens P, Bachmann MF. 2010. Versatile virus-like particle carrier for epitope based vaccines. PLoS One. 5(3):e9809.

19. Lu Y, Chan W, Ko BY, VanLang CC, Swartz JR. 2015. Assessing sequence plasticity of a virus-like nanoparticle by evolution toward a versatile scaffold for vaccines and drug delivery. Proceedings of the National Academy of Sciences. 112(40):12360-12365.

20. Poon B, Hsu J, Gudeman V, Chen I, Grovit-Ferbas K. 2005. Formaldehyde-treated, heat-inactivated virions with increased human immunodeficiency virus type 1 env can be used to induce high-titer neutralizing antibody responses. Journal of virology. 79(16):10210-10217.

21. Poon B, Safrit J, McClure H, Kitchen C, Hsu J, Gudeman V, Petropoulos C, Wrin T, Chen I, Grovit-Ferbas K. 2005. Induction of humoral immune responses following vaccination with envelope-containing, formaldehyde-treated, thermally inactivated human immunodeficiency virus type 1. Journal of virology. 79(8):4927-4935.

22. Klockenbusch C, Kast J. 2010. Optimization of formaldehyde cross-linking for protein interaction analysis of non-tagged integrin BioMed Research International. 2010.

23. Metz B, Kersten GF, Hoogerhout P, Brugghe HF, Timmermans HA, De Jong A, Meiring H, ten Hove J, Hennink WE, Crommelin DJ. 2004. Identification of formaldehyde-induced modifications in proteins reactions with model peptides. Journal of Biological Chemistry. 279(8):6235-6243.

24. Jensen S, Thompson L, Harry E. 2005. Cell division in bacillus subtilis: Ftsz and ftsa association is z-ring independent, and ftsa is required for efficient midcell z-ring assembly. Journal of bacteriology. 187(18):6536-6544.

25. Micsonai A, Wien F, Kernya L, Lee Y-H, Goto Y, Réfrégiers M, Kardos J. 2015. Accurate secondary structure prediction and fold recognition for circular dichroism spectroscopy. Proceedings of the National Academy of Sciences. 112(24):E3095-E3103.

26. Kennedy-Darling J, Smith LM. 2014. Measuring the formaldehyde protein–DNA cross-link reversal rate. Analytical chemistry. 86(12):5678-5681.

27. Rutenber E, Katzin BJ, Ernst S, Collins EJ, Mlsna D, Ready MP, Robertus JD. 1991. Crystallographic refinement of ricin to 2.5 å. Proteins: Structure, Function, and Bioinformatics. 10(3):240-250.

28. Wen Y, Waltman A, Han H, Collier JH. 2016. Switching the immunogenicity of peptide assemblies using surface properties. ACS nano. 10(10):9274-9286.

29. Lu H, Wang J, Bai Y, Lang JW, Liu S, Lin Y, Cheng J. 2011. Ionic polypeptides with unusual helical stability. Nature communications. 2:206.

30. Studier FW, Moffatt BA. 1986. Use of bacteriophage t7 rna polymerase to direct selective high-level expression of cloned genes. Journal of molecular biology. 189(1):113-130.

31. Zimm BH. 1948. Apparatus and methods for measurement and interpretation of the angular variation of light scattering; preliminary results on polystyrene solutions. The Journal of Chemical Physics. 16(12):1099-1116.

32. Hu L, Trefethen JM, Zeng Y, Yee L, Ohtake S, Lechuga-Ballesteros D, Warfield KL, Aman MJ, Shulenin S, Unfer R. 2011. Biophysical characterization and conformational stability

of ebola and marburg virus-like particles. Journal of pharmaceutical sciences. 100(12):5156-5173.

3.6. Figures and Tables

3.6.1 Tables

Table 3.1. Size analysis of LS and LS_PB10 capsid constructs. Hydrodynamic diameter and polydispersity was determined by DLS, elution volume (V_R) by SEC, and absolute molecular weight by MALS. Error values are standard deviations (N=3). See Figure 3.1 for description of samples.

Sample	Hydrodynamic Diameter (nm)	Polydispersity	V_R (mL)	Measured MW (MDa)	Theoretical MW (MDa)
LS	15.5±0.2	0.032	13.4±0.1	0.95±0.02	0.97
LS_PB10_12	18.2±0.2	0.067	12.5±0.1	1.08±0.01	1.09
LS_PB10_12 CL	18.2±0.5	0.071	12.8±0.1	1.12±0.01	NA
LS_PB10_34	17.6±0.0	0.045	12.5±0.2	1.07±0.01	1.08
LS_PB10_34 CL	17.6±0.2	0.034	12.8±0.0	1.11±0.01	NA
LS_PB10_56	18.8±0.3	0.031	12.4±0.1	1.07±0.01	1.11
LS_PB10_56 CL	19.1±0.1	0.007	12.6±0.0	1.18±0.01	NA
LS_PB10_78	18.4±0.2	0.071	12.3±0.1	1.09±0.01	1.11
LS_PB10_78 CL	18.6±0.1	0.062	12.4±0.0	1.16±0.01	NA

Theoretical MW was calculated by multiplying the average molecular weight of each monomer with sixty. **NA** indicates that it is not possible to predict the theoretical MW for crosslinked constructs.

Table 3.2. Anti-ricin and anti-lumazine synthase antibody titers in sera of mice immunized with LS_PB10 constructs. Groups of mice (n=3 mice/group) were immunized with 100 μg of LS_PB10 constructs. Serum samples were collected from the mice after the second (Day 42) and third (Day 84) immunizations. NT indicates "not tested" because of insufficient sample volume for analysis. The anti-ricin end-point titers for the group treated with LS were not detected and therefore not shown.

Treatment	Mouse #	Anti-ricin end-point titer Day 42	Anti-ricin end-point titer Day 84	Anti-lumazine synthase end-point titer Day 84
LS_PB10_12	1	1600	800	100000
	2	400	400	50000
	3	400	100	NT*
LS_PB10_12CL	1	50	100	NT
	2	0	200	200000
	3	100	3200	200000
LS_PB10_34	1	200	400	50000
	2	0	100	200000
	3	0	100	100000
LS_PB10_34CL	1	400	> 3200	50000
	2	200	> 3200	100000
	3	100	100	50000
LS_PB10_56	1	50	3200	NT
	2	50	1600	50000
	3	0	400	NT
LS_PB10_56CL	1	0	200	50000
	2	3200	1600	200000
	3	100	400	400000
LS_PB10_78	1	200	1600	100000
	2	100	400	200000
	3	100	800	100000
LS_PB10_78CL	1	0	200	50000
	2	50	200	200000
	3	0	100	100000

Supplemental Table 3.S1. The amino acid sequence of linkers and corresponding DNA primers

used for generation of each construct

| Sample	Linker	Primer sequence 5'→3'	
LS_PB10_12	EAAAK	Forward	GAAGCCGCGGCCAAAAACC AAGAAGACGCAGAAGC
		Reverse	TTTGGCCGCGGCTTCTTTGGCCGC GGCTTCTGCCCAGTGTTTCGACAG
LS_PB10_34	GSAAS	Forward	GGCTCTGCAGCATCTAACC AAGAAGACGCAGAAGC
		Reverse	AGATGCTGCAGAGCCTG CCCAGTGTTTCGACAGAT
LS_PB10_56	GSAGSAAGSGEF	Forward	GCAGGCTCTGAATTCAAC CAAGAAGACGCAGAAGCA
		Reverse	GAATTCAGAGCCTGCTGCAGAGCCTG CAGAGCCTGCCCAGTGTTTCGACAGAT

3.6.2. Figures
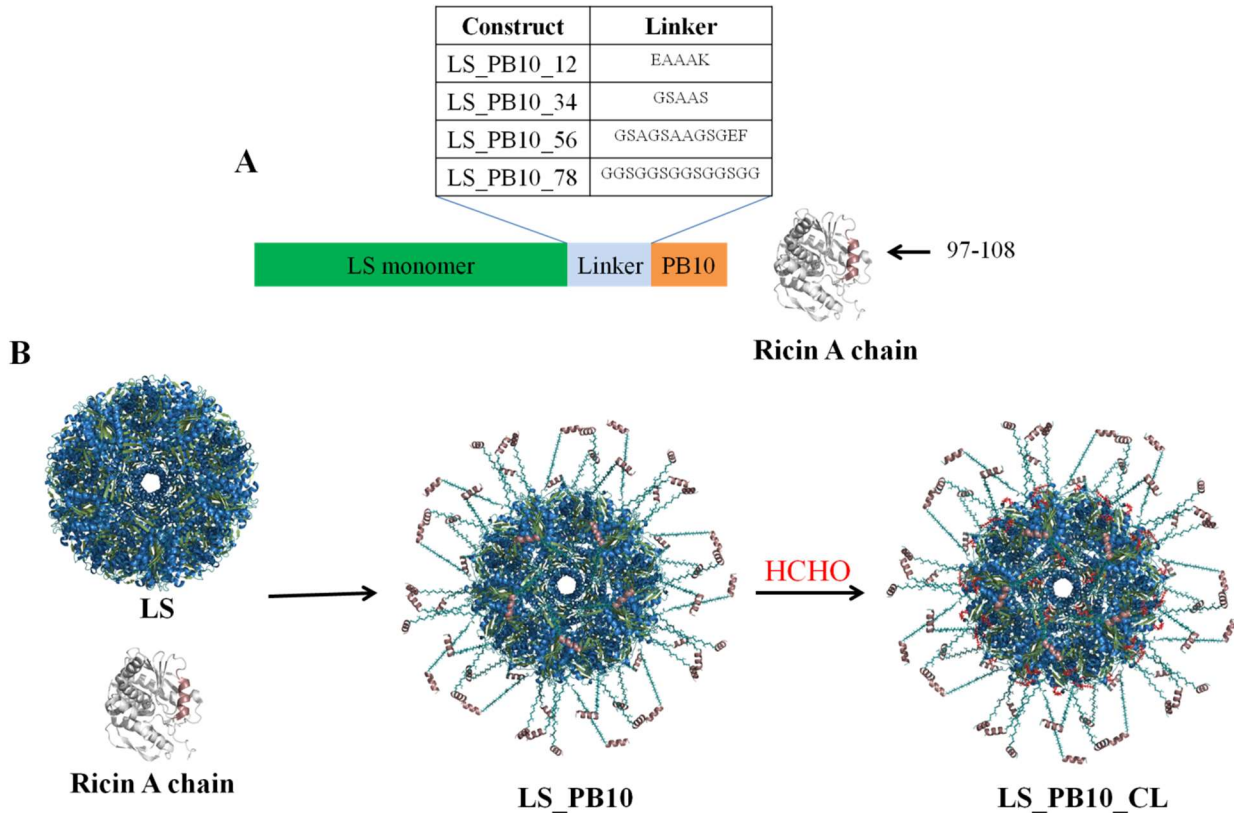
Figure 3.1. Schematic overview of design of vaccine antigens in this study. (A) LS_PB10 constructs with four different linkers and corresponding sample identification code; the sequence of PB10 peptide is "NQEDAEAITHLF" (B) Hypothetical 3-D structure of LS_PB10 and LS_PB10_CL constructs (CL indicates formaldehyde crosslinking). The *in silico* model was manually constructed by combining the 60-fold lumazine synthase structure from *B. anthracis* (PDBID: 4V7G), with the linear PB10 epitope from *R. communis* (PDBID: 3SRP), enjoined by an extended glycine-serine linker. The PB10 epitope is shown in dirty violet color. The possible covalent bonds induced by formaldehyde crosslinking are shown in red color. The hypothetical structures were modeled using the program PyMOL v 1.7 (https://www.pymol.org/).
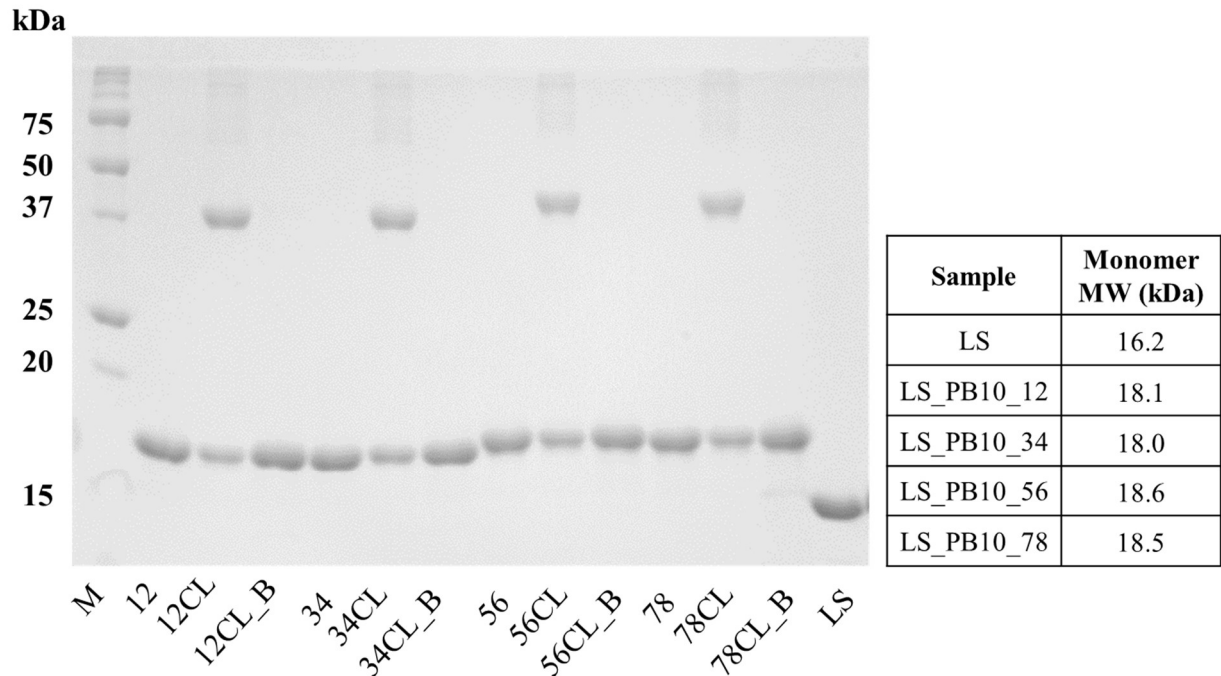
Sample	Monomer MW (kDa)
LS	16.2
LS_PB10_12	18.1
LS_PB10_34	18.0
LS_PB10_56	18.6
LS_PB10_78	18.5

Figure 3.2. Reducing SDS-PAGE (12%) analysis of LS and LS_PB10 capsid constructs. Two micrograms of protein were loaded in each lane. M, (molecular ladder); 12, (LS_PB10_12); 12CL, (LS_PB10_12 CL no boiling); 12CL_B, (LS_PB10_12 CL 30 min boiling); 34, (LS_PB10_34); 34CL, (LS_PB10_34 CL no boiling); 34CL_B, (LS_PB10_34 CL 30 min boiling); 56, (LS_PB10_56); 56CL, (LS_PB10_56 CL no boiling); 56CL_B, (LS_PB10_56 CL 30 min boiling); 78, (LS_PB10_78); 78CL, (LS_PB10_78 CL no boiling); 78CL_B, (LS_PB10_78 CL 30 min boiling); LS (LS no boiling). See Figure 3.1 for description of samples. For boiling treatment, samples were mixed with sample buffer and boiled for 30 min before sample loading, while other samples were kept at room temperature in presence of sample buffer for 30 min. Two microgram of protein was loaded in each lane. The theoretical molecular weights of the monomer for each construct are listed in the table.
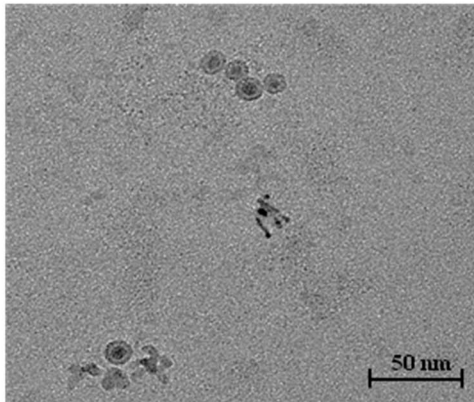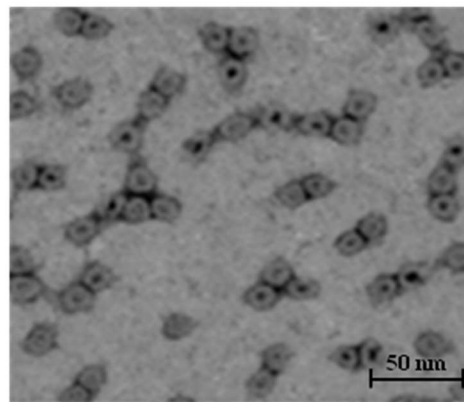
Figure 3.3. Transmission electron microscopy images of (A) LS (With kind permission from Springer Science and Business Media(173)) and (B) LS_PB10_78

Figure 3.4. Comparison of the secondary structure of LS and LS_PB10 constructs in PBS buffer at 25 ⁰C (A) Circular dichroism spectra of LS, LS_PB10_12 and LS_PB10_12CL samples; (B) Comparison of the mean residual molar ellipticity at 222 nm for LS and LS_PB10 constructs. Error bars are standard deviations (N=3). See Figure 3.1 for sample composition.

Figure 3.5. Comparison of the tertiary structure of LS and LS_PB10 constructs in PBS buffer at 25 °C. (A) The emission spectra of for LS, LS_PB10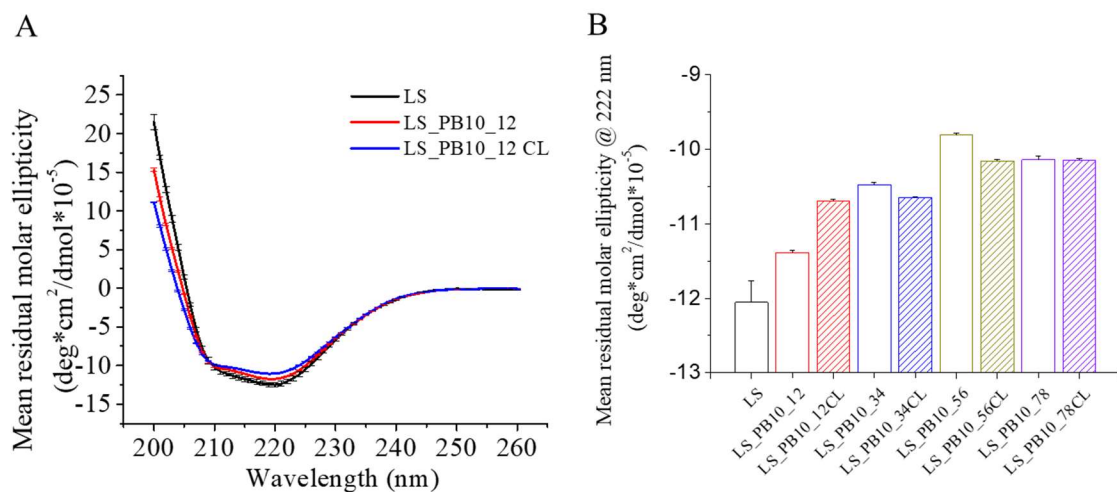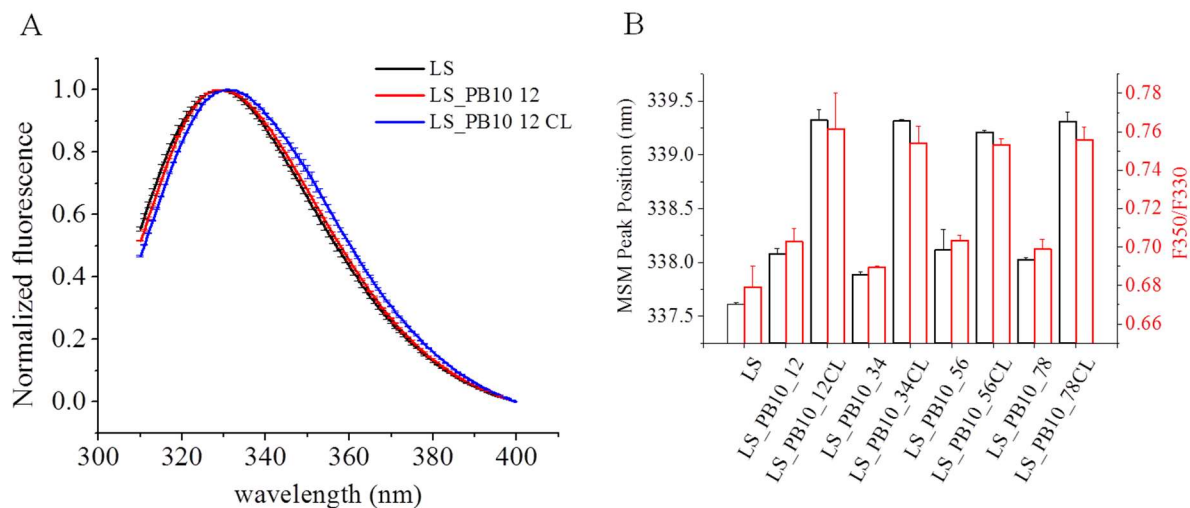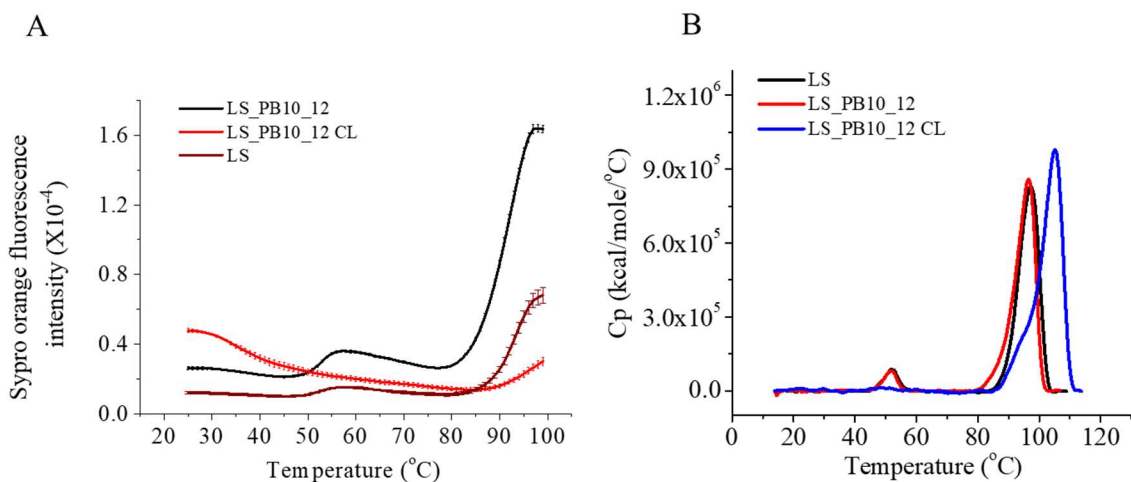_12 and LS_PB10_12CL (B) The mean spectra mass peak position and the ratio of fluorescence intensity at 350 nm to 330 nm for LS and LS_PB10 samples. Error values are standard deviations (N=3). See Figure 3.1 for sample composition.

Sample	T_m1 (°C)		T_m2 (°C)	
	Sypro orange	DSC	Sypro orange	DSC
LS	52.5 ± 0.10	51.8 ± 0.16	93.6 ± 0.10	96.7 ± 0.35
LS_PB10_12	53.0 ± 0.06	51.5 ± 0.05	92.4 ± 0.10	96.6 ± 0.06
LS_PB10_12 CL	NA	NA	> 100	105.2 ± 0.06
LS_PB10_34	52.0 ± 0.00	51.1 ± 0.05	93.1 ± 0.15	96.5 ± 0.06
LS_PB10_34 CL	NA	NA	> 100	105.2 ± 0.06
LS_PB10_56	52.4 ± 0.06	51.4 ± 0.89	93.1 ± 0.10	96.6 ± 0.06
LS_PB10_56 CL	NA	NA	> 100	105.2 ± 0.10
LS_PB10_78	53.0 ± 0.06	52.0 ± 0.36	92.6 ± 0.17	96.5 ± 0.06
LS_PB10_78 CL	NA	NA	> 100	104.6 ± 0.17

Figure 3.6. Thermal stability of LS and LS_PB10 constructs in PBS buffer. (A) Extrinsic SYPRO Orange fluorescence thermal melting curves of LS, LS_PB10_12, and LS_PB10_12 CL constructs. (B) DSC thermograms of LS, LS_PB10_12, and LS_PB10_12 CL constructs. The corresponding T_m values for LS and LS_PB10 samples are displayed. Error values are standard deviations (N=3). See Figure 3.1 for sample composition.
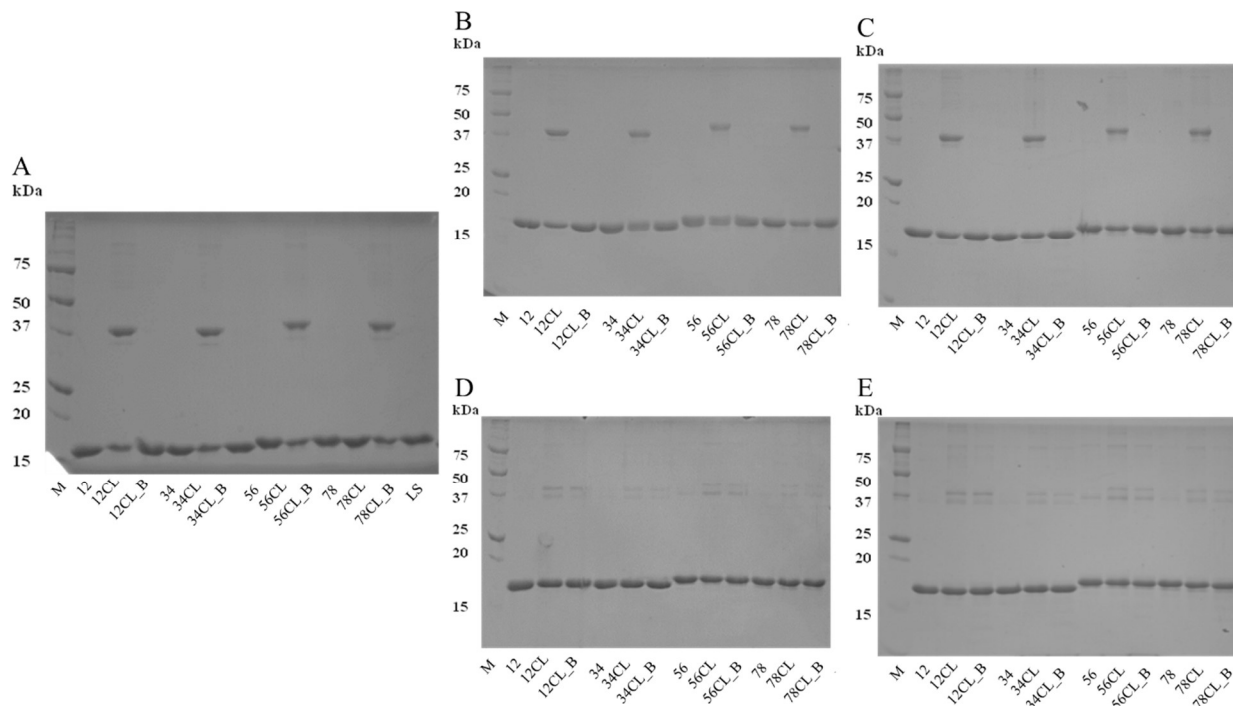
Figure 3.7. Chemical stability study of LS_PB10 constructs at 4 ᵒC and 37 ᵒC for a period of one month by SDS-PAGE analysis. (A) Day 0; (B) Day 15 at 4 ᵒC; (C) Day 30 at 4 ᵒC; (D) Day 15 at 37 ᵒC; (E) Day 30 at 37 ᵒC. M, (molecular ladder); 12, (LS_PB10_12); 12CL, (LS_PB10_12 CL no boiling); 12CL_B, (LS_PB10_12 CL 30 min boiling); 34, (LS_PB10_34); 34CL, (LS_PB10_34 CL no boiling); 34CL_B, (LS_PB10_34 CL 30 min boiling); 56, (LS_PB10_56); 56CL, (LS_PB10_56 CL no boiling); 56CL_B, (LS_PB10_56 CL 30 min boiling); 78, (LS_PB10_78); 78CL, (LS_PB10_78 CL no boiling); 78CL_B, (LS_PB10_78 CL 30 min boiling); LS (LS no boiling). See Figure 3.1 for sample composition.
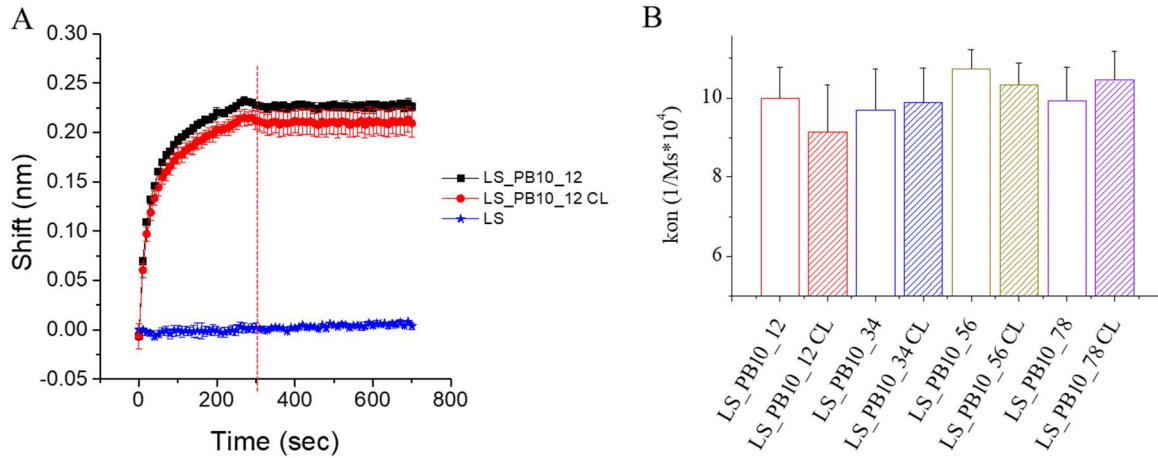
Figure 3.8. Binding kinetic of LS_PB10_12 (at 4.17 nM) with mouse PB10 IgG. (A) Sensorgram of LS_PB10_12, LS_PB10_12_CL and LS; Association phase (0 to 300 sec) and dissociation phase (300 to 700 sec) were shown. (B) The association rate constants of LS_PB10 samples with mouse PB10 IgG determined from bio-layer interferometry. Error bars are standard deviations (N=3). See Figure 3.1 for sample composition.
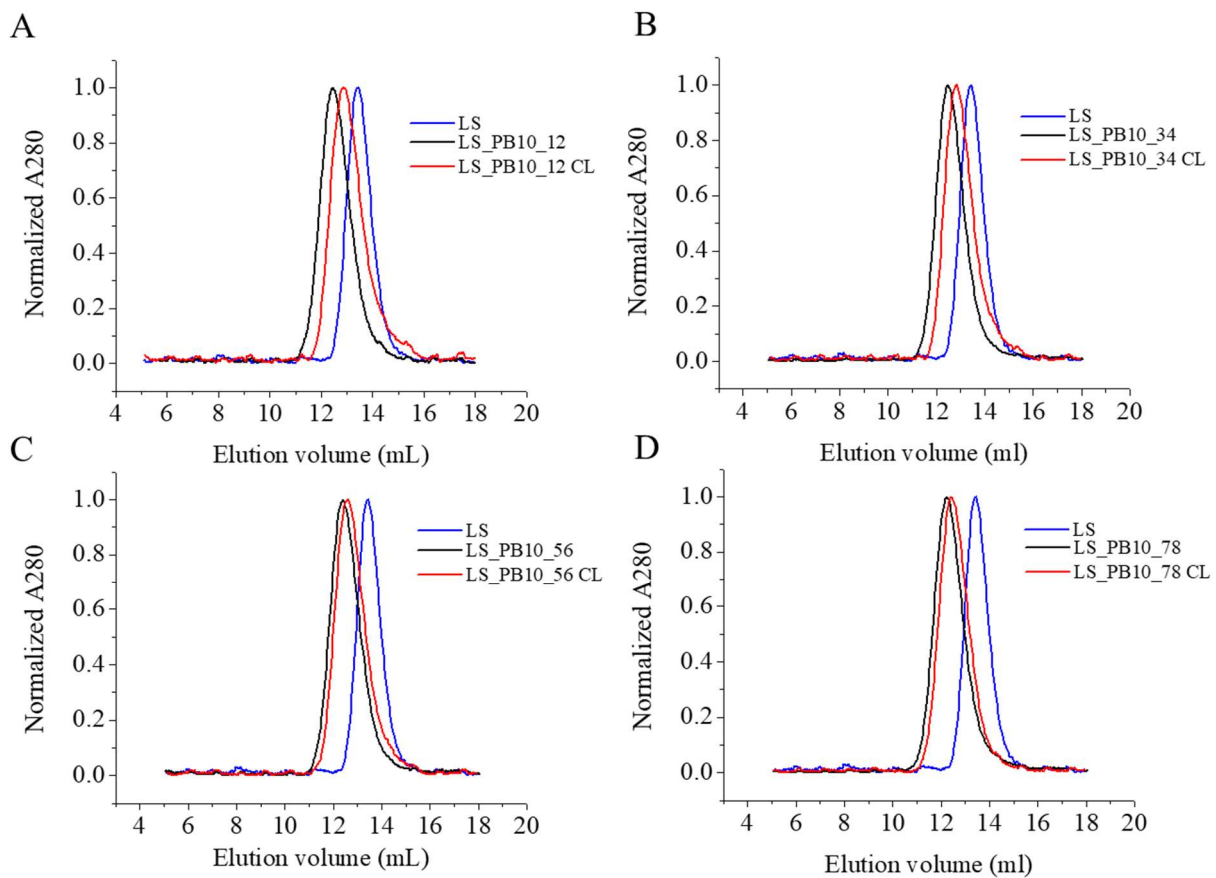
Supplemental Figure 3.S1. Normalized elution peaks of LS and LS_PB10 constructs by size exclusion chromatography. (A) LS_PB10_12 and LS_PB10_12_CL; (B) LS_PB10_34 and LS_PB10_34_CL; (C) LS_PB10_56 and LS_PB10_56_CL; (D) LS_PB10_78 and LS_PB10_78_CL. LS SEC elution peak was plotted in each graph for comparison.
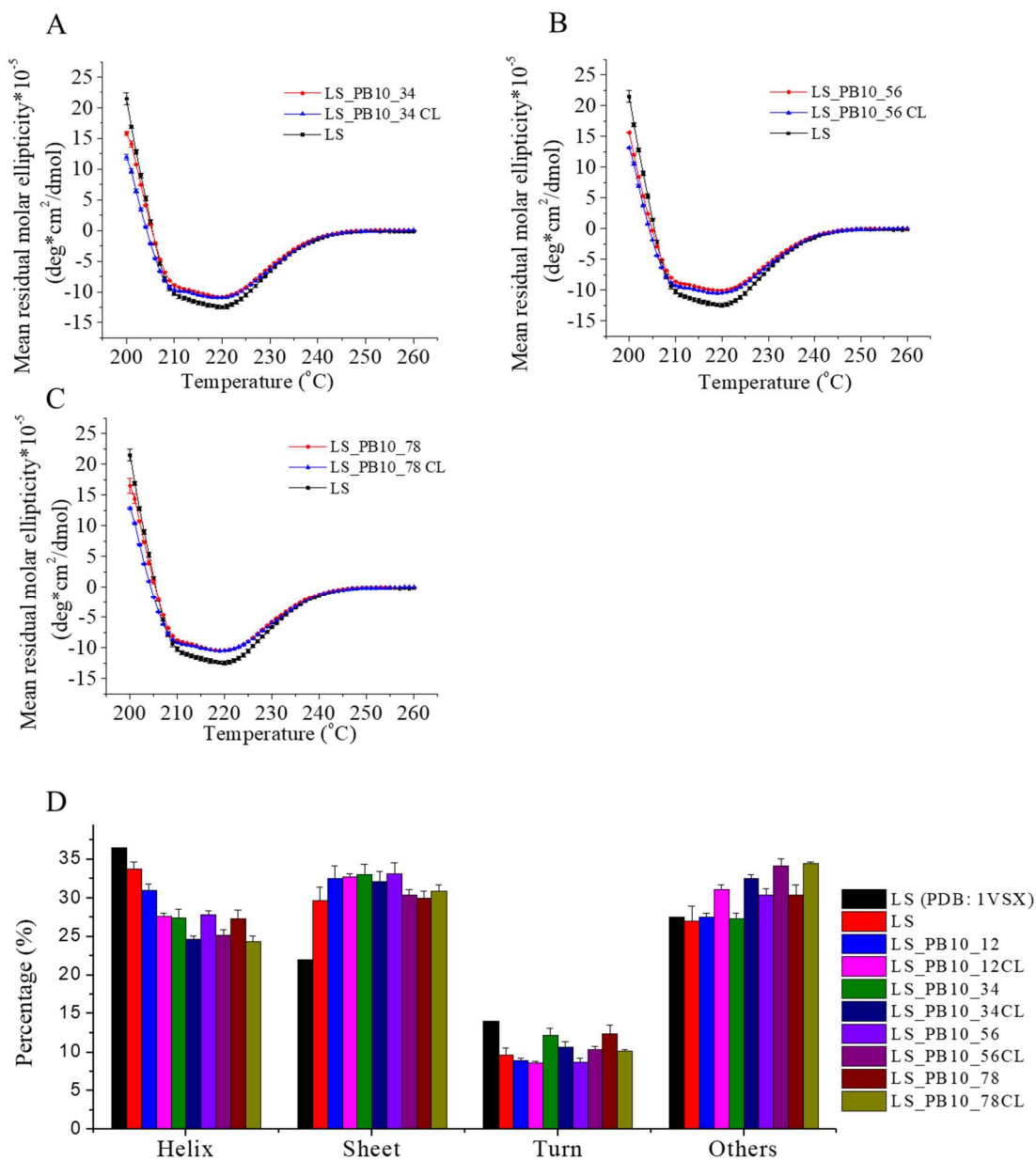
Supplemental Figure 3.S2. Circular dichroism spectra of LS and LS_PB10 constructs in PBS buffer at 25 °C (A) LS_PB10_12 and LS_PB10_12CL samples (A) LS_PB10_34 and LS_PB10_34_CL; (B) LS_PB10_56 and LS_PB10_56_CL; (C) LS_PB10_78 and LS_PB10_78_CL. The far-UV CD spectrum of LS was plotted in each spectrum and graph for

comparison. (D) The secondary structure content for LS and LS_PB10 constructs deconvoluted

using BeStSel. Error bars are standard deviations (N=3). See Figure 3.1 for sample composition.
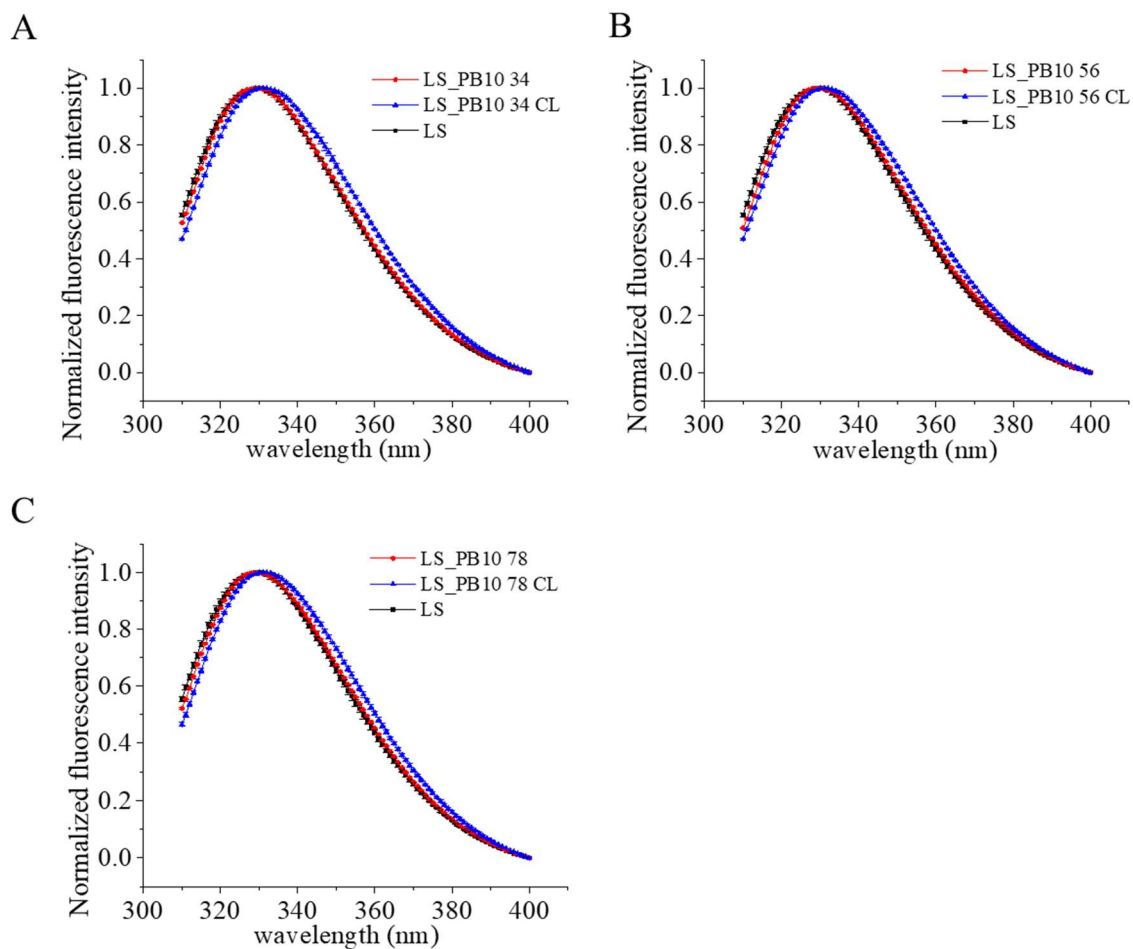
Supplemental Figure 3.S3. Intrinsic fluorescence spectra of LS and LS_PB10 constructs in PBS

buffer at 25 °C. (A) LS_PB10_34 and LS_PB10_34_CL; (B) LS_PB10_56 and LS_PB10_56_CL;

(C) LS_PB10_78 and LS_PB10_78_CL. The emission spectrum of LS was plotted in each image

for comparison. Error bars are standard deviations (N=3). See Figure 3.1 for sample composition.
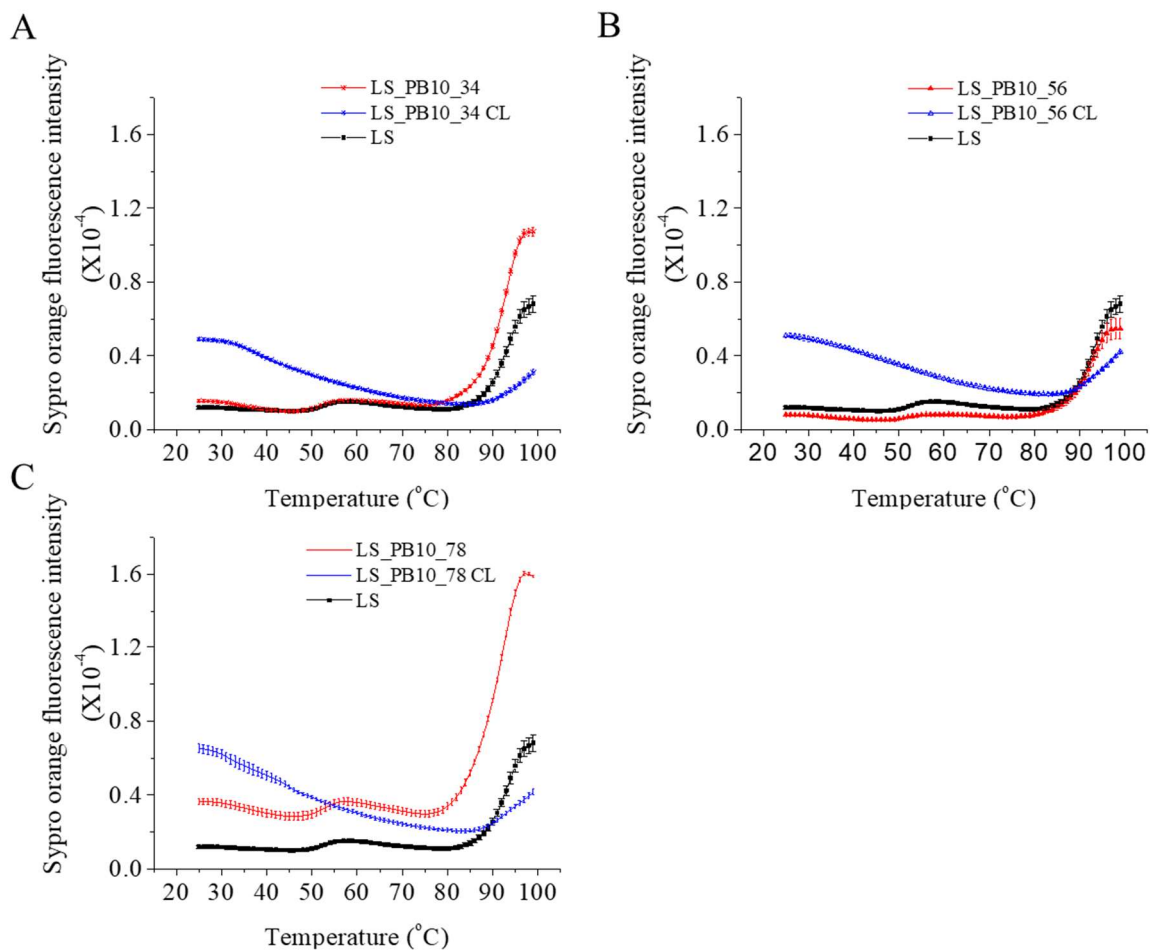
Supplemental Figure 3.S4. Extrinsic SYPRO Orange fluorescence thermal melting curves of LS and LS_PB10 constructs in PBS buffer. (A) LS_PB10_34 and LS_PB10_34_CL; (B) LS_PB10_56 and LS_PB10_56_CL; (C) LS_PB10_78 and LS_PB10_78_CL. The thermal melting curve of LS was plotted in each graph for comparison. Error values are standard deviations (N=3). See Figure 3.1 for sample composition.
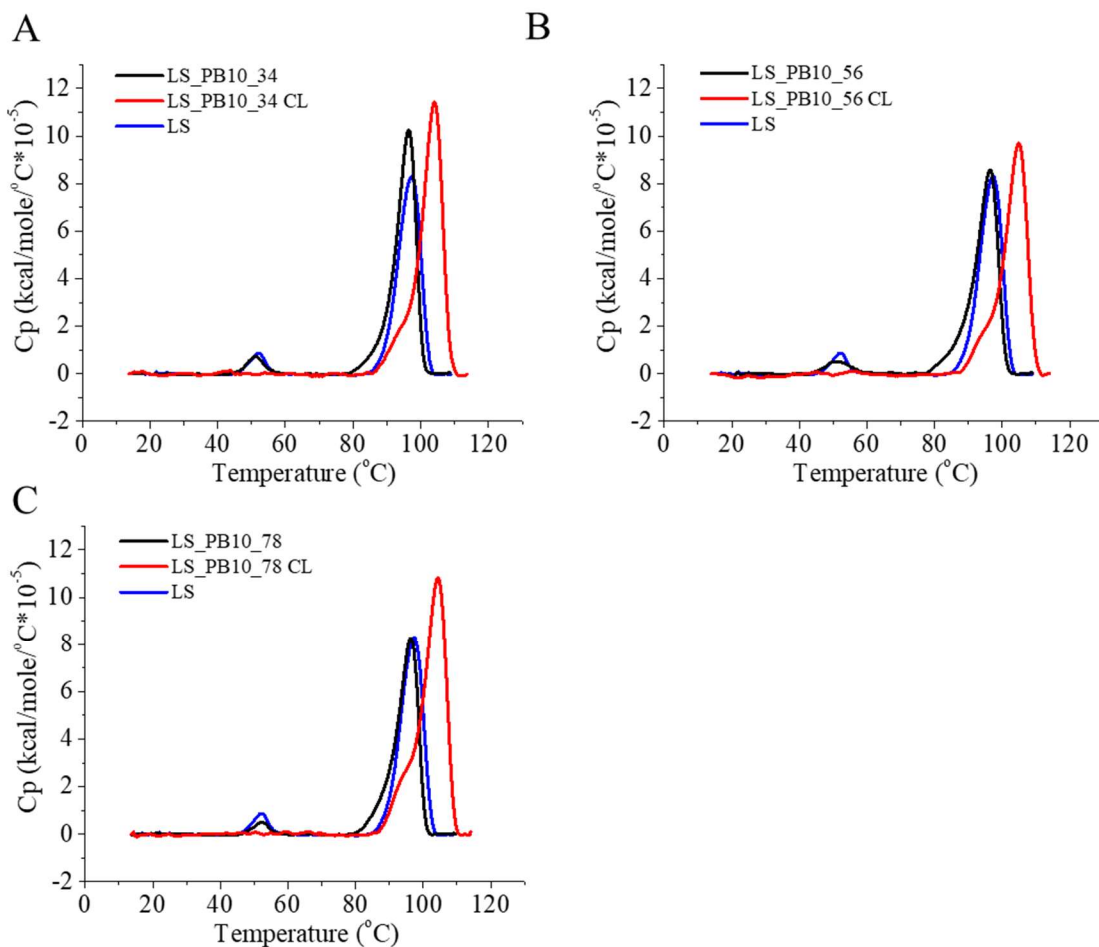
Supplemental Figure 3.S5. DSC thermograms of LS and LS_PB10 constructs in PBS buffer. (A) LS_PB10_34 and LS_PB10_34_CL; (B) LS_PB10_56 and LS_PB10_56_CL; (C) LS_PB10_78 and LS_PB10_78_CL. The thermogram of LS was plotted in each graph for comparison. See Figure 3.1 for sample composition.
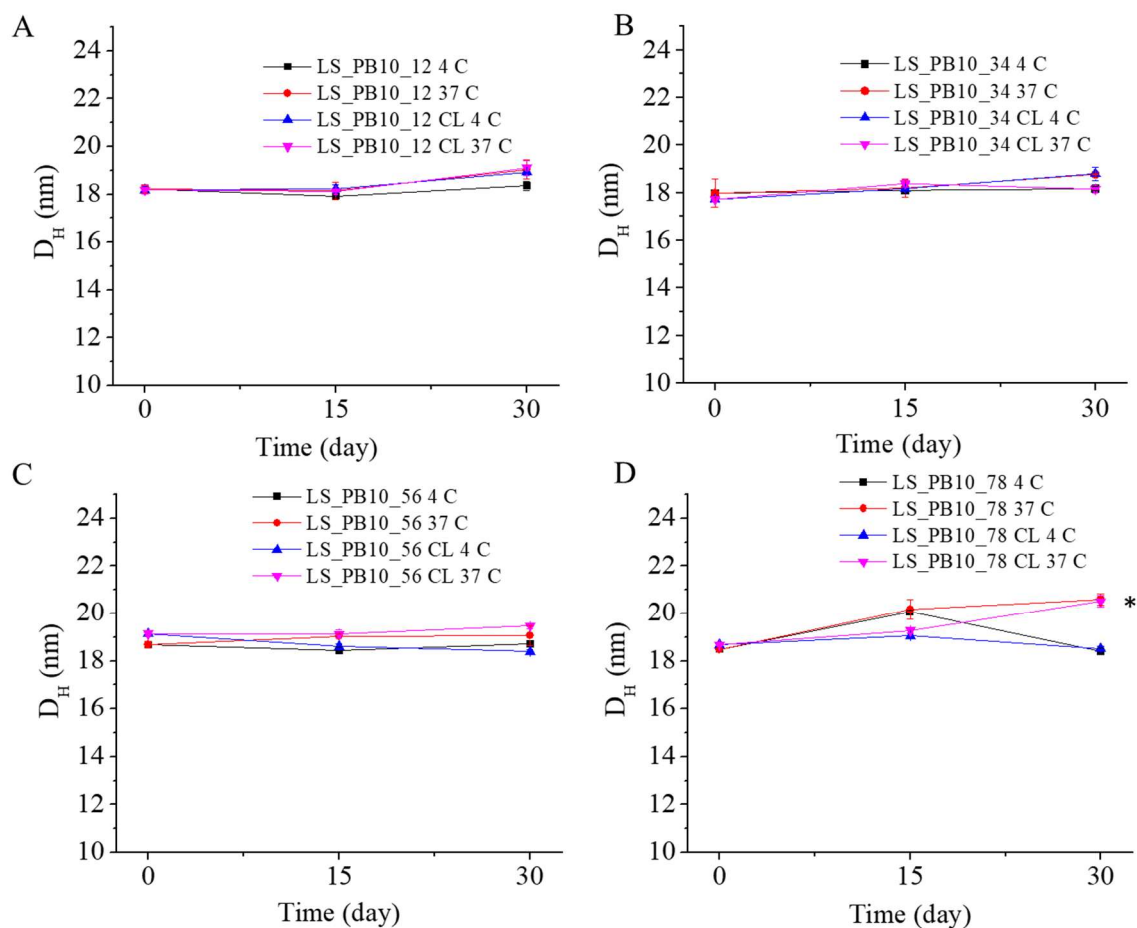
Supplemental Figure 3.S6. Colloidal stability study on LS_PB10 capsid constructs at 4 °C and 37 °C for a period of one month. The hydrodynamic diameter of each sample was measured by DLS. LS_PB10_78 (day 30, 37 °C) and LS_PB10_78 CL (day 30, 37 °C) showed significant differences from their corresponding samples on day 0 in hydrodynamic diameter (* indicates $p <$ 0.05). Comparisons were analyzed with paired t-tests. Values of $p < 0.05$ were considered statistically significant. Error bars are standard deviations (N=3). See Figure 3.1 for sample composition.
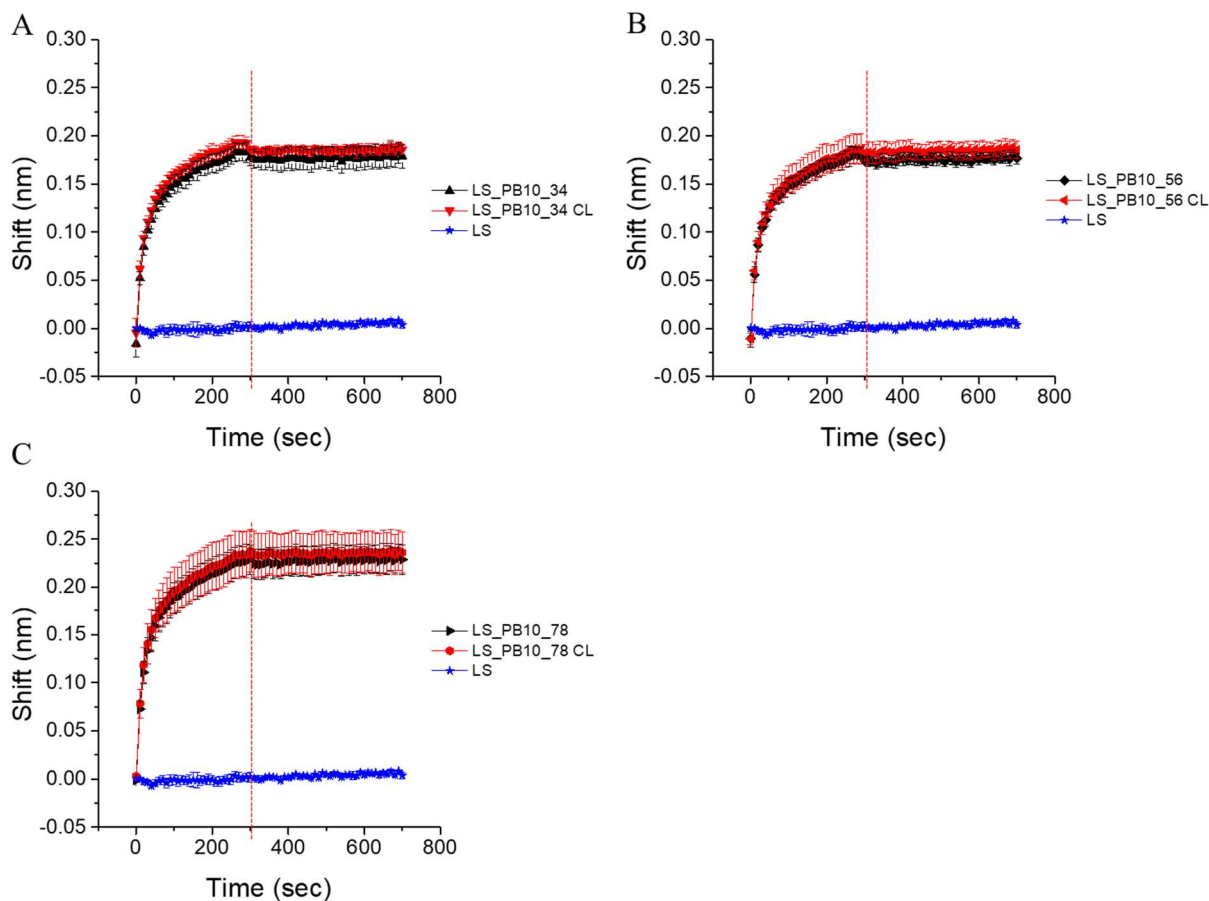
Supplemental Figure 3.S7. Kinetic binding curves of LS_PB10 constructs (4.17 nM) with mouse

PB10 IgG (30 nM). Association phase (0 to 300 sec) and dissociation phase (300 to 700 sec) were

shown. The measurements were done in triplicate. (A) LS_PB10_34 and LS_PB10_34_CL; (B)

LS_PB10_56 and LS_PB10_56_CL; (C) LS_PB10_78 and LS_PB10_78_CL. The binding curve

of LS was plotted in each graph for comparison (N = 3). See Figure 3.1 for sample composition.
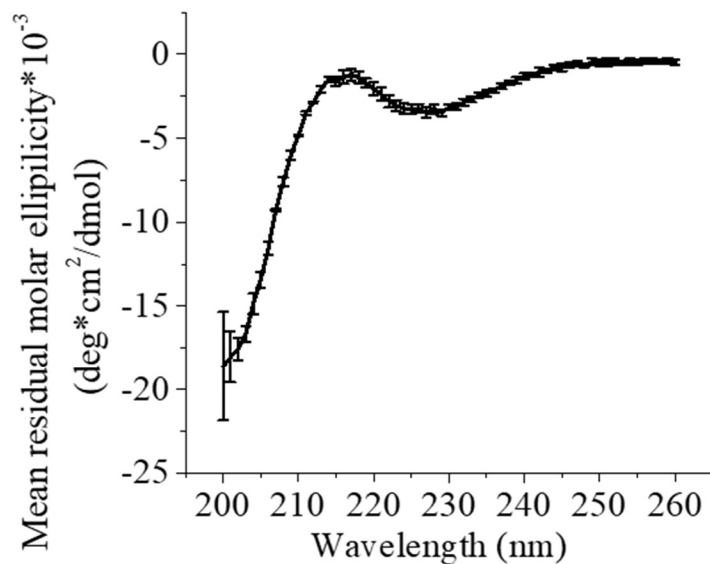
Secondary Structure	Helix	Sheet	Turn	Others
Content (%)	0.1 ± 0.0	15.8 ± 5.2	20.6 ± 0.4	63.5 ± 4.9

Supplemental Figure 3.S8. Far UV circular dichroism spectrum of PB10 peptide (at 0.2 mg/ml) in PBS at 25 °C; the content of secondary structure was deconvoluted using BeStSel (198). Error bars are standard deviations (N=3).

Chapter 4: Effect of Two Emulsion-Based Adjuvants on the Structure and

Thermal Stability of *S. aureus* Alpha-toxin

4.1. Introduction

Subunit vaccines contain defined macromolecular components identified from a pathogen that are capable of eliciting protective immunity.(207) They are usually recombinant proteins and possess many advantages over other vaccine types (e.g. live attenuated and inactivated viruses and bacteria) such as an improved safety profile, a highly defined nature, ease of production and potential for lower cost of goods.(207, 208) One important limitation of subunit vaccines is that they usually induce relatively weak immunogenicity owing to their inability to replicate and/or lack of other immunostimulatory components such as pathogen-associated molecular pattern molecules to induce innate and cellular immunity.(209) To ensure the successful immunization of subunit vaccines, they are often administered with adjuvants to boost host immune responses.(209)

Oil-in-water (O/W) emulsion-based adjuvants are an important class of adjuvants used for subunit vaccines.(210-212) These emulsions usually use squalene as the oil phase, which is a naturally occurring lipid found in plants, animals and humans. Suitable surfactants (e.g., Tween 80, Span 85 etc.) are used to stabilize oil droplets dispersed in the aqueous environment. Currently, two squalene-based emulsion adjuvants (MF59 and AS03) have been approved for commercial use. (213-215) Potent immunopotentiators, such as monophosphoryl lipid A (MPLA), can be added to emulsion-based adjuvants to further improve their adjuvanticity. For example, a squalene emulsion containing a Glucopyranosyl Lipid Adjuvant (GLA), a synthetic form of MPLA, is currently used in a phase II trial for a respiratory syncytial virus vaccine.(216, 217) In this work, MedImmune emulsion. 0 (ME.0) and Stable Emulsion (SE) O/W emulsions were investigated. Both contain squalene as the oil phase. ME.0 and SE use histidine and ammonium phosphate buffers as their aqueous phase, respectively. The surfactants used in ME.0 and SE are PS 80 and a combination of 1, 2-dimyristoyl-sn-glycero-3-phosphocholine (DMPC) and Pluronic F68,

respectively. In ME.0, sucrose is employed as an osmolyte, whereas glycerol is used in SE. SE also contains vitamin E which serves as an antioxidant and has also been shown to exert immunostimulatory activity.(218, 219)

The protein antigen studied in this work is alpha toxin (AT) derived from *Staphylococcus aureus*. AT is one of the key virulent factors involved in *S. aureus* infection (220) and has been found to be protective in animal models.(221) AT is a promising vaccine candidate for protection against antibiotic resistant staphylococcus infection in high risk populations, especially patients hospitalized for surgery.[7] The wild type AT is expressed by S. aureus extracellularly as a water soluble monomer and self-assembles into a homo-oligomeric heptamer with a transmembrane domain.(222) The AT monomer consists of 293 amino acid with a molecular weight of 33.2 kDa. The AT used in this study is a mutant of the wild type AT which lacks the ability to self-assemble.

Emulsion adjuvants can be formulated with vaccine antigens in two different formats: single vial or separate vials in which antigen and adjuvant are mixed prior to administration.(223) If antigen and adjuvant are compatible with each other, they can be formulated in a single vial to reduce manufacturing costs and provide ease of administration. Single vial formulation is therefore a more favorable option, especially as the commercial dosage form.(208) However, if antigens are not compatible with adjuvants over long-term storage, they must be stored separately before administration to ensure the safety and efficacy of a vaccine. This option is often implemented in early clinical trials when limited stability data are available. An understanding of emulsion/antigen interactions and how these interactions influence the structure and stability of antigens is necessary to rationally decide the type of formulation (e.g. single vial or separate vial) and to further optimize the formulation to offer maximum antigen stability.(224-226)

Since emulsions are usually optically turbid due to strong light scattering, this poses challenges for analytical characterization of antigens in their presence. Many routinely used spectroscopic techniques (such as Circular Dichroism (CD), UV absorption, and some forms of fluorescence) are often not suitable for this purpose because of the interference by light scattering.(227) In the present study, a set of biophysical techniques capable of analyzing turbid protein samples were selected to investigate the secondary, tertiary structural integrity and overall conformation stability of protein antigens upon mixing with emulsion-based adjuvants. These techniques include Fourier transform infrared (FT-IR) and intrinsic fluorescence spectroscopy and differential scanning calorimetry (DSC). (228) We have successfully used these techniques to characterize the effects of two oil-in-water (O/W) emulsion systems (designated as ME.0 and SE) on *Staphylococcal aureus* alpha toxin (AT), a potential vaccine antigen.

4.2. Materials and Methods

4.2.1. Materials

Frozen stock of recombinantly produced and purified AT in PBS buffer (pH 7.4) was obtained from Medimmune LLC (Gaithersburg, MD). The AT stock concentration was found to be 0.51 mg/ml (extinction coefficient, $A\frac{0.1\%}{280\,nm} = 1.93$) by UV absorption spectroscopy and this value was used for sample preparation. Two oil-in-water emulsion-based adjuvants, ME.0 stock (2X) and SE stock (3X), were provided by MedImmune LLC (Gaithersburg, MD). ME.0 stock (2X) contains 20mM histidine at pH 6.0, 10% sucrose, 4% squalene and 1% PS80. SE stock (3X) is composed of 25mM ammonium phosphate, 5.1% squalene, 1.1% DMPC, 30ug/mL vitamin E, 2.37% w/v glycerol, and 0.037% w/v pluronic F68, at pH 5.6.

4.2.2. Sample preparation

ME.0 stock (2X) and SE stock (3X) were prepared by MedImmune LLC (Gaithersburg, MD) using a previously described protocol.(208) Briefly, squalene and surfactant were mixed and sonicated to achieve homogenous mixing of the oil phase. The aqueous phase was then added to the oil phase. The mixture was again homogenized using a Silverson L5M-A standard mixer (East Longmeadow, MA) and then subjected to microfluidization to generate milky emulsions of around 100 nm in size using a Microfluidics 110P microfluidizer (Microfluidics, Boston, MA). AT/ME.0 or AT/SE mixtures were prepared by mixing AT in PBS with an emulsion stock (ME.0 stock (2X) or SE stock (3X)) to achieve a final protein concentration of 0.2 mg/ml containing emulsion at 1X concentration.

In the component study, we aimed to study the effects of different emulsion components on AT (as per Table 4.1). AT was mixed with each water-soluble component of the emulsions at the same volumetric ratio as used in the AT/ME.0 or AT/SE mixture. S0 was prepared by diluting AT in PBS to achieve a concentration of 0.2 mg/ml. The compositions of all test samples and their identification codes (M1 to M5 and S1 to S5) are listed in Table 4.1. For example, M1 was prepared by mixing AT in PBS (at 0.4 mg/mL) with 20 mM Histidine buffer, pH 6.0 at a volumetric ratio of 1:1. ME.0 (1X) and SE (1X) diluted using PBS were used as control samples. M2 was made by mixing AT in PBS (at 0.4 mg/mL) with a mixture solution containing 20 mM Histidine buffer (pH 6.0) and 10% sucrose at a volumetric ratio of 1:1. ME.0 (1X) and SE (1X) diluted using PBS were used as control samples. The mixtures were equilibrated at 4 °C overnight before analysis.

4.2.3. UV-visible absorption spectroscopy

The absorption spectrum of AT stock was collected using a UV/Visible spectrophotometer (Agilent Technologies, Santa Clara, CA) equipped with a diode array detector. The absorption

spectra were corrected for scattering contributions by subtraction of an extrapolation of the logarithm of the optical density in a non-absorbing region (350 nm to 400 nm) to the far UV region.

4.2.4. FT-IR spectroscopy

FT-IR spectroscopic analysis was performed using a Tensor-27 FT-IR spectrometer (Bruker, Billerica, MA) equipped with a Bio-ATR cell. The detector was cooled with liquid N_2 for 20 min prior to use and the interferometer was purged continuously with N_2 gas. A total of 256 scans were recorded from 4000 to 900 cm^{-1} with a 4 cm^{-1} resolution. Buffer/emulsion background spectra were collected and subtracted from the sample spectra. Atmospheric compensation, baseline adjustment and second derivative calculations were applied using OPUS V6.5 (Bruker, Billerica, MA) software. To compare the initial state of the samples, spectra collected at 20 °C were deconvoluted into a set of mixed Gaussian/Lorentzian bands, using the build-in Levenberg-Maquardt algorithm from the OPUS V6.5 software. Thermal unfolding experiments were performed with the temperature ramped from 20 to 90 °C or 99 °C (for AT in SE) at increments of 2.5 °C per step and an equilibration time of 2 min at each temperature. The second derivative of each spectrum was calculated with nine point smoothing. The thermal unfolding curves of AT were constructed by plotting the second derivative signal at 1621 cm^{-1} (an indication of intermolecular β-structure and protein aggregation) as a function of temperature. The melting temperature (T_m) was calculated by a first derivative method using Origin 2017 (OriginLab; Northampton, MA).

4.2.5. Intrinsic fluorescence spectroscopy

Intrinsic tryptophan fluorescence spectra were obtained using a fluorescence plate-reader (Fluorescence Innovations, Minneapolis, MN) equipped with a tunable pulsed dye laser, a high-

speed digitizer and a temperature controlled 384-well sample holder (Torrey Pines Scientific, Carlsbad, CA). This fluorometer has two detectors: a charge coupled device (CCD) spectrometer and a photomultiplier tube (PMT), permitting recording of steady-state fluorescence and time-resolved intrinsic fluorescence, respectively. The emission signal was collected at 180° (front face geometry) and then sent through a 300 nm long pass filter (Thorlabs Inc., Newton, NJ), which blocks the excitation light from entering the detector. For time-resolved fluorescence recording, the signal was further passed through a 360 nm (± 23 nm) band-pass filter before reaching the PMT. For steady-state fluorescence measurement, a right angle prism mirror was placed behind the 300 nm long pass filter to direct the emission light through an optical fiber to the CCD detector. Samples were loaded into a 364 well plate (Hard-Shell 384-well PCR plates) and silicon oil (ThermoFisher Scientific, Waltham, MA) was added to avoid sample evaporation by covering the sample surface during temperature runs. Samples were excited at 295 nm (>95% tryptophan emission). Temperature ramps were set from 20 to 99 °C with an increment of 1 °C per step and an equilibration time of 2 min at each temperature.

Steady-state emission spectra were collected using a CCD detector from 310 to 400 nm with an integration time of 100 ms. The mean center of spectra mass peak position (MSM peak position) and ratio of the area under the curve (AUC) from two regions (315 to 325 nm and 345 to 355 nm; $F_{345-355}/F_{315-325}$) were calculated using Matlab (MathWorks; Natick, MA). The MSM peak values are approximately 8 to 10 nm higher than the actual peak position but their use results in a better signal to noise ratio.(229)

Time-resolved intrinsic fluorescence data was obtained by recording fluorescence lifetime decay waveforms within a time scale of 100 ns. Two parameters (sum and moment) were calculated from the raw waveform by the FII data analysis software (Fluorescence Innovations,

Minneapolis, MN). Sum (in mV*ns) is the peak area under the waveform curve and represents the intensity of the overall emission collected by the PMT during an acquisition whereas moment (in ns) is defined as the center of the waveform where it equally divides the peak area under the curve. The moment represents the intensity-averaged lifetime of the waveform plot and its mathematical definition was previously described.(230, 231) Those two parameters were plotted against temperature and a first derivative method was used to find the T_m employing Origin 7.0 (OriginLab; Northampton, MA).

4.2.6. Differential scanning calorimetry (DSC)

DSC was performed using a MicroCal VP-Capillary calorimeter (Malvern, UK) equipped with an autosampler. The temperature was ramped from 10 to 100 ^{o}C at a scan rate of 1 ^{o}C/min. The sample cell was equilibrated for 15 min at 10 ^{o}C at the beginning of each run using a filtering period of 16 sec. Samples were loaded into a 96-well plate. The plate was sealed and kept inside a sample container maintained at 5 ^{o}C. Apparent transition temperatures were calculated using a non-two-state equilibrium model in Origin 7.0 (OriginLab; Northampton, MA).

4.2.7. Dynamic light scattering (DLS) and zeta potential

DLS and zeta potential measurements were performed using a Zetasizer Nano ZS Helix (Malvern Instruments, Columbia, MD) equipped with a He-Ne laser 633nm and backscattering detection (173°). In the DLS experiment, emulsion samples were run without dilution because the hydrodynamic size of emulsions were previously found to be independent of dilution (up to 1000 fold).(208) Samples (50 µL) were loaded into a Helix micro cuvette (Malvern Instruments, Columbia, MD) with a Teflon stopper. Ten measurements were taken with an acquisition time of 10 sec per measurement. Samples were heated from 15 to 90 ^{o}C with a step of 2.5 ^{o}C and an

equilibration time of 2 min at each step. The Z-average diameters were calculated for emulsion samples using a cumulant analysis. AT in PBS failed to produce consistent Z-average diameters due to its low molecular weight (33 kDa) and low concentration (0.2 mg/mL), therefore the derived count rate was reported instead. For the zeta potential measurement, samples were diluted two fold in water before analysis. Samples were measured in disposable folded capillary cells at 25 °C. The zeta-potential was calculated based on net electrophoretic mobility of sample particles using Henry's and the Smoluchowski approximations.

4.2.8. High-Performance Size-Exclusion Chromatography (HPSEC)

HPSEC analysis was performed using a Shimadzu HPLC system by measuring the fluorescence intensity at 330 nm upon excitation at 295nm. For HPSEC analysis, a TSKgel G3000SWXL column (7.8 mm × 300 mm) was used along with a TSKgel SWXL guard column (6.0 mm × 40 mm) from Tosoh Bioscience (King of Prussia, PA). A mobile phase composed of 0.2 M sodium phosphate, pH 6.8 was used. The concentrations of AT were maintained at 0.2 mg/mL by diluting with PBS, ME.0 or SE and 50 μL of sample was injected. The flow rate was 0.7 mL/min, and samples were held at 5°C in the auto sampler tray prior to injection.

4.2.9. Statistics

Statistical analyses between the control sample (i.e. AT in PBS or S0) and other test samples were performed using an independent two-sample t-test with equal variance. The variance equality was confirmed using the Levene's test. Values of $p < 0.05$ were considered to be statistically significant.

4.3. Results

4.3.1. FT-IR analysis of Recombinant AT with O/W Emulsions

The FTIR spectra in the Amide I region (1600-1700 cm^{-1}) of AT under various conditions and the corresponding deconvoluted spectra are shown in Figure 4.1 (panels A1 to A3). At 20 °C, in contrast to AT in PBS buffer, AT showed a statistically significant increase in alpha-helix content and decrease in beta-sheet content in the presence of SE rather than ME.0 (Figure 4.1, panel C1). Upon thermal stress, AT under all three conditions showed increases in the peak intensity at 1621 cm^{-1} corresponding to an increasing inter-molecular β-sheet content indicative of protein aggregation. This change is substantial for AT in PBS and in ME.0, but relatively minor for AT in SE (Figure 4.1, panels B1 to B3). Thermal unfolding profiles of AT monitored by the second derivative signal at 1621 cm^{-1} showed two transitions (Figure 4.1, panel C2). AT in PBS had two transitions at 56.6 ± 0.5 (T_m1) and 69.7 ± 0.5 (T_m2). In contrast to AT in PBS, AT in ME.0 showed slightly lowered T_m1 values, but decreased T_m2 values to a larger extent. SE significantly thermally stabilized AT as reflected by an increase of 15 °C and 22 °C in T_m1 and T_m2 values, respectively. The decreased extent of thermally induced protein aggregation observed for AT in SE can possibly be attributed to a stabilizing interaction between AT and SE.

4.3.2. Steady state intrinsic fluorescence spectroscopy analysis of recombinant AT with O/W Emulsions

Intrinsic fluorescence spectra of AT in PBS, ME.0 and SE at 20 °C were background subtracted and normalized for comparison. AT in PBS and in ME.0 shared similar emission spectra with an emission λ_{max} around 332 nm at 20 °C, suggesting the protein's overall tertiary structure was not significantly altered by the presence of ME.0. AT in SE, however, manifested a blue shifted spectrum with a λ_{max} at 327 nm (Figure 4.2 A) reflecting on average less exposure of the Trp residues to the aqueous environment. Since each AT molecule contains eight Trp residues,

blue shifts are indicative of overall protein tertiary structure changes and may indicate hydrophobic interactions between AT and SE.

Both emulsions contains fluorescent components and shows significant fluorescence emission signals from 310 to 400 nm when excited at 295 nm. Thermal melting curves were plotted for both protein samples and emulsions to separately study their thermal transitions. ME.0 itself showed a thermal transition around 67 °C. SE, however, did not show a clear transition from 20 to 99 °C. Thermal unfolding profiles of AT in PBS showed only one thermal transition (Figure 4.2B and 4.2C). This transition was accompanied by a red shift in the MSM peak position and an increasing $F_{320-330}/F_{350-380}$ ratio, suggesting AT had a greater solvent exposure of tryptophan residues during thermal unfolding. AT in ME.0 showed combined transitions derived from AT and ME.0 (Figure 4.2B and 4.2C). The protein transition of AT in ME.0 showed similar changes (i.e. increasing MSM peak position and $F_{320-330}/F_{350-380}$ ratio) as seen in PBS. Conversely, AT in SE showed an opposite trend (i.e., a blue shift in MSM peak position and a decrease in $F_{320-330}/F_{350-380}$ ratio) during its thermal transition (Figure 4.2B and 4.2C). One possible explanation could be that AT interacted with SE during thermal unfolding with increasing exposure to the oil phase. Unfolding profiles monitored by both MSM peak positon and $F_{320-330}/F_{350-380}$ ratio showed similar T_m values (Figure 4.2 D). ME.0 slightly destabilized AT by a decrease of 4 - 5 °C in T_m, whereas SE enhanced the T_m of AT by approximately 12 °C.

4.3.3. Time-resolved intrinsic fluorescence analysis of Recombinant AT with O/W Emulsions

To tease out the effects of these complex O/W emulsions on AT protein stability, a component study was performed by studying the thermal stability of AT in the presence of water-soluble components using time-resolved intrinsic fluorescence spectroscopy. In the sum-

temperature plot (Figure 4.3, panels A1 and A2), the decreasing trend line indicates thermal quenching of AT fluorescence. Moment is a lifetime-derived empirical parameter which reflects the overall polarity of the neighboring environment of tryptophan residues within a protein. AT in PBS (S0) monitored by both sum and moment showed one thermal transition (Figure 4.3, panels A1 and A2). The thermal transition exhibited an increase in the sum (collected at 360 nm) indicating an increasing population of exposed tryptophan residues in the protein during unfolding. An increase in the moment was observed for AT in PBS during thermal unfolding.

In contrast to S0, AT in M1 had a lower T_m by 4 °C probably because of a pH drop and/or change in salt composition after mixing AT in PBS (pH 7.4) with histidine buffer (20 mM, pH 6.0) (Figure 4.3, panel A3). Compared to M1, a minor drop in the T_m of AT was observed when mixed with 1% PS80 (M2), while adding 10 % sucrose (M3) slightly stabilized AT. Mixing both 1% PS80 and 10 % sucrose with AT (M4) showed effects by both of these two components (i.e., a thermally destabilizing and stabilizing effect from PS80 and sucrose, respectively). Compared to S0, AT in ME.0 (M5) produced decreased protein thermal stability probably attributable to a change in the buffer composition upon mixing AT with ME.0.

In the component study of SE, AT mixed with water-soluble components of SE (samples referred to as S1 to S4) showed similar T_m values which were lower than that of S0. This suggests that ammonium phosphate (25 mM, pH 5.6) thermally destabilized AT, probably because of a drop in pH and/or change in salt composition. This effect was also observed for M1. In S4, because of the poor water solubility of DMPC, saturated DMPC aqueous solution was used and its concentration was lower than that used in SE (1.1%). It is possible that DMPC at the higher concentration present in SE may affect AT stability to a larger extent. AT in SE (S5), however, had a T_m as high as 71 °C (Figure 4.3 B1 to B3). This dramatic thermal stabilization effect on AT

is probably due to interactions between AT and the oil phase of SE consisting of squalene, vitamin E and DMPC (at 1.1%, a concentration higher than its aqueous solubility).

4.3.4. Differential scanning calorimetry analysis of recombinant AT with O/W Emulsions

DSC was performed to study the effect of emulsions on the overall conformational stability of AT. AT in PBS (S0) underwent two distinct thermal transitions ($T_m1 = 58.0$ ºC and $T_m2 = 69.2$ ºC, a relatively minor transition) (Figure 4.4A). The thermal unfolding of AT in PBS, ME.0 and SE was found to be irreversible as determined by rescanning the sample after one thermal unfolding cycle (data not shown). ME.0 showed two major transitions: the first one centered near 65.9 ºC and the second one with a sudden large increase in heat capacity above 80 ºC (see Supplementary Figure 4.S1). The first transition, also seen by intrinsic fluorescence spectroscopy, may correspond to a structural change in the emulsion, while the second one probably reflects the complete decomposition of the emulsion system. The AT/ME.0 mixture (M5) exhibited transitions from both protein and emulsion with the second thermal transition of AT and that of ME.0 partially overlapped. ME.0 lowered both T_m1 and T_m2 of AT significantly (compare samples M5 vs. S0 in Figure 4.4A). On the other hand, the T_m of ME.0 decreased by 3.5 ºC in the presence of AT indicating that partially unfolded AT may slightly destabilize ME.0. For the component study, DSC was performed to study the effects of various components on the T_m of AT. Each component showed a similar effect on melting temperatures (T_m1 and T_m2) of AT as indicated by the lifetime fluorescence component study (Figure 4.4A M1 to M4). This result further suggests that the destabilization effect of ME.0 on AT is because of the change in buffer composition upon mixing.

In the range of 10 to 100 ºC, SE showed one thermal transition around 25.3 ºC, corresponding to a gel-liquid phase transition of DMPC [232] (Figure 4.4B and Supplementary

Figure S1). This result was further confirmed by examining saturated DMPC solution in 25 mM ammonium phosphate (the concentration of DMPC is less than 1.1%) by DSC which showed a transition at 24.6 °C (Figure 4.4B). Upon mixing AT with SE (S5), the T_m of SE was not significantly altered by AT. SE, however, increased both T_m1 and T_m2 of AT by 13.7 and 25.9 °C, respectively (compare samples S5 vs. S1 in Figure 4.4B). The component study was continued by mixing AT with the water-soluble components present in SE. The DSC results correlate well with the intrinsic fluorescence data. It shows that the change in buffer composition upon mixing (S1) induced a destabilization effect on AT thermal stability while neither 2.37% glycerol (S3) nor 0.037% F68 (S2) had a further significant effect on the T_m of AT. Mixing saturated DMPC (S4) with AT produced only a minor increase in protein T_m1 and T_m2. Overall, all of water soluble components of SE did not show a major stabilization effect on AT T_m. The dramatic stabilization effect of SE (S5) on AT is therefore probably due to the interaction between AT and the oil phase containing squalene, vitamin E and DMPC (at 1.1%).

4.3.5. Dynamic light scattering (DLS) and zeta potential analysis of recombinant AT with O/W Emulsions

DLS was performed to investigate the effect of temperature on the colloidal stability of the samples. As shown in Figure 4.5A, the derived count rate (i.e. the intensity of light scattering) of AT in PBS showed a dramatic increase above 52.5 °C, indicating the aggregation of AT in PBS. This result is in good agreement with the stability data reported above. SE did not show dramatic changes in their hydrodynamic sizes between 15 and 90 °C, suggesting the high colloidal stability of SE upon thermal stress (Figure 4.5B). The size of SE above 90 °C was not measured because of instrumental constraint. The addition of AT to SE did not change the overall size of emulsion nanoparticles. In addition, the first unfolding event of AT (around 70 °C seen by DSC etc.) did not

significantly alter the emulsion size. In contrast, heating caused ME.0 to aggregate above 60 °C (Figure 4.5C). The addition of AT into ME.0 further decreased the onset aggregation temperature by approximately 3 °C, which is consistent with the DSC data. Zeta potential analysis shows that AT had a slight negative zeta potential at pH 7.4 due to its pI value (~ 6.85) (Figure 4.S2). Both ME.0 and AT in ME.0 had a slightly negative zeta potential, presumably due to negatively charged impurities (such as free fatty acids (233)) in PS80. In contrast, SE showed a neutral zeta potential. AT in SE also showed a near zero potential probably because the mixing AT (pH 7.4) with SE (pH 5.6) results in a mixture with a pH closer to the pI of AT.

4.3.6. High-Performance size-exclusion chromatography (HPSEC) analysis of recombinant AT with O/W Emulsions

SEC was performed to study the impact of the interactions of AT and ME.0/SE on retention time of the protein and the individual emulsions. Figure 4.6 shows the SEC chromatograms for AT in PBS, and when mixed with ME and SE. AT has a single peak eluting at ~16.9 min (Fig. 6A). Both ME.0 and SE elute at 8 to 9 min (Figure 4.6A and 4.6B). When mixed with ME.0, the retention time of AT does not change significantly and the recovery of AT was found to be 99.7 ± 0.1 % (Supplementary Table 4.S1). When AT is mixed with SE, the peak corresponding to AT is missing while the peak at 9 min had a larger peak area than the peak area of SE alone (Figure 4.6B). This result may indicate that the AT is bound to the SE and co-elutes with the emulsion.

4.4. Discussion

In the present study, the effects of two squalene based emulsion adjuvants (ME.0 and SE) on the structure and stability of recombinant AT, a potential vaccine candidate for antibiotic resistant *Staph* infection, were investigated. The wild type AT is expressed as water soluble

monomer and self-assembles into a heptameric structure with a transmembrane domain.(222) AT used in this study is a mutant of the wild type AT and may still have favorable interactions with phospholipid bilayers (i.e. DMPC) and/or the hydrophobic oil phase in the emulsion adjuvants. FT-IR, intrinsic tryptophan fluorescence, DSC and DLS were performed to investigate protein structure and the thermal stability of AT in the presence of emulsions. These results are summarized in Table 4.2. FTIR spectra of AT at 20 °C indicate that AT had an increased alpha helix content, but decreased the amount of beta sheet in the presence of SE. This effect on AT is negligible for ME.0, but more pronounced in the presence of SE. Previous work has reported that protein/oil interactions induced a protein to undergo a transition from beta sheet to more non-native alpha helix content in a β-lactoglobulin/hexadecane system.(234) At 20 °C, a significant blue shift (λ_{max} changed from 332 to 327 nm) was observed in the intrinsic fluorescence emission spectrum of AT in SE, rather than AT in ME.0. This result correlates with FTIR data indicating that SE but not ME.0 induced substantial structural alterations of AT in SE.

Protein thermal stability analysis shows that ME.0 slightly decreased the T_m of AT, while it was significantly enhanced in the presence of SE. A component study was further conducted by characterizing AT in the presence of the individual water-soluble components of the test emulsions with the goal of identifying the components responsible for alterations of protein stability. The data shows that the destabilizing impact of ME.0 on AT is probably because of a change in the buffer composition upon mixing ME.0 which contains 20 mM histidine (pH 6.0) with AT in PBS (pH 7.4). In the case of AT in SE, because none of the water soluble components produced a thermal stabilization effect on AT, it seems probable that the thermal stabilization of SE is due to interactions between AT and the oil phase of SE consisting of squalene, vitamin E and DMPC.

SE significantly altered the secondary and tertiary structures of AT and improved its thermal stability. This was again probably because of the adsorption of AT onto the oil phase. Proteins at oil-water interfaces have previously shown enhanced resistance to thermal stress.(234) Zhai has reported no significant changes in the secondary structure of β-lactoglobulin adsorbed to nonpolar hexadecane up to 76 °C at which point the same protein in solution lost its secondary structure.(234) When protein molecules interact with hydrophobic oil, they usually tend to reorient their apolar patches towards the oil surface to enhance apolar interactions. This is usually accompanied by structural changes in proteins. In this case, an interconversion from beta sheet to alpha helix was observed for AT in the presence of SE. Upon adsorption to SE, AT showed less exposure of Trp residues to the polar environment and an increased thermal stability. DLS analysis indicates that SE exhibited higher colloidal stability than ME.0 in response to heating. The addition of AT decreased the stability of ME.0 but did not impact SE (at least up to 90 °C). The zeta potential data show that SE had a relatively neutral surface, suggesting that the ionic attraction between SE and AT is probably negligible, further arguing that the potential interaction is hydrophobically driven. In addition, HPSEC data showed a nearly complete loss in the recovery of AT when mixed with SE, but not ME.0, indicating a high degree of interaction with SE, which possibly resulted in the co-elution of AT with SE.

Both ME.0 and SE are squalene based oil-in-water emulsions, but they interact with AT quite differently. They mainly differ in the type and concentration of surfactants. This might be responsible for the difference in their effects on protein structure and stability. In a stable emulsion system, oil droplets are coated by stabilizing surfactants. Protein molecules need to displace surfactant to adsorb onto the surface of an oil phase. In the case of ME.0, AT probably failed to compete with polysorbate 80 (at 0.5%) for binding to the surface of oil droplets. On the other hand,

AT probably was better able to displace the surfactants of SE (DMPC and pluronic F68) to establish interactions with its oil phase. It is also possible that AT interact with the lipid layer of DMPC at the concentration of 1.1% used in SE, which is significantly higher than its aqueous solubility. It is worthwhile mentioning that during the unfolding of AT, the emulsions had undergone (SE) or were undergoing (ME.0) thermal transitions (Figure 4.4). It is possible that emulsion structural changes contribute to the observed changes in protein thermal stability.

FTIR, intrinsic fluorescence spectroscopy and DSC have shown significant robustness in characterizing the structure and conformational stability of alpha-toxin (AT), a vaccine candidate for *Staph* infection, in the presence of highly scattering squalene based emulsion adjuvants. The component study further helped to dissect the effect of each water soluble component on the protein antigen. These biophysical methods along with the component study can be considered a case study to be applied to study the structure and stability of other protein antigens in a variety of adjuvant emulsion systems, further guiding the development and optimization of emulsion-adjuvanted vaccine formulations.

4.5. References

1. Moyle PM, Toth I. 2013. Modern subunit vaccines: Development, components, and research opportunities. ChemMedChem. 8(3):360-376.

2. Iyer V, Cayatte C, Marshall JD, Sun J, Schneider-Ohrum K, Maynard SK, Rajani GM, Bennett AS, Remmele RL, Bishop SM. 2017. Feasibility of freeze-drying oil-in-water emulsion adjuvants and subunit proteins to enable single-vial vaccine drug products. J Pharm Sci. 106(6):1490-1498.

3. Leroux-Roels G. 2010. Unmet needs in modern vaccinology: Adjuvants to improve the immune response. Vaccine. 28:C25-C36.

4. Garçon N, Vaughn DW, Didierlaurent AM. 2012. Development and evaluation of as03, an adjuvant system containing α-tocopherol and squalene in an oil-in-water emulsion. Expert review of vaccines. 11(3):349-366.

5. Ott G, Barchfeld GL, Chernoff D, Radhakrishnan R, van Hoogevest P, Van Nest G. 1995. Mf59 design and evaluation of a safe and potent adjuvant for human vaccines. Vaccine design. Springer. p. 277-296.

6. Podda A, Del Giudice G. 2003. Mf59-adjuvanted vaccines: Increased immunogenicity with an optimal safety profile. Expert review of vaccines. 2(2):197-204.

7. Jackson LA, Campbell JD, Frey SE, Edwards KM, Keitel WA, Kotloff KL, Berry AA, Graham I, Atmar RL, Creech CB. 2015. Effect of varying doses of a monovalent h7n9 influenza vaccine with and without as03 and mf59 adjuvants on immune response: A randomized clinical trial. Jama. 314(3):237-246.

8. Reed SG, Orr MT, Fox CB. 2013. Key roles of adjuvants in modern vaccines. Nature medicine. 19(12):1597-1608.

9. O'Hagan D, Ott G, De Gregorio E, Seubert A. 2012. The mechanism of action of mf59–an innately attractive adjuvant formulation. Vaccine. 30(29):4341-4348.

10. Behzad H, Huckriede AL, Haynes L, Gentleman B, Coyle K, Wilschut JC, Kollmann TR, Reed SG, McElhaney JE. 2011. Gla-se, a synthetic toll-like receptor 4 agonist, enhances t-cell responses to influenza vaccine in older adults. J Infect Dis. 205(3):466-473.

11. Sun J, Remmele RL, Sanyal G. 2016. Analytical characterization of an oil-in-water adjuvant emulsion. AAPS PharmSciTech.1-10.

12. Wu D, Meydani SN. 2008. Age-associated changes in immune and inflammatory responses: Impact of vitamin e intervention. J Leukocyte Biol. 84(4):900-914.

13. Morel S, Didierlaurent A, Bourguignon P, Delhaye S, Baras B, Jacob V, Planty C, Elouahabi A, Harvengt P, Carlsen H. 2011. Adjuvant system as03 containing α-tocopherol modulates innate immune response and leads to improved adaptive immunity. Vaccine. 29(13):2461-2473.

14. Wardenburg JB, Bae T, Otto M, DeLeo FR, Schneewind O. 2007. Poring over pores: A-hemolysin and panton-valentine leukocidin in staphylococcus aureus pneumonia. Nature medicine. 13(12):1405-1406.

15. Adhikari RP, Karauzum H, Sarwar J, Abaandou L, Mahmoudieh M, Boroun AR, Vu H, Nguyen T, Devi VS, Shulenin S. 2012. Novel structurally designed vaccine for s. Aureus α-hemolysin: Protection against bacteremia and pneumonia. PLoS One. 7(6):e38567.

16. Song L, Hobaugh MR, Shustak C, Cheley S, Bayley H, Gouaux JE. 1996. Structure of staphylococcal alpha-hemolysin, a heptameric transmembrane pore. Science. 274(5294):1859-1866.

17. Ott G, Radhakrishnan R, Fang J-H, Hora M. 2000. The adjuvant mf59: A 10-year perspective. Springer. p. 211-228.

18. Fox CB, Kramer RM, Barnes V L, Dowling QM, Vedvick TS. 2013. Working together: Interactions between vaccine antigens and adjuvants. Therapeutic advances in vaccines. 1(1):7-20.

19. Dey AK, Malyala P, Singh M. 2014. Physicochemical and functional characterization of vaccine antigens and adjuvants. Expert review of vaccines. 13(5):671-685.

20. Kumru OS, Joshi SB, Smith DE, Middaugh CR, Prusik T, Volkin DB. 2014. Vaccine instability in the cold chain: Mechanisms, analysis and formulation strategies. Biologicals. 42(5):237-259.

21. Ji T, Urry D. 1969. Correlation of light scattering and absorption flattening effects with distortions in the circular dichroism patterns of mitochondrial membrane fragments. Biochemical and biophysical research communications. 34(4):404-411.

22. li Zhai J, Day L, Aguilar M-I, Wooster TJ. 2013. Protein folding at emulsion oil/water interfaces. Current opinion in colloid & interface science. 18(4):257-271.

23. Hu L, Joshi SB, Andra KK, Thakkar SV, Volkin DB, Bann JG, Middaugh CR. 2012. Comparison of the structural stability and dynamic properties of recombinant anthrax protective antigen and its 2-fluorohistidine-labeled analogue. J Pharm Sci. 101(11):4118-4128.

24. Petersen KJ, Peterson KC, Muretta JM, Higgins SE, Gillispie GD, Thomas DD. 2014. Fluorescence lifetime plate reader: Resolution and precision meet high-throughput. Rev Sci Instrum. 85(11):113101.

25. Wei Y, Larson NR, Angalakurt SK, Middaugh CR. 2018. Improved fluorescence methods for high-throughput protein formulation screening. SLAS TECHNOLOGY. (in press)

26. Gilman T, Kauffman JW, Pownall HJ. 1981. Raman spectroscopy of the thermal properties of reassembled high-density lipoprotein: Apolipoprotein ai complexes of dimyristoylphosphatidylcholine. Biochemistry. 20(3):656-661.

27. Brandner JD. 1998. The composition of nf-defined emulsifiers: Sorbitan monolaurate, monopalmitate, monostearate, monooleate, polysorbate 20, polysorbate 40, polysorbate 60, and polysorbate 80. Drug Dev Ind Pharm. 24(11):1049-1054.

28. Zhai J, Wooster TJ, Hoffmann SV, Lee T-H, Augustin MA, Aguilar M-I. 2011. Structural rearrangement of β-lactoglobulin at different oil–water interfaces and its effect on emulsion stability. Langmuir. 27(15):9227-9236.

4.6. Figures and Tables

4.6.1. Tables

Table 4.1. Identification codes and components of test samples subjected to the component study. All test samples used for the component study contained AT with a concentration of 0.2 mg/ml. S0 is AT in PBS (at 0.2 mg/ml). ME.0 (1X) and SE (1X) diluted using PBS were used as control samples. S0, M5 and S5 are denoted as AT in PBS, AT in ME.0 and AT in SE, respectively in FTIR, steady-state fluorescence, and HPSEC studies. * For S4, AT was mixed with saturated aqueous solution of DMPC with a concentration lower than 1.1% used in SE.

S0	AT in PBS (at 0.2 mg/mL)			
ME.0 component study samples	AT in PBS (0.4 mg/ml) mixed with (1/1, v/v)			
	20mM Histidine pH 6.0	10% Sucrose	1% PS80	4% Squalene
M1	+			
M2	+	+		
M3	+		+	
M4	+	+	+	
M5	+	+	+	+
SE component study samples	AT in PBS (0.3 mg/ml) mixed with (2/1, v/v)				
	25mM Ammonium Phosphate pH 5.6	Pluronic F68 0.037% (w/v)	Glycerol 2.37% (w/v)	DMPC 1.1%	5.1% Squalene 30 μg/mL Vitamin E
S1	+				
S2	+	+			
S3	+		+		
S4	+			+*	
S5	+	+	+	+	+

Table 4.2. Summary of biophysical data sets of AT in ME.0 or SE compared to AT in buffer alone. The biophysical techniques used in this study and corresponding parameters investigated are listed. The relative change in these parameters for AT in ME.0 or SE relative to AT in PBS.

Technique	Biophysical parameter studied		AT in ME.0	AT in SE
FT-IR	2nd structure content at 20 ºC	α-helix	no change	↑ 12% @ 20 ºC
		β-sheet	no change	↓13% @ 20 ºC
		random coil	no change	no change
	T_{m1}		↓ 2.9 ºC	↑ 14.6 ºC
	T_{m2}		↓ 9.3 ºC	↑ 23.2 ºC
Steady-state fluorescence	T_m by MSM peak position		↓ 4.0 ºC	↑ 12.0 ºC
	T_m by ratio		↓ 5.4 ºC	↑ 10.7 ºC
Time resolved fluorescence	T_m by moment		↓ 4.2 ºC	↑ 12.2 ºC
	T_m by sum		↓ 4.3 ºC	↑ 13.6 ºC
DSC	T_{m1}		↓ 2.0 ºC	↑ 13.7 ºC
	T_{m2}		↓ 8.4ºC	↑ 25.9 ºC
SEC	Recovery of AT		99.7%	~ 0%

Supplemental Table 4.S1. Peak areas and recovery of AT elution peaks from the size exclusion chromatography analysis. Both AT in PBS and AT in ME.0 have a protein concentration of 0.2 mg/mL. Errors indicate standard deviation (N=3).

Samples	Protein peak area (mAU*min)	Recovery of AT (%)
AT in PBS (0.2 mg/mL)	4539987 ± 26168	100
AT in ME.0 (0.2 mg/mL)	4527663 ± 6454	99.72 ± 0.14

$$\text{The recovery of AT in ME.0} = \frac{\text{Protein peak area of AT in ME.0}}{\text{Protein preak area of AT in PBS}} *100\%$$
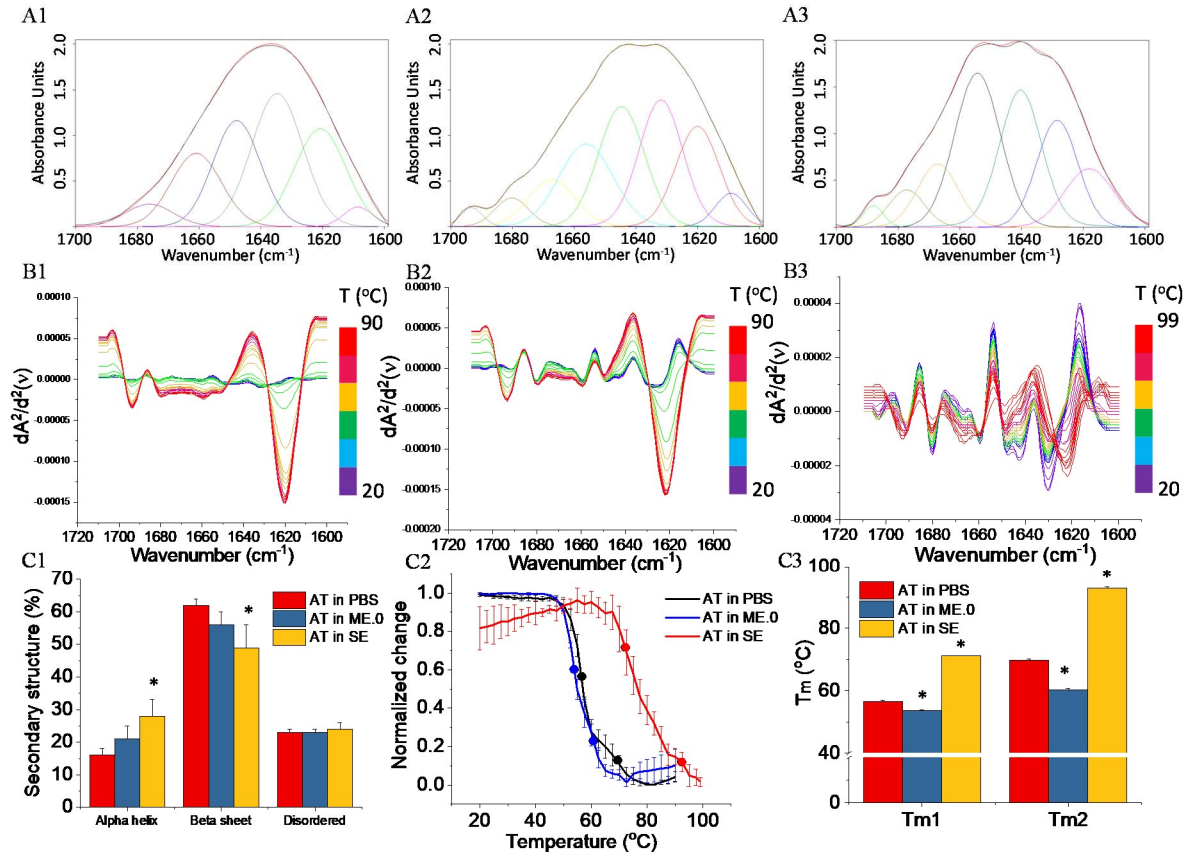
4.6.2. Figures

Figure 4.1. Structure and stability of AT in presence and absence of ME.0 and SE emulsions as measured by FTIR. FTIR spectra of (A1) AT in PBS at 20 °C; (A2) AT with ME.0 at 20 °C; (A3) AT with SE at 20 °C. The black and red lines represent the raw and fitted FTIR spectra, respectively. The deconvoluted spectra are shown in various colors. Spectra with peaks between 1649-1659 cm^{-1} are assigned as α helix; spectra with peaks between 1620-1640 cm^{-1} or 1661-1700 cm^{-1} are assigned as β sheet. Other peaks are assigned as disordered. Second derivative of FTIR spectra monitoring the thermal unfolding of (B1) AT in PBS from 20 to 90 °C; (B2) AT with ME.0 from 20 °C to 90 °C; (A3) AT with SE from 20 °C to 99 °C. (C1) The secondary structural contents of AT determined by deconvolution analysis. AT in SE, but not AT in ME.0, showed a statistically significant difference with AT in PBS in protein secondary structure contents. * p < 0.05. (C2)

Thermal melting curve of AT monitored by changes in the signal at 1621 cm^{-1}. Round dots on each melting curves indicate melting temperatures. (C3) Comparison of thermal melting temperature values of AT under various conditions (N = 3). * $p < 0.05$.
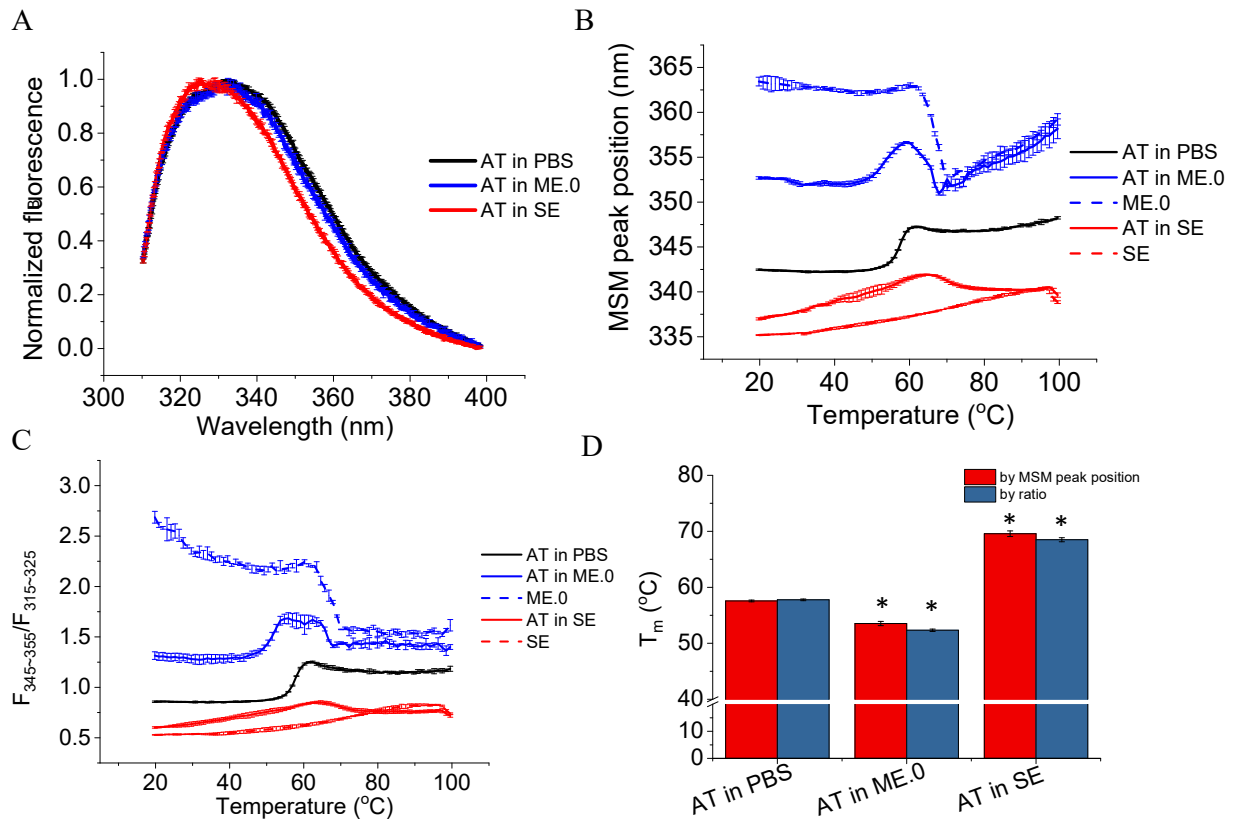
Figure 4.2. Tertiary structure analysis of AT in presence and absence of ME.0 and SE emulsions as monitored by intrinsic fluorescence spectroscopy. (A) Normalized fluorescence spectra of AT at 20 °C. Thermal unfolding profiles monitored by (B) MSM peak position and (C) ratio of the area under the curve (AUC) from two regions ($F_{320-330}/F_{350-380}$) (E) Summary of Tm values. Error bars indicate standard deviation (N=3). * $p < 0.05$.
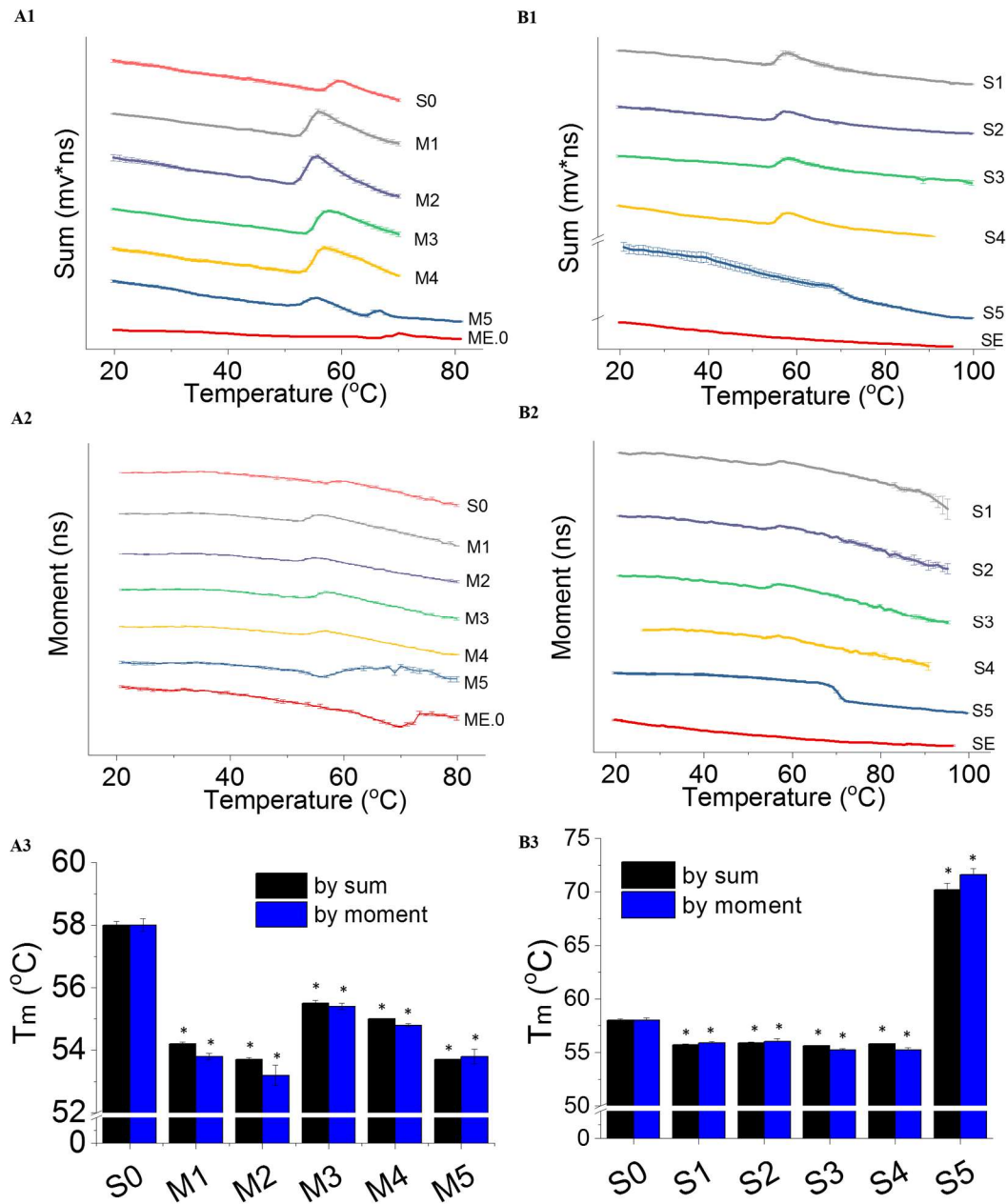
Figure 4.3. Thermal unfolding profiles of AT in the presence of various components of ME.0 emulsion as measured by time resolved fluorescence spectroscopy. The sum (A1) and moment (A2) values of AT emission waveforms; of SE monitored by sum (B1) and moment (B2) of AT emission waveforms. Corresponding Tm values are summarized (panels A3 and B3). Error bar indicates standard deviation (N=3). * p < 0.05. See Table 1 for sample composition.

Samples	S0	M1	M2	M3	M4	M5	S1	S2	S3	S4	S5
$T_{m1}(^oC)$	58.0 ±0.02	55.4 ±0.02 *	55.3 ±0.03 *	56.4 ±0.04 *	56.2 ±0.02 *	56.0 ±0.05 *	55.5 ±0.03 *	55.5 ±0.01 *	55.3 ±0.02 *	56.7 ±0.23 *	71.7 ±0.07 *
$T_{m2}(^oC)$	69.2 ± 0.16	66.9 ±0.16 *	66.8 ±0.04 *	67.7 ±0.07 *	67.2 ±0.03 *	60.8 ±0.37 *	67.3 ±0.17 *	67.0 ±0.12 *	67.8 ±0.27 *	67.9 ±0.61 *	95.1 ±0.06 *
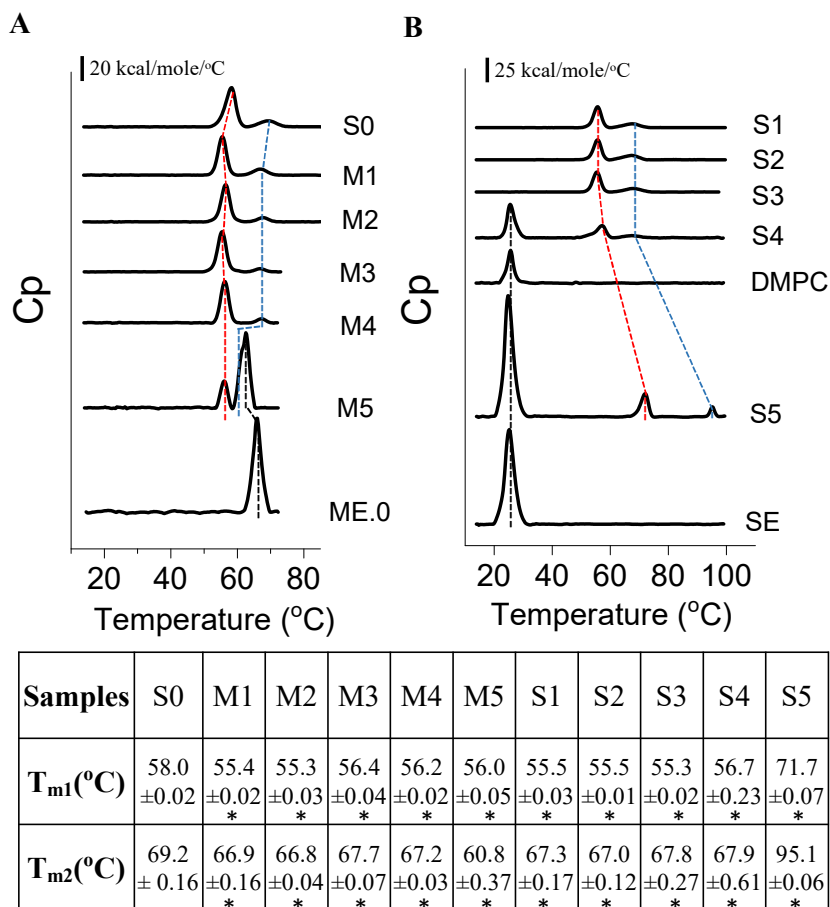
Figure 4.4. DSC thermograms of AT, emulsions, and AT in the presence of various components of emulsions (A) ME.0 and (B) SE. The first (T_m1) and second (T_m2) thermal transitions of AT are indicated by red and blue dashed lines, respectively. The transition derived from emulsions (ME.0 and SE) is indicated using black dashed line. Apparent melting temperature values are summarized in the table. Errors indicate standard deviation (N=3). See Table 1 for sample composition. * p < 0.05.
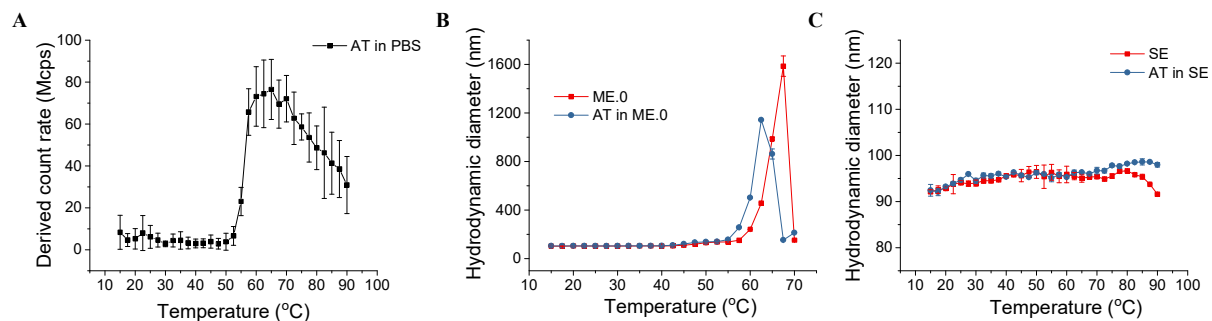
Figure 4.5. The temperature dependent colloidal stability of AT in PBS (A), AT in ME.0 (B), and AT in SE (C) measured by dynamic light scattering. Errors indicate standard deviation (N=3). See Table 1 for sample composition.
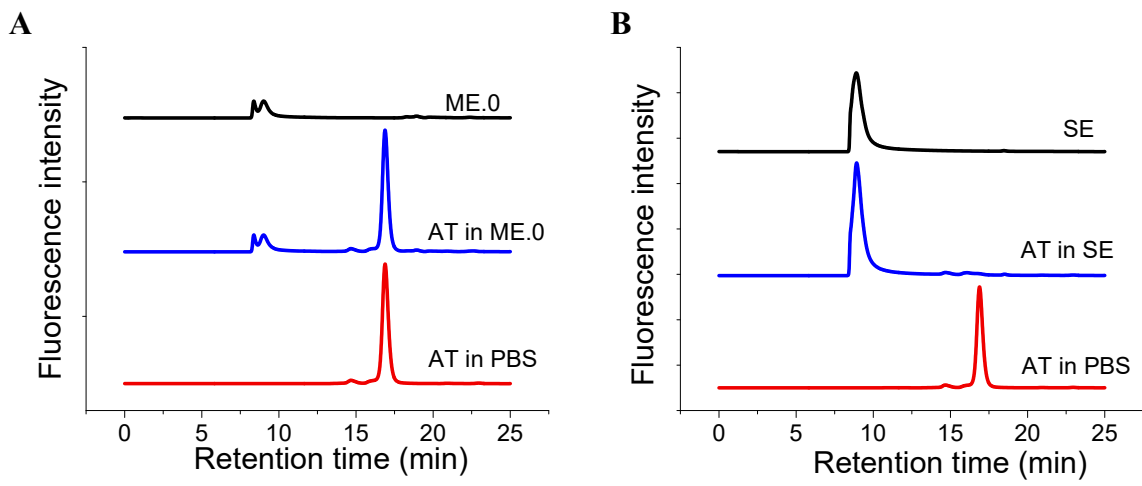
Figure 4.6. HPSEC chromatograms of ME.0 and AT in ME.0 (A); SE and AT in SE (B). The chromatography of AT in PBS was shown in both plots for comparison.
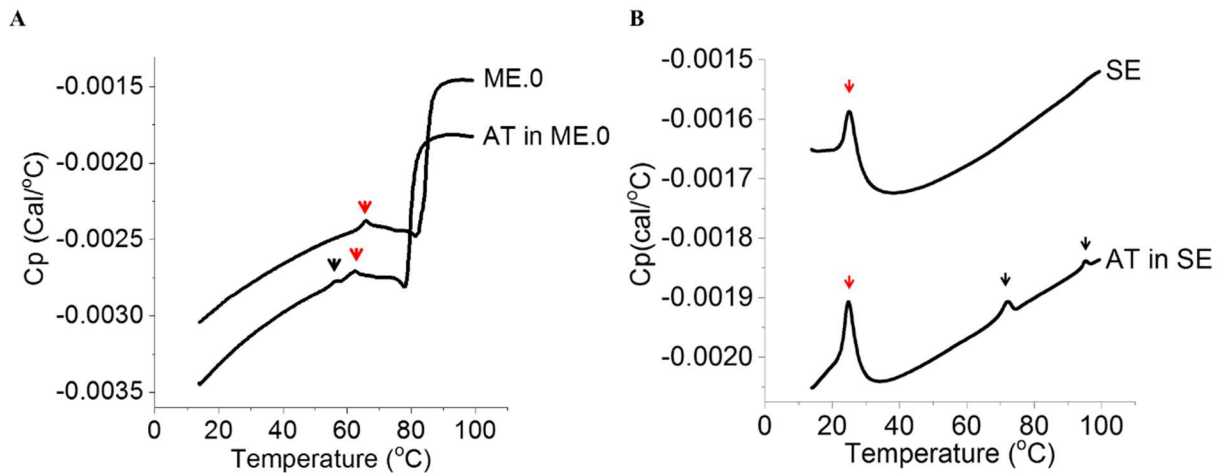
Supplemental Figure 4.S1. Uncorrected DSC thermograms of ME.0 alone and AT in ME.0 (A) and SE alone and AT in SE (B). Black arrow indicates the thermal transitions of the protein. Red arrows point to transitions derived from the emulsion. Both ME.0 and AT in ME.0 samples showed a sudden increase in the heat capacity above 80 °C.
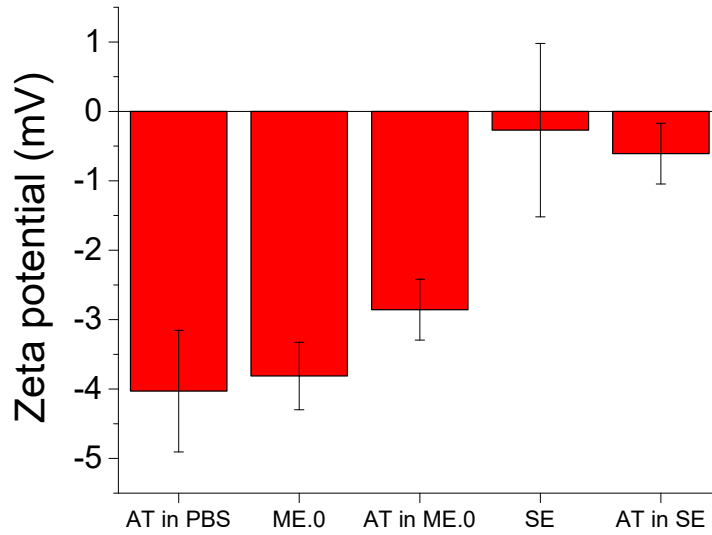
Supplemental Figure 4.S2. The zeta potentials of AT in PBS, ME.0, AT in ME.0, SE and AT in

SE at 25 °C. Errors indicate standard deviation (N=3). See Table 1 for sample composition.

Chapter 5: Improved fluorescence methods for high-throughput protein

formulation screening

5.1. Introduction

Proteins are complex molecules with unique three-dimensional structures. The integrity of such structures is critical to protein biological function. Proteins in solution, however, are only marginally stable with a relative low free energy of unfolding (~ 5-10 kcal/mole at 25 $^\circ$C) (235). Therefore, optimization of formulation conditions for proteins must ensure their structural stability during manufacturing, shipping, and storage. Protein formulation optimization requires the identification of the optimal pH, ionic strength, and excipient conditions from a large set of potential conditions in a rapid and cost-effective manner. To quickly differentiate protein stability in various formulations, the structural stability of a protein is usually evaluated under a stressed condition (commonly elevated temperature). During a thermal melting experiment, protein structural stability can be reflected by melting temperatures (T_m), which are measured by monitoring a biophysical signal sensitive to protein structure. For example, vibrational spectroscopy and far UV circular dichroism (CD) can monitor protein secondary structures, and fluorescence and near UV CD is often used to probe protein tertiary structures. The overall thermal stability of proteins is frequently investigated using differential scanning calorimetry.

Specific therapeutic needs often call for unique formulation conditions for optimal clinical uses, which presents substantial analytical challenges during formulation development. For example, subunit vaccines often are often formulated with adjuvants (e.g. aluminum salts, emulsion, etc.) for enhanced immunogenicity. Another example is monoclonal antibodies (mAbs), which frequently need to be formulated at high concentrations (50 to 200 mg/mL) to enable subcutaneous or intramuscular administration for better patient compliance (236). The highly scattering adjuvanted samples or strongly absorbing high concentration mAbs are not easily analyzed using absorption or conventional intrinsic fluorescence based techniques. In addition, the

formulation development of high concentration mAbs is limited by the large consumption of protein. The optimization of such protein formulations is therefore often conducted indirectly in transparent solutions containing relatively low protein concentrations (e.g. 0.1 to 1 mg/mL) for the sake of ease of analysis and conservation of materials (237). Formulation screening data obtained under such convenient conditions, however, may fail to predict the situation under a more commercially relevant condition. In fact, many studies have found the destabilization effects by protein adsorption to Alhydrogel (238, 239). Research has also shown that the thermal stability of proteins (e.g. mAbs) can be concentration dependent (240). It is possible that protein thermal stability in a commercial formulation (e.g. at high concentrations or in the presence of adjuvants) may be affected to different extents by excipients compared to that in model conditions (i.e. low concentrations in clear solutions). Therefore, there is a need to develop a high-throughput platform permitting direct optimization for analytically challenging, but pharmaceutically relevant formulations.

In the present study, we explored the utility of an intrinsic fluorescence based system integrating a front face geometry (suitable for the analysis of turbid and high concentration samples) into a high-throughput microplate. This platform has the following features: 1) low sample consumption: 2) rapid fluorescence acquisition; 3) front-face geometry; 4) free of the use of external dyes; 5) capability to record both time-resolved (TRF) and steady-state fluorescence (SSF). We have developed a general workflow using this system for direct optimization of challenging protein formulations. A key step of this workflow is the selection of a suitable method to generate T_m values. The effect of T_m calculation methods on T_m values was investigated and differences seen can be attributed to the linear nature of the response to unfolding. Choosing a parameter with a linear response is preferable to generate accurate T_m values. It is also shown that

TRF may be used as an alternative technique to SSF for formulation screening purpose. We also found significant discrepancies in the excipient screening results performed under simplified conditions (i.e. proteins at 0.2 mg/mL in clear solutions) and pharmaceutically relevant conditions (e.g. adjuvanted or high protein concentrations). This result demonstrates the importance of direct formulation optimization of commercially relevant conditions. In addition, we also show the potential use of intrinsic fibril fluorescence to study the thermally induced formation of fibrils in high concentration mAb samples.

5.2. Materials and Methods

5.2.1. Reagents

Lysozyme, RiVax, and a mAb were selected as model proteins. Lyophilized lysozyme powder from chicken egg white was purchased from Sigma-Aldrich (St. Louis, MO). RiVax (a mutated form of the A-chain of ricin used as a vaccine (237)) was expressed and purified in-house using a protocol previously described (241). The mAb was obtained from Janssen Research & Development, LLC (Horsham, Pennsylvania) (242, 243). Sodium phosphate dibasic, sodium citrate, and sodium chloride were purchased from Fisher Scientific (Hampton, NH). Excipient stock solutions used in this study were obtained from the Solubility & Stability Screen Reagents (Hampton Research, Aliso Viejo, CA) unless otherwise stated. The Solubility & Stability Screen Reagents are a set of commonly used excipients formulated in water.

5.2.2. Sample preparation

For the pH screening study, these three model proteins were prepared in 20 mM citrate phosphate isotonic (having an ionic strength of 150 mM adjusted by NaCl) buffers (pH 3.0, 4.0, 5.0, 6.0, 7.0, and 8.0) at a concentration of 0.2 mg/mL. RiVax or the mAb was then subjected to an excipient screening study in which each protein (at 0.4 mg/mL) was mixed with an equal volume of each of 40 excipient stock solutions such that the final buffer contained 20 mM citrate phosphate isotonic buffer, pH 6.0.

Out of the 40 excipients studied, nine excipients with three different effects (stabilizing, destabilizing, and neutral) were selected to further investigate their effects on the thermal stability of proteins in commercially relevant conditions. These conditions include the presence of Alhydrogel (Brenntag Biosector, Denmark) in the final formulation of RiVax and high protein concentrations (50 to 200 mg/mL) commonly used in formulations of mAbs. For this study, RiVax (at 0.2 mg/mL) was prepared in 10 mM histidine isotonic buffer (pH 6.0) containing 2 mg/mL of Alhydrogel in the absence or presence of excipients. Protein was adsorbed for 2 h at room temperature prior to further analysis. The binding efficiency of RiVax was evaluated by quantifying protein using the Bradford assay (Pierce™ Coomassie Plus Assay Kit, Thermo Scientific, Waltham, MA) after centrifuging down the Alhydrogel. mAb samples at various concentrations (80, 40, 16, 1.6, and 0.2 mg/mL) were prepared in 20 mM citrate phosphate isotonic buffer (pH 6.0) for the thermal stability study. mAb samples at 80 mg/mL in the same buffer containing excipient stock solutions were also prepared. All the protein samples were analyzed on 384-well plates (Hard-Shell 384-well PCR plates, Bio-Rad, Hercules, CA) and silicon oil (ThermoFisher Scientific, Waltham, MA) was added onto sample to avoid evaporation during temperature studies. Sample plates were centrifuged to remove air bubbles if needed.

5.2.3. Instrumentation

The diagram of the fluorescence plate reader which is manufactured by Fluorescence Innovations, Inc. (Minneapolis, MN) used in this study is shown in **Figure 5.1A** (244). It contains four key components: a laser source, a photomultiplier tube (PMT), a charge-coupled device (CCD) spectrometer, and a temperature controlled sample plate holder. The laser source consists of two lasers: a tunable dye laser (280 nm to 305 nm) and a combination laser (350 and 532 nm). The PMT measures the time-resolved fluorescence (TRF), while the CCD records the steady state fluorescence (SSF) from 300 to 450 nm. The temperature controlled sample holder is able to accommodate a 384-well plate. This instrument has two modes: TRF and SSF. The mode can be switched by a mirror referred to here as the "emission mirror". The emission mirror is not used in the TRF mode in which the emitted light goes to the PMT after a band pass filter. When the emission mirror is in place, the emission signal is directed to the CCD for the measurement of SSF.

5.2.4. Steady State and Time Resolved Fluorescence

In the SSF mode, the emission mirror is placed to acquire Trp emission spectra. The excitation laser wavelength was set at 295 nm (> 95% Trp emission). A 310 nm long pass dichroic mirror was used to block excitation light from entering the CCD. Measurements were performed using an integration time of 100 ms. A temperature ramp from 10 to 90 °C with an increment of 2.5 °C per step was used. Samples were equilibrated for 2 min at each temperature at which point the signal stopped changing. The same temperature ramp was also used for the TRF mode.

The TRF mode records fluorescence decay waveforms as previously described (245). The PMT voltage was set at 500 V. The dye laser (at 295 nm) was used for measuring Trp TRF. A 310 nm long pass dichroic mirror and a 360/23 nm band pass filter were used. The combo laser (at 350

nm), a 405 long pass dichroic mirror, and a 485/20 nm band pass filter were used to monitor the TRF derived from the formation of fibrils in high concentration mAb samples upon thermal stress.

5.2.5. Data Analysis

As shown in **Figure 5.1 C1** and **5.D1**, raw data (spectra from SSF and waveforms from TRF) were used to calculate melting temperatures (T_m). The raw data were first processed with in-house Python scripts to derive the following two parameters: intensity and moment at each temperature (**Figure 5.1 C2 and 5.D2**). Intensity represents the peak area under the curve for a spectrum or waveform. Moment is defined as the center of a spectrum or waveform where it vertically divides the peak area under the curve into two halves. The mathematical expressions for these two parameters are shown as follows:

$$\text{Intensity} = \int I(x)dx \tag{1}$$

$$\text{Moment} = \frac{\int I(x)x\,dx}{\int I(x)\,dx} \tag{2}$$

where x is wavelength (SSF) or time (TRF), I(x) is the fluorescence signal. Intensity was integrated from 300 to 400 nm (SSF) or from 10 to 60 ns (TRF). Moment can also be described as mean spectral center of mass in intrinsic tryptophan fluorescence studies as previously described (68, 174). Plotting intensity or moment versus temperature generates a melting curve to describe a thermal unfolding event. Each melting curve was further processed to obtain T_m values employing two commonly used methods: a six parameter fitting (fit) method (**Figure 5.1 C2 and D2**) or a 1st derivative (f'(T)) method (**Figure 5.1 C3 and D3**). The six parameter fit was performed with Matlab (MathWorks, Natick, MA) using the following expressions:

$$\text{Observed signal} = \frac{1}{1+K} * (b_1 + m_1 * (T + 273.15)) + \frac{K}{1+K} * (b_2 + m_2 * (T + 273.15))$$

(3)

$$K = \exp\left(-\frac{\Delta H}{R} * \left(\frac{1}{T+273.15} - \frac{1}{T_m+273.15}\right)\right) \tag{4}$$

where K is the unfolding constant and b_1 and m_1 are the intercept and slope of the native state baseline, respectively. b_2 and m_2 are the intercept and slope of the unfolded state baseline, respectively. T is the temperature in °C and ΔH is the enthalpy of unfolding. R is the ideal gas constant ($1.987\mathrm{e}\text{-}3$ kcalmol^{-1}K^{-1}) and T_m is the melting temperature in °C. For the 1st derivative method, a cubic spline was used to interpolate all points of a melting curve. Intensity or moment were interpolated every 0.01 °C. The temperature at the absolute maximum value was taken as the T_m.

As illustrated in **Figure 5.1B**, both types of fluorescence (SSF vs. TRF) were recorded in the pH screening study. Two parameters (moment and intensity) were calculated from each set of fluorescence data to generate four melting curves in total. Two fitting methods (1st derivative vs. six-parameter fitting) were then applied to each melting curve to calculate T_m. Therefore, eight T_m values can be obtained at most for each sample. The optimal T_m generation method for each protein was selected for the excipient screening study. Eight sets of T_m values can be obtained at most for each sample. The method used to generate the T_m was expressed using an abbreviated nomenclature consisting of the type of fluorescence, the parameter used to measure the melting curve, and the derivation method. For example, "TR_moment_f'(T)" indicates that time resolved fluorescence is performed, moment is plotted as a function of temperature to generate the melting curve, and a 1st derivative method is used to calculate the T_m value.

5.3. Results

5.3.1. pH screening for lysozyme, RiVax and a mAb

The pH dependent thermal stability of three model proteins (lysozyme, RiVax, and a mAb) were investigated using both SSF and TRF. These proteins were analyzed at 0.2 mg/mL in 20 mM citrate phosphate isotonic buffers (pH 3.0 to 8.0). At pH 3.0, RiVax did not show a thermal transition presumably due to the unfolding of RiVax at low pH. This is confirmed by a large red shift in the emission peak position of RiVax at pH 3.0 at 10 °C (data not shown). The other two proteins showed thermal transitions in all pH conditions examined. As shown in **Figure 5.2 A1**, eight T_m values were obtained for the mAb at pH 4.0 to 8.0. For the other samples (the mAb at pH 3.0 or the other proteins under all pH conditions), however, melting curves derived using some parameters did not show a detectable transition and the corresponding T_m values can not be calculated. For example, intensity based melting curves of lysozyme from SSF measurement did not show an observable thermal transition. The order of thermal stability of RiVax (**Figure 5.2 A2**) and lysozyme (**Figure 5.2 A3**) is as follows: pH 6.0 > 5.0 > 7.0 > 8.0 > 4.0 > 3.0 and pH 5.0 > 4.0 > 6.0 > 7.0 > 8.0 > 3.0, respectively. These results are in good agreement with previously published data (237, 243, 246). The mAb at pH 4.0 and 3.0 showed significantly lower thermal stability compared to the other pH conditions. The mAb at pH 5.0 to 8.0 showed similar T_m values. By averaging the T_m generated from all methods, the mAb at pH 6.0 showed the highest T_m value and was therefore selected as the base buffer condition for the following excipient study.

5.3.2. T_m correlation plots

For the same protein sample tested using this fluorescence plate reader, T_m values generated using different methods can be slightly different. For instance, the T_m of RiVax generated using TR_moment_f'(T) is higher than that obtained using TR_intensity_f'(T) (**Figure 5.2 A2**). We therefore studied the dependency of T_m values on each of three factors: the type of fluorescence measurement (SSF vs. TRF), the parameter derived (intensity vs. moment), and the data fitting method (1st derivative vs. six parameter fitting). Three T_m correlation plots for each factor were then constructed (**Figure 5.2 B1-B3**) by varying one factor at a time while keeping the other two factors the same. Lysozyme data are only included in the T_m correlation plot for the data fitting method (**Figure 5.2 B2**) because of its limited T_m data sets. As shown in **Figure 5.2 B1**, the data sit exactly on the Y = X line indicating that the T_m values obtained from SSF and TRF agree. This suggests that TRF may be used as an equivalent alternative to SSF for protein fluorescence screening. A high degree of correlation was again observed for the T_m values obtained by using the six parameter or 1st derivative method (**Figure 5.2 B2**). We found, however, that the 1st derivative procedure seems to be a more sensitive method than the six parameter fit. As shown in **Figure 5.2 A2**, TR_intensity_f'(T) and SS_intensity_f'(T), but not TR_intensity_fit or SS_intensity_fit, generated reliable T_m values. The better sensitivity of the 1st derivative method may be because it is less susceptible to the noisy baseline and is parameter free. Therefore, the 1st derivative method was selected to calculate T_m values in the following excipient screening studies. T_m values generated using moment or intensity, however, are offset from the Y = X line for both RiVax and the mAb (**Figure 5.2 B3**). In the case of RiVax, the moment T_m is significantly higher than the intensity T_m. For the mAb, however, the opposite trend was observed.

5.3.3. Simulation to explain the discrepancy between T_m values by moment versus by intensity

To explain the discrepancy in T_m values generated using the intensity and moment methods, we simulated thermally induced changes of these two parameters as a function of the degree of unfolding (i.e. the percentage loss of native state) during a SSF thermal melt study. Thermal unfolding of proteins usually results in a red shift in Trp emission spectra due to increased exposure of the indole side chains to the polar aqueous solvent. Depending on the relative intensity of the emission spectrum of the unfolded state, three scenarios (I, II and III) are proposed here (**Figure 5.3A**). To simplify the simulation, the intrinsic thermal quenching effect on the fluorescence of native and unfolded state is not considered and a two-state unfolding process is assumed. At any extent of unfolding, the observed emission spectrum is assumed to be a linear combination of both native and unfolded state signals:

$$\text{Observed spectrum } (\lambda, X) = \text{native spectrum } (\lambda) * (1\text{-}X) + \text{unfolding spectrum } (\lambda) * X$$

$$(5)$$

where X is the degree of unfolding and λ is wavelength. The moment and intensity are calculated from the observed emission spectrum and are then plotted as a function of degree of unfolding (**Figure 5.3B-5.3D**). The corresponding temperature for each degree of unfolding is calculated using the Van't Hoff equation (equation (4)) to plot melting curves (**Figure 5.3B-5.3D Inset**). For case I, the unfolded state shows increased intensity compared to the native state. As illustrated in **Figure 5.3B**, intensity is found to be linearly proportional to the degree of unfolding. The 50% intensity alteration point (indicated by red dots) corresponds to a degree of unfolding of 50% and a "true" T_m of 72 °C. Moment, however, shows a concave down relationship with the degree of unfolding. At the 50% moment alteration point, the degree of unfolding is only 21% resulting in an "erroneous" T_m with a lower value (~70 °C). The thermally unfolded state of the mAb falls under case I and therefore shows a moment T_m lower than the intensity T_m (**Figure 5.2 B3**). In the

case of scenario III, an opposite trend is observed in which the unfolded state has a lower intensity than the native state. Intensity and moment show a linear and concave up dependency with the degree of unfolding, respectively, causing the moment T_m to be higher than the intensity T_m. This scenario applies to RiVax. Scenario II is an extreme case where the unfolded state has the same intensity as the native state. The intensity remains constant through thermal unfolding making it an uninformative parameter with which to monitor thermal unfolding. The moment under such circumstance has a linear relationship with the degree of unfolding and therefore can be used to obtain the "true" T_m. These guidelines will also apply to explain the differences of T_m values observed in the TRF mode. In summary, the parameter with a linear dependence on the degree of unfolding should be used to generate the accurate T_m values. Intensity is such one type of parameter and should be preferred over moment to derive a T_m. Therefore, intensity is selected for the mAb for the following excipient screening studies. In the extreme case II, moment, but not intensity, can be used to derive the true T_m. RiVax showed only a very weak transition when monitored by intensity, causing difficulty in deriving the T_m using intensity (Supplemental **Figure 5.S1**). This, in fact, suggests that the fluorescence of unfolded RiVax is only slightly different than its native state, indicating moment is nearly linear with the degree of unfolding. In addition, moment derived melting curves should result in T_m values with better reproducibility for RiVax compared to intensity derived ones because moment melting curves show a more pronounced transition with a better sensitivity and are less effected by spectral noise. Therefore, it seems reasonable to use the moment instead of intensity for RiVax during the excipient screening study.

5.3.4. Excipient screening for RiVax and the mAb at 0.2 mg/mL in solution

The mAb and RiVax were further subjected to an excipient screening study. Lysozyme was not examined due to its high intrinsic stability. An isotonic buffer of 20 mM citrate phosphate

at pH 6.0 was chosen for this study because both proteins showed the highest thermal stability in this buffer based on the pH screening study described above. The stabilization or destabilization effects of excipients are indicated by the change in T_m (ΔT_m) of the protein in their presence. A positive ΔT_m generally indicates an increase in protein thermal stability. Based on the study performed above, we selected SS_intensity_f'(T) and SS_moment_f'(T) to generate T_m values for the mAb and RiVax, respectively. As shown in **Figure 5.4**, most osmolytes tested (1 M sucrose, 1 M sorbitol, 0.375 M trehalose) were found to be stabilizers for both proteins probably due to preferential exclusion effects (247). The addition of glycerol (25%, v/v) resulted an increase in RiVax T_m, but had no significant effect on the mAb. An approximately 4 °C increase in T_m was observed for the mAb in the presence of 0.5 M sodium sulfate, which had negligible effects on RiVax. Most amino acid excipients did not show dramatic effects on both proteins except arginine chloride, which decreased the T_m values by 3 and 10 °C for the mAb and RiVax, respectively. The destabilizing excipients for both proteins include chaotropes (e.g. 250 mM urea, 250 mM guanidine HCl, 250 mM KSCN), cyclodextrins and polymers (e.t. PEG, PVP etc.). The mechanisms responsible for the destabilizing effects of these excipients have been discussed previously (247, 248).

5.3.5. Excipient screening of RiVax with/without Alhydrogel

RiVax, as a subunit vaccine candidate, is formulated with adjuvants (e.g. Alhydrogel) to enhance its immunogenicity. In this study, a base buffer of 10 mM histidine isotonic buffer (pH 6.0) was used to avoid the use of phosphate buffers, which could significantly reduce the binding of RiVax to Alhydrogel (AlOH). The thermal stability of RiVax (at 0.2 mg/mL) in the absence or presence of AlOH (2 mg/mL) was studied and the effects of excipients on RiVax under these two conditions were studied. Based on the initial excipient study (**Figure 5.4**), nine agents were tested

to illustrate an array of effects. The excipients were classified into three categories: stabilizing, destabilizing, and neutral. Accordingly, the melting curves for each type of excipient were plotted together. All excipients showed a similar effect on the thermal stability of RiVax in histidine-containing solution compared to the study performed in 20 mM citrate phosphate buffer (pH 6.0). Similar to the results of Peek and coworkers (249), we found that RiVax adsorbed to AlOH had significantly lower thermal stability, reflected by a decrease in T_m or an increase of the moment peak position at 10 °C or a combination of both (**Figure 5.5**). For instance, RiVax in the base buffer adsorbed to AlOH had a decrease of about 17 °C in T_m and an increase of almost 2 nm in moment peak positon. This indicates that the perturbed tertiary structure of RiVax on the surface of AlOH is associated with a dramatic decrease in its thermal stability. All three stabilizers (sucrose, glycerol, and glycine) decreased the initial moment peak position of RiVax in the presence of AlOH to a level equivalent to the folded state and increased the T_m, but less than the T_m increase of RiVax in the His buffer (**Figure 5.5 A1**). This indicates that these compounds are able to stabilize the tertiary structure of adsorbed RiVax but fail to fully rescue its solution stabilization. **Figure 5.5 A2** also shows that some excipients do not produce significant effects on the thermal stability or tertiary structure of RiVax in both the absence or presence of AlOH. **Figure 5.5 A3** shows that RiVax adsorbed onto AlOH in the presence of destabilizers did not show any thermal transitions and had an increased moment peak position at 10 °C, suggesting an unfolded state. This indicates an extensive loss of protein tertiary structure. The binding of RiVax to AlOH in these experiments was tested by quantifying RiVax in the supernatant after centrifugation. As shown in **Figure 5.5 B1**, all excipients except the stabilizers (sucrose, glycerol, and glycine) produced complete adsorption onto AlOH. The three stabilizers significantly reduced the amount of RiVax bound to AlOH by 4-14%. This suggests that these stabilizers may thermally stabilize adsorbed

RiVax by weakening their interactions with AlOH, which destabilizes the tertiary structure of RiVax. The addition of 0.05% PS 80 only slightly destabilized RiVax, but it was completely unfolded when absorbed to AlOH (**Figure 5.5 B2** and **B3**). The increase in the initial moment peak position somewhat correlates with the decrease in the T_m. In solution, sucrose (0.5 M) and glycerol (12.5%) show better stabilization effects on RiVax than glycine (250 mM). However, when adsorbed to RiVax, glycine (250 mM) is a better stabilizer than sucrose (0.5 M) and glycerol (12.5%). These results suggest a large discrepancy between the effects on excipients on RiVax in His buffer and that in adjuvanted solutions.

5.3.6. Excipient screening of the mAb at 0.2 mg/mL and 80 mg/mL

Excipient screening studies for mAbs are routinely performed at low concentration (e.g. 0.1 – 1.0 mg/mL) due to limited protein quantity and ease of analysis, while actual commercial drug products often contain mAbs at very high concentration (50 to 200 mg/mL). The thermal stability of mAbs has been previously shown to be dependent on protein concentration (240). The dependency of T_m on protein concentration (0.2 to 80 mg/mL) in 20 mM citrate phosphate isotonic buffer (pH 6.0) was investigated here. **Figure 5.6 A** shows that the T_m values of the mAb gradually decrease as the mAb concentration increases and the effect is more pronounced at lower protein concentrations. We then studied if excipients affect the thermal stability of the mAb at high or low concentrations differently. Thus, their effects on T_m (ΔT_m) of the mAb at 0.2 mg/mL or 80 mg/mL were further studied using Trp intrinsic fluorescence. As shown in **Figure 5.6 B**, 0.05% (v/v) PS 80 and 60 mM histidine did not produce major effects on the T_m at 0.2 or 80 mg/mL. The other excipients resulted in a significantly larger ΔT_m value at 80 mg/mL compared to the mAb at 0.2 mg/mL. For example, 1 M sucrose had an enhanced stabilization effect on the mAb at 80 mg/mL. Glycerol (25%, v/v) did not thermally stabilize the mAb at 0.2 mg/mL, but improved the T_m of the

mAb at 80 mg/mL by over 2 °C. Urea (at 250 mM) decreases the T_m of the mAb at 0.2 mg/mL by about 2 °C but did not result in detectable destabilization effects at 80 mg/mL. A similar result was observed for 1.5% (w/v) PEG 3350. The destabilization effects of 135 mM arginine and 250 mM guanidine HCl were significantly less at 80 mg/mL in contrast to their effects on the mAb at 0.2 mg/mL. Therefore, it is clear that the excipient screening results (reflected by ΔT_m) obtained using the mAb at 0.2 mg/mL sometimes fail to predict the results at 80 mg/mL.

Previous studies have reported that formation of fibrils by several proteins upon stress (e.g. elevated temperature) produced a characteristic fluorescence (ex: 355 nm and em max: 470 nm) (250-252). The mAb used in this study has been found to form fibrils at elevated temperature driven by the formation of intermolecular β sheet (242). We here tested the feasibility of studying the formation of fibrils by monitoring this florescence. We monitored this fluorescence using TRF using an excitation of 350 nm and emission of 485 ± 20 nm. During thermal unfolding, an increase in the intensity of such fluorescence was observed for the mAb at 80 mg/mL (Supplemental **Figure 5.S2**), but not at 0.2 mg/mL (data not shown), probably due to the relatively low quantum yield of the fibril fluorescence. The T_m values calculated using the 1st derivative method from the fibril fluorescence of the mAb at 80 mg/mL showed a good correlation between the data from the Trp fluorescence study. This suggests the potential use of this method as a formulation monitor to measure the aggregation of high concentration mAbs.

5.4. Discussion

In the present study, a high-throughput platform for the optimization of protein pharmaceutical formulations based on intrinsic fluorescence is described. It employed both TR

and SS modes. Three model proteins (lysozyme, mAb, and RiVax) were tested to investigate the feasibility of using this platform for formulation development. These three proteins in a selected standard condition (0.2 mg/ml in clear solution) were first subjected to a pH screening study to identify optimal buffer conditions. Various T_m generation methods were employed to calculate the T_m. Accordingly, an optimal generation method was selected for an excipient screening study. The mAb and RiVax were further subjected to excipient studies under both standard and pharmaceutically relevant conditions. The results show significant discrepancy in the excipient screening data (reflected by ΔT_m) of proteins studied under the simplified reference condition versus more commercially relevant conditions.

In the pH screening study, T_m values of each model protein generated using various methods overall show a similar trend across all pH conditions tested. A more detailed analysis of the dependency of T_m on these generation methods suggests that the type of fluorescence used (TR versus SS fluorescence) and the data fitting method (1st derivative versus six-parameter fit) do not significantly affect the final T_m values. The parameter selected to monitor protein thermal unfolding (intensity versus moment), however, has a significant impact on T_m values. We attempted to explain these results by simulating the correlation between changes in the parameter signal and the degree of protein unfolding. The simulation study suggests that, in most cases, fluorescence intensity is able to reflect the degree of unfolding in a linearly proportional manner, making the T_m derived from intensity a "true" value. Moment, however, is not linearly dependent on the degree of unfolding in most cases and therefore often results in a "false" T_m value. Similar work by Žoldák *et al.* suggested fluorescent intensity ratio, a commonly used parameter, does not generate reliable T_m value because it is not linearly proportional to the population of macrostates (253).

The advantages of this high-throughput platform are better manifested in the excipient screening study. This technique is based on the intrinsic fluorescence of tryptophan in protein molecules. It is therefore label-free and potential interfering extrinsic probes can be avoided. Secondly, sample consumption is minor. It requires only 10 μl of sample at 0.2 mg/mL (i.e. 2 μg) per well, which means less than 1 mg of protein is needed even if all 384 wells are used. Third, a standard thermal scanning of a 384 well plate only takes 4 to 5 h using the thermal ramp described in the methods section. Finally, the front-face geometry between the sample plate and detection makes it possible to study samples under challenging conditions such as high concentration and highly scattering conditions.

This fluorescence platform was further applied to study the effects of several selected excipients on RiVax and a mAb under difficult formulation conditions. In the case of RiVax, the protein was first adsorbed to AlOH (forming a turbid solution) and excipient effects on protein tertiary structures and melting temperature were studied. A previous study has employed extrinsic fluorescence for the high-throughput formulation screening of aluminum adjuvanted vaccines (254). However, common detergents such as Triton X100, poloxamers, and PS80 cannot be tested because they produce excessive background signals which seriously interference with measurements or may themselves interact with excipients. In contrast, with this intrinsic fluorescence based high-throughput platform, such detergents can be tested. We were also able to observe stabilization effects of sucrose, glycerol, and glycine on AlOH adsorbed RiVax. Our findings are in good agreement with previous work, which observed a decreased thermal stability of RiVax when adsorbed to AlOH and found that such destabilizing effects were only partially diminished by the addition of 15% glycerol. We also observed that these stabilizers reduced the binding efficiency of RiVax to AlOH. It is possible that these excipients partially stabilize

adsorbed RiVax by decreasing the binding affinity of RiVax to AlOH. Possible mechanisms include: 1) a preferential exclusion effect, which prevents the increase in the exposed surface area induced by protein adsorption to AlOH and 2) a competitive binding effect between excipients and RiVax to AlOH (255). It is critical to study the thermal stability of adsorbed antigen to optimize formulations and to better understand the *in vivo* stability of such proteins. The use of a large quantity of stabilizer (1M sucrose, 25% glycerol, or 250 mM glycine) only increased the T_m of adsorbed RiVax to near physiological temperature (37 °C). Upon vaccination, due to the loss of stabilizing effects of these excipients, adsorbed RiVax may adopt an altered tertiary structure at 37 °C. This may partially explain the unsatisfactory immunogenicity of RiVax even when adsorbed to AlOH (256). It would be interesting to study the dissociation and structural behavior of adsorbed RiVax and other protein antigens when exposed to physiological environments to better understand effects on immunogenicity.

In the case of the mAb, excipient effects on high concentration mAb were investigated. The requirement for a sample volume as low as 10 µl facilitates such excipient screening. Thus, for a mAb at 100 mg/mL, only 1 mg of protein is required for each excipient condition. The sample volume can be potentially further reduced if needed. The effects of excipients on the thermal stability of the mAb examined here are quite distinctive. Osmolytes (e.g. 1 M sucrose and 25% glycerol) show a better stabilization effect on the mAb (at 80 mg/mL) than the more dilute mAb (at 0.2 mg/mL), especially for 25% glycerol, which did not thermally stabilize the mAb (at 0.2 mg/mL). This discrepancy is probably due to a more pronounced preferential exclusion effect for high concentrations of the mAb. On the other hand, the destabilizers become less effective for the high concentration mAb possibly because of a decreased destabilizer/protein molar ratio. In addition, the good agreement between T_m values obtained using fibril fluorescence and those

generated using Trp fluorescence shows that the formation of fibrils is concurrent with the unfolding of the protein. In other words, the kinetics of fibril formation may be much faster than the unfolding process, suggesting the unfolding process may be the rate-limiting step. The implementation of fibril fluorescence for studies of mAbs could provide the following insights: 1) the formation of fibril as an alternative to look at the aggregation behavior of mAb; and 2) a better understanding of the kinetic processes of thermal unfolding and aggregation of mAbs.

This study establishes a general workflow based on protein intrinsic fluorescence for direct optimization of protein formulations. Key steps involve a pH screening study, selection of a parameter for monitoring thermal unfolding, and a final excipient screening study. This work highlights the importance of performing the excipient screening under pharmaceutically relevant conditions (e.g. high protein concentration formulation or adjuvanted formulation with high turbidity).

5.5. References

1. Dill KA. 1990. Dominant forces in protein folding. Biochemistry. 29(31):7133-7155.

2. Shire SJ, Shahrokh Z, Liu J. 2004. Challenges in the development of high protein concentration formulations. J Pharm Sci. 93(6):1390-1402.

3. Peek LJ, Brey RN, Middaugh CR. 2007. A rapid, three-step process for the preformulation of a recombinant ricin toxin a-chain vaccine. J Pharm Sci. 96(1):44-60.

4. Peek LJ, Martin TT, Elk Nation C, Pegram SA, Middaugh CR. 2007. Effects of stabilizers on the destabilization of proteins upon adsorption to aluminum salt adjuvants. J Pharm Sci. 96(3):547-557.

5. Jones LS, Peek LJ, Power J, Markham A, Yazzie B, Middaugh CR. 2005. Effects of adsorption to aluminum salt adjuvants on the structure and stability of model protein antigens. Journal of Biological Chemistry. 280(14):13406-13414.

6. Harn N, Allan C, Oliver C, Middaugh C. 2007. Highly concentrated monoclonal antibody solutions: Direct analysis of physical structure and thermal stability. J Pharm Sci. 96(3):532-546.

7. Wahome N, Sully E, Singer C, Thomas JC, Hu L, Joshi SB, Volkin DB, Fang J, Karanicolas J, Jacobs DJ. 2016. Novel ricin subunit antigens with enhanced capacity to elicit toxin-neutralizing antibody responses in mice. J Pharm Sci. 105(5):1603-1613.

8. Telikepalli SN, Kumru OS, Kalonia C, Esfandiary R, Joshi SB, Middaugh CR, Volkin DB. 2014. Structural characterization of igg1 mab aggregates and particles generated under various stress conditions. J Pharm Sci. 103(3):796-809.

9. Kalonia C, Toprani V, Toth R, Wahome N, Gabel I, Middaugh CR, Volkin DB. 2016. Effects of protein conformation, apparent solubility, and protein–protein interactions on the rates

and mechanisms of aggregation for an igg1monoclonal antibody. J Phys Chem B. 120(29):7062-7075.

10. Schaaf TM, Peterson KC, Grant BD, Bawaskar P, Yuen S, Li J, Muretta JM, Gillispie GD, Thomas DD. 2017. High-throughput spectral and lifetime-based fret screening in living cells to identify small-molecule effectors of serca. SLAS DISCOVERY: Advancing Life Sciences R&D. 22(3):262-273.

11. Gruber SJ, Cornea RL, Li J, Peterson KC, Schaaf TM, Gillispie GD, Dahl R, Zsebo KM, Robia SL, Thomas DD. 2014. Discovery of enzyme modulators via high-throughput time-resolved fret in living cells. Journal of biomolecular screening. 19(2):215-222.

12. Wei Y, Wahome N, VanSlyke G, Whitaker N, Kumar P, Barta ML, Picking WL, Volkin DB, Mantis NJ, Middaugh CR. 2017. Evaluation of lumazine synthase from bacillus anthracis as a presentation platform for polyvalent antigen display. Protein Sci.

13. Wei Y, Wahome N, Kumar P, Whitaker N, Picking WL, Middaugh CR. 2017. Effect of phosphate ion on the structure of lumazine synthase, an antigen presentation system from bacillus anthracis. J Pharm Sci.

14. Blumlein A, McManus JJ. 2013. Reversible and non-reversible thermal denaturation of lysozyme with varying ph at low ionic strength. Biochimica et Biophysica Acta (BBA)-Proteins and Proteomics. 1834(10):2064-2070.

15. Kamerzell TJ, Esfandiary R, Joshi SB, Middaugh CR, Volkin DB. 2011. Protein–excipient interactions: Mechanisms and biophysical characterization applied to protein formulation development. Advanced drug delivery reviews. 63(13):1118-1159.

16. Ohtake S, Kita Y, Arakawa T. 2011. Interactions of formulation excipients with proteins in solution and in the dried state. Advanced drug delivery reviews. 63(13):1053-1073.

17. Peek LJ, Martin TT, Elk Nation C, Pegram SA, Middaugh CR. Effects of stabilizers on the destabilization of proteins upon adsorption to aluminum salt adjuvants. J Pharm Sci. 96(3):547-557.

18. Pinotsi D, Buell AK, Dobson CM, Kaminski Schierle GS, Kaminski CF. 2013. A label-free, quantitative assay of amyloid fibril growth based on intrinsic fluorescence. ChemBioChem. 14(7):846-850.

19. Pinotsi D, Grisanti L, Mahou P, Gebauer R, Kaminski CF, Hassanali A, Kaminski Schierle GS. 2016. Proton transfer and structure-specific fluorescence in hydrogen bond-rich protein structures. Journal of the American Chemical Society. 138(9):3046-3057.

20. Bhattacharya A, Bhowmik S, Singh AK, Kodgire P, Das AK, Mukherjee TK. 2017. Direct evidence of intrinsic blue fluorescence from oligomeric interfaces of human serum albumin. Langmuir. 33(40):10606-10615.

21. Žoldák G, Jancura D, Sedlák E. 2017. The fluorescence intensities ratio is not a reliable parameter for evaluation of protein unfolding transitions. Protein Science. 26(6):1236-1239.

22. Ausar SF, Chan J, Hoque W, James O, Jayasundara K, Harper K. 2011. Application of extrinsic fluorescence spectroscopy for the high throughput formulation screening of aluminum-adjuvanted vaccines. J Pharm Sci. 100(2):431-440.

23. Singh K, Mohan S. 2004. Adsorption behavior of selected monosaccharides onto an alumina interface. Journal of colloid and interface science. 270(1):21-28.

24. Vitetta ES, Smallshaw JE, Schindler J. 2012. Pilot phase ib clinical trial of an alhydrogel-adsorbed recombinant ricin vaccine. Clinical and Vaccine Immunology. 19(10):1697-1699.
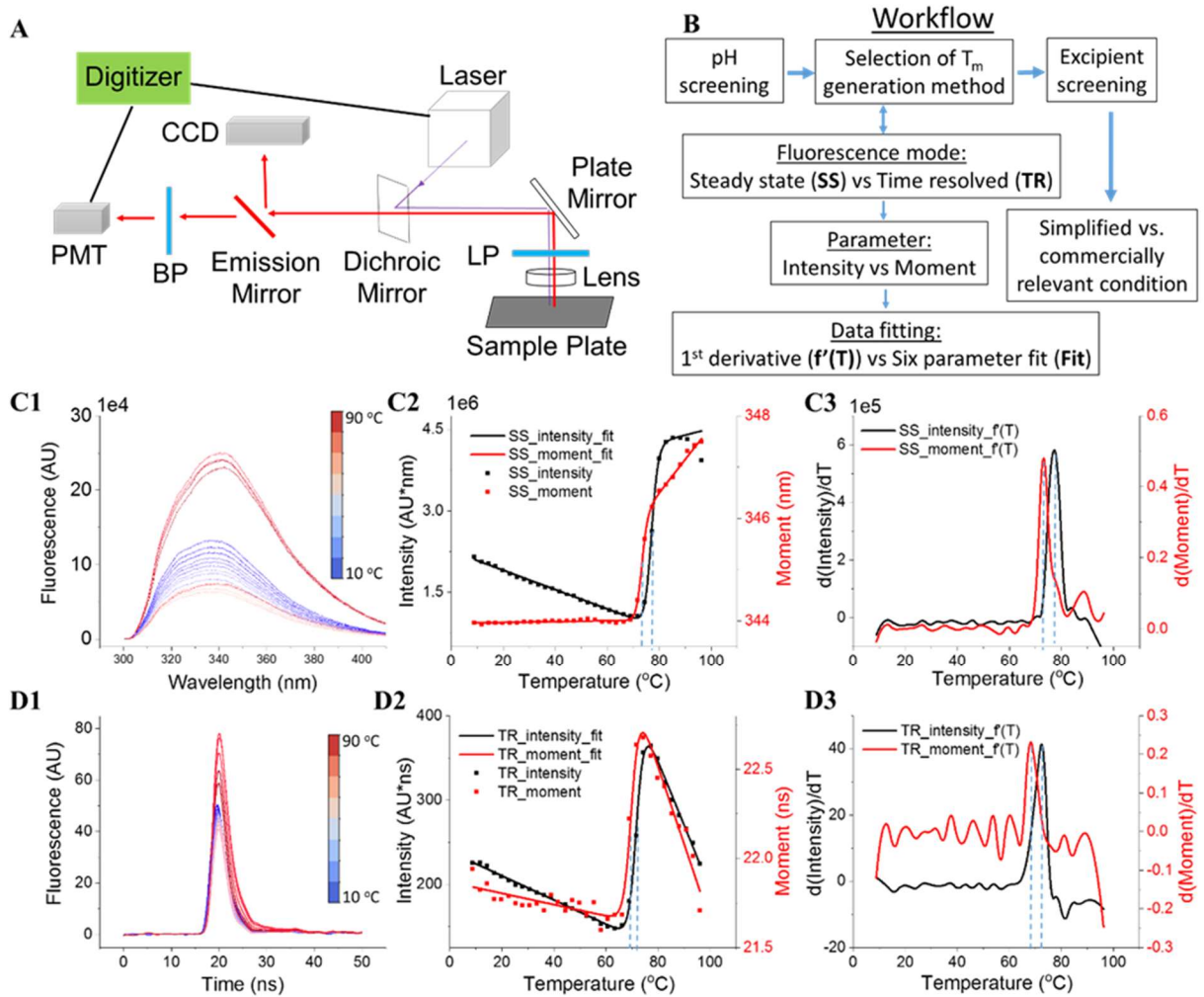
5.6. Figures

Figure 5.1. (**A**) A schematic diagram of the high throughput fluorescence plate reader. This instrument is capable of recording both time resolved and steady state fluorescence. An emission mirror is placed to direct the emission signal to a CCD detector for the measurement of steady state fluorescence. Otherwise, the time resolved fluorescence signal is recorded by a PMT. (Modified from Schaaf (244)) (**B**) A general workflow for the formulation optimization of proteins using this fluorescence plate reader. Thermal melting study of protein samples using intrinsic steady-state fluorescence (**C1-C3**) or time-resolved fluorescence (**D1-D3**). Representative temperature dependent raw fluorescence spectra (**C1**) of samples; processed melting curves

monitored by moment (red dot) or intensity (black dot). Fitted melting curves using six parameter fitting method are shown as continuous line (**C2**); Calculation of melting temperature (T_m) using first derivative (**C3**). Representative temperature dependent raw waveform (**D1**) of samples; processed melting curves monitored by moment (red dot) or intensity (black dot). Fitted melting curves using six parameter fitting method are shown as continuous line (**D2**); further calculation of melting temperature (T_m) using first derivative (**D3**). The dashed lines indicate T_m.
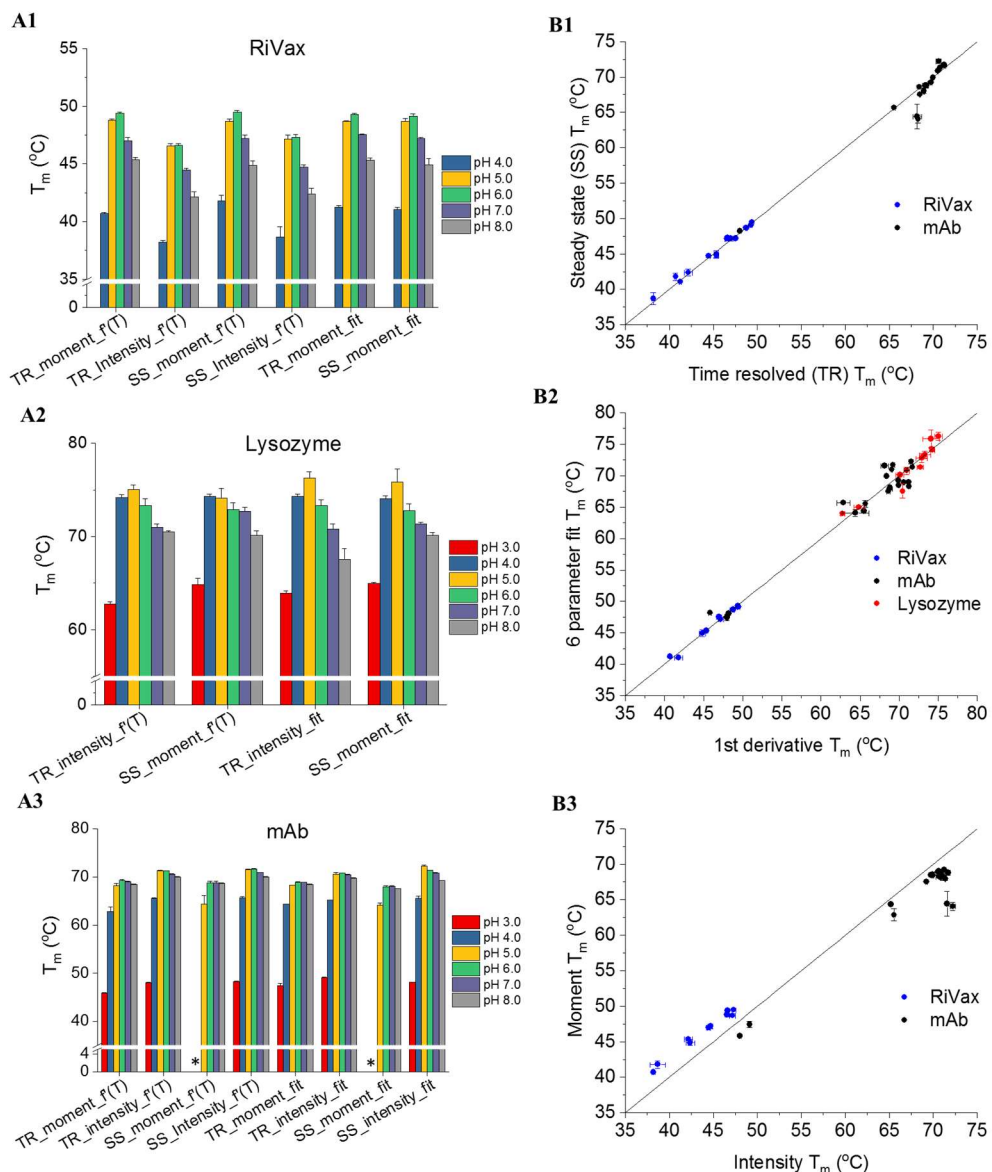
Figure 5.2. pH screening for RiVax, lysozyme, and mAb using Trp fluorescence (A) and comparison of T_m values obtained from different methods (B). Summary of pH dependent melting temperatures (T_m) of RiVax (A1), lysozyme (A2), and the mAb (A3) in citrate-phosphate buffers pH 3.0 to 8.0. The correlation plots of melting temperatures (T_ms) obtained using steady-state fluorescence versus time-resolved fluorescence (B1), six-parameter fit versus first derivative method (B2), and intensity versus mean spectra mass (B3). The straight lines (Y = X) in B1-B3

are added for visual guidance. * indicates that no obvious thermal transition was observed. Error bars indicate standard deviations (N=3).
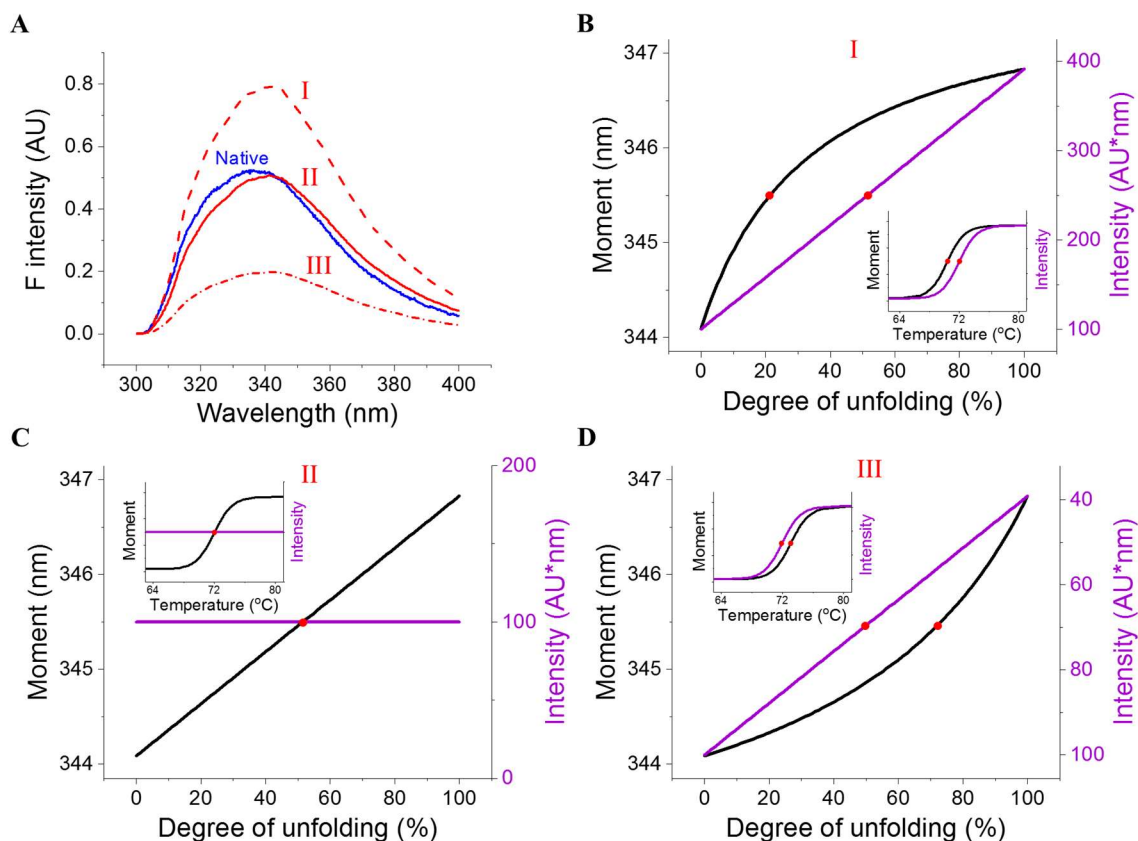

Figure 5.3. Simulation of thermal unfolding monitored by moment and intensity of steady state fluorescence. (A) Spectra of native and unfolded states. Three cases (I, II, and III) are proposed to describe different scenarios of fluorescence of the unfolded state depending on the relative fluorescence intensity to its native state. Case I, II, and III have unfolded states with higher, lower, and the same fluorescence intensities in contrast to the native state, respectively. Correlation plots of moment or intensity with the degree of unfolding and melting curves (shown in inset) for case I (**B**), II (**C**), and III (**D**). The simulated thermal transitions are performed using a "true" T_m of 72 °C and ΔH_{vH} of 200 kcal/mol.
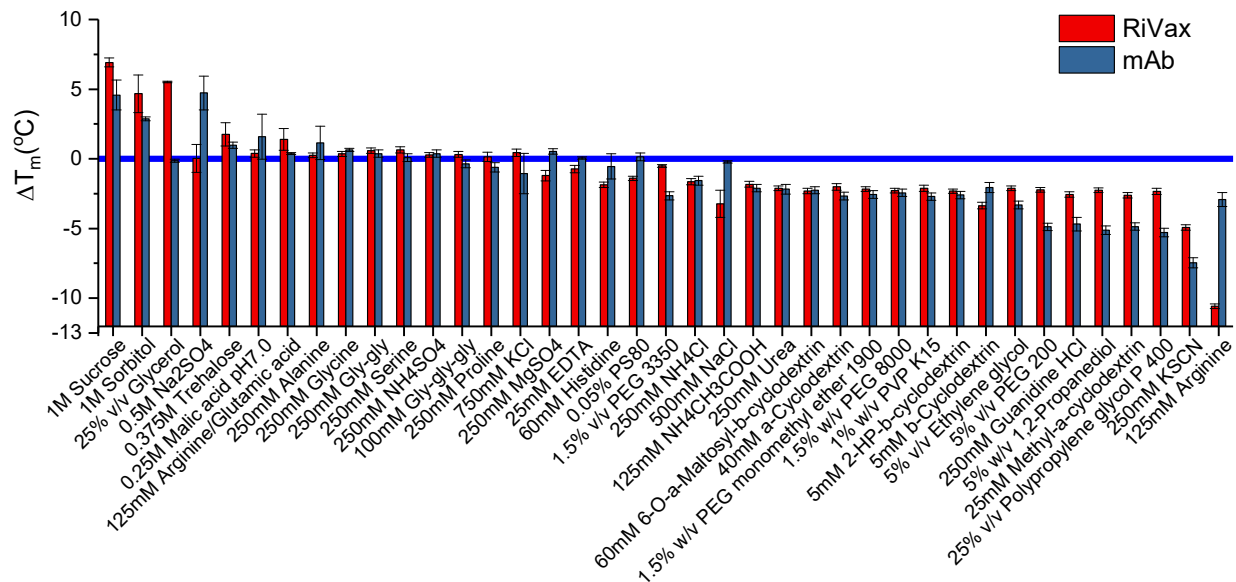
Figure 5.4. Excipient screening study for RiVax and the mAb (at 0.2 mg/mL) in 20 mM citrate-phosphate isotonic buffer pH 6.0 using Trp fluorescence. The stabilization or destabilization effects of excipients are indicated by the change in the T_m (ΔT_m) of the protein in the presence of excipients. A reference line at no change in the T_m ($\Delta T_m = 0$ °C) is shown. Error bars indicate standard deviations (N=3).
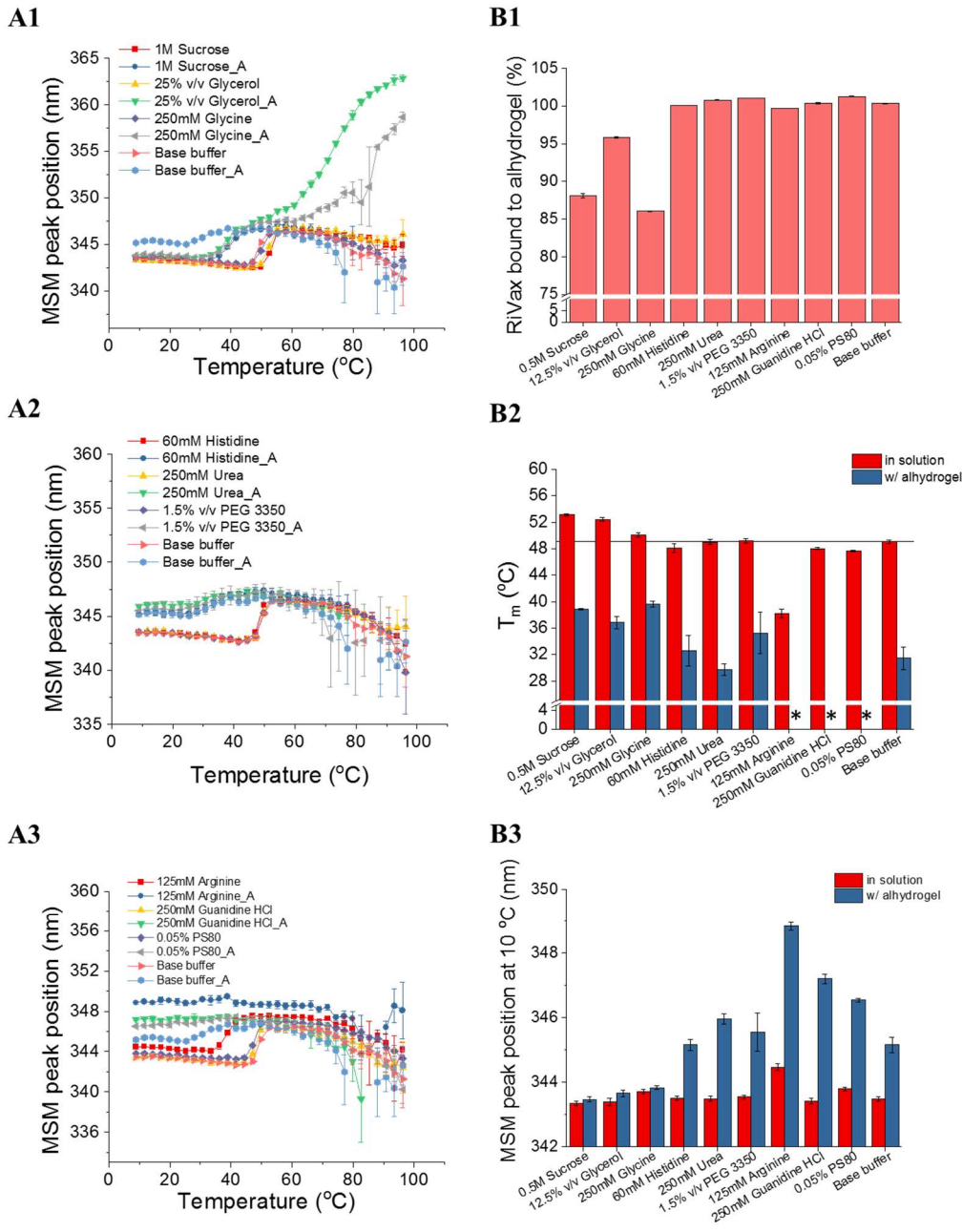
Figure 5.5. Comparison of the effects of excipients on the thermal stability of RiVax in histidine 20 mM isotonic buffer pH 6.0 in the absence or presence of 2 mg/mL Alhydrogel. Thermal melting curves of RiVax in the absence or presence of Alhydrogel (A1-A3). In total, ten excipients were tested. According to their effects on the thermal stability of RiVax in the presence or absence of Alhydrogel, they are classified into three groups: stabilizer (A1), excipient showing no significant

effect (A2), and destabilizer (A3). Melting curves for RiVax in base buffer were included in each figure for comparison. The effects of excipients on the binding of RiVax to Alhydrogel (B1); Comparison of the impact of excipients on T_m values of RiVax in the presence or absence of Alhydrogel (B2). The reference line at 49 $^{\circ}$C corresponds the T_m of RiVax in 20 mM histidine isotonic buffer pH 6.0. Comparison of the impact of excipients on MSM peak positions of RiVax at 10 $^{\circ}$C in the presence or absence of Alhydrogel (B3). * indicates that no obvious thermal transition was observed. Error bars indicate standard deviations (N=3).
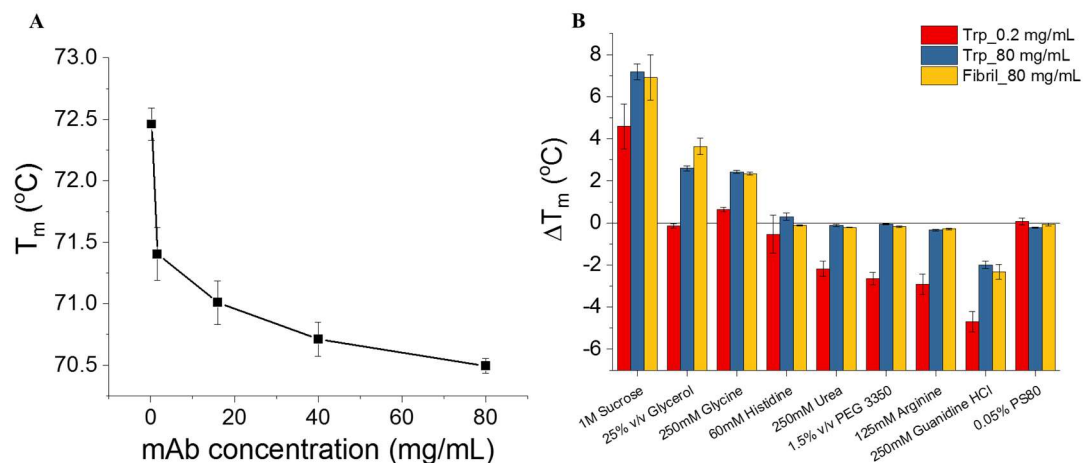
Figure 5.6. Excipient screening of the mAb at 80 mg/mL in 20 mM citrate phosphate isotonic buffer using Trp intrinsic fluorescence and fibril intrinsic fluorescence. (A) Concentration dependent T_m values. (B) Comparison of the effect of excipients on T_m values of the mAb at 0.2 mg/mL (analyzed using Trp fluorescence) or 80 mg/mL (analyzed using Trp fluorescence and fibril fluorescence). Error bars indicate standard deviations (N=3).
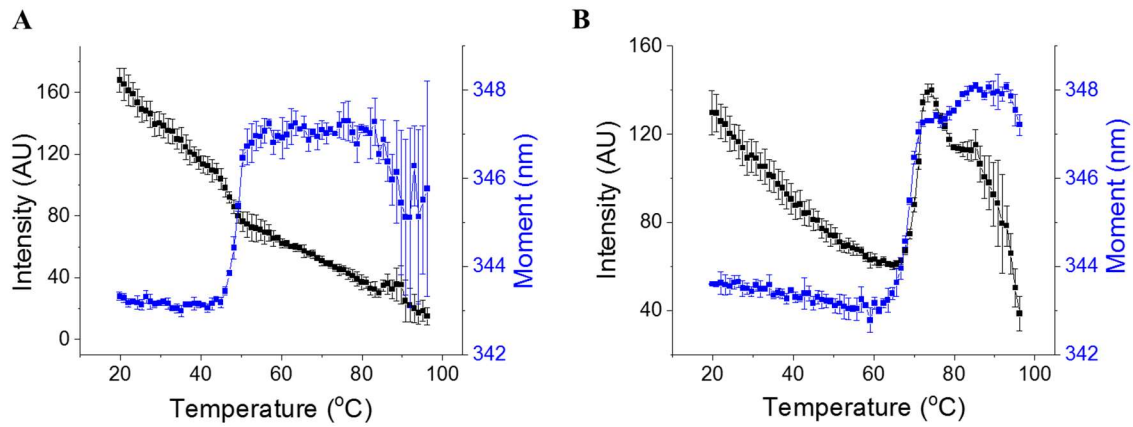
Supplemental Figure 5.S1. Melting curves of RiVax (**A**) and the mAb (**B**) in 20 mM citrate phosphate buffer isotonic buffer pH 6.0 monitored by moment or intensity from steady state fluorescence measurement. Error bars indicate standard deviations (N=3).
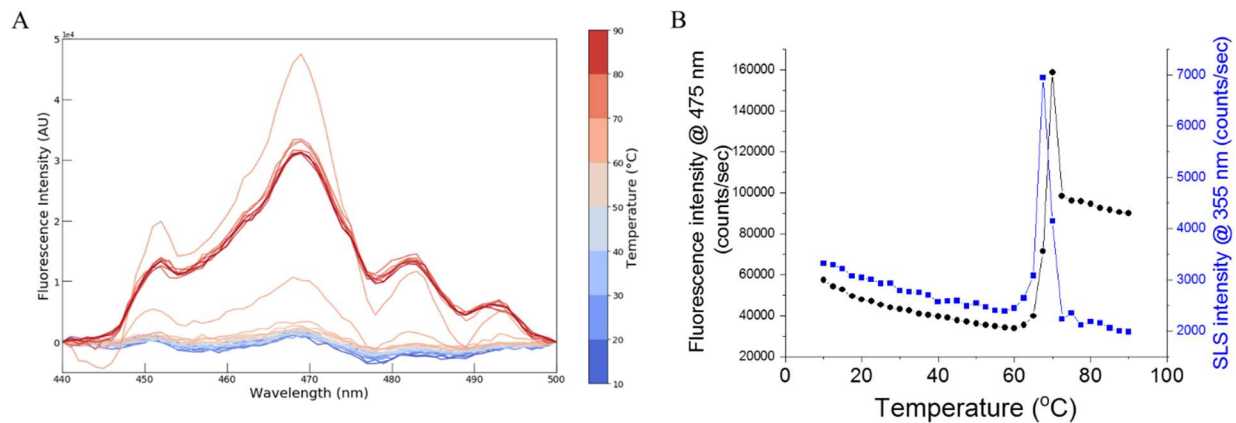
Supplemental Figure 5.S2. Thermal melting of the mAb at 80 mg/mL in 20mM citrate phosphate isotonic buffer recorded using fluorescence and light scattering. The emission spectra of fibril excited at 355 nm (A); Melting curves monitored using fluorescence and static light scattering at 355 nm (B).

Chapter 6: Conclusions and Future Directions

6.1. Overview

Subunit vaccines are highly defined components of a pathogen that can elicit host immune responses against the pathogen (257). Compared to other vaccine types (e.g. live attenuated, killed), subunit vaccines are potentially much safer for human use and therefore often a preferable form. Its improved safety profile, however, comes at a price. One of the biggest challenges subunit vaccines are facing is their relatively low immunogenicity due to two primary reasons: 1) their monovalent nature and 2) the lack of immunostimulatory molecules, which are present in the other vaccine types. The corresponding strategies to overcome these two issues are polyvalent antigen display and the use of adjuvants, respectively.

Polyvalent antigen display enhances the antigen immunogenicity by enabling the "avidity" interaction between a polyvalent antigen with B-cell receptors (BCRs) (121). A B-cell contains on its surface numerous BCRs, bivalent transmembrane immunoglobulin molecules. The function of the BCRs is to recognize and bind to an antigen's B-cell epitope, which eventually activates the B-cell. A monovalent antigen can only bind to a single binding site of a BCR. Since polyvalent antigens display multiple copies of the same types of epitopes in an ordered manner, it is able to bind to more than one BCR simultaneously. This polyvalent binding event, also referred as "crosslinking", creates a much more stable BCR-antigen complex and induces stronger downstream immune responses than monovalent binding. This strategy can be applied to augment the immunogenicity of monovalent antigens by simply clustering them on a nanoparticle scaffold system. A common approach is to genetically fuse the antigen of interest to a self-assembling protein scaffold such that antigens can be polyvalently presented upon correct assembly of the scaffold. Several self-assembling proteins have shown great potentials as vaccine presentation scaffolds. In this thesis, we investigated the feasibility of a polymeric bacterial protein called

lumazine synthase (LS) for polyvalent antigen display (258). LS consists of 60 subunits and forms an icosahedral structure with a size around 16 nm. Therefore, it can accommodate up to 60 copies of foreign antigens on its N or C terminus.

The use of adjuvants is another effective strategy to improve the immunogenicity of subunit vaccines. Commonly used adjuvants include aluminum salts, emulsions, MPLA, etc. A suitable adjuvant is selected depending on which type of immune responses (Th1 and/or Th2) is required for the efficacy of co-administered antigens. Adjuvants can potentially interact with antigen molecules in solution by different mechanisms. The effects of such interaction forces on the stability of both antigen and adjuvants (i.e. antigen-adjuvant compatibility) need to be rigorously characterized before a rational dosage form can be proposed. If they are compatible with each other over the period of storage, they can be stored in a single vial for the purpose of saving storage cost and the ease of administration. Otherwise, they should be stored separately and mixed together immediately before administration. Emulsion-based adjuvants for human use are generally oil-in-water emulsions. They often use squalene as the oil phase, which provides a hydrophobic interface for adsorption of antigens with hydrophobic patches. Emulsions are heterogeneous systems containing several other components, e.g. surfactants and antioxidants, which may also interact with antigens. As a part of this thesis, we utilized a variety of biophysical tools to study the effects of two emulsion-based adjuvants on the structure and stability of a mutant of the α-toxin from *S. aureus*, a promising vaccine candidate against antibiotic-resistant *S. aureus* infection.

Since biologics in solution are subject to both physical and chemical degradations, optimization of protein formulations is critical to ensure their storage stability. The goal of liquid protein formulation screening is to identify solution conditions (pH, salts, and excipients) that provide the maximal protein stability. To screen formulations in a timely manner, we study

protective effects of a diverse array of formulation conditions on the stability of a protein exposed to one or more stressed conditions often in a high-throughput manner. Because protein stabilities contain four primary facets: conformational, chemical, colloidal, and interfacial, a corresponding stress condition need to be used to study each aspect. For example, proteins are often exposed to heat to screen formulations that can stabilize protein conformation. Protein conformation stability is often reflected using a stability indicating parameter, the most common one being a protein's melting temperature (T_m). It is generally assumed that the more a formulation condition increases T_m, the better stabilizing effect it has. Protein T_m can be measured using many biophysical techniques including FTIR, CD, fluorescence, DSC, etc. Among these, fluorescence is a popular method because of its ability to be employed in a high-throughput manner and its relatively high sensitivity.

Specific therapeutic needs often require unique formulations (high concentration mAbs, adjuvanted vaccines). Such conditions can pose significant analytical challenges during their formulation screening. For example, high concentration mAbs strongly absorb light and may cause inner filtering effects in conventional intrinsic fluorescence. Turbid adjuvanted vaccines highly scatter light and can interfere with fluorescence signals. To avoid these challenges, they are often screened under simplified conditions (i.e. using a clear solution in the absence of adjuvants or the use of a low mAb concentration). However, there exist significant differences between the simplified and commercially relevant conditions. For instance, antigen/adjuvant interactions are absent under the simplified condition. Short-range interactions are missing in low mAb concentration samples. We found that these differences could result in discrepancies in formulation screening results performed under these two conditions. It is, therefore, preferable to perform formulation screening under a commercially relevant condition. In a later chapter of this thesis, we

presented a workflow for direct formulation screening of analytically challenging but commercially relevant formulations (e.g. high concentration mAbs, turbid adjuvanted vaccines, etc.) using a novel high-throughput fluorescence plate reader.

6.2. Conclusions and future Directions

6.2.1. Chapter 2

In chapter 2, we studied the structural properties and stability of LS using various biophysical tools. Chemical unfolding of LS in PBS buffer was performed using urea or guanidine hydrochloride as a denaturant. Guanidine was found to be more effective than urea in altering protein structure. Urea at 8.5 M was not able to disrupt the oligomeric state of LS. In contrast, guanidine at 2 M was able to distort the icosahedral structure of LS. A molten globular state was observed for LS in the present of 1.5 M guanidine HCl. Such states were highly prone to aggregate and eventually precipitated out of solution. The pH-dependent thermal stability of LS was studied over a pH range of 5.0 to 8.0 and a temperature range of 10 to 90 °C. A large data set was collected of LS's secondary structure by circular dichroism (CD), tertiary structure by fluorescence, quaternary structure by light scattering, and overall conformational stability by differential scanning calorimetry (DSC). Such data sets were then integrated to generate an empirical phase diagram and radar charts for visual presentation of the stability of LS as a function of pH and temperature. Five distinct phase regions were identified. The stability of LS was found to be highly sensitive to solution pH. LS tended to aggregate when the pH value is less than 5.0. The main thermal transition (T_m2) of LS was above 80 °C. Fluorescence and DSC also detected a small early transition (T_m1) that was not seen by CD and light scattering. The origin of T_m1 was further investigated. LS contains 60 binding sites for phosphate anions and can form LS/phosphate

complex in phosphate containing buffers. The molecular origin of T_m1 was found to be due to the thermal dissociation of phosphate ions from the LS/phosphate complex. Free LS adopts an "open" conformation with more exposed hydrophobic patches compared to the LS/phosphate complexes, which has a more "closed" conformation. The main transition arises from the combination of thermal dissociation of the icosahedral structure, unfolding, and consequent aggregation.

It would be interesting to obtain a cryo-EM or crystal structure of the free LS and compare it with the crystal structure of the LS/phosphate complex currently available in the PDB database. Such structural difference would provide useful insights into structural alterations at the atomic level and may confirm the "breathing" motion of LS proposed by several laboratories to explain the possible release mechanism of lumazine from the cavity of LS to the bulk solution (257). It may also be worthwhile to perform a molecular dynamic simulation to visualize the "breathing" motions mediated by phosphate binding.

6.2.2. Chapter 3

In chapter 3, we utilized LS as a polyvalent scaffold to develop vaccines against ricin toxin. Ricin is a highly poisonous toxin produced in caster beans and has long been considered as a potential bioterrorism agent. Since there are no approved ricin vaccines and the current vaccine candidates under development fail to produce long-term protections in humans, we aimed to develop highly immunogenic ricin vaccines to protect the public, military, and first responders using a polyvalent antigen display strategy. A linear neutralizing epitope, designated as PB10, was genetically fused to the C terminus of an LS subunit. The resulting fusion protein successfully assembled and formed a nanoparticle (LS_PB10) displaying in total 60 copies of PB10 epitopes on the surface. Fusion of PB10 did not affect secondary or tertiary structure of the scaffold.

LS_PB10 showed extremely tight binding affinity to a mouse antibody targeting the PB10 epitope. Such strong affinity may be partially attributable to the polyvalency of the PB10 epitope on LS. LS_PB10 elicited moderate levels of serum titers against ricin in mouse post three immunizations. Unfortunately, these titers failed to protect mice from toxification of ricin during a challenge study. Possible reasons include: 1) the use of the PB10 epitope alone may not be able to provide complete protection; 2) the immunodominant role of LS may induce epitope suppression; 3) the loss of the PB10 peptide's secondary structure may compromise the quantity and/or quality of induced anti-ricin titers. Overall, LS is a promising scaffold as a vaccine scaffold. It, however, suffers a critical drawback-its intrinsically high immunogenicity, and this is indeed a common issue for protein-based scaffolds for vaccine use. PEGylation of the surface of a scaffold surface has been found to be an effective means to immunologically mask the scaffold (141). The display of a relatively large epitope to cover the surface of a scaffold may also be worth considering.

Since PB10 itself seems to be insufficient to provide protection against ricin, it might be worth trying to make LS-based combination vaccines using multiple neutralizing epitopes. Initial attempts to express LS-based ricin vaccines presenting several other linear epitopes in *E.coli* systems were not successful due to the formation of inclusion bodies. The expression systems and/or conditions may be optimized to achieve a soluble fusion protein with correct assembly. In addition, the majority of neutralizing epitopes on ricin have been found to be conformational rather than linear, therefore an LS-based vaccine using conformational epitopes may be promising. However, presenting a conformational epitope on the surface of a scaffold can be quite challenging because it would require careful design of a construct to ensure the correct folding of the conformational epitope. An easier and more straightforward idea is to present a mutant of the ricin A chain (RiVax or RVEC) on LS. The surface of LS, however, is not large enough to display 60

copies of the mutant. In theory, using a longer rigid linker to present the mutant further way from the scaffold could provide enough space to accommodate 60 copies of the mutant. Polyvalent display of a ricin mutant using a different protein scaffold with sufficient surface area may be an alternative. Many other scaffold systems (e.g. gold nanoparticle, liposome, silica, etc.) can also be explored to develop highly immunogenic ricin vaccines.

6.2.3. Chapter 4

Adjuvants are often used to boost immune responses of subunit vaccines. A key interest related to the development of adjuvanted formulations is understanding the compatibility between antigens and adjuvants. Antigens can interact with antigens via various types of interactions, which may affect the stability of the components. In this chapter, we studied the interactions of two emulsion-based adjuvants (ME.0 and SE) with a mutant of *S. aureus* alpha toxin (AT), a *S. aureus* vaccine candidate, using a diverse array of biophysical tools. Both emulsions use squalene as their oil phase with a similar particle size of around 100 nm. The major difference is the type of surfactants used. ME.0 contains PS80, while SE uses DMPC and Pluronic F68. In addition, SE also contains vitamin E as an antioxidant and immunostimulatory component. Size exclusion chromatography (SEC) showed that AT strongly interacted with SE because injection of the AT/SE mixture resulted in co-elution of these two components. Conversely, AT in the presence ME.0 eluted at the same time as AT in PBS buffer, suggesting a negligible interaction between AT and ME.0. FTIR analysis indicated that SE induced a β-sheet to α-helix conversion in the secondary structure of AT, and intrinsic fluorescence found a slight but significant blue shift in the Trp emission spectra of AT in the presence of SE. ME.0, however, did not have a significant effect on structures of AT. AT in PBS exhibited two thermal transitions by DSC analysis. The addition of SE dramatically raised the melting temperatures by more than 10 °C, while ME.0 slightly

decreased these two melting temperatures. We then studied effects of individual water-soluble components of emulsions on the thermal stability of AT. It was found that the thermal stabilization effect of SE on AT is probably due to interactions of AT with the oil phase (squalene, vitamin E, DMPC, etc.), and that ME.0 destabilized AT because of changes in solution conditions (pH, salt concentrations, etc.) upon mixing. On the other hand, ME.0 in the presence of AT showed decreased colloidal stability compared to ME.0 alone upon heating. SE in the presence of AT mixtures shared similar colloidal stability with SE alone. This study illustrated the applicability of a set of biophysical tools to characterize and understand antigen/adjuvant interactions.

Although we have proposed that AT interacts with the oil phase of SE, an exact mechanism of SE/AT interaction remains unclear. This may be elucidated by labeling lipid using fluorescence dyes or performing NMR experiments. Hydrogen deuterium exchange mass spectrometry may be utilized to identify the interaction interfaces on AT. It would also be interesting to study other stability aspects (chemical and interfacial) of AT in the presence of these two emulsions. Furthermore, long-term stability studies of AT/emulsion mixtures at selected storage condition (e.g. 2 to 8 °C) should be conducted to justify a final dosage form (single-vial vs. separate-vial). The wild type AT self-assembles into a heptamer and contains a lipid membrane bound segment. AT used in this study is a mutant of the wild type and lacks the ability to self-assemble. Its sequence information is not available for proprietary reasons, but it would be worth the effort to look into the crystal structural information of the wild type AT to better understand mechanisms of AT/emulsion interactions.

6.2.4. Chapter 5

In this chapter, we compared protein formulation screening studies performed under simplified conditions versus commercially relevant but analytically challenging conditions using a fluorescence plate reader. This novel instrument is equipped with a 295 nm laser as the excitation source, a temperature controllable 384-well sample plate holder, and 2 detectors (a CCD and PMT for steady-state and time-resolved fluorescence measurement, respectively). The front-face geometry of the sample plate and the requirement of a low sample volume (5 ~ 10 μl) minimize inner filter effects for high concentration protein samples. The use of a long-pass filter (≥ 310 nm) effectively blocks Raleigh scattering and allows collection of high quality fluorescence data for turbid adjuvanted samples. Since formulation rank orders are based on protein T_m values in this study, we first explored different methods to obtain T_m values. We performed a pH screening study using citrate-phosphate buffers (pH 3.0 to 8.0) for three model proteins: a mAb, lysozyme, and RiVax (a vaccine candidate for ricin toxin, see above). Sample T_m values were generated by running two fluorescence modes (steady-state versus time-resolved), deriving two stability indicating parameters (intensity or moment) to plot melting curves, and finally using two fitting methods (six parameter fitting versus first derivative). In total, up to eight T_m values (2*2*2) were generated for a sample. We then compared these eight T_m values and found that T_m values are independent of the fluorescence mode and the data fitting method. The derived stability indicating parameter (moment or intensity) used to plot melting curves can affect T_m values. We explained such dependencies by simulating both moment and intensity as a function of temperature during a hypothetical thermal unfolding event of a protein. It was found that, in most cases, intensity is linearly proportional to the degree of unfolding. In contrast, moment can exhibit a concave-up or concave-down relationship with the degree of unfolding depending on the relative fluorescence intensity of the protein's native state over its unfolded state. A key take-home message is that a

parameter that is linear with the degree of unfolding can generate a real T_m and therefor is preferred for use.

We then performed excipient screening studies for the mAb at 0.2 versus 80 mg/mL, representing a simplified and commercially relevant condition, respectively. We found that the magnitude of excipient effects (reflected by ΔT_m) are different for these two conditions. Stabilizers (e.g. 1M sucrose, 25% glycerol, etc.) resulted in a larger increase in ΔT_m on the mAb at 80 mg/mL, probably due to a more pronounced preferential exclusion effect of excipients on high concentration mAb samples. Destabilizers (e.g. 250 mM Urea, 125 mM Arginine, etc.) became less effective for the high concentration mAb possibly because of a lower excipient/protein molar ratio.

RiVax has been found to adsorb onto aluminum hydroxide in solution, and the adsorption significantly destabilized the protein by a decrease of more than 10 °C in T_m (259). We then studied RiVax in clear solution (a simplified condition) versus in the presence of aluminum hydroxide (a commercially relevant condition). We observed both excipient rank orders and ΔT_m values are different for these two conditions. We found that 12.5% glycerol and 250 mM glycine are a better stabilizer for RiVax in clear solution and that in the presence of aluminum hydroxide, respectively. It was later found that, compared to glycerol, glycine can weaken destabilizing interactions between RiVax and aluminum hydroxide to a larger extend than glycerol. In addition, several destabilizers (PS80, guanidine HCl, etc.) slightly decreased the T_m of RiVax in clear solution by 1.5 °C, but extensively unfolded the protein in the presence of aluminum hydroxide manifesting no thermal transitions (10~90 °C). We hypothesized that this is because of a synergetic destabilization effect of aluminum hydroxide and destabilizing excipients on RiVax.

The high-throughput fluorometer used in this study shows significant potentials for the development of challenging formulations. In this study, we demonstrated its applicability for screening high concentrations of a mAb and turbid vaccine formulations containing aluminum hydroxide. It would be interesting to test the feasibility of using this instrument to screen other types of challenging formulations, such as vaccines containing emulsion-based adjuvants. In addition, this fluorescence instrument may be upgraded with an ability to measure protein aggregation simultaneously. This would help to capture a more comprehensive picture about the stability profiles of a protein of interest and benefit its formulation development.

6.3. References

1. Ladenstein R, Fischer M, Bacher A. The lumazine synthase/riboflavin synthase complex: shapes and functions of a highly variable enzyme system. The FEBS journal. 2013;280(11):2537-63.

2. Wei Y, Wahome N, VanSlyke G, Whitaker N, Kumar P, Barta ML, et al. Evaluation of lumazine synthase from bacillus anthracis as a presentation platform for polyvalent antigen display. Protein Sci. 2017;26(10):2059-72.

3. Wei Y, Kumar P, Wahome N, Mantis NJ, Middaugh CR. Biomedical Applications of Lumazine Synthase. J Pharm Sci. 2018.

4. Bianchi E, Joyce JG, Miller MD, Finnefrock AC, Liang X, Finotto M, et al. Vaccination with peptide mimetics of the gp41 prehairpin fusion intermediate yields neutralizing antisera against HIV-1 isolates. Proceedings of the National Academy of Sciences. 2010;107(23):10655-60.

5.   Peek LJ, Brey RN, Middaugh CR. A Rapid, Three-Step Process for the Preformulation of aRecombinant Ricin Toxin A-Chain Vaccine. J Pharm Sci. 2007;96(1):44-60.